



Nanoparticles of molecular photoswitches based on spin-crossover Fe(II) complexes with photoisomerizable ligands

Luong-Lam Nguyen

► To cite this version:

Luong-Lam Nguyen. Nanoparticles of molecular photoswitches based on spin-crossover Fe(II) complexes with photoisomerizable ligands. Inorganic chemistry. Université Paris Sud - Paris XI, 2014. English. NNT : 2014PA112267 . tel-01211090

HAL Id: tel-01211090

<https://theses.hal.science/tel-01211090>

Submitted on 3 Oct 2015

HAL is a multi-disciplinary open access archive for the deposit and dissemination of scientific research documents, whether they are published or not. The documents may come from teaching and research institutions in France or abroad, or from public or private research centers.

L'archive ouverte pluridisciplinaire **HAL**, est destinée au dépôt et à la diffusion de documents scientifiques de niveau recherche, publiés ou non, émanant des établissements d'enseignement et de recherche français ou étrangers, des laboratoires publics ou privés.

UNIVERSITE DE PARIS-SUD

ÉCOLE DOCTORALE DE CHIMIE DE PARIS-SUD

Institut de Chimie Moléculaire et des Matériaux d'Orsay

DISCIPLINE : CHIMIE INORGANIQUE

THÈSE DE DOCTORAT

Soutenue le 08/10/2014

par

Luong Lam NGUYEN

NANOPARTICULES DE PHOTOCOMMUTATEURS
MOLECULAIRES BASES SUR DES COMPLEXES DE FE(II) A
CONVERSION DE SPIN ET A LIGANDS PHOTO-
ISOMERISABLES

Directeur de thèse : Dr Marie-Laure BOILLLOT (Directrice de recherches, Université Paris-Sud)

Composition du jury :

Président du jury : Prof. Talal MALLAH (Professeur, Université Paris-Sud)

Rapporteurs : Dr Jean-François LETARD (Directeur de recherches, Université de Bordeaux)

Dr Sébastien FLOQUET (Directeur de recherches, Université de Versailles)

Examineurs : Dr Gabor MOLNAR (Directeur de recherches, LCC-Toulouse)

UNIVERSITE PARIS-SUD

DOCTORAL SCHOOL OF CHEMISTRY OF PARIS-SUD

Institut de Chimie Moléculaire et des Matériaux d'Orsay

SPECIALITY : CHEMISTRY

THESIS

Ph-D defense, Oktober 8, 2014

by

Luong Lam NGUYEN

NANOPARTICLES OF MOLECULAR PHOTOSWITCHES BASED ON SPIN-CROSSOVER Fe(II) COMPLEXES WITH PHOTOISOMERIZABLE LIGANDS

Thesis Supervisor : Dr Marie-Laure BOILLOT (Directrice de recherches, Université Paris-Sud)

Jury Committee :

President : Prof. Talal MALLAH (Professeur, Université Paris-Sud)

Reviewer: Dr Jean-François LETARD (Directeur de recherches, Université de Bordeaux)

Reviewer: Dr Sébastien FLOQUET (Directeur de recherches, Université de Versailles)

Examinator : Dr Gabor MOLNAR (Directeur de recherches, LCC-Toulouse)

Remerciements

Cette thèse a été effectuée dans l'Equipe de Chimie Inorganique de l'Institut de Chimie Moléculaire et des Matériaux d'Orsay (UMR 8182) de l'Université Paris-Sud.

Je remercie vivement ma directrice de thèse, le Docteur Marie-Laure Boillot, pour m'avoir encadré et soutenu pendant ces trois années de thèse.

Je voudrais exprimer ma gratitude aux Docteurs Jean-Francois Létard et Sébastien Floquet, qui ont accepté d'être rapporteurs de ma thèse. Je souhaite également remercier sincèrement le Docteur Gabor Molnar et le Professeur Talal Mallah pour avoir accepté de juger mon travail.

Merci également à toutes les personnes de l'ICMMO avec lesquelles j'ai eu l'occasion de travailler : François Brisset pour la mesure de EDS, Régis Guillot pour la diffraction des rayons X sur monocristal, Eric Rivière pour m'avoir enseigné l'art des mesures magnétiques.

Je remercie également les nombreux collaborateurs extérieurs qui ont largement contribué aux résultats présentés dans ce manuscrit : pour la spectrométrie Raman et la Microscopie optique, Lionel Rechignat et Gabor Molnar (LCC, Toulouse); également pour des mesures de spectrométrie Raman, Ali Tfayli (Faculté de pharmacie, Chatenay).

Je remercie très chaleureusement le Ministère de l'Education et de la Formation du Vietnam, l'Université des Sciences et Technologies de Hanoi et le Consortium de USTH pour m'avoir donné la chance d'étudier et de travailler en France.

Je remercie enfin le CROUS de Versailles et Campus-France pour m'avoir aidé pendant ces trois années.

Je remercie mes parents pour l'éducation et le soutien qu'ils m'ont donnés. Merci également à mes sœurs pour leurs encouragements.

Je remercie tout particulièrement ma femme et ma fille qui m'ont permis de faire tout cela et attendu pendant plus de trois ans.

Merci à toutes et à tous ...

Contents

Abbreviations.....	1
Introduction	2
Introduction	3
Reference.....	5
Chapter I.....	7
I. 1 Introduction.....	8
I.1.1 The Spin-Crossover Properties.....	9
I.1.1.1 Ligand-Field Considerations	9
I.1.1.2. Thermodynamical Analysis	12
I.1.1.3. Thermally-Induced Spin-Crossover at Solid-State.....	12
I.1.1.4. Pressure-Induced Spin-Crossover.....	13
I.1.2. Theoretical Models.....	14
I.1.2.1. Model of Slichter and Drickamer	14
I.1.2.2. Model of Sorai and Seki (Domain Model)	16
I.1.2.3. Model of Spiering.....	16
I.1.2.4. Elastic Ising-like Model.....	17
I.2. Examples of iron SCO Systems.....	17
I.2.1. Monomeric SCO Systems	17
I.2.1.1. Intermolecular Interactions Influence.....	18
I.2.1.2. Importance of Polymorphism	19
I.2.1.3. Influence of Solvent Molecules.....	19
I.2.1.4. Influence of Non-Coordinating Anions.....	20
I.2.2. Polymeric SCO Systems	20
I.2.2.1. One-dimensional SCO Systems.....	20
I.2.2.2. Two-dimensional SCO Systems.....	21
I.2.2.3 Three-dimensional SCO Systems.....	21
I.3. Light-Induced Spin-Crossover : The LIESST Approach.....	23
I.4. Light Induced Spin Change based on LD-LISC Process.....	25
I.4.1. Introduction	25
I.4.2. LD-LISC Effect in Iron Complexes	27
I.4.2.1 LD-LISC Effect in Iron(II) Complexes	27

I.4.2.2. LD-LISC Effect in Iron(III) Complexes.....	31
I.5. SCO Nanomaterials and Thin Films	32
I.5.1. Elaboration of Nanoparticles: Fundamental Concept	32
I.5.2. Methods for the Preparation of Spin-Crossover Nanoparticles	34
I.5.2.1. Reverse Micelle Method.....	34
I.5.2.2. Sol-gel Method	36
I.5.2.3. Laser Ablation Method.....	36
I.5.3. SCO Thin Films	37
I.5.3.1. Langmuir-Blodgett	37
I.5.3.2. Spin Coating	37
I.5.3.3. Constructive Method	38
I.5.3.4 Vacuum Sublimation	38
References	40
Chapter II.....	46
II.1. Introduction	47
II.2. Results	48
II.2.1. Characterization of the Precursor.....	48
II.2.1.1. X-ray Structure Analysis.....	48
II.2.1.2. TGA Analysis.....	51
II.2.1.3. Observation of Crystals upon the Thermal Evolution.....	52
II.2.2. Elaboration of $\text{Fe}^{\text{II}}(\text{Me}_2\text{-bpy})_2(\text{NCSe})_2$	53
II.3. Discussion.....	60
II.4. Experimental.....	61
II.4.1. Chemical Syntheses	61
II.4.2. Physical Measurements.....	62
II.5. Conclusions	64
References	65
Chapter III	68
III.1 Introduction	69
III.2. Experimental	70
III.2.1. Syntheses	70
III.2.1.1. t-msbpy Isomer	70

III.2.1.2. 4-methyl-2,2'-bipyridine-4'-carboxaldehyde	70
III.2.1.3. c-msbpy Isomer.....	71
III.2.1.4. Photocyclized Ligand.....	71
III.2.1.5. [Fe(msbpy) ₃](NCSe) ₂ .nH ₂ O.....	72
III.2.2. Physical Measurements	73
III.3. Results and Discussion.....	74
III.3.1. Structural Characterization of t-msbpy.....	74
III.3.2. Electronic Absorption of msbpy Isomers	75
III.3.3. Photoisomerization of msbpy Isomers	76
III.3.3.1. UV-Vis Measurements.....	76
III.3.3.2. ¹ H NMR Measurements.....	77
III.3.3.3. Reactivity of msbpy Isomers upon a 254 nm Irradiation.....	78
III.3.4. Iron(II) Complexes Characterizations	79
III.3.4.1. Electronic Absorption of [Fe(msbpy) ₃](NCSe) ₂ .nH ₂ O Complexes.....	79
III.3.4.2. Photoisomerization of [Fe(msbpy) ₃](NCSe) ₂ .nH ₂ O Complexes under UV Excitation	80
III.3.4.3. Reactivity of [Fe(msbpy) ₃](NCSe) ₂ .nH ₂ O Complexes under High-energy Excitation	81
III.3.5. Analysis of Results	82
III.4. Conclusions	85
Footnotes	85
References	86
Chapter IV	88
IV.1. Introduction.....	89
IV.2. Experimental Section	90
IV.2.1. Nanoparticles Syntheses :.....	90
IV.2.2. PMMA Thin Films of Fe(t-msbpy) ₂ (NCSe) ₂	92
IV.3. Physical Measurements.....	93
IV.3. Results and Discussion.....	94
IV.3.1. Elaboration of Nanoparticles.....	94
IV.3.2. Investigation of Nanoparticles Dispersed in PMMA Thin Films.....	102
IV.3.3. Analysis of Results.....	112

IV.4. Conclusions.....	113
References	115
Conclusions	117
Appendix	121
Appendix: Chapter II.....	122
Appendix: Chapter III	131
Appendix: Chapter IV	144

Abbreviations

ϵ :	Molar extinction coefficient	NCS :	isothiocyanato
λ :	Wavelength	NCS_e :	isoselenocyanato
χ_M :	Molar magnetic susceptibility	NPs :	Nano-Particles
c-msbpy :	4-methyl-4'-cis-styryl-2,2'-bipyridine	P :	Pressure
E :	Energy	Phen :	1,10-phenanthroline
EDS :	Energy-Dispersive X-ray Spectroscopy	PMMA :	Polymethyl Methacrylate
G :	Gibbs free energy	PSS :	Photo-Stationary State
H :	Enthalpy	S :	Entropy
HS :	High Spin	SCO :	Spin Crossover
L :	Ligand	T :	Temperature
LD-LISC :	Ligand-Driven Light-Induced Spin Change	T_c or T_{1/2} :	Transition Temperature
LIESST :	Light-Induced Excited Spin State Trapping	TEM :	Transmission Electron Microscopy
LS :	Low Spin	t-msbpy :	4-methyl-4'-trans-styryl-2,2'-bipyridine
M :	Metal	V :	Volume
Me₂-bpy :	4,4'-dimethyl-2,2'-bipyridine		
MLCT :	Metal-to-Ligand Charge-Transfer		
MPs :	Micro-Particles		

Introduction

Introduction

A contemporary challenge in materials science, that is the design of functional systems for high-density information storage, can be addressed through the optical switching of bistable molecular materials^[1]. Iron (II) spin-crossover^[2] complexes stand out as excellent candidates in the development of such bistable and photoswitchable systems. Indeed, these compounds exist in two electronic spin states (low-spin, $S = 0$ and high spin, $S = 2$) with distinctive physical properties (magnetic, optical, structural and vibrational) that interconvert under the effect of various stimuli including light. In spin-crossover type materials, the light-induced excited spin state trapping (LIESST) effect^[3] proceeds as established by Hauser, via the low-spin metal centered excitation, then the coupled electronic and structural relaxations leading at cryogenic temperatures, to the trapping in the metastable high-spin state. High working temperature and long lifetime of the photoinduced state may be achieved by alternative approaches, using either a macroscopic transformation of the solid (photoinduced phase transition)^[4] or the synergy at the molecular level between the spin crossover and the photoswitching of kinetically stable components. This second approach is the ligand-driven light induced spin change (LD-LISC) effect,^[5] first demonstrated at ICMMO laboratory, which consists in the incorporation of a photoisomerizable ligand in the coordination sphere of a spin-crossover center. It has been developed with different photoactivable groups (stilbenoids,^[6] diarylethene,^[7] diazobenzene,^[8]). Recently, strategies based on a large configurational relaxation of ligands^[9] or a change of the number of donating atoms of ligands^[10] have been also explored.

Photoinduced transformations of molecular switches^[11] were usually investigated in solution, in highly diluted composites and more scarcely in crystalline materials.^[12,3] Nevertheless, the exploitation of photoactivable materials requires their integration in functional devices and also their adaptation for optimized properties, for instance the photoconversion related to the depth of light penetration. Therefore, the nanoscale downsizing of these functionalized materials represents an important issue for applicative goals (photonic, molecular memory and switching devices) and for fundamental investigations focusing on the switching properties as a function of size reduction and environment.^[13] Along this line, important developments on methods and materials have been done recently. Different classes of switchable materials (spin-crossover, photochromic compounds) have been prepared as nanoparticles by top-down^[14] or bottom up^[15,16,17] approaches. The group has especially

focused on the nanoscale processing of molecular materials^[18] and the integration of particles in stabilized, well-adapted and easy-to-handle materials.^[19]

The objective of the present work is to investigate the metal-centered spin-crossover, the ligand-centered photoswitching and the ligand-driven light-induced spin change properties with functionalized Fe^{II} complexes in the form of nanoparticles dispersed in transparent thin films. For this investigation, we have selected a set of mononuclear complexes incorporating a bipyridine ligand substituted either with a methyl group (electronic and structural function) or a styryl group (photoactivable function). The introduction in the coordination sphere of three (strong ligand-field case) or two (intermediate ligand-field strength) bipyridine ligands (with NCSe⁻ co-ligands) has allowed the modulation of the ligand-field strength experienced by the metal ion in different systems. Optical and thermal switching properties of solids have been investigated in polycrystalline powders and in dispersion of size-reduced objects (micro-, nanoparticles).

In chapter I of this manuscript, we have reported the general properties of spin-crossover materials, the methods developed for the nanoscale processing and the photoswitching properties of this class of materials. In chapter II, is presented the elaboration of micro- and nanoparticles derived from a Fe(Me₂-bpy)₂(NCSe)₂ spin-crossover compound. In chapter III, the photoactivity of a styryl attached bipyridine in free-base molecules and diamagnetic Fe(II) complexes is investigated in solution. In chapter IV, the elaboration of spin-crossover nanoparticles based on the latter Fe(II) complexes is described; the switching of these particles embedded in thin films and the LD-LISC effect are investigated. The work presented in chapter II that has been done with the contributions of Gabor Molnar and coworkers, has been published in New Journal of Chemistry, 2014 (DOI: 10.1039/C4NJ01257G).

Reference

- [1] Special issue on ‘Molecular materials in electronic and optoelectronic devices’: *Acc. Chem. Res.*, 1999, 32, p. 191; O. Sato, J. Tao and Y.-Z. Zhang, *Angew. Chem., Int. Ed.*, 2007, **46**, 2152.
- [2] Spin-Crossover in Transition Metal Compounds, Gütllich P., Goodwin H. A. Eds., *Top. Curr. Chem.*, Springer, Heidelberg, 2004, Vol. 233-235; Spin-Crossover Materials: Properties and Applications; Halcrow M. A., Wiley, Chichester, 2013; Sato O., Tao J., Zhang Y.-Z. *Angew. Chem. Int. Ed.* **2007**, 46, 2152.
- [3] S. Decurtins, P. Gütllich, H. Spiering and A. Hauser, *Inorg. Chem.*, 1985, **24**, 2174; A. Hauser, *Top. Curr. Chem.*, 2004, **234**, 155.
- [4] S. Bonhommeau, G. Molnar, A. Galet, A. Zwick, J. A. Real, J. Mc Garvey and A. Bousseksou, *Angew. Chem., Int. Ed.*, 2005, **44**, 4069.
- [5] C. Roux, J. Zarembowitch, B. Gallois, T. Granier and R. Claude, *Inorg. Chem.*, 1994, **33**, 2273; M.-L. Boillot, J. Zarembowitch and A. Sour, *Top. Curr. Chem.*, 2004, **234**, 261
- [6] M.-L. Boillot, S. Pillet, A. Tissot, E. Rivière, N. Claiser, C. Lecomte *Inorg. Chem.* 2009, 48, 4729 ; A. Tissot, M.-L. Boillot, S. Pillet, E. Codjovi, K. Boukheddaden, L. M. lawson-Daku *J. Phys. Chem. C* 2010, 114, 21715.
- [7] K. Sénéchal-David, N. Zaman, M. Walko, E. Halza, E. Rivière, R. Guillot, B. L. Feringa, M.-L. Boillot *Dalton Trans.* 2008, 1932 ; Y. Garcia, V. Ksenofontov, R. Lapouyade, A. D. Naik, F. Robert, P. Gütllich *Opt. Mater.* 2011, 33, 942 ; M. Nihei, Y. Suzuki, N. Kimura, Y. Kera, H. Oshio *Chem. Eur. J.* 2013, 19, 6946 ; M. Milek, F. Heinemann, M. M. Khusniyarov *Inorg. Chem.* 2013, 52, 11585.
- [8] Y. Hasegawa, S. Kume, H. Nishihara *Dalton Trans.* 2009, 280 ; Y. Hasegawa, K. Takahashi, S. Kume, H. Nishihara *Chem. Commun.* 2011, 47, 6846 ; K. Takahashi, Y. Hasegawa, R. Sakamoto, M. Nishikawa, S. Kume, E. Nishibori, H. Nishihara *Inorg. Chem.* 2012, 51, 5188 ; Y. Hasegawa, R. Sakamoto, K. Takahashi, H. Nishihara *Inorg. Chem.* 2013, 52, 1658.
- [9] C. Brady, P. L. Callaghan, Z. Ciunik, C. G. Coates, A. Døssing, A. Hazell, J. J. McGarvey, S. Schenker, H. Toftlund, A. X. Trautwein, H. Winkler and J. A. Wolny, *Inorg. Chem.*, 2004, 43, 4289–4299 ; M.M.N. Wolf, R. Groß, C. Schumann, J. A. Wolny, V. Schünemann, A. Døssing, H. Paulsen, J. J. McGarvey *Phys. Chem. Chem. Phys.* 2008, 10, 4264.

- [10] S. Venkataramani, U. Jana, M. Dommaschk, F. D. Sönnichsen, F. Tuczek, R. Hergès *Science* 2011, 331, 445 ; S. Thies, H. Sell, C. Bornholdt, C. Schütt, F. Köhler, F. Tuczek, R. Hergès *Chem. Eur. J.* 2012, 18, 16368.
- [11] B. L. Feringa *J. Org. Chem.* **2007**, 72, 6635-6652 ; B. L. Feringa, *Molecular Switches*, Wiley-VCH, Darmstadt, Germany 2001.
- [12] *Photochromism : Molecules and Systems*, Elsevier Science, H. Dürr and H. Bouas-Laurent Eds, 2003 ; Special issue on Photochromism: Memories and switches, *Chem. Rev.* 2000, 100, 1685 ; K. Amimoto, T. Kawato *Journal of Photochemistry and Photobiology C: Photochemistry Reviews* 6 (2005) 207–226.
- [13] A. Bousseksou, G. Molnár, L. Salmon, W. Nicolazzi, *Chem. Soc. Rev.* 2011, 40, 3313–3335.
- [14] A. Spangenberg, R. Métivier, J. Gonzalez, K. Nakatani, P. Yu, M. Giraud, A. Léaustic, R. Guillot, T. Uwada, T. Asahi *Adv. Mater.* 2009, 21, 309.
- [15] N. Sanz, A. C. Gaillot, P.L. Baldeck, A. Ibanez *J. Mater. Chem.*, **2000**, 10, 2723.
- [16] (a) E. Coronado, J. R. Galan-Mascaros, M. Monrabal-Capilla, J. Garcia-Martinez and P. Pardo-Ibanez, *Adv. Mater.*, 2007, 19, 1359; (b) T. Forestier, S. Mornet, N. Daro, T. Nishihara, S. Mouri, K. Tanaka, O. Fouche, E. Freysz and J.-F. Létard, *Chem. Commun.*, 2008, 4327; (c) T. Forestier, A. Kaiba, S. Pechev, D. Denux, P. Guionneau, C. Etrillard, N. Daro, E. Freysz and J.-F. Létard, *Chem.–Eur. J.*, 2009, 15, 6122; (d) J. R. Galan-Mascaros, E. Coronado, A. Forment-Aliaga, M. Monrabal-Capilla, E. Pinilla-Cienfuegos and M. Ceolin, *Inorg. Chem.*, 2010, 49, 5706; (e) A. Tokarev, L. Salmon, Y. Guari, W. Nicolazzi, G. Molnar and A. Bousseksou, *Chem. Commun.*, 2010, 46, 8011; (f) L. Salmon, G. Molnar, D. Zitouni, C. Quintero, C. Bergaud, J.-C. Micheau and A. Bousseksou, *J. Mater. Chem.*, 2010, 20, 5499; (g) C. Faulmann, J. Chahine, I. Malfant, D. de Caro, B. Cormary and L. Valade, *Dalton Trans.*, 2011, 40, 2480; (h) A. Tokarev, L. Salmon, Y. Guari, G. Molnar and A. Bousseksou, *New J. Chem.*, 2011, 35, 2081.
- [17] J. Larionova, L. Salmon, Y. Guari, A. Tokarev, K. Molvinger, G. Molnar and A. Bousseksou, *Angew. Chem., Int. Ed.*, 2008, 47, 8236.
- [18] A. Tissot, L. Rechinat, A. Bousseksou, M.-L. Boillot *J. Mater. Chem.* 2012, 22, 3411 ; P. Chakraborty, M.-L. Boillot, A. Tissot, A. Hauser *Angew. Chem. Int. Ed.* 2013, 52, 7139.
- [19] A. Tissot, J.-F. Bardeau, E. Rivière, F. Brisset and M.-L. Boillot, *Dalton Trans.*, 2010, 39, 7806 ; R. Bertoni, M. Lorenc, A. Tissot, M. Servol, M.-L. Boillot, E. Collet *Angew. Chem. Int. Ed.* 2012, 51, 7485.

Chapter I

Chapter I

Spin-State Switching of Spin-Crossover Materials, Nanoscale Processing and Conversion with Light

I. 1 Introduction

The first report on spin-crossover (SCO) phenomenon was done by Cambi and al^[1] in 1931. The temperature dependent magnetic moments of iron(III) tris-dithiocarbamate materials was described as resulting from an equilibrium between the two magnetic isomers. Later, Baker and al^[2] have recognized the occurrence of strongly cooperative spin transitions of iron(II) complexes of general formula $[\text{Fe}(\text{L})_2(\text{X})_2]$ (where $\text{L} = 2,2'$ -bipyridine, 1,10-phenanthroline and $\text{X} = \text{NCSe}^-$, NCS^-). For some of them, the abrupt switching between the low-spin state at low temperature and the high-spin state at high temperature was associated to a hysteresis effect. Therefore, the research works have been centered on the elaboration of new spin-crossover materials and subsequent investigations and theoretical analyses of cooperative processes. The spin-crossover process was identified for various transition metal complexes including iron(III) ($3d^5$), iron(II) ($3d^6$), cobalt(II) ($3d^7$), cobalt(III) ($3d^6$) and manganese(III) ($3d^4$) ions.^[3]

The SCO field has received further interest, when Kahn and Kröber^[4] in the early nineties have demonstrated, that such materials could be useful for technological applications (display, optical storage).^[4-5] Using a class of Fe^{II} -triazole polymeric materials undergoing cooperative spin transitions with relatively large thermal hystereses, these authors have shown, that the temperature range of bistability (or memory effect) might be centered at ambient temperature by appropriate chemical modifications.

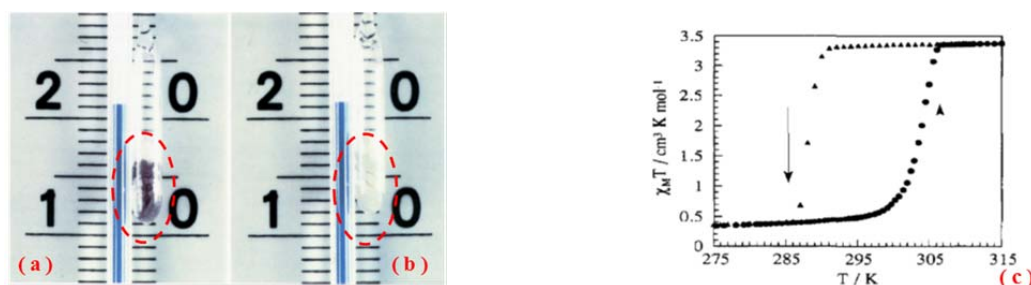


Figure 1: Images of the $\text{Fe}(\text{Htrz})_{3-3x}(\text{4-NH}_2\text{-trz})_{3x}(\text{ClO}_4)_2 \cdot n\text{H}_2\text{O}$ complex with $x = 0.05$ in the LS (a, pink color) and HS (b, white color) states at the room temperature; the curve of $\chi_M T$ vs T (χ_M = molar magnetic susceptibility, T =temperature) presents a hysteresis loop centered at ca. 295 K (c).^[4]

In the **Figure 1**, the bistability in the hysteresis loop is illustrated by the powder colored in pink (low-spin state) or white (high spin state) at 21°C depending on the thermal history of the Fe^{II}-triazole solid.^[4]

Light Induced Excited Spin State Trapping (LIESST) effect was discovered by Decurtins, Hauser and Güthlich^[6] who showed in 1984 that the spin state switching could be triggered at low temperature by light irradiation. From this seminal discovery of LIESST, important developments have emerged, that cover a broad field: photomagnetism, switchable molecular materials, multifunctional compounds and new research areas aiming to control the state of matter.

The current research on this class of compounds, considered as archetypes of bistable and switchable molecular materials, is directed towards the downsizing and processing of materials, the incorporation into multifunctional devices for probing their technological potentialities and addressing the fundamental issues related to the scaling effects.

The first paragraph will deal with the ligand-field considerations allowing the molecular properties to be rationalized; we will then briefly discuss the variety of solid state properties reported in the literature as well as related theoretical models, approaches for photo-induced spin-crossover and finally, we will describe basic features concerning nanochemistry applied to spin crossover materials.^[7]

I.1.1 The Spin-Crossover Properties

I.1.1.1 Ligand-Field Considerations

The spin-crossover (SCO) phenomenon occurs in 3d⁴-3d⁷ pseudo-octahedral (O_h) transition metal complexes^[7a, 7c, d] under the effect of a weak external perturbation (T, P, hν, H, ...) when the low spin (LS) or high spin (HS) state of the metal ion are in a close energy proximity. In the case of 3d⁶ iron(II) ions, the SCO process takes place between the diamagnetic (S=0) and paramagnetic (S=2) states associated to the electronic configurations shown in **Figure 2**. From Ligand-field theory, the five 3d iron(II) ion's orbitals in an ideal octahedral coordination geometry split into non-bonding t_{2g} orbitals (d_{xy}, d_{yz} and d_{zx}) and anti-bonding e_g orbitals (d_{x²-y²} and d_{z²}) pointing towards the ligand donor atoms. The energy difference between the t_{2g} and e_g orbitals is called the ligand-field strength parameter (Δ), while P denotes the mean spin-pairing energy. The Fe^{II} ion (3d⁶) in this environment is found

in two electronic configurations depending on Δ and P values. In a strong ligand field (Δ larger than P), the six 3d electrons will fully pair up in the t_{2g} orbitals of lowest energy.

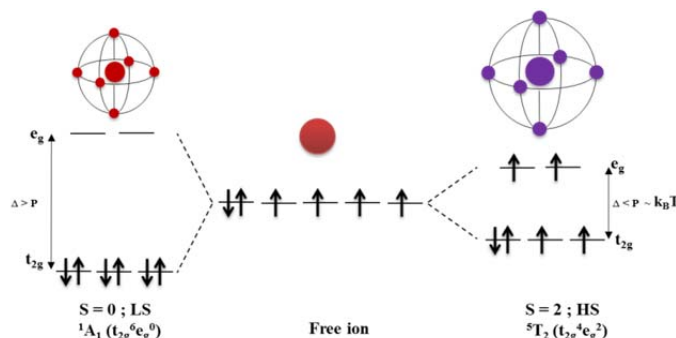


Figure 2: Electronic configurations of an octahedral 3d⁶ iron(II) complex. The relative stabilization of the LS state and HS states depends on the importance of Δ , the energy gap between the t_{2g} and the e_g orbitals and the mean spin-pairing energy P .

The $(t_{2g})^6(e_g)^0$ configuration gives rise to a low-spin (LS, $S = 0$, 1A_1) electronic state. Conversely, if Δ is smaller than P (case of weak ligand field), the 6 electrons will occupy the five 3d orbitals according to Hund's rule with a maximum spin multiplicity as for the free ion. The $(t_{2g})^4(e_g)^2$ configuration gives rise to a fundamental high-spin (HS, $S = 2$, 5T_2) electronic state. When Δ and P compare, a spin state switching between the LS and HS states may occur under the effect of a small external perturbation. This phenomenon named spin-crossover (or spin transition in case of cooperative transformation) is accompanied by the switching of all properties including the structural ones.

Indeed (it must be emphasized that) the change of electronic configuration (from $t_{2g}^6e_g^0$ to $t_{2g}^4e_g^2$) is coupled to the rearrangement of the coordination sphere. The distances between metal and donor atoms of ligands necessarily lengthen in the HS state due to the population of antibonding e_g orbitals and the loss of π backdonation effect resulting from $(t_{2g}^6e_g^0)$ configuration. This LS–HS rearrangement thus corresponds to a molecular swelling (ca. 3-5 %, estimated from the volume change of the unit-cell volume per formula unit, $(V_{HS}-V_{LS})/V = \Delta V_{HL}/V = \text{ca. } 25 \text{ \AA}^3$) and a change of the average metal-donor atoms distance (ca. 10 %, $\Delta r_{HL} = r_{HS}-r_{LS} = 0.20 \text{ \AA}$ for Fe(II) ion). It means that the ligand field strength Δ , which varies as $1/r^n$ ($n = 5-6$) on the average metal–ligand distance, increases by a factor estimated to ca. $1.75 = \Delta_{LS}/\Delta_{HS}$. Other factors influencing this Δ parameter are the nature and charge of donor atoms and the valence of metal ion. The spin-crossover process can be monitored through changes in magnetic, optical, vibrational or structural responses.

In **Figure 3**, the Tanabe-Sugano diagram of a transition metal ion with a $3d^6$ configuration (for example, iron(II)) shows the energies of the excited electronic states relative to the ground state in units of the Racah parameter B (electron-electron repulsion) as a function of the ligand field strength (also given in units of B).^[8]

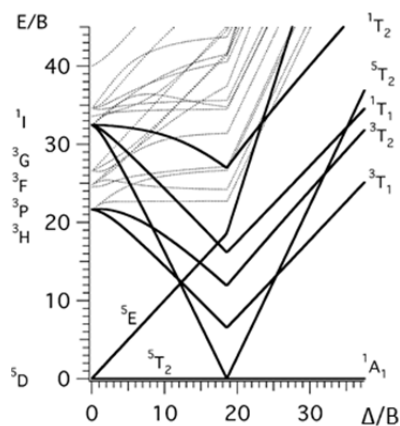


Figure 3: Tanabe-Sugano diagram for a transition metal ion with six d electrons.^[8b]

Under the effect of the ligand field, the free ion ground state (5D) splits into the 5T_2 ($t_{2g}^4 e_g^2$) HS state (ground state) and a 5E_g ($t_{2g}^3 e_g^3$) excited state. Above the critical value of the ligand field strength, the 1A_1 ($t_{2g}^6 e_g^0$) LS state is stabilized relative to the HS state and it becomes the electronic ground state^[8a]. In the vicinity of the crossover, when the zero point energy difference between the two spin states $\Delta E^{\circ}_{HL} = \Delta E^{\circ}_{HS} - \Delta E^{\circ}_{LS}$ compares to the thermal energy kT , the spin state switching results from a change of temperature. It has to be noted that the continuous variation of Δ/B parameter plotted in **Figure 3** does not correspond to geometries maintained at equilibrium because of the structural reorganization at the crossover leading to distinct Δ_{LS} and Δ_{HS} parameters, distinct vibrational modes.

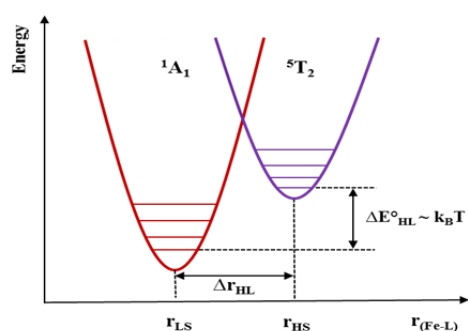


Figure 4: Representation of the potential energy wells of the 1A_1 and 5T_2 states of an iron(II) SCO system determined by the thermodynamic.

The spin-crossover process is most conveniently discussed on the basis of the diagram pictured in **Figure 4** showing potential energy curves of each state as a function of the metal-donor atom distance (r_{Fe-L}). The larger the vertical shift ΔE°_{HL} , the higher the temperature at which the spin-crossover occurs.

The most common way to control the spin-state of a SCO compound is a variation of temperature. The range of thermal stability of LS and HS species is

I.1.1.2. Thermodynamical Analysis

For an assembly of Fe(II) spin crossover species in equilibrium with their environment, we have to consider the variation of standard Gibbs free energy ($\Delta G_{HL} = G_{HS} - G_{LS}$) that comprises enthalpic ($\Delta H_{HL} = H_{HS} - H_{LS}$) and entropic ($\Delta S_{HL} = S_{HS} - S_{LS}$) contributions.

$$\Delta S_{HL} = S_{HS} - S_{LS} = \Delta S_{HL}^{spin} + \Delta S_{HL}^{vib} > 0$$

$$\text{as, } \Delta S_{HL}^{spin} = R[\ln(2S+1)_{HS} - \ln(2S+1)_{LS}] = R\ln(5) > 0$$

$$\text{and } \Delta S_{HL}^{vib} = \Delta S_{intra}^{vib} + \Delta S_{inter}^{vib} \text{ with } \Delta S_{intra}^{vib} \gg \Delta S_{inter}^{vib} > 0$$

The higher electronic (spin multiplicity, $2S+1 = 5$ (HS, $S=2$) or $2S+1 = 1$ (LS, $S=0$)) and vibrational (mainly at intra-molecular level) degeneracies in the HS state result in a positive ΔS_{HL} entropy variation. At the transition temperature ($T_{1/2}$), the fractions of spin crossover species in the HS (n_{HS}) and LS state are equal ($n_{LS} = 1 - n_{HS} = 1/2$) and $\Delta G_{HL} = \Delta H_{HL} - T\Delta S_{HL}$ vanishes. Therefore $\Delta H_{HL} = T_{1/2}\Delta S_{HL}$ is a positive component and at very low temperature, the stable phase ($\Delta G_{HL} > 0$ as $H_{HL} \gg T\Delta S_{HL}$) is the LS one. Conversely, at high temperature, the stable phase is the HS one. Therefore the switching between the low-spin state at low temperature and the high spin state at high temperature is an entropy-driven process. Typical values for Fe(II) spin crossover complexes are $\Delta S_{HL} = 40\text{-}65 \text{ Jmol}^{-1}\text{K}^{-1}$ while the sole electronic contribution due to the spin degeneracy is $R\ln(2S_{HS}+1)/(2S_{LS}+1) = 13.4 \text{ Jmol}^{-1}\text{K}^{-1}$.

I.1.1.3. Thermally-Induced Spin-Crossover at Solid-State

Upon a thermal spin-crossover, the change of bond distances (and bond angles) of a coordination complex is associated to a local distortion in the lattice that produces stresses on the neighboring sites and by extension on the sites constituting the whole solid. Therefore the process depends on the solid-state properties, especially on the ability of the solid to accommodate structural changes through cooperative elastic interactions. This assertion is supported by the comparison of spin-crossover behaviors of distinct solid-state modifications pertaining to the same molecular compound (**Section I.3.1**).

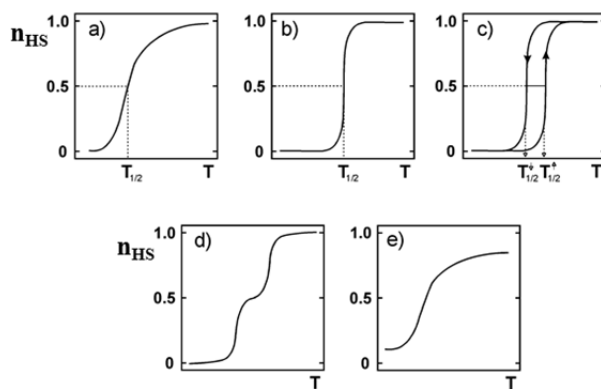


Figure 5: The nature of spin transition behaviors for SCO system in the solid states: a) gradual, b) abrupt, c) hysteretic, d) step-wise, e) incomplete.^[7a]

In **Figure 5**, are schematized the variety of spin-crossover curves observed at solid state: progressive (a), cooperative (b), hysteretic (c), step-wise (d) or uncompleted gradual (e) conversion. The transformations with variable cooperative character and occurrence of thermal hysteresis have been rationalized from different theoretical models (**Section I.2**).

I.1.1.4. Pressure-Induced Spin-Crossover

The SCO phenomenon may also result from the effect of an applied pressure. We know that the metal ligand bond distances and the molecular volume are larger in the HS state than in the LS one.^[9] Therefore the application of a positive pressure stabilizes the LS species of lower volume. Depending on the importance of pressure, some decrease of metal-ligand bond distances and thus a change of the intramolecular vibrational entropy may be also expected.

The enthalpic contribution is written as,

$$\Delta H = \Delta E + P\Delta V$$

for taking into account the $P\Delta V$ energy term due to the pressure forces ($\Delta V = V_{\text{HS}} - V_{\text{LS}}$, difference of volume between HS and LS states and P , applied pressure). In absence of applied pressure, $P_{\text{atm}}\Delta V$ is small and ΔH is approximated by ΔE . In the general case, we can define the gap between the potential energy curves by the equation:

$$\Delta E_{\text{HL}}^{\circ}(P) = E_{\text{HL}}^{\circ} + P\Delta V_{\text{HL}}^{\circ}$$

In **Figure 6**, is schematically shown the influence of pressure on the potential energy wells of the spin states of an iron(II) ion. By increasing the applied pressure, the zero point energy

difference ΔE_{HL}° increases by $P\Delta V_{HL}^\circ$, whereas the activation energy ΔW_{HL}° decreases. This change along the vertical axis shifts the spin transition to higher temperatures.

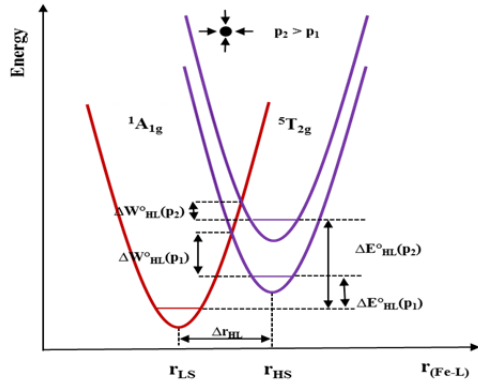


Figure 6: Scheme showing the influence of the applied pressure on the LS and HS potential wells of iron(II)

The relationship between the characteristic temperature ($T_{1/2}$) at which the spin-crossover is halfway completed and the pressure is given by a Clausius-Clapeyron type equation:

$$\frac{\partial T_{1/2}}{\partial P} = \frac{\Delta V}{\Delta S_{HL}}$$

Depending on the nature of SCO systems, the applied pressure can lead to a decrease or increase of the cooperative character of the transition.

I.1.2. Theoretical Models

Different macroscopic thermodynamical or microscopic Ising like approaches have been developed for rationalizing the main features of the spin-crossover phenomenon including the observation of gradual, abrupt or hysteretic transformations in the solid state, the role of elastic interactions or dynamical evolutions resulting from photoexcitation studies.

I.1.2.1. Model of Slichter and Drickamer

The thermodynamical model proposed by Slichter and Drickamer was derived from the model of regular solid solutions.^[10] In the Gibbs free energy, an interaction term $\Gamma(n_{HS}, T, P)$ was added to the enthalpic and entropic contributions due to the mixing of N_A molecules in the HS and LS state:

$$G = n_{LS}G_{LS} + n_{HS}G_{HS} - TS_{mix} + \Gamma$$

$$\Gamma(n_{HS}, T, P) = \gamma n_{HS}(1-n_{HS})$$

where $S_{\text{mix}} = -R(n_{LS} \ln n_{LS} + n_{HS} \ln n_{HS})$ is the mixing entropy and γ the interaction parameter, $n_{HS} = 1 - n_{LS}$ the high spin molar fraction, G_{HS} (or G_{LS}) the standard Gibbs free energy of N_A molecules in the HS (LS) state.

G_{LS} is considered as the origin of energy and $\Delta G = \Delta H - T\Delta S$, so G is written:

$$G = n_{HS}\Delta H + (1 - n_{HS})\Delta G_{LS} + RT[(1 - n_{HS})\ln(1 - n_{HS}) + n_{HS}\ln(n_{HS}) - n_{HS}\Delta S/R]$$

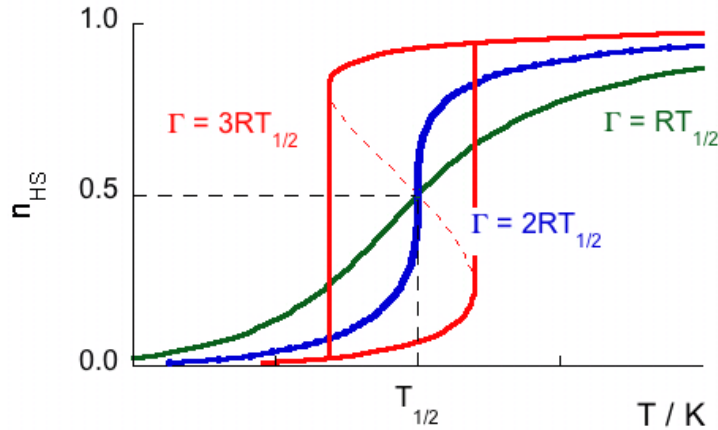


Figure 7: Variation of HS molar fraction versus temperature, calculated by Slichter and Drickamer model with $\Delta H = 7 \text{ kJ.mol}^{-1}$, $\Delta S = 50 \text{ Jmol}^{-1}\text{K}^{-1}$ and $T_{1/2} = 140 \text{ K}$.

The equilibrium condition, the derivative $(\frac{\partial G}{\partial n_{HS}})_{T, P} = 0$ leads to the relationship between T and the HS fraction:

$$T [R \ln((1 - n_{HS})/n_{HS}) + \Delta S] = \Delta H + \gamma(1 - 2n_{HS})$$

As shown in **Figure 7**, different features are considered depending on γ and $T_{1/2}$ values:

- For $\gamma < 2RT_{1/2}$, the cooperativity parameter is low, the derivative $\frac{\partial T}{\partial n_{HS}}$ is always positive between $n_{HS} = 0$ and 1 and the n_{HS} versus T curve is continuous. This process is named spin crossover (case of non- or weakly interacting complexes).
- For $\gamma = 2RT_c$, the derivative vanishes for $n_{HS} = 0.5$, the transition curve is very abrupt at $T_{1/2}$ (case of strongly cooperative solids, designed by the term spin transition).
- For $\gamma > 2RT_{1/2}$, the cooperativity is very high, the derivative vanishes for two values of n_{HS} and thus the transition curve occurs with a thermal hysteresis corresponding to the two temperature extremes. The observation of a thermal hysteresis associated to a spin transition characterizes a first-order phase transition.

This model allows an analysis of the spin crossover curve as a function of an interaction parameter and the thermodynamic ones.

I.1.2.2. Model of Sorai and Seki (Domain Model)

From experimental investigations based on heat capacity measurements of cooperative compounds $\text{Fe(II)(phen)}_2(\text{X})_2$ ^[11] and others,^[12] (with phen = 1,10-phenanthroline, X = NCS and NCS₂), Sorai and Seki have considered that the molecules with the same spin state form domains and thus, interact in the crystal lattice. The size of these domains is unchanged whatever the temperature value. These authors have introduced two related parameters: “N”, the number of domains per mole of compound and “n”, the number of molecules per domain (nN=1). In the molar Gibbs energy, the mixing entropy S_{mix} was developed as :

$$S_{\text{mix}} = k(N \ln N - n_{\text{HS}}N \ln n_{\text{HS}}N - (1 - n_{\text{HS}})N \ln(1 - n_{\text{HS}}N))$$

The relationship between temperature and HS fraction was extracted from the equation

$$\left(\frac{\partial G}{\partial n_{\text{HS}}}\right)_{T, P} = 0,$$

$$n_{\text{HS}} = \frac{1}{1 + \exp\left(\frac{n\Delta H}{R}\left(\frac{1}{T} - \frac{1}{T_{1/2}}\right)\right)}$$

including the number of molecules per domain “n”. The larger the n value (or the larger the size of domain), the smaller the N number of domains, and the more abrupt the transition. This approach was applied to the analysis of very abrupt transformations without hysteresis.

I.1.2.3. Model of Spiering

In the previous phenomenological approaches, the intermolecular interactions were taking into account without considering their physical origin. Spiering has proposed an interesting model based on the elasticity properties and their fundamental role on the cooperativity of spin-crossover materials.^[13] The latter results from the local lattice distortion associated to the relatively large variation of metal-ligand bond distances (ca. 10 %) and the propagation of the strain fields in the crystal.

In this model, the spin-crossover centers are described by hard spheres (of HS and LS volumes) inserted into holes (of fixed sizes) within an homogeneous, isotropic and elastic medium. It can be shown that this model leads to an equation similar to the one of Slichter

and Drickhamer model except that the interaction term ($\Delta - 2n_{\text{HS}}\Gamma$) should be replaced by $(1 - 2n_{\text{HS}})$. The Δ and Γ terms are parameters depending on the difference of volume between the HS and LS species and also on the bulk modulus of the crystal. In this model, the spin-crossover cooperativity related to long-range interactions increases with the difference of volume between the HS and the LS species and also with the stiffness of solid. This model was extended to the case of an anisotropic deformation of the spin crossover compound.

I.1.2.4. Elastic Ising-like Model

The Ising-like approach derived from Wajnflasz^[14] works has been widely developed for the simulation of spin crossover curves and the analysis of size effects on the spin transition. The metal center is modeled by a system with two levels, with distinct degeneracies, each level corresponding to a given electronic configuration.^[15] The Ising Hamiltonian \mathcal{H} can be written as

$$\mathcal{H} = -J \sum_{i \neq j}^N \sigma_i \sigma_j + \left(\frac{\Delta_{\text{eff}}(T)}{2} \right) \sum_i^N \sigma_i$$

where J is the interaction parameter between the centers, $\sigma_i = \pm 1$ stands for fictitious spin of the i center (-1: for LS state, +1: for HS state), $\Delta_{\text{eff}}(T)$ stands for $\Delta_{\text{eff}} = (\Delta - (k_B T/2) \ln g)$ in which Δ is the energy difference between the LS and HS states, and g is the degeneracy ratio $g = g_{\text{HS}}/g_{\text{LS}}$ between HS and LS states. The transition temperature corresponds to $\Delta_{\text{eff}} = 0$, $2\Delta = (k_B T_{1/2}) \ln g$. This Hamiltonian was solved in the mean-field approximation. Bousseksou and coworkers have modified this Ising-like model to take into account the contribution of intramolecular vibrations within the thermodynamical parameters.^[15a, 16]

I.2. Examples of iron SCO Systems

Numerous classes of spin-crossover materials (based on Fe(II), Fe(III) and Co(II) mononuclear compounds, polynuclear compounds, coordination polymers) are described in different reviews.^[7b, 17]

I.2.1. Monomeric SCO Systems

The structural analyses allow distinguishing packing controlled by intermolecular forces in between the complexes (case of electrically neutral complexes) and/or involving counter-ions, possibly solvent molecules (case of charged complexes). The versatility of molecular packing

is shown by polymorphism that can be exploited for analyzing the magnetostructural relationship. In the following, some examples are described.

I.2.1.1. Intermolecular Interactions Influence

The spin-crossover behavior and the cooperative character of molecular materials critically depend on the intermolecular interactions (hydrogen bonding, aromatic π - π stacking interactions or Van der waals interactions). In **Figure 8** is shown the thermal properties observed for a family of $\text{Fe}(\text{L})_2(\text{NCS})_2$ spin-crossover compounds isolated with $[\text{N}_2]$ bidentate ligands (L being btz = 2,2'-bithiazoline, phen = 1,10-phenanthroline or dppz = dipyrido[3,2-a:2',3'-c]phenazine). The bidentate ligands are aliphatic and distorted (btz), aromatic (phen) or aromatic with an extended π system (dppz). From the magnetostructural analysis of these similar compounds, it was pointed the importance of intermolecular interaction based on π -stacking interactions. In their absence (btz) the molecular packing only results from Van der waals contact while in presence of π - π stacking effects involving the polyaromatic ligand (phen and dppz), the solids were structured in densely packed and strongly interacting complexes in a 2-D organization. The strong cooperativity manifested here by the abrupt transition (phen) and the occurrence of a thermal hysteresis (dppz) is directly related to the structuration of these solids via a network of strong π -stacking interactions.^[18] Therefore, the presence of π -stacking interactions, together with their strength and directionality, are important parameters that have been exploited for the design of cooperative and bistable solids. It can be added that the crystallization of the compound synthesized with dppz with a solvent molecule also influences the magnetic behavior.

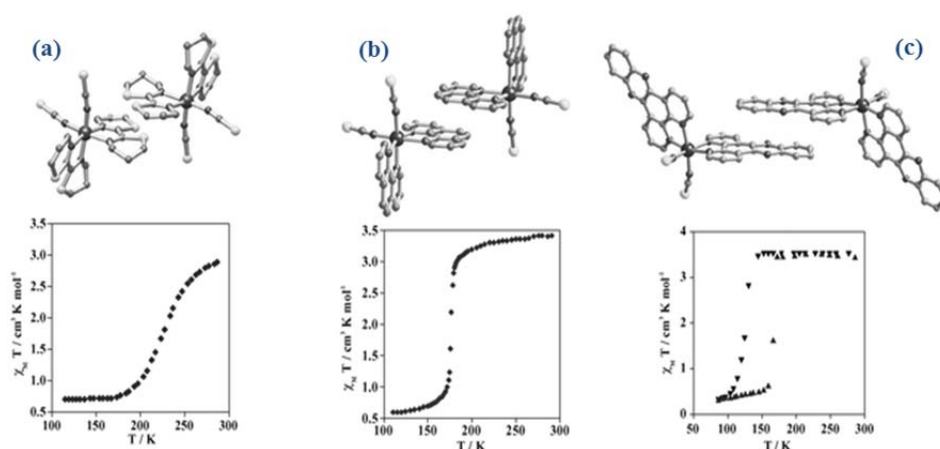


Figure 8: Structure representation of intermolecular interactions and magnetic properties of the complexes: $\text{Fe}(\text{btz})_2(\text{NCS})_2$ (a), $\text{Fe}(\text{phen})_2(\text{NCS})_2$ (b), $\text{Fe}(\text{dppz})_2(\text{NCS})_2 \cdot \text{pyridine}$ (c).^[18]

I.2.1.2. Importance of Polymorphism

The polymorphism known as the ability of a compound to exist at least in two crystalline forms characterized by distinct arrangements (or architectures, conformations) of molecules in the solid is common property in the material science. Tao and coworkers have reviewed the importance of polymorphism on the spin-crossover properties.^[19] One nice example is provided by the fac-[Fe(dppa)₂(NCS)₂] compounds (where dppa = 3-aminopropyl-bis(2-pyridylmethyl)amine) which crystallize in the form of yellow green plates A (triclinic space group P1), yellow prisms B (monoclinic space group P2_{1/c}), and pale yellow elongated hexagonal plates C (orthorhombic space group Pbca). The magnetic behaviors of these polymorphs, determined from variable temperatures magnetic susceptibility measurements, are: (A) a gradual and complete spin crossover (at $T_{1/2} \sim 176$ K); (B) a paramagnetic behavior corresponding to a S=2 state; (C) a very cooperative transition with a 8 K hysteresis loop (at $T_{1/2} = 120$ K).

I.2.1.3. Influence of Solvent Molecules

The solvent molecule inserted in the lattice via supramolecular effects (π -stacking, hydrogen bonding or Van der Waals interactions), necessarily impacts the solid-state properties of spin-crossover compounds. As shown in literature, it may modulate the ligand-field strength (as a consequence of interaction with the donor atoms), contribute to the collective transformation of the lattice (propagation of elastic deformations) or play a role of spacer leading to the unit-cell expansion. Their influence on the spin-crossover process is related to the nature, strength and dimensionality of interactions in the range of temperature of the process. In the family of Fe(2-pic)₃Cl₂.S complexes (2-pic = 2-picolylamine and S = water, methanol, ethanol) studied by Gütllich and coworkers,^[20] the ground state properties of complexes clearly depend on the nature of the solvent molecule. The dihydrate compound (triclinic phase, P1) exists in a LS form at any temperature. The monohydrate compound exhibits a spin transition with a huge hysteresis ($T_{up} = 295$ K, $T_{down} = 204$ K). The methanolate derivative (orthorhombic phase, Pbca) shows a gradual spin crossover centered at $T_{1/2} = 150$ K. Finally, the compound isolated with ethanol (monoclinic, P2_{1/c}), characterized by a two-step process centered at 121 K, was shown to result from a symmetry breaking upon successive order-disorder phase transitions that are coupled to the spin crossover process and involving the solvent molecule.^[21]

I.2.1.4. Influence of Non-Coordinating Anions

The importance of crystalline structure on the spin-crossover properties was also illustrated in the case of non-coordinating anions. Lemerrier and co-workers^[22] have investigated a family of $[\text{Fe}(\text{TRIM})_2(\text{A})_x\text{S}]$ ($\text{TRIM} = 4\text{-(4-imidazolylmethyl)-2-(2-imidazolylmethyl)imidazole}$, $\text{A} = \text{F}^-, \text{Cl}^-, \text{Br}^-$ ($\text{S} = \text{MeOH}$), I^- ($\text{S} = \text{MeOH}$)) complexes. The hydrogen bonding interactions between anions and imidazole rings affect the ligand field strength around the metal center, as demonstrated by an impressive variation of the characteristic temperature of the spin crossovers ($[\text{Fe}(\text{TRIM})_2](\text{F})_2$ that is essentially HS above 50 K, $[\text{Fe}(\text{TRIM})_2](\text{I})_2\cdot\text{MeOH}$, $T_{1/2} = 380$ K). The trend observed by the authors supports a decrease of the temperature of spin transition with an increase of inductive effect (or halides electronegativity).^[22]

I.2.2. Polymeric SCO Systems

The role of intermolecular interactions in cooperative solids can be played by ligands bridging several metal centers in coordination polymers. Such polymers (one-, two or three-dimensional systems) form classes of robust spin-transition materials with enhanced cooperative properties.^[7a, 7c, 18]

I.2.2.1. One-dimensional SCO Systems

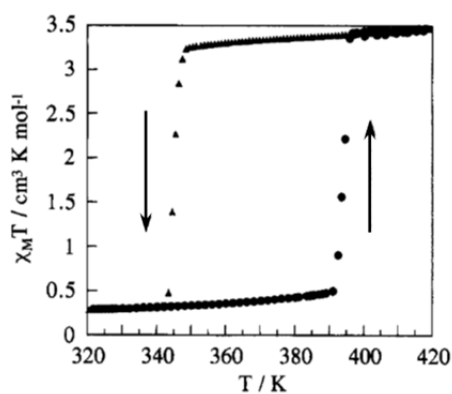


Figure 9: Temperature dependence of $\chi_M T$ of $[\text{Fe}(\text{H-trz})_2(\text{trz})](\text{BF}_4)$ complex; where H-trz is 1,2,4-1H-triazole.^[23]

The chemistry of N-donating ligands based on triazole with iron(II) ions initiated at Novosibirsk and Leiden,^[24] has led to one of the most investigated series of spin-transition polymeric materials.^[18, 25] Kröber and co-workers have reported the very abrupt spin transition of $\text{Fe}(\text{H-trz})_2(\text{trz})(\text{BF}_4)$, centered at 365 K with a large hysteresis ($T_{1/2} \uparrow = 385$ K, $T_{1/2} \downarrow = 345$ K) and analyzed this finding in the perspective of the design of molecular memory.^[23]

I.2.2.2. Two-dimensional SCO Systems

Vreugdenhil and co-workers have elaborated with a bis-triazole derivative the neutral $\text{Fe}(\text{btr})_2(\text{NCS})_2 \cdot \text{H}_2\text{O}$ (where btr is 4,4'-bis-1,2,4-triazole) 2D compound^[26] whose single-crystal X-ray structure (in **Figure 10**) shows a 2D network of interconnected Fe(II) sites.

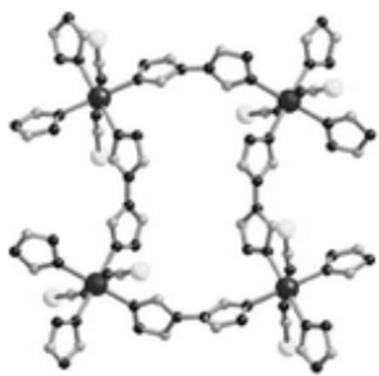


Figure 10 Structural representation of $\text{Fe}(\text{btr})_2(\text{NCS})_2 \cdot \text{H}_2\text{O}$ complex

The successive plans also interact via a hydrogen bonding interaction between a water molecule and the non-bonded nitrogen atom of the triazole moiety. The strongly cooperative spin transition at ca. 134 K associated to a 20 K hysteresis characterizes the monohydrated compound. By replacing bis-triazole by another bidentate and rigid spacer, the 4,4'-bipyridine, in the 2D $\text{Fe}(\text{bipy})_2(\text{NCX})_2 \cdot \text{Solv}$ ($\text{X} = \text{S}$ or Se , $\text{Solv} = 4\text{CHCl}_3$) compound, Adam and co-workers have

reported a special example of a cooperative spin transition occurring in two steps and thermal hysteresis ($\text{X}=\text{S}$) or a half spin transition ($\text{X}=\text{Se}$).^[27] These behaviors were accounted for by a spin state switching coupled to a crystal phase transition and a change of space group.

I.2.2.3 Three-dimensional SCO Systems

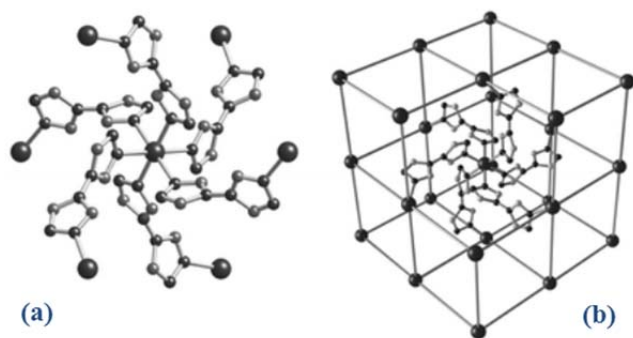


Figure 11: Coordination sphere of the Fe(II) center (a) and its 3D connectivity (b) in $[\text{Fe}(\text{btr})_3](\text{ClO}_4)_2$. The hydrogen atoms and the perchlorate anions are omitted for clarity.^[18, 28]

A 3D structure, based on the coordination of three 4,4'-bis-1,2,4-triazole per Fe(II) ion in a $[\text{Fe}(\text{btr})_3](\text{ClO}_4)_2$ compound (**Figure 11**) in presence of a non coordinating anion, was described by Garcia and co-workers.^[28] The magnetic behavior consists in a two-steps spin transition, a gradual one at high temperature and a cooperative one with a thermal hysteresis at low

temperature (**Figure 12**). The first order phase transition manifested by the thermal hysteresis preserves the space group of the solid. Thus the stepwise behavior was rationalized as

resulting from successive conversions of two complexes with slightly different ligand-field strengths and environments in the unit-cell.

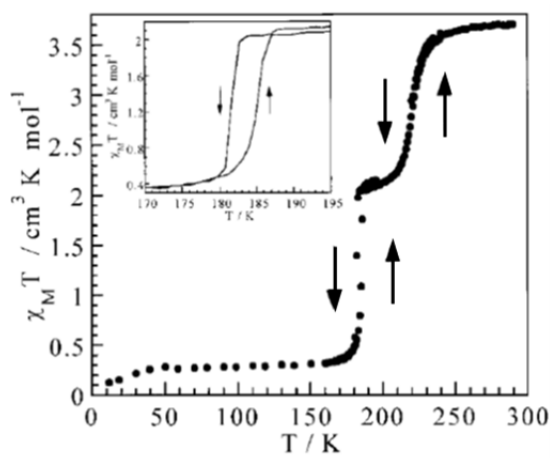


Figure 12: Temperature dependence of the $\chi_M T$ product of $\text{Fe}(\text{btr})_3(\text{ClO}_4)_2$ complex.^[28]

porous coordination polymers displays strongly cooperative spin transitions and bistabilities centered around room temperature. The bistability can be chemically modulated by guest molecules (gas, solvent) and detected by thermochromism, findings that have been investigated for applications as sensors.^[30]

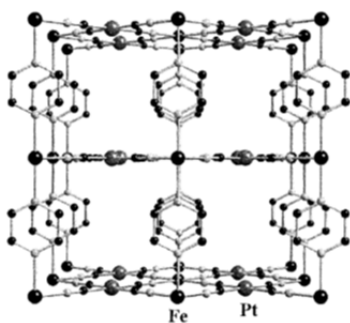


Figure 13: Structure of the 3D Hofmann-like frameworks of $\text{Fe}(\text{pyrazine})_2\text{Pt}^{\text{II}}(\text{CN})_4 \cdot 2\text{H}_2\text{O}$.^[30]

structure) and the width of hysteresis (extended cooperative interactions) increase in 3D structures with respect to the 2D ones.

More recently, a series of 3D Hofmann-like frameworks exhibiting unique spin-crossover properties has been developed in Valencia and in Kyoto.^[29] In the $\text{Fe}(\text{pyrazine})_2[\text{M}^{\text{II}}(\text{CN})_4] \cdot 2\text{H}_2\text{O}$ (where M is Ni, Pd, Pt) compounds, the Fe(II) ions bound to tetracyanometallates form dense planes that are interconnected via the coordination of Fe(II) to bidentate spacers like pyrazine (in **Figure 13**: structure of $\text{Fe}(\text{pyrazine})_2[\text{Pt}^{\text{II}}(\text{CN})_4] \cdot 2\text{H}_2\text{O}$). As shown by Niel and co-workers,^[30] this family of

The importance of the lattice stiffness and dimensionality of framework on the magnetic bistability was nicely demonstrated by the comparison between the properties of Hofmann-like frameworks build with a pyrazine (3D structures) and a pyridine (2D analogues) linker. As displayed in **Figure 14**, both the characteristic $T_{1/2}$ temperature (stabilization of LS species in the more rigid

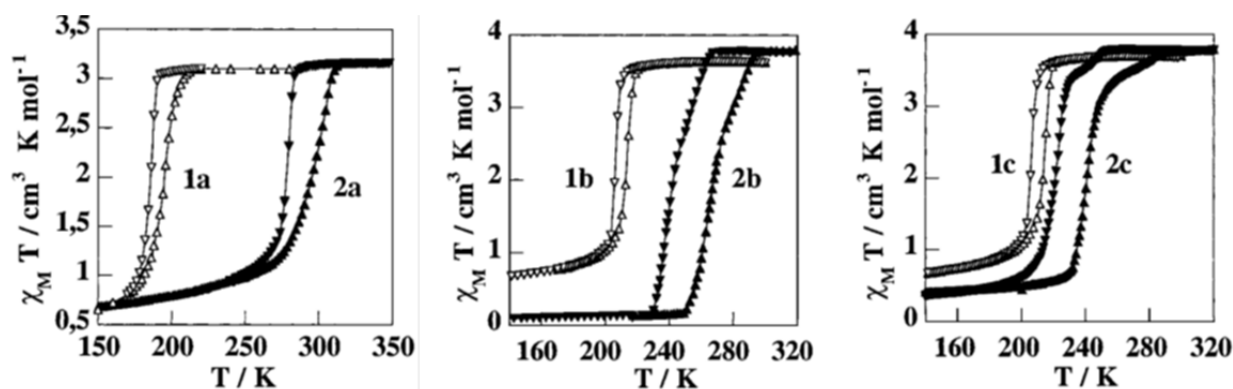


Figure 14: Comparison of temperature independence of the $\chi_M T$ of 2D $\text{Fe}(\text{pyridine})_2[\text{M}^{\text{II}}(\text{CN})_4]$ (1a-c) with 3D $\text{Fe}(\text{pyrazine})_2[\text{M}^{\text{II}}(\text{CN})_4] \cdot 2\text{H}_2\text{O}$ (2a-c) where $M = \text{Ni}$ (a), Pb (b), Pt (c).^[30]

I.3. Light-Induced Spin-Crossover : The LIESST Approach

Light-induced phenomena are important for triggering the spin state switching in molecular materials as they allow efficient and rapid transformations that may be implemented by playing with a number of variable parameters in size-reduced systems. The first light-induced spin-state change of a spin-crossover compound was recognized by McGarvey and co-workers.^[31] The authors have used the nanosecond laser irradiation to perturb the equilibrium between the singlet (^1A) and quintet (^5T) states of different iron(II) complexes in solutions. The excitation with a wavelength lying in the LS metal-ligand charge transfer (MLCT, $(d_\pi)^6(\pi^*)^0$ to $(d_\pi)^5(\pi^*)^1$ transition) absorption band has provided spectroscopic evidences for the formation of transient HS species and has allowed the kinetic analysis of the ground state recovery. In 1984, Decurtins and coworkers revealed that the irradiation at cryogenic temperature of a iron(II) spin-crossover single-crystal with a green Ar^+ laser produces a quantitative LS to HS conversion as the HS form remains trapped during hours if the temperature is lower than 50 K. The discovery of this phenomenon named “Light-Induced Excited Spin State Trapping” (LIESST) was followed by the one of the reverse-LIESST effect by Hauser,^[32] who has resolved the mechanism shown in **Figure 15**.^[33]

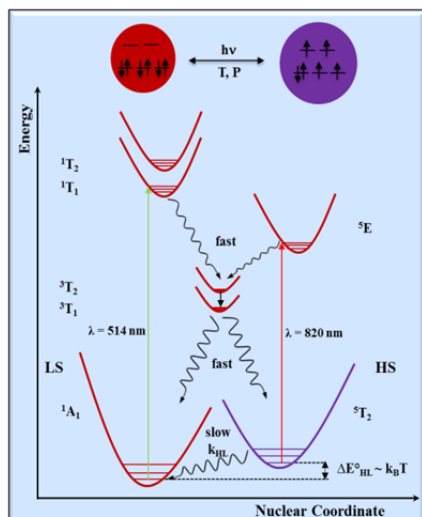


Figure 15: Schematic of proposed mechanism of LIESST and reverse-LIESST effects of iron (II) SCO complexes.^[18]

barrier between the two potential wells, requires relatively high temperature. The low temperature relaxation rates are controlled by the nuclear tunneling effect. Thus depending on the compound, the trapping of HS state may be observed during weeks at sufficiently low temperature. As shown in **Figure 15**, the reverse-LIESST effect occurs by irradiating with red light ($\lambda_{\text{exc}} = 820 \text{ nm}$) the compound prepared at low temperature in the metastable HS state. The excitation induces the transition from 5T_2 to 5E states and then the excited 5E state relaxes to the 1A_1 ground state via the 3T_1 state.

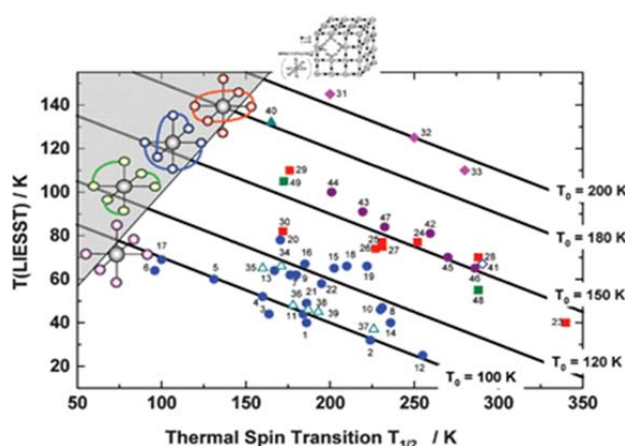


Figure 16: Variation of T_{LIESST} versus $T_{1/2}$, the characteristic temperature at which the conversion is halfway completed.^[34]

In **Figure 15**, the green light ($\lambda_{\text{exc}} = 514.5 \text{ nm}$) induces the excitation from the ground state 1A_1 (LS state) to the excited spin singlet MLCT or ligand-field (LF) states. These excited states have short lifetimes and relax within picoseconds to the lowest LS excited state, 1T_1 . The relaxation to the ground state may take place via two ways, one way back to the ground state (1A_1) via the spin triplet state 3T_1 , another way from 3T_1 to the metastable HS state (5T_2). At low temperature, the metastable HS state has a very long lifetime. Indeed, a radiative process is forbidden ($\Delta S=2$ spin-state change). The thermal relaxation process, that is determined by the overcoming of the energy

A number of iron(II) SCO materials exhibiting the LIESST effect has been reported and Létard and co-workers have proposed to use a T_{LIESST} temperature for the comparison of their HS to LS relaxation properties. The T_{LIESST} value corresponds to the temperature at which the derivative of the physical response (like magnetization) is optimal (for comparison purpose the scanning rate of the measurement should be 0.3 K min^{-1}).^[34] From this database, it was possible

to show main tendencies in the plot of T_{LIESST} versus $T_{1/2}$ (**Figure 16**).

In **Figure 17** is plotted the variation of the $\chi_M T$ product vs the temperature for a compound undergoing a strongly cooperative spin transition associated to a thermal hysteresis.

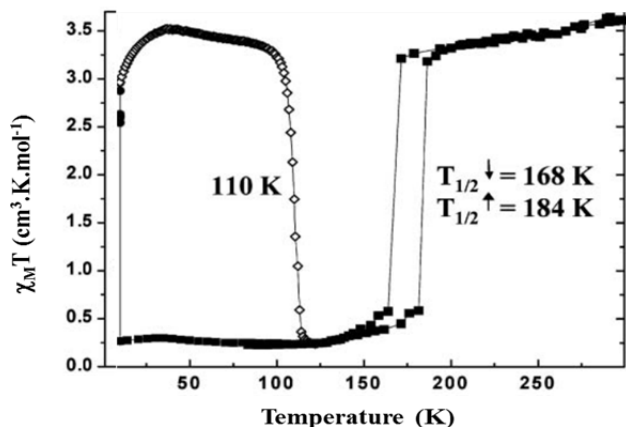


Figure 17: Temperature dependence of $\chi_M T$ for $\text{Fe}(\text{bpp})_2(\text{BF}_4)_2$ showing the thermal spin-crossover (■), the effect of light irradiation at 10 K (●), and the $T(\text{LIESST})$ experiment (◇).^[34]

The *in-situ* photoexcitation at 10 K was revealed by the increase of $\chi_M T$ value from a value typical for a LS species up to the value expected for a fully HS species. The light was switched off and the measurement was pursued up to ca. 100 K in darkness. A plateau was observed up to ca. 100 K and above this temperature, the signal decayed down to values expected for the LS ground state as in this range of temperature, the relaxation rate became much larger than the typical time scale of the technique.

These observations characterize a photomagnetic effect associated to the LIESST effect.

I.4. Light Induced Spin Change based on LD-LISC Process

I.4.1. Introduction

As mentioned above, the discovery of the LIESST effect has demonstrated the possibility to control the spin-state of molecular materials by light and the present investigations focus on mechanism, dynamic of the underlying molecular and solid-state processes, and also on systems and conditions required for slowing down the LIESST relaxation even at temperature close to the ambient one.^[34] It was recently reported that convenient optical excitation may convert a spin-transition material within the hysteresis loop centered around room temperature but this requires nanosecond laser with important heating effects.^[35]

One prototypical molecular system whose geometric and electronic structure efficiently switch upon light irradiation is the retinal, the polyene chromophore in the visual system. The investigation of this primary transformation, as those of a number of photoresponsive compounds (like spiropyran, spiroxazine, chromene, fulgide, diarylethene, stilbene or azobenzene)^[36] constitutes the active field of photo-chemistry and photophysics. The

properties of these materials based on organic (and more scarcely inorganic)^[37] components were explored for fundamental knowledge and technological applications (such as optical switches in memory devices, optical information storage and display devices).^[5]

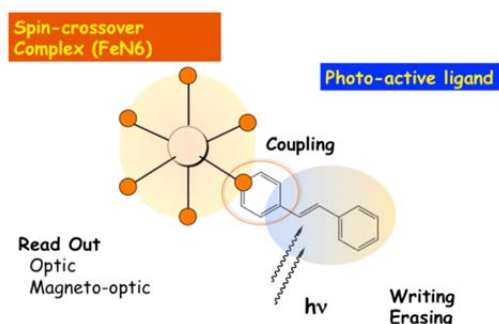


Figure 18: Scheme of LD-LISC complexes, in which the spin-crossover metal ion M is coordinated to a photoisomerizable ligand.^[38]

Therefore, Zarembowich and coworkers have proposed an original approach for elaborating non-destructive optical memories based on the coupling between a photoresponsive ligand and a spin-crossover complex. The approach named Ligand-driven light-induced spin change effect allows the separation of the writing/erasing (ligand functionality, for example

trans-cis photoisomerization of stilbenoids) and read-out (response of the spin-crossover ion). The light is used to switch the ligand structure and to modify the electronic environment of the metal ion (or ligand-field strength). A suitable variation of the ligand-field strength drives the spin-state conversion of the metal ion and the change of the related properties (**Figure 18**).

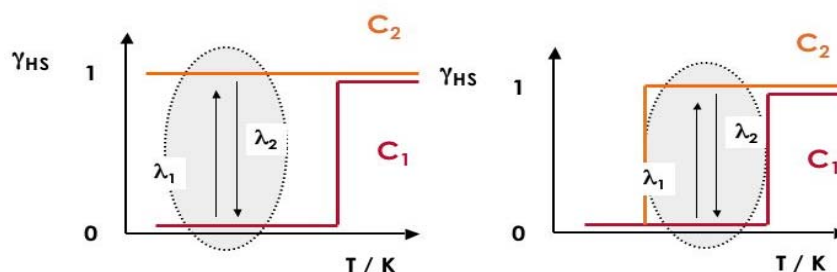


Figure 19: The magnetic behaviors of complexes (noted C_1 , C_2) incorporating each isomer of ligand are different on a range of temperature as a first one presents almost degenerated low-spin and high-spin states (spin-crossover case, C_1) and the second one, a larger energy gap between the two spin states (for example a stabilization of HS state, C_2). The photoisomerization of ligands (λ_1 , λ_2) is expected to trigger the reversible spin state conversion of the metal ion, when at the working temperature C_1 is in the LS ground state ($\nu_{HS}=0$) and C_2 , in the HS state ($\nu_{HS}=1$).^[38-39]

The essential criterion of long lifetimes of photoisomers at ambient temperature is determined by the energy barriers between the ligand isomers and the ligand field strength of coordinating groups and thus on the molecular engineering.

I.4.2. LD-LISC Effect in Iron Complexes

I.4.2.1 LD-LISC Effect in Iron(II) Complexes

In the very first report on LD-LISC by Roux and co-workers,^[39] the 4-styrylpyridine (stpy) was selected as photoisomerizable ligand. Each isomer being thermally stable because of energy barriers much higher than kT , the authors have incorporated each of them in $\text{Fe(II)(stpy)}_4(\text{NCS})_2$ complexes (noted C_t or C_c depending on the trans- or cis-stpy isomer). The C_t complex exhibits a thermal SCO centered around 108 K whereas the C_c analogue remains in the HS state at any temperature (in **Figure 20**). It was checked that as expected, the ligand-field strength was determined by the ligand configuration and was strongly enhanced for the most planar isomer (trans-stpy). One limitation pointed here was the temperature required for probing the photoisomerization and any LD-LISC effect as for such values ($T < 100$ K) the values reported for quantum yields of isomerization are especially weak.

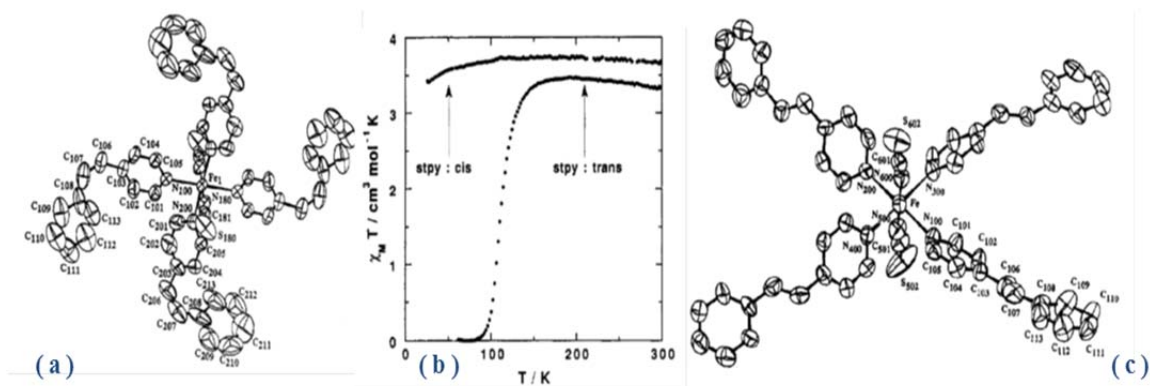


Figure 20: Molecular structures of $\text{Fe(cis-stpy)}_4(\text{NCS})_2$ (a) and $\text{Fe(trans-stpy)}_4(\text{NCS})_2$ (c) complexes at 293 K; The hydrogen atoms are omitted for clarity. Temperature dependence of the $\chi_M T$ product for both complexes (b).^[39]

Therefore the working temperature was shifted to higher values by varying the anionic ligand ($X^- = \text{NCBH}_3^-$, NCBPh_3^-) and increasing the ligand field strength.^[40] Boillot and co-workers have demonstrated the LD-LISC effect at 140 K with $\text{Fe(stpy)}_4(\text{NCBPh}_3)_2$ complexes processed in cellulose acetate films. Optical measurements were used to analyze the thermal spin crossover as well as the temperature independent behavior of C_t and C_c , respectively. The comparison between these spectra and those collected after the thin films irradiation ($T =$

140 K, $\lambda_{ct} = 260$ nm and $\lambda_{tc} = 322$ nm) indicated the formation of photostationary states containing the photoisomers with the corresponding spin states as shown by the temperature dependence of their spectra (**Figure 21**).

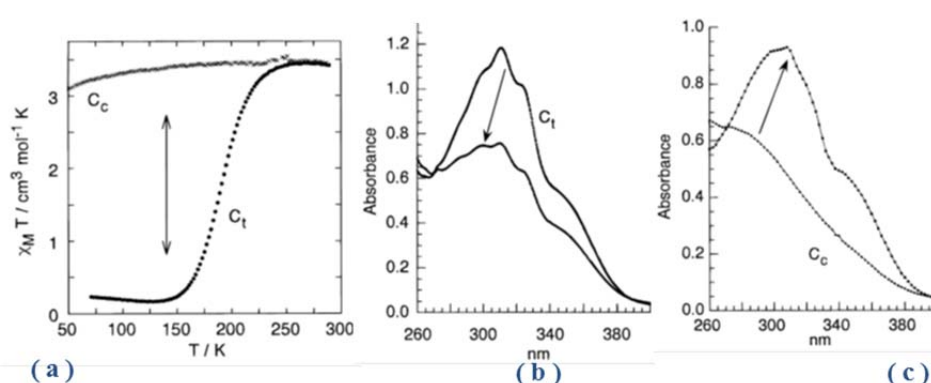


Figure 21: Temperature dependence of $\chi_M T$ for $\text{Fe}(\text{stpy})_4(\text{NCBPh}_3)_2$ complexes (a). The 140 K UV-visible spectra of $\text{Fe}(\text{stpy})_4(\text{NCBPh}_3)_2$ in cellulose acetate film before and after the irradiation: (b) C_t irradiated at 322 nm, (c) C_c irradiated at 260 nm.^[40]

The photomagnetism associated to the ligand isomerization was evidenced later with complexes of this series. The stilbenoids are strong UV absorber and thus a high dilution of samples in soft matrices was required for optimizing the light penetration and allowing the configurational changes of the $-\text{C}=\text{C}-$ double bond. Conversely, the magnetic behavior of spin-crossover complexes processed in polymeric matrices is hardly determined by standard magnetic measurements, as, in such highly diluted samples, the paramagnetic responses become much more weaker than the diamagnetic ones. Therefore prior to this investigation conducted with NCSe analogues,^[41] the magnetic properties of complexes dispersed in PMMA thin films were examined by magnetic circular dichroism measurements.^[42] The working temperature for probing the LD-LISC activity was fixed at 130 K, as C_c was found in the HS state and C_t , partly in the LS state. The photomagnetic measurements were performed at 130 K on thin films irradiated ($\lambda_{\text{exc}} = 355$ nm) within the SQUID magnetometer. The results are presented in **Figure 22**.

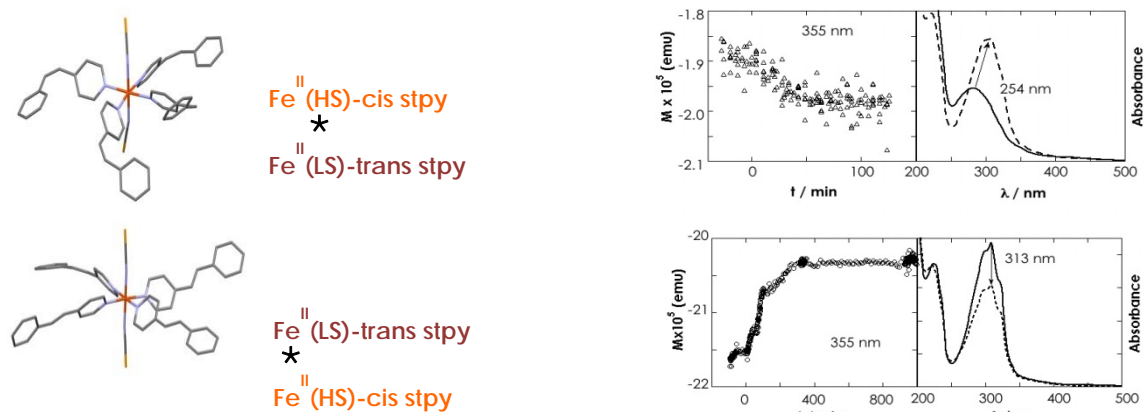


Figure 22: (left) Molecular structures of $\text{Fe}(\text{stpy})_4(\text{NCSe})_2$ complexes ;(right) The evolution of PMMA films doped with $\text{Fe}(\text{stpy})_4(\text{NCSe})_2$ versus the irradiation time ($\lambda_{\text{exc}} = 355, 313$ or 254 nm): the 130 K magnetization and optical absorption of the complex formed with trans-stpy (top) or cis-stpy (bottom) isomer.^[41]

As the analyses of single-crystal X-ray structures indicated a large fraction of free-volumes in the unit cells of both $\text{Fe}(\text{II})$ compounds, this investigation was pursued on the crystalline samples.^[43] Evidences were provided for an unidirectional and quantitative $\text{cis} \rightarrow \text{trans}$ isomerization of stpy that was detected from a visible excitation corresponding to an MLCT pathway. This solid-state transformation has led to a large change of electronic environment of the metal ion as shown by the magnetic switching between a HS ground state (starting isomer with cis-stpy) and a spin-crossover behavior (photoproduct), this first observation in a pure solid was related to the LD-LISC effect.

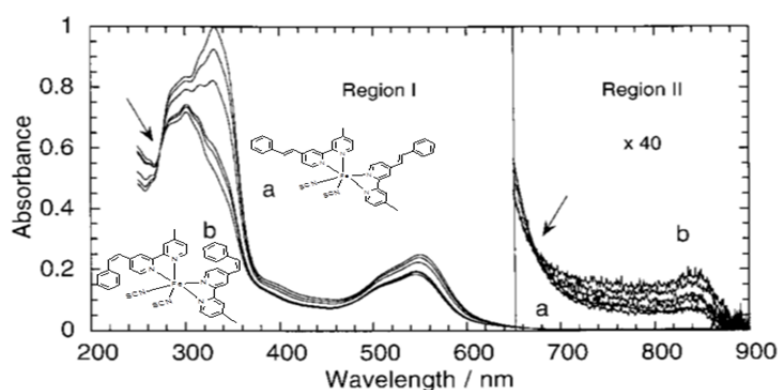


Figure 23: UV-visible spectra of an acetonitrile solution of $\text{Fe}(\text{trans-msbpy})_2(\text{NCS})_2$ before (a, initial spectrum) and after (b, photostationary state) irradiation with $\lambda_{\text{exc}} = 334$ nm.^[44]

The general method for increasing the working temperature up to room temperature, that is an important criterion for LD-LISC applications, consists to increase the ligand-field strength around the spin-crossover metal ion. This was achieved by substituting in the $\text{Fe}(\text{II})$ coordination sphere

monodentate (pyridine derivatives) by bidentate (bipyridine derivatives) ligands. Boillot and

coworkers^[44] have reported with $\text{Fe}(\text{trans-msbpy})_2(\text{NCS})_2$ (trans-msbpy = 4-methyl-4'-trans-styryl-2,2'-bipyridine) the first LD-LISC effect at room temperature in solution. Evidences of these ligand- and metal-centered transformations were provided by optical and NMR measurements (**Figure 23**).

Along this approach, the Nihishara's team has elaborated Fe(II) complexes containing tridentate ligands^[45] substituted by styryl group.

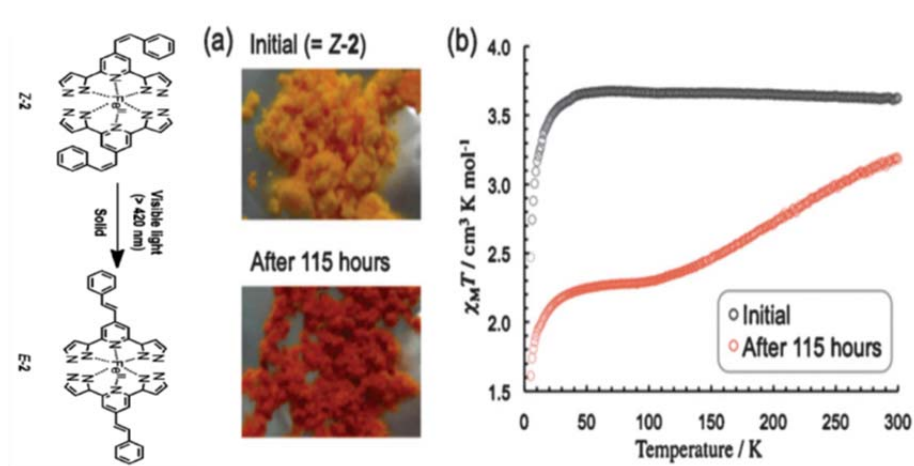


Figure 24: Photoisomerization of cis-(Z-2) to trans-(E-2) (a) and temperature dependence of $\chi_M T$ for Z-2 before and after its irradiation with visible light (>420 nm) for 115 hours.^[45a]

The $\text{Fe}(\text{cis-2,6-di(1H-pyrazol-1-yl)-4-styrylpyridine})_2(\text{BF}_4)_2$ complex (Z-2) was shown to react at solid state as shown in **Figure 24**. The visible irradiation induces a one way cis-to-trans photoisomerization and concomitantly the metal ion conversion between a HS species and a spin-crossover one leading to LD-LISC effect at room temperature (**Figure 24**).

Various photoactivable functions (isomerization of double-bond, electrocyclization, proton transfer) may be considered for triggering the spin-state conversion based on LD-LISC. Accordingly, different photochemical characteristics (excitation wavelength, quantum yield, thermal or optical reversion) of the organic part may be exploited in combination with the spin-crossover ones. Hasegawa and co-workers have investigated the properties of soluble $[\text{Fe}(\text{L})_3](\text{BF}_4)_2 \cdot 3\text{H}_2\text{O}$ (L = phenyl(2-pyridin-2-yl-3H-benzimidazol-5-yl)diazene) complexes incorporating a bidentate ligand substituted by a azobenzene function. Upon the transformation of the spin crossover complex (**Figure 25**), which was induced by irradiating the solution at room temperature, a reversible change of magnetic susceptibility, i.e. a photomagnetic effect, was resolved by NMR measurements.

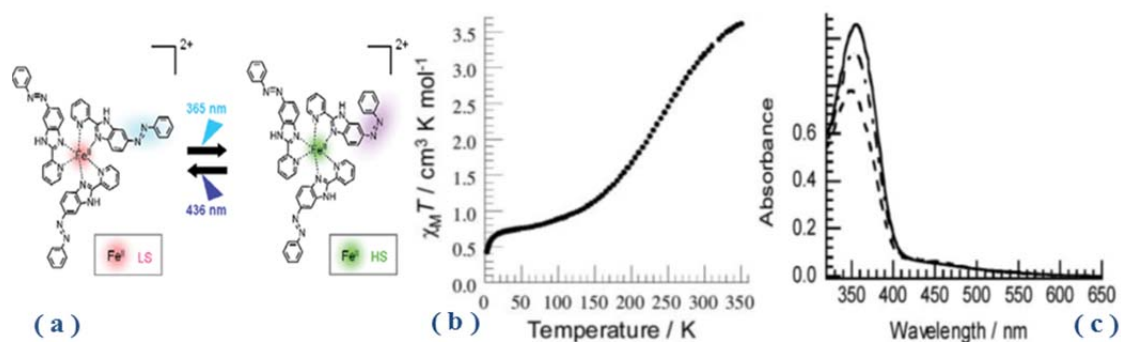


Figure 25: (a) Schematic drawing of Fe(II) complexes; (b) Temperature dependence of $\chi_M T$ for the trans-complex in solid state; (c) room temperature UV-Visible spectra of the trans-complex in acetone (solid line), in photostationary states obtained after irradiation at 365 nm (dotted line) and 436 nm (broken line).^[46]

Diarylethene molecules offer enormous advantages (large and optically reversible photochromism, high quantum yields, resistance to fatigue and potentially crystalline photochromism) that have been exploited by a few groups in combination with spin-crossover type Fe(II) components. A solid-state photochromism was observed for a HS Fe(II) complex isolated with a diarylethene monopyridyl ligand.^[47] It was concluded from the weak modulation of the paramagnetic susceptibility at room temperature, that a stronger ligand-field strength was required for ensuring a thermal spin crossover behavior of one photoresponsive complex and thus changing the metal ion spin state through the LD-LISC effect. Recently this issue was addressed with a neutral $[\text{Fe}(\text{bpz})_2(\text{phen})]$ complex ((bpz = dihydrobis(1-pyrazolyl)borate) incorporating a bidentate photoactive phen ligand (phen = 5,6-bis(2,5-dimethyl-3-thienyl)-1,10-phenanthroline).^[48] The authors have reported an efficient photoswitching of magnetic properties in solution at room temperature that was driven by the photocyclization/photocycloreversion of ligand. At solid-state, low temperature LIESST and reverse LIESST effects were required to achieve the reversible spin state switching of the spin-crossover compound as the latter crystallized with the inactive isomer of ligand.

I.4.2.2. LD-LISC Effect in Iron(III) Complexes

The LD-LISC approach may be applied to any metal ion capable of undergoing a spin crossover. It was probed with a few Fe(III) complexes including a pentadentate Schiff base and a monodentate photoswitchable ligand. The spin crossover $\text{Fe}(\text{salten})(\text{mepepy})\text{BPh}_4$ (H_2salten = 4-azaheptamethylene-1,7-bis(salicylideneminate); mepepy = 1-(pyridine-4-yl)-2-

(N-methylpyrrol-2-yl)ethane)^[49] compound was investigated in solution with RMN and optical measurements which indicated that the trans → cis isomerization of the –CH=CH– group here induced with blue light was associated to a slight decrease of the 293 K magnetic susceptibility. Analogues of this complex with styrylpyridine isomers were reported by Hirose and coworkers.^[50] The phenylazopyridine was selected by Bannwarth and coworkers^[51] for studying the switching properties of Fe(salten)(3-azpy)BPh₄ and Fe(salten)(4-azpy)BPh₄ spin crossover complexes in solutions. The fact that the photoisomerization of azpy coordinated to a Fe(III) ion - predominantly HS - was associated to a very small magnetic change was rationalized from DFT calculations. In view of the larger effects detected with Fe(II) complexes, the authors have proposed to account for the results by the weakness of π -backbonding in Fe(III) complexes and the limitation due to an unique photoactive center per metal ion.

I.5. SCO Nanomaterials and Thin Films

I.5.1. Elaboration of Nanoparticles: Fundamental Concept

It is well established that materials processed at nanoscale present unique properties as a consequence of their limited size, the importance of surface over volume ratio or their shape considerably impact chemical (for instance reactivity) or physical (collective or macroscopic) properties. The nanoparticles are elaborated by different approaches such as the top-down approach (based on physical techniques) or the bottom-up approach (based on colloidal chemistry). The research in this area has been intensified as today, applications of nanoparticles in electronic devices, medicine, chemical catalysis demonstrate the considerable potentialities related to the nanoscale control of properties.

The chemical approach used for the elaboration of nanoparticles lies on the solid precipitation in solution. The nucleation and growth processes that should be controlled have been rationalized by a kinetic model first proposed by LaMer and co-worker.^[52] The formation of particles in a solvent occurs as soon as the solute concentration exceeds the compound solubility at equilibrium. Therefore, the formation of particles requires the use of supersaturated solution, that is prepared by going away from equilibrium for example with the compound dissolution at high temperature followed by a sudden cooling (or by adding reactants). At this stage, the precipitation takes place through nucleation and growth processes.^[53] One distinguishes the homogeneous nucleation corresponding to the formation of small nuclei. The driving force of this reaction is the thermodynamical instability of the

supersaturated solution that is reflected by the balance in overall free energy ΔG between a negative term, the free energy variation associated to the solid formation and a positive term, the energy required for the appearance of a liquid-solid interface (**Figure 26**):

$$\Delta G = -\frac{4}{V}\pi r^3 k_B \ln(S) + 4\pi r^2 \gamma$$

V being the volume of the precipitated species; r , the radius of the nuclei, k_B , the Boltzmann constant; S , the supersaturation ratio, and γ , the surface free energy per unit of surface area.

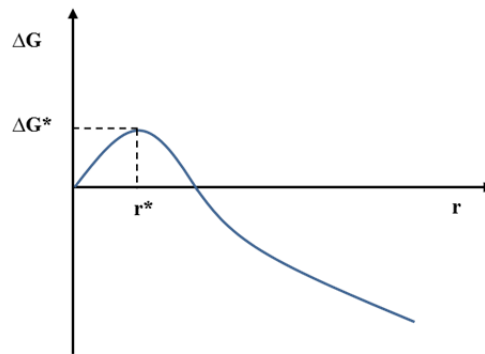


Figure 26: Curve of the overall free energy ΔG as a function of the particle size r corresponding to the case of a supersaturation solution.^[53b]

When $S > 1$ (supersaturation case, **Figure 27**), ΔG shows a positive maximum at a critical size, r^* . The critical nuclei r^* can be calculated from $d\Delta G/dr = 0$:

$$r^* = \frac{2V\gamma}{3k_B T \ln(S)}$$

The maximum of free energy ΔG^* is the activation energy for nucleation. The larger nuclei with $r > r^*$ will be stabilized (decrease of ΔG) by additional growing while, the smaller ones ($r < r^*$) will be dissolved. The formation of seeds (step I in **Figure 27**) reduces the concentration of solute and leads to the slowing down, stopping of nucleation reactions. This is followed by the step of nuclei growing (step II in **Figure 27**), which takes place till the solute concentrations reach the values associated to the equilibrium state. During this step, the growth of smaller particles is the quickest as a consequence of a more important driving force. The slow evolution - the Ostwald ripening - (step III in **Figure 27**) occurs when the solute concentration becomes closer to the limit of solubility. The small particles, that are unstable, dissolve and the deposition of matter onto larger particles gives rise to the broadening of size distributions.^[52, 54]

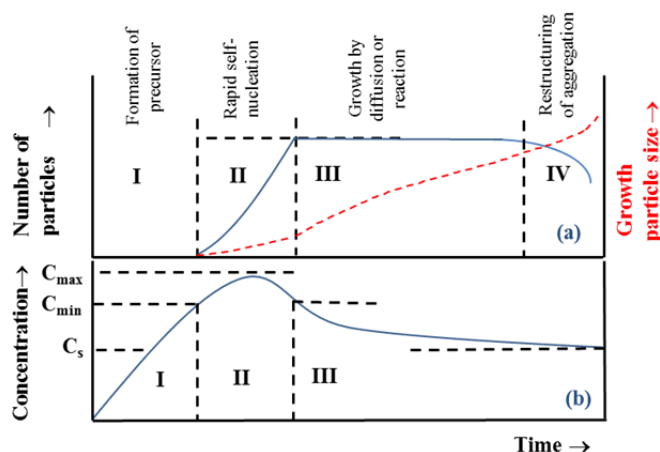


Figure 27: Evolution during the processes of nucleation/growth according to the model proposed by LaMer: (a) Number of particles and growth of particle size in solution; and (b) concentration of soluble precursors in function of time.^[52, 55]

From this mechanism, it appears that the elaboration of nanoparticles requires (i) the preparation of highly supersaturated solution (the larger the number of seeds, the smaller the sizes), (ii) the sudden formation of seeds (in order to avoid concomitant growth of particles), (iii) to stabilize the nanoparticles and prevent the Ostwald ripening by adding surface protecting reagents or by confining particles in suitable matrices.

I.5.2. Methods for the Preparation of Spin-Crossover Nanoparticles

Different approaches (reverse micelle method, sol-gel method, sudden precipitation) were developed for the elaboration of spin-crossover nanoparticles. The methods were dictated by the solubility and chemical stability of precursors and products, the selected application or investigation.^[7b, 56]

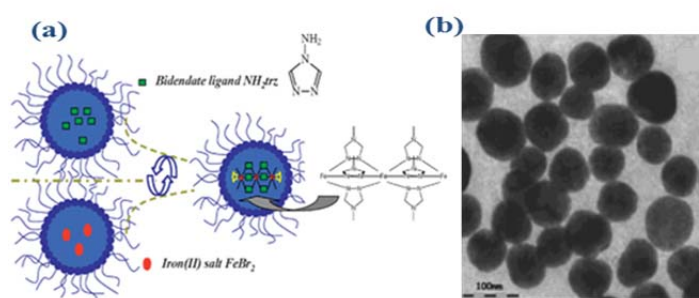


Figure 28: Schematic representation of the reverse micelles method used for the synthesis of Fe(NH₂trz)₃Br₂ nanoparticles (a); TEM image of 70 nm nanoparticles (b).^[57]

I.5.2.1. Reverse Micelle Method

Coordination polymers nanoparticles were elaborated with the reverse micelle method. It consists in the preparation of water-in-oil emulsions in presence of surfactants (molecules

with hydrophobic tail-groups and hydrophilic head-groups). It was introduced by L  tard and co-workers for the synthesis of 70 nm nanoparticles of $\text{Fe}(\text{NH}_2\text{trz})_3\text{Br}_2$ (NH_2trz is 4-amino-1,2,4-triazole)^[5a, 57] (**Figure 28**). The magnetic investigation of nanoparticles shows a spin transition with a thermal hysteresis. Coronado and co-workers^[58] have successfully elaborated 15 nm nanoparticles of $\text{Fe}(\text{NH}_2\text{trz})_3(\text{BF}_4)$ (in **Figure 29**).

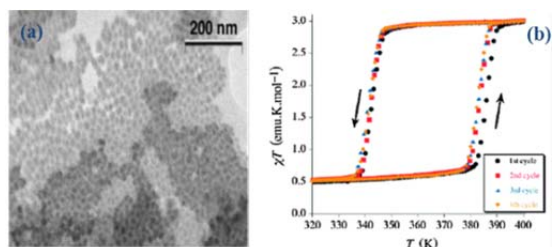


Figure 29: TEM image of $\text{Fe}(\text{NH}_2\text{trz})_3(\text{BF}_4)$ nanoparticles with size ~ 15 nm (a); and magnetic properties (b).^[58]

The striking result was the observation of almost unchanged 43 K hysteresis loop ($T_{1/2}\uparrow = 386$ K and $T_{1/2}\downarrow = 343$ K) (in **Figure 29**) with respect to the compound described in literature. In 2010, the same authors have shown that the mean size of the $\text{Fe}(\text{Htrz})_2(\text{trz})(\text{BF}_4)$ nanoparticles may be tuned down to 6 ± 3 nm with a narrow size distribution. The presence of a 29 K thermal hysteresis was confirmed by magnetic measurements.

The groups of Real and Mallah selected another series of spin transition compounds with a higher dimensionality. The nanocrystals of $\text{Fe}(\text{pz})[\text{Pt}(\text{CN})_4] \cdot 2\text{H}_2\text{O}$ ^[7d, 56] were synthesized with sizes ranging between 230-8 nm by playing with the precursors concentrations. Different features appear from the comparison between the spin crossover properties of bulk and nanoparticles. With the size reduction, the hysteresis width decreases and vanishes (size ~ 15 nm), the spin crossover curves become smoother, shift to lower temperature values and the fraction of spin-crossover species decrease. These observations were ascribed to the size effect.^[59]

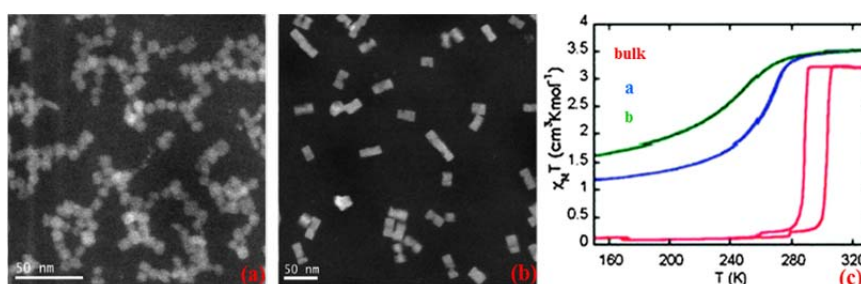


Figure 30: TEM images of nanoparticles of $\text{Fe}(\text{pz})[\text{Pt}(\text{CN})_4]$ with a size of 7.7 ± 1.2 nm (a) and of 14.7 ± 2.3 nm (b); and their magnetic properties compared with bulk (c).^[59]

The importance of the alteration of coordination sites constituting the surfaces was first pointed in relation with HS residues. From the elaboration of nanoparticles (fixed size) with

various coating on the surfaces (SiO_2 , monodentate ligands, chelating agents), Catala and coworkers have described an interesting matrix-dependent cooperativity.^[60]

I.5.2.2. Sol-gel Method

The control of nucleation and growth of particles may be achieved by precipitation and confinement in the silica pores of thin films. This approach well adapted for the elaboration of photoswitchable materials was probed with a spin-crossover compound of molecular nature $\text{Fe}(\text{mepy})_3\text{tren}(\text{PF}_6)_2$. Boillot's group^[61] used the sol-gel technique to elaborate spherical nanoparticles dispersed in silica thin films. The control of particles size (from 47-730 nm) was achieved by varying the condensation time of the mixture of precursors to form the gel. The nanoparticles were constituted by an essentially amorphous phase characterized by a spin crossover behavior distinct to that of the starting material.

I.5.2.3. Laser Ablation Method

Nakatani's group has successfully applied a Top-Down method (by laser ablation) to photochromic molecular materials.^[62] Upon the excitation with an intense laser pulse, the organic solids dispersed in solution were progressively reduced in size. This reaction was assisted by the photoswitching of diarylethene molecules located at the crystallites surface in presence of a second excitation. The elaboration of nanoparticles (size 220 nm) colloidal solutions has allowed the authors to analyze the photochromic behaviors of molecules in various states.

I.5.3. SCO Thin Films

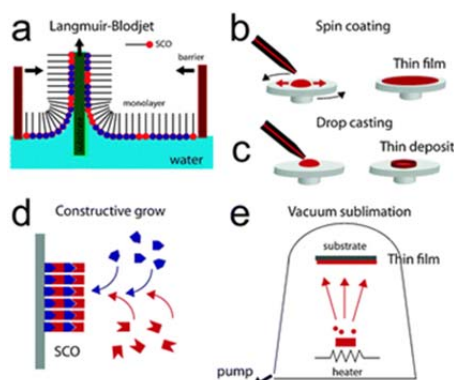


Figure 31: Schematic representation of the main methods used for the growth of thin films: Langmuir-Blodgett (a), spin coating (b), drop casting (c), constructive method (d) and vacuum sublimation (e).^[63]

The development of SCO materials that present high potentialities as memory devices, displays, sensors, hybrid electronics and others for technological applications imposes the material processing and the control of their nanoscale properties. Thin films that appear as the most advanced approach for this, can be elaborated by several techniques (**Figure 31**).^[7d, 56, 63-64]

I.5.3.1. Langmuir-Blodgett

The Langmuir-Blodgett (LB) technique consists to form molecular monolayers on a liquid-air interface and to sequentially transfer the layer onto a solid substrate by dipping the latter in the solution (in **Figure 31a**). It requires the multistep synthesis^[65] of molecules with hydrophilic heads and hydrophobic chains, the stabilization of the coordination compounds at liquid-air interface^[66] and the control of monolayer transfer. This supramolecular approach was first reported by Kahn and coworkers with an archetypical spin-crossover $\text{Fe}^{\text{II}}(\text{phen})_2(\text{NCS})_2$ derivative. The authors have elaborated LB films and extracted from infrared measurements, a thermal spin crossover curve ($T_{1/2} = 260 \text{ K}$) that retains some cooperative character. Conversely, the lost of 2D organization,^[66] that was observed upon the thin film annealing, changed the fraction of spin-crossover species. It was proposed that the increase of the latter might derive from the relaxation of strains in the 2D monolayers. LB films of $\text{Fe}(\text{III})$, $\text{Co}(\text{III})$ and $\text{Mn}(\text{III})$ complexes were elaborated and investigated.^[56, 63]

I.5.3.2. Spin Coating

Spin coating is one of most used method for the preparation of thin films of SCO compounds. Thin films are formed by deposition of droplets of a solution on rotating substrate (in **Figure**

31b). The quality of thin film (homogeneity, thickness, transparency) can be controlled through different parameters (rotation speed, temperature, viscosity of solution) and the nature of components (SCO compounds, solvent, additional polymers for instance SiO₂ or PMMA) and substrate. The characteristics of thin films were easily varied for various investigations (optical,^[61] magneto-optical,^[42] luminescence,^[67] measurements), determination of electrical resistance change,^[68] elaboration of an organic electroluminescent device.^[69]

I.5.3.3. Constructive Method

The elaboration of SCO thin films^[7d, 63-64] of a 3D SCO coordination compounds of Fe(pz)[M(CN)₄] (where M is Ni, Pd, or Pt; pz is pyrazine) was achieved owing to the constructive method, or layer by layer assembly approach.

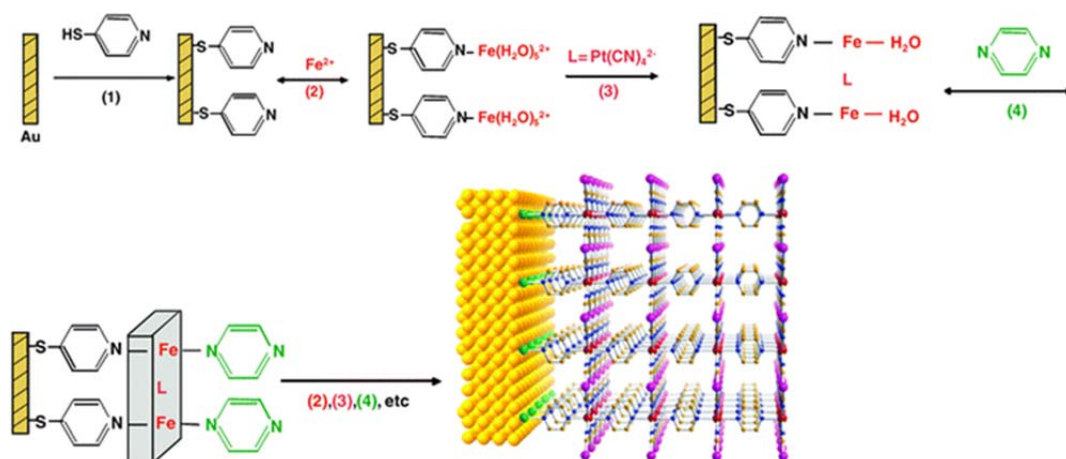


Figure 32: Schematic procedure of the layer by layer assembly approach of Fe(pz)[Pt(CN)₄] thin films.^[70]

In **Figure 32** is schematically described the whole process, starting first with the functionalization of gold surface with a mercaptopyridinyl group and then, the step by step building of the framework through the assembly of metalocyanate and pyrazine components. This approach allows a fine control of thickness (at nanometric scale), roughness and composition and provides quasi-epitaxial films. Different Fe(L)[M(CN)₄] metal-organic frameworks (where L is a bidentate linker) were successfully processed with this method.

I.5.3.4 Vacuum Sublimation

In the last years, the literature has provided a few examples of spin-crossover thin films elaborated with vacuum sublimation. The thin films were produced in a vacuum sublimation chamber in which the solid placed in a crucible was heated under high vacuum. The solid evaporates and condenses on the surface of a substrate, the deposition rate being controlled by

a quartz crystal balance.^[63] The method was successfully applied to $\text{Fe}(\text{phen})_2(\text{NCS})_2$ or $\text{Fe}(\text{H}_2\text{Bpz})_2(\text{phen})$ and $\text{Fe}(\text{H}_2\text{Bpz})_2(\text{bipy})$ (where H_2Bpz is bis(pyrazolyl)borate, phen is 1,10-phenanthroline, bipy is 2,2'-bipyridine). The deposition of such coordination compounds appears very challenging to control and thus requires especially robust precursors.

References

- [1] a) L. Cambi and L. Szegő, *Berichte der deutschen chemischen Gesellschaft (A and B Series)* 1931, 64, 2591-2598; b) L. Cambi and L. Malatesta, *Ber. Dtsch. Chem. Ges. B* 1937, 70, 2067-2078.
- [2] W. A. Baker and H. M. Bobonich, *Inorganic Chemistry* 1964, 3, 1184-1188.
- [3] a) Y. Garcia and P. Gülich in *Thermal Spin Crossover in Mn(II), Mn(III), Cr(II) and Co(III) Coordination Compounds*, Vol. 234 Springer Berlin Heidelberg, 2004, pp. 49-62; b) C. J. Ballhausen and A. D. Liehr, *Journal of the American Chemical Society* 1959, 81, 538-542; c) R. C. Stoufer, D. H. Busch and W. B. Hadley, *Journal of the American Chemical Society* 1961, 83, 3732-3734.
- [4] J. Krober, E. Codjovi, O. Kahn, F. Groliere and C. Jay, *Journal of the American Chemical Society* 1993, 115, 9810-9811.
- [5] a) J.-F. Létard, P. Guionneau and L. Goux-Capes in *Towards Spin Crossover Applications*, Vol. 235 Springer Berlin Heidelberg, 2004, pp. 221-249; b) A. Hauser, *Angewandte Chemie International Edition* 2013, 52, 10419-10419.
- [6] S. Decurtins, P. Gülich, C. P. Köhler, H. Spiering and A. Hauser, *Chemical Physics Letters* 1984, 105, 1-4.
- [7] a) P. Gutlich, Y. Garcia and H. A. Goodwin, *Chemical Society Reviews* 2000, 29, 419-427; b) M. A. Halcrow, *Polyhedron* 2007, 26, 3523-3576; c) O. Kahn in *Molecular Magnetism*, Vol. WILEY-VCH, New York, 1993; d) A. Bousseksou, G. Molnar, L. Salmon and W. Nicolazzi, *Chemical Society Reviews* 2011, 40, 3313-3335.
- [8] a) A. Hauser in *Ligand Field Theoretical Considerations*, Vol. 233 Eds.: P. Gülich and H. A. Goodwin), Springer Berlin Heidelberg, 2004, pp. 49-58; b) S. Sugano, Y. Tanabe and H. Kamimura, *Academic*, New York 1970, 33.
- [9] V. Ksenofontov, A. Gaspar and P. Gülich in *Pressure Effect Studies on Spin Crossover and Valence Tautomeric Systems*, Vol. 235 Springer Berlin Heidelberg, 2004, pp. 23-64.
- [10] C. P. Slichter and H. G. Drickamer, *The Journal of Chemical Physics* 1972, 56, 2142-2160.
- [11] M. Sorai and S. Seki, *Journal of Physics and Chemistry of Solids* 1974, 35, 555-570.
- [12] M. Sorai in *Heat Capacity Studies of Spin Crossover Systems*, Vol. 235 Springer Berlin Heidelberg, 2004, pp. 153-170.

- [13] a) H. Spiering, E. Meissner, H. Köppen, E. W. Müller and P. Gülich, *Chemical Physics* 1982, 68, 65-71; b) H. Spiering in *Elastic Interaction in Spin-Crossover Compounds*, Vol. 235 Springer Berlin Heidelberg, 2004, pp. 171-195.
- [14] J. Wajnflasz, *physica status solidi (b)* 1970, 40, 537-545.
- [15] a) J.-P. Tuchagues, A. Bousseksou, G. Molnár, J. McGarvey and F. Varret in *The Role of Molecular Vibrations in the Spin Crossover Phenomenon*, Vol. 235 Springer Berlin Heidelberg, 2004, pp. 84-103; b) W. Nicolazzi, J. Pavlik, S. Bedoui, G. Molnár and A. Bousseksou, *The European Physical Journal Special Topics* 2013, 222, 1137-1159; c) A. Bousseksou, J. Nasser, J. Linares, K. Boukheddaden and F. Varret, *J. Phys. I France* 1992, 2, 1381-1403.
- [16] A. Bousseksou, H. Constant-Machado and F. Varret, *J. Phys. I France* 1995, 5, 747-760.
- [17] a) *Spin Crossover in Transition Metal Compounds I-III*, Springer-Verlag, Berlin, Heidelberg, New York, 2004, p; b) M. A. Halcrow in *Spin-Crossover Materials: Properties and Applications*, Vol. Wiley, 2013, p. 564; c) H. O. Keith S. Murray, Jose Antonio Real in *Special Issue: Spin-Crossover Complexes (Cluster Issue)*, Vol. 5-6 WILEY-VCH Verlag GmbH & Co. KGaA, Weinheim, pp. 574-1067; d) K. S. Murray, *European Journal of Inorganic Chemistry* 2008, 2008, 3101-3121; e) J. A. Real, A. B. Gaspar, V. Niel and M. C. Muñoz, *Coordination Chemistry Reviews* 2003, 236, 121-141.
- [18] J. A. Real, A. B. Gaspar and M. C. Munoz, *Dalton Transactions* 2005, 2062-2079.
- [19] J. Tao, R.-J. Wei, R.-B. Huang and L.-S. Zheng, *Chemical Society Reviews* 2012, 41, 703-737.
- [20] P. Gülich in *Spin crossover in iron(II)-complexes*, Vol. 44 Springer, Berlin, 1981, p. 112.
- [21] D. Chernyshov, M. Hostettler, K. W. Törnroos and H.-B. Bürgi, *Angewandte Chemie International Edition* 2003, 42, 3825-3830.
- [22] G. Lemerrier, N. Bréfuel, S. Shova, J. A. Wolny, F. Dahan, M. Verelst, H. Paulsen, A. X. Trautwein and J.-P. Tuchagues, *Chemistry – A European Journal* 2006, 12, 7421-7432.
- [23] J. Kroeber, J.-P. Audiere, R. Claude, E. Codjovi, O. Kahn, J. G. Haasnoot, F. Groliere, C. Jay and A. Bousseksou, *Chemistry of Materials* 1994, 6, 1404-1412.
- [24] L. G. Lavrenova and O. G. Shakirova, *European Journal of Inorganic Chemistry* 2013, 2013, 670-682.

- [25] a) J. G. Haasnoot, *Coordination Chemistry Reviews* 2000, 200–202, 131-185; b) M. C. Muñoz and J. A. Real, *Coordination Chemistry Reviews* 2011, 255, 2068-2093.
- [26] W. Vreugdenhil, J. G. Haasnoot, O. Kahn, P. Thuery and J. Reedijk, *Journal of the American Chemical Society* 1987, 109, 5272-5273.
- [27] C. J. Adams, M. C. Muñoz, R. E. Waddington and J. A. Real, *Inorganic Chemistry* 2011, 50, 10633-10642.
- [28] Y. Garcia, O. Kahn, L. Rabardel, B. Chansou, L. Salmon and J. P. Tuchagues, *Inorganic Chemistry* 1999, 38, 4663-4670.
- [29] M. Ohba, K. Yoneda, G. Agustí, M. C. Muñoz, A. B. Gaspar, J. A. Real, M. Yamasaki, H. Ando, Y. Nakao, S. Sakaki and S. Kitagawa, *Angewandte Chemie International Edition* 2009, 48, 4767-4771.
- [30] V. Niel, J. M. Martinez-Agudo, M. C. Muñoz, A. B. Gaspar and J. A. Real, *Inorganic Chemistry* 2001, 40, 3838-3839.
- [31] J. J. McGarvey and I. Lawthers, *Journal of the Chemical Society, Chemical Communications* 1982, 906-907.
- [32] A. Hauser, *Chemical Physics Letters* 1986, 124, 543-548.
- [33] S. Decurtins, P. Gutlich, K. M. Hasselbach, A. Hauser and H. Spiering, *Inorganic Chemistry* 1985, 24, 2174-2178.
- [34] J.-F. Letard, *Journal of Materials Chemistry* 2006, 16, 2550-2559.
- [35] S. Bonhommeau, G. Molnár, A. Galet, A. Zwick, J.-A. Real, J. J. McGarvey and A. Bousseksou, *Angewandte Chemie International Edition* 2005, 44, 4069-4073.
- [36] S. Kume and H. Nishihara in *Metal-based Photoswitches Derived from Photoisomerization*, Vol. 123 (Ed. V. W. Yam), Springer Berlin Heidelberg, 2007, pp. 79-112.
- [37] P. Güthlich, Y. Garcia and Y. Woike, *Coord. Chem. Rev.* 2001, 219–221, 839-879.
- [38] M.-L. Boillot, J. Zarembowitch and A. Sour in *Ligand-Driven Light-Induced Spin Change (LD-LISC): A Promising Photomagnetic Effect*, Vol. 234 Springer Berlin Heidelberg, 2004, pp. 261-276.
- [39] C. Roux, J. Zarembowitch, B. Gallois, T. Granier and R. Claude, *Inorganic Chemistry* 1994, 33, 2273-2279.

- [40] M.-L. Boillot, C. Roux, J.-P. Audi re, A. Dausse and J. Zarembowitch, *Inorganic Chemistry* 1996, 35, 3975-3980.
- [41] M. L. Boillot, S. Pillet, A. Tissot, E. Riv  re, N. Claiser and C. Lecomte, *Inorganic Chemistry* 2009, 48, 4729-4736.
- [42] J. S. Kolb, M. D. Thomson, M. Novosel, K. S  n  chal-David,   . Riv  re, M.-L. Boillot and H. G. Roskos, *Comptes Rendus Chimie* 2007, 10, 125-136.
- [43] A. Tissot, M.-L. Boillot, S. b. Pillet, E. Codjovi, K. Boukheddaden and L. v. M. Lawson Daku, *The Journal of Physical Chemistry C* 2010, 114, 21715-21722.
- [44] M.-L. Boillot, S. Chantraine, J. Zarembowitch, J.-Y. Lallemand and J. Prunet, *New Journal of Chemistry* 1999, 23, 179-184.
- [45] a) Y. Hasegawa, K. Takahashi, S. Kume and H. Nishihara, *Chemical Communications* 2011, 47, 6846-6848; b) K. Takahashi, Y. Hasegawa, R. Sakamoto, M. Nishikawa, S. Kume, E. Nishibori and H. Nishihara, *Inorganic Chemistry* 2012, 51, 5188-5198.
- [46] Y. Hasegawa, S. Kume and H. Nishihara, *Dalton Transactions* 2009, 280-284.
- [47] K. Senechal-David, N. Zaman, M. Walko, E. Halza, E. Riviere, R. Guillot, B. L. Feringa and M. L. Boillot, *Dalton Transactions* 2008, 1932-1936.
- [48] a) M. Milek, F. W. Heinemann and M. M. Khusniyarov, *Inorganic Chemistry* 2013, 52, 11585-11592; b) M. Nihei, Y. Suzuki, N. Kimura, Y. Kera and H. Oshio, *Chemistry – A European Journal* 2013, 19, 6946-6949.
- [49] A. Sour, M.-L. Boillot, E. Riv  re and P. Lesot, *European Journal of Inorganic Chemistry* 1999, 1999, 2117-2119.
- [50] S. Hirose, S. Hayami and Y. Maeda, *Bull. Chem. Soc. Jpn.* 2000, 73, 2059-2066.
- [51] A. Bannwarth, S. O. Schmidt, G. Peters, F. D. S  nnichsen, W. Thimm, R. Herges and F. Tuczek, *European Journal of Inorganic Chemistry* 2012, 2012, 2776-2783.
- [52] V. K. LaMer and R. H. Dinegar, *Journal of the American Chemical Society* 1950, 72, 4847-4854.
- [53] a) B. L. Cushing, V. L. Kolesnichenko and C. J. O'Connor, *Chemical Reviews* 2004, 104, 3893-3946; b) C. Burda, X. Chen, R. Narayanan and M. A. El-Sayed, *Chemical Reviews* 2005, 105, 1025-1102.

- [54] M. A. Watzky and R. G. Finke, *Journal of the American Chemical Society* 1997, 119, 10382-10400.
- [55] J.-P. JOLIVET, *De la solution à l'oxyde*, EDP Science, Paris, 1994, p.
- [56] P. N. Martinho, C. Rajnak and M. Ruben in *Nanoparticles, Thin Films and Surface Patterns from Spin-Crossover Materials and Electrical Spin State Control*, Vol. John Wiley & Sons Ltd, 2013, pp. 375-404.
- [57] T. Forestier, S. Mornet, N. Daro, T. Nishihara, S.-i. Mouri, K. Tanaka, O. Fouche, E. Freysz and J.-F. Letard, *Chemical Communications* 2008, 4327-4329.
- [58] E. Coronado, J. R. Galán-Mascarós, M. Monrabal-Capilla, J. García-Martínez and P. Pardo-Ibáñez, *Advanced Materials* 2007, 19, 1359-1361.
- [59] F. Volatron, L. Catala, E. Rivière, A. Gloter, O. Stéphan and T. Mallah, *Inorganic Chemistry* 2008, 47, 6584-6586.
- [60] Y. Raza, F. Volatron, S. Moldovan, O. Ersen, V. Huc, C. Martini, F. Brisset, A. Gloter, O. Stephan, A. Bousseksou, L. Catala and T. Mallah, *Chemical Communications* 2011, 47, 11501-11503.
- [61] A. Tissot, J.-F. Bardeau, E. Riviere, F. Brisset and M.-L. Boillot, *Dalton Transactions* 2010, 39, 7806-7812.
- [62] a) J. Piard, R. Metivier, M. Giraud, A. Léaustic, P. Yu and K. Nakatani, *New Journal of Chemistry* 2009, 33, 1420-1426; b) A. Spangenberg, R. Métivier, J. Gonzalez, K. Nakatani, P. Yu, M. Giraud, A. Léaustic, R. Guillot, T. Uwada and T. Asahi, *Advanced Materials* 2009, 21, 309-313; c) A. Patra, R. Metivier, J. Piard and K. Nakatani, *Chemical Communications* 2010, 46, 6385-6387.
- [63] M. Cavallini, *Physical Chemistry Chemical Physics* 2012, 14, 11867-11876.
- [64] D. R. Talham and M. W. Meisel, *Chemical Society Reviews* 2011, 40, 3356-3365.
- [65] a) A. Ruaudel-Teixier, A. Barraud, P. Coronel and O. Kahn, *Thin Solid Films* 1988, 160, 107-115; b) P. Coronel, A. Barraud, R. Claude, O. Kahn, A. Ruaudel-Teixier and J. Zarembowitch, *Journal of the Chemical Society, Chemical Communications* 1989, 193-194.
- [66] H. Soyer, C. Mingotaud, M. L. Boillot and P. Delhaes, *Langmuir* 1998, 14, 5890-5895; H. Soyer, E. Dupart, C. J. Gomez-Garcia, C. Mingotaud, P. Delhaès *Adv. Mater.* 1999, 11, 382; J.-F. Létard, O. Nguyen, H. Soyer, C. Mingotaud, P. Delhaès, O. Kahn *Inorg. Chem.* 1999, 38, 3020.

- [67] C. M. Quintero, I. y. A. Gural'skiy, L. Salmon, G. Molnar, C. Bergaud and A. Bousseksou, *Journal of Materials Chemistry* 2012, 22, 3745-3751.
- [68] M. Matsuda and H. Tajima, *Chemistry Letters* 2007, 36, 700-701.
- [69] M. Matsuda, H. Isozaki and H. Tajima, *Thin Solid Films* 2008, 517, 1465-1467.
- [70] S. Cobo, G. Molnár, J. A. Real and A. Bousseksou, *Angewandte Chemie International Edition* 2006, 45, 5786-5789.
- [71] a) G. Agustí, S. Cobo, A. B. Gaspar, G. Molnár, N. O. Moussa, P. Á. Szilágyi, V. Pálfi, C. Vieu, M. Carmen Muñoz, J. A. Real and A. Bousseksou, *Chemistry of Materials* 2008, 20, 6721-6732; b) C. Bartual-Murgui, L. Salmon, A. Akou, C. Thibault, G. Molnar, T. Mahfoud, Z. Sekkat, J. A. Real and A. Bousseksou, *New Journal of Chemistry* 2011, 35, 2089-2094.
- [72] S. Shi, G. Schmerber, J. Arabski, J.-B. Beaufrand, D. J. Kim, S. Boukari, M. Bowen, N. T. Kemp, N. Viart, G. Rogez, E. Beaurepaire, H. Aubriet, J. Petersen, C. Becker and D. Ruch, *Applied Physics Letters* 2009, 95, -.
- [73] H. Naggert, A. Bannwarth, S. Chemnitz, T. von Hofe, E. Quandt and F. Tuczek, *Dalton Transactions* 2011, 40, 6364-6366.

Chapter II

Chapter II**Fe(Me₂-bpy)₂(NCSe)₂ Spin-Crossover Micro- and Nanoparticles Showing a Spin-State Switching Close to Room Temperature**

We present the study of nano- and microparticles of the Fe(Me₂-bpy)₂(NCSe)₂ spin-crossover complex elaborated from the diamagnetic precursor [Fe(Me₂-bpy)₃](NCSe)₂.S. Two solvates of the latter were characterized by single-crystal X-ray structures at 100 K (S = 2MeOH or 3H₂O). The extraction of one Me₂-bpy per metal ion in [Fe(Me₂-bpy)₃](NCSe)₂.S was achieved either by thermolysis at temperature higher than 150 °C or by precipitation in an anti-solvent, leading to a polycrystalline or particulate powder of Fe(Me₂-bpy)₂(NCSe)₂. This chemical conversion was investigated with TGA, powder X-ray diffraction, IR, Raman and magnetic measurements. The S = 0 ↔ S = 2 spin-crossover of Fe(Me₂-bpy)₂(NCSe)₂ centered at *ca.* 340 K is almost complete at low temperature (HS residue ≤ 5 % below 250 K) while at 370 K, the HS fraction can be estimated at ~ 0.7; features, that are preserved whatever the size of particles (56, 460 and 1200 nm) as a consequence of the weak cooperativity of the process occurring at high temperature and the molecular nature of particles. This approach leading to a dispersion of small particles in a polymer suits for the preparation of materials of optical quality, via the stabilization and processing of nanoparticles in convenient matrices to form thin film.

II.1. Introduction

The spin-crossover materials form a class of switchable molecular materials whose transformation under external stimuli produces major changes of spin state-dependent and structural properties.^[1] These features related to the vibronic nature of the process, may give rise to cooperative and hysteretic transitions at temperatures close to the ambient one, a behavior that confer to the materials interesting potentialities for technological applications.^[2] In the last decade, considerable research efforts devoted to the elaboration of bistable spin transition materials, and subsequent downsizing and processing have been achieved and testify of this. It has been shown that the ability to switch such materials over a range of temperature between two stable (or metastable) spin states was preserved down to a typical size of 4 nm, 10 nm or 30 nm, depending

on the chemical nature of compounds (and strength of cooperative elastic interactions, stiffness and environments of particles).^[3]

The spin-state switching can be controlled by light. At low temperature, the light-induced excited spin state trapping (LIESST) allows achieving a bistability between the photoinduced metastable HS state and the LS ground state for a number of Fe^{II} compounds.^[4] Such solid-state transformations were performed with poorly absorbing samples, i.e. either very thin (or highly doped) single-crystals or small amounts of powder. The elaboration of nanosized molecular solids appears as a key feature for the investigation of the photoswitching properties (mechanism, dynamic) in the solid-state and for elaborating devices.^[5-6]

In our studies of photoswitchable iron(II) compounds based on the so-called ligand-driven light-induced spin-change process (LD-LISC) combining a photoisomerizable ligand and a spin-crossover center,^[7] we have focussed on new complexes that appear well adapted for probing their ability to be switched around room temperature in different environments and scales. We report here the preliminary study of the Fe(Me₂-bpy)₂(NCSe)₂ precursor prior to any functionalization of the ligand with a photoactive group. For this investigation, we have revisited the preparation of Fe(Me₂-bpy)₂(NCSe)₂,^[8] from a parent compound^[9] [Fe(Me₂-bpy)₃](NCSe)₂·3H₂O which remains diamagnetic at any temperature and may be also precipitated in the form of particles in presence of an anti-solvent.^[10] We have investigated the chemical nature of these particles, their physical properties from magnetic, optical, vibrational measurements and then discussed the observations with respect to literature.

II.2. Results

II.2.1. Characterization of the Precursor

II.2.1.1. X-ray Structure Analysis

Single-crystals of hydrated complexes were easily isolated from crystallogenesis in methanol in the presence of traces of water. The crystalline structures show variable packing involving the salt and water molecules with only minor changes in the cation (in appendix of chapter II). We focus here on the compound of formula [Fe(Me₂-bpy)₃](NCSe)₂·2CH₃OH which appears to have the best crystalline quality. This solvate was obtained as dark red single-crystals by slow evaporation of a methanolic

solution. It crystallizes in the triclinic P-1 space group and its structure collected at 100 K consists of cationic complexes, NCSe^- anions and methanol molecules. Crystal data collection and refinement parameters are described in **Table 1**. Selected bond lengths and molecular parameters are collected in **Table 2**.

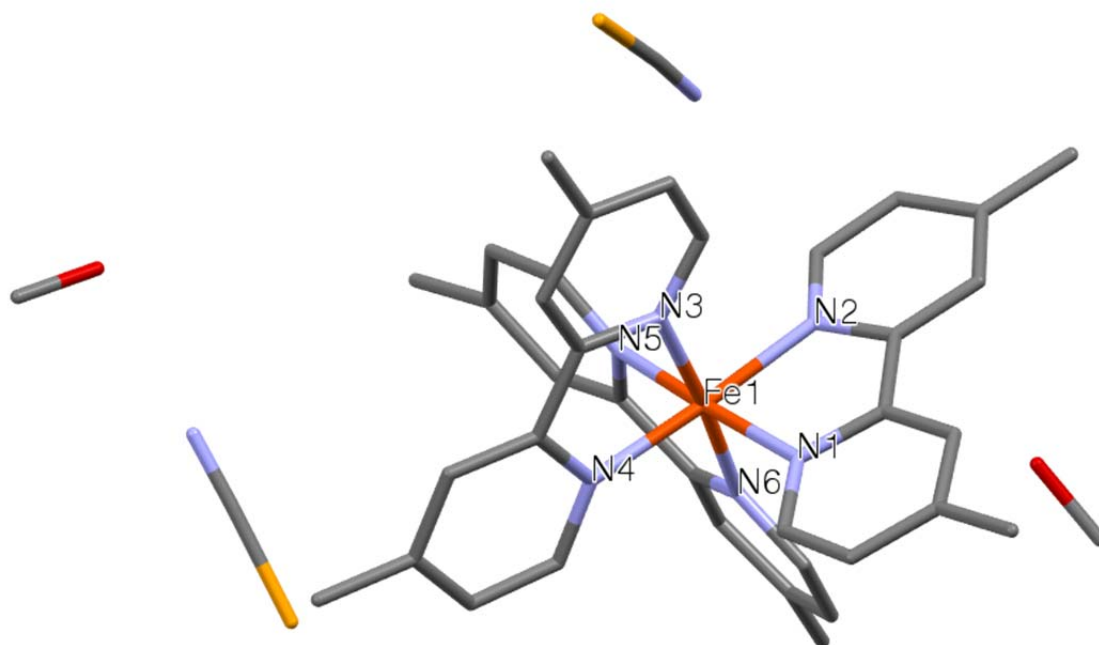


Figure 1: Molecular structure of $[\text{Fe}(\text{Me}_2\text{-bpy})_3](\text{NCSe})_2 \cdot 2\text{CH}_3\text{OH}$ at 100 K. Hydrogen atoms are omitted for clarity.

In **Figure 1**, the molecular structure of the cation shows an Fe^{II} ion in the $[\text{N}_6]$ environment of three bidentate ligands. Average bond lengths, Σ and ζ parameters (see caption of **Table 2**) are typical for a low-spin Fe^{II} ion and fully compare with values reported for the $[\text{Fe}(\text{Me}_2\text{-bpy})_3](\text{NCS})_2 \cdot 3\text{H}_2\text{O}$ analogue ($\langle \text{Fe-N} \rangle = 1.965(3) \text{ \AA}$, $\Sigma = 62.9^\circ$, $\zeta = 0.024 \text{ \AA}$ respectively).^[11]

The complexes related by the inversion centre form dimers with bipyridine ligands of two adjacent sites lying in almost parallel planes (inter-ring C-C distances at 3.769 and 3.885 \AA for C28-C28 and C27-C31, respectively). The NCSe^- anions are involved in short Van der Waals contacts between the N atoms and the H-C groups (in ortho or meta position) of bpy rings or the H-O group of methanol.

Table 1 Crystal data and structure refinement for $[\text{Fe}^{\text{II}}(\text{Me}_2\text{-bpy})_3](\text{NCSe})_2 \cdot 2\text{CH}_4\text{O}$ at 100 K.

Compound and Temperature	$[\text{Fe}^{\text{II}}(\text{Me}_2\text{-bpy})_3](\text{NCSe})_2 \cdot 2\text{CH}_4\text{O}$ 100 K
Empirical formula	$\text{C}_{40} \text{H}_{44} \text{Fe} \text{N}_8 \text{O}_2 \text{Se}_2$
Formula weight	882.60
Crystal system	triclinic
Space group	P -1
a (Å)	10.5940(5)
b (Å)	14.2967(7)
c (Å)	14.5177(8)
α (°)	84.8660(10)
β (°)	68.8300(10)
γ (°)	77.3390(10)
V (Å ³)	2000.46(18)
Z	2
Density (calc.) (g.cm ⁻³)	1.465
$F(000)$	900
θ range (°)	1.46 - 36.42
Collected data	36266
Unique data	16446
R_{int}	0.0262
Data($I > 2\sigma(I)$)/restraints/parameters	11527/0/488
Goodness-of-fit on F^2	1.035
$R1$ [$I > 2\sigma(I)$]	0.0632
$wR2$ [$I > 2\sigma(I)$]	0.1633
$R1$ (all data)	0.0978
$wR2$ (all data)	0.1832

The arrangement of dimers is stabilized via numerous and moderate contacts located in planes parallel to bc ; weaker interactions being observed in-between the planes. Finally even at 100 K, the disorder of atomic position remains marked for the N and O atoms

of methanol molecules as well as for the NCSe^- anion that interact only with the solvent.

Table 2 The geometry of the Fe site surroundings

	100 K
Fe-N bonds (Å)	
Fe-N ₁	1.959(2)
Fe-N ₂	1.960(2)
Fe-N ₃	1.974(2)
Fe-N ₄	1.974(2)
Fe-N ₅	1.965(2)
Fe-N ₆	1.968(2)
<Fe-N>	1.967(2)
$\zeta(\text{Å})^a$	0.032
$\Sigma(^{\circ})^a$	52.5

$$\langle Fe-N \rangle = \frac{1}{6} \sum_{i=1}^6 d_{Fe-N_i} \quad \zeta = \sum_{i=1}^6 |Fe-L_i - \langle Fe-L \rangle| \quad \Sigma = \sum_{i=1}^{12} |90 - \phi_i|$$

II.2.1.2. TGA Analysis

Heating the red polycrystalline powder (**Figure 2**) leads to the removal of three water molecules (plateau at ca. 115 °C). Between 140 and ca 175 °C, a new variation of weight corresponds to the removal of one $\text{Me}_2\text{-bpy}$ ligand per formula unit, as confirmed by the elemental analysis of the purple powder (see below).

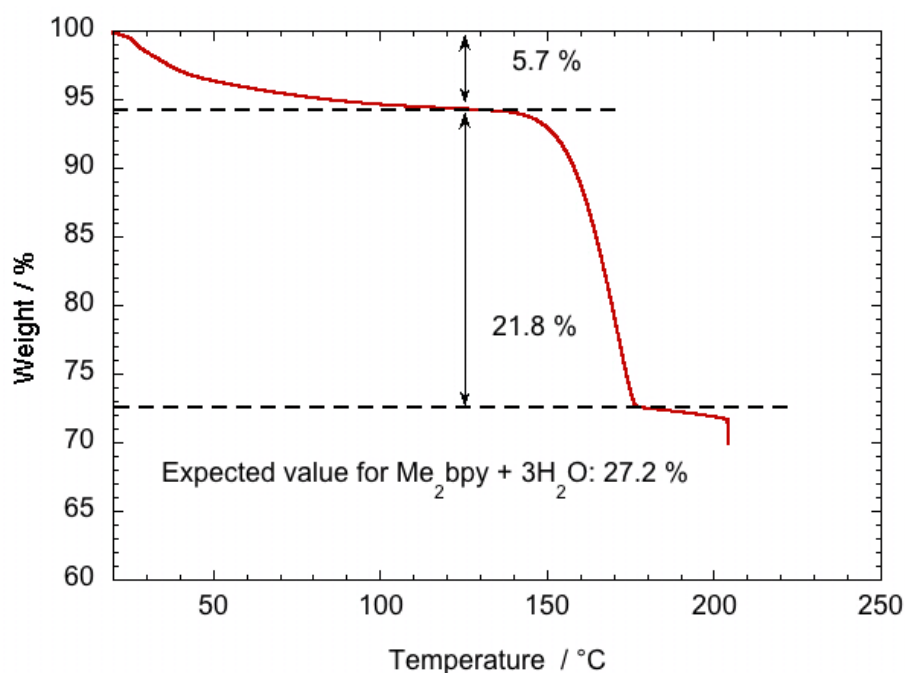


Figure 2: TGA analysis of $[\text{Fe}(\text{Me}_2\text{-bpy})_3](\text{NCSe})_2 \cdot 3\text{H}_2\text{O}$ performed at 2 °C/min under air atmosphere.

II.2.1.3. Observation of Crystals upon the Thermal Evolution

This thermal reactivity was monitored between 107 and 204 °C with optical microscopy by recording images of both $[\text{Fe}(\text{Me}_2\text{-bpy})_3](\text{NCSe})_2$ solvates (Solvent = CH_3OH or H_2O) in the crystalline form. The **Figure 3a** shows the 160 °C isothermal evolution of the red square-shaped methanolate sample. The image selected at an 11 min reaction time indicates the formation of a number of stripes parallel to the left edge of the crystal, then later the crystal color strongly darkens and the macroscopic change of volume becomes apparent. The transformation achieved after 100 min essentially preserves the shape of the solid (linear variation of edges size and angle, in appendix of chapter II). The **Figure 3b** presents the evolution with temperature of the platelets of hydrated compound. The sequence starts with the dehydrated material at 107 °C, that was heated to 155 °C (scanning rate = 1 °C/min), temperature at which the variation was stopped for 55 min for studying the stage corresponding to the ligand release. A number of flower-type patterns emerge close to the crystal edges or to the areas rich in crystalline defects and then, growth in a concentric manner and coalesce in the whole volume. The solid deformation also appears through the proliferation of defects in between crystalline fragments and the change of crystal dimensions (in appendix of chapter II) and volume.

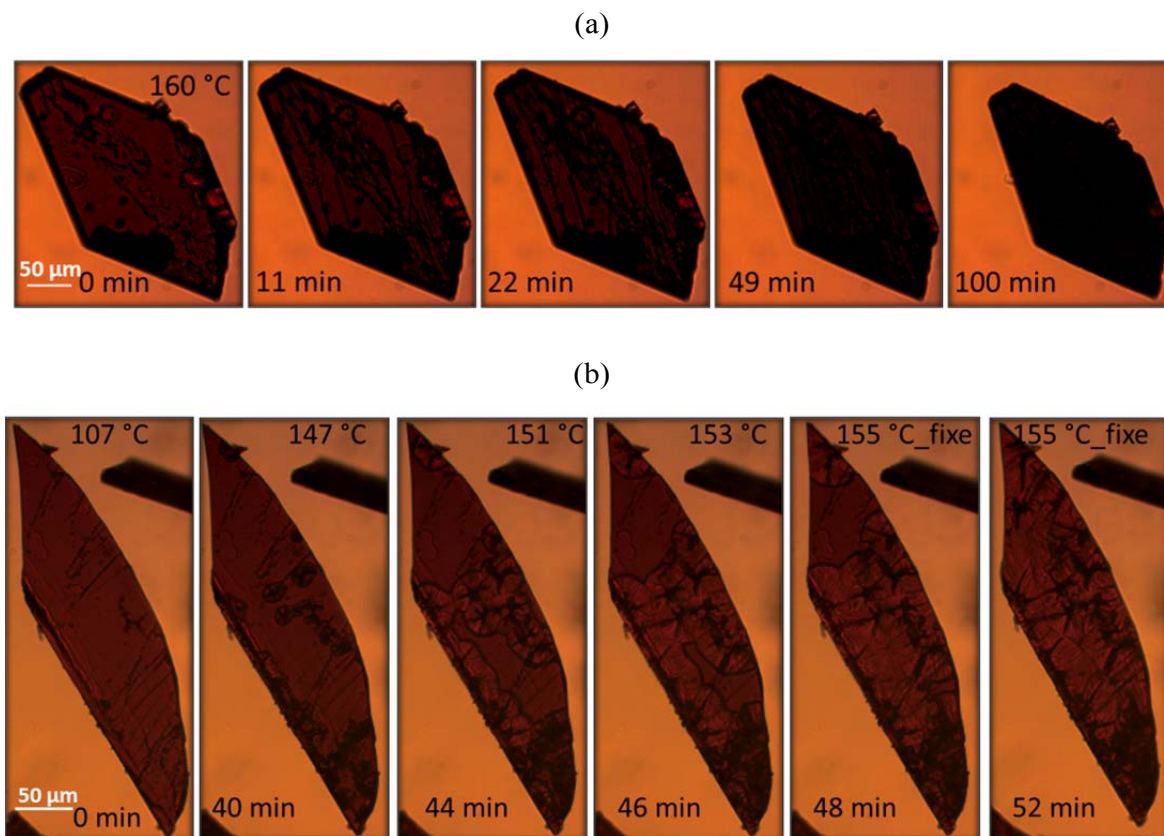


Figure 3: Optical microscopy images of $[\text{Fe}(\text{Me}_2\text{-bpy})_3](\text{NCSe})_2 \cdot \text{S}$ ($\text{S} = \text{CH}_3\text{OH}$ or H_2O) after the desolvation stage: (a) the 160 °C isothermal evolution of the red square-shaped methanolate sample; (b) evolution of the initially hydrated sample upon heating from 107 to 155 °C (scanning rate of 1°C/min) and then staying at 155 °C.

II.2.2. Elaboration of $\text{Fe}^{\text{II}}(\text{Me}_2\text{-bpy})_2(\text{NCSe})_2$

The polycrystalline powder : $\text{Fe}^{\text{II}}(\text{Me}_2\text{-bpy})_2(\text{NCSe})_2$ was prepared according to an uncommon solvent-free approach^[12-13] that was early mentioned in the reports on $\text{Fe}^{\text{II}}(\text{phen})_2(\text{NCS})_2$ syntheses. It was optimized from the thermal behavior of the cationic precursor as determined above.

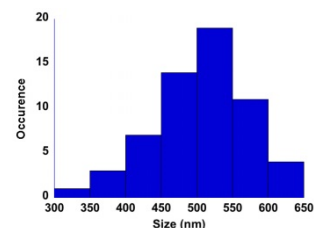
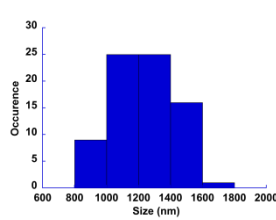
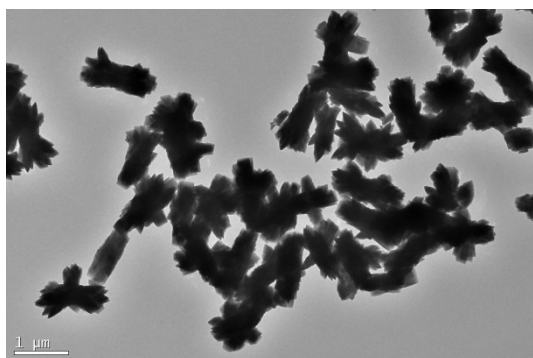
The X-ray diffractograms 293 K of the powder of precursor, before (red color) and after (violet color) the thermal reaction are superimposed in **Figure S2** (in appendix of chapter II). The disappearance of Bragg reflections specific to the cationic precursor ($2\theta = 6.6, 9.9, 12.7$ and 30.8°) and the appearance of new sharp Bragg reflections ($8.5, 12.2, 18.7$ and 21.9°) indicate the complete transformation of the former as well as the crystallinity of the product.

The comparison of the two IR spectra ($T = 293$ K in **Figure S3**, in appendix of chapter II) confirms the drastic change of the coordination sphere around the metal ion. The well-known band near 2100 cm^{-1} associated to the NC stretching mode of NCSe^- is centred at $2061 \pm 4\text{ cm}^{-1}$ for the $[\text{Fe}(\text{Me}_2\text{-bpy})_3](\text{NCSe})_2 \cdot 3\text{H}_2\text{O}$ salt. After the thermal treatment, the two double bands (2061 and $2070 \pm 4\text{ cm}^{-1}$, 2098 and $\sim 2103 \pm 4\text{ cm}^{-1}$) are typical of *cis* positioned NCSe ligands, N-coordinated to a HS and LS Fe^{II} ion, respectively.^[13,14,15,16] The molecular rearrangement also gives rise to changes of intensity and splitting of bands, and to the appearance in the low frequency range of new vibrational frequencies (419 , 515 , 630 and $845 \pm 4\text{ cm}^{-1}$). We can infer from the TGA, powder X-ray, IR measurements and the color change that the thermal decomposition of the cationic precursor in the present conditions results in the formation of a polycrystalline powder of $\text{Fe}^{\text{II}}(\text{Me}_2\text{-bpy})_2(\text{NCSe})_2$. The fact that two NCSe stretching modes, separated by $35\text{-}40\text{ cm}^{-1}$, can be observed by IR spectroscopy suggests the coexistence in this solid of HS and LS Fe^{II} complexes at room temperature. This will be further examined by magnetic measurement (see below).

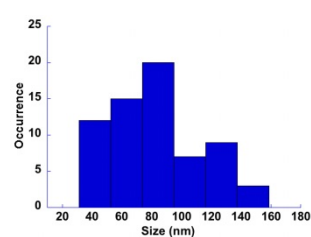
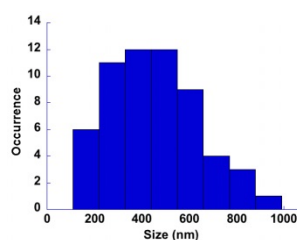
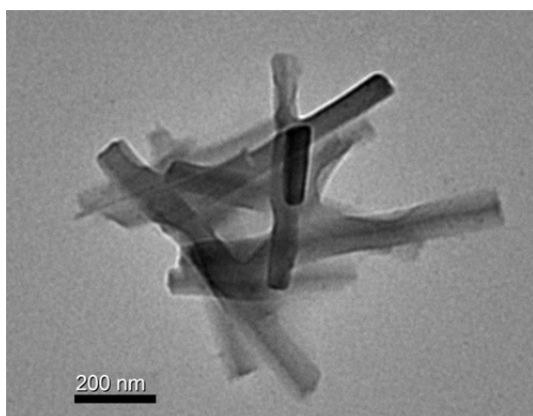
Micro- and nanocrystals: the compound was prepared in the form of particles by using the dissociative equilibrium between the cationic species and the poorly soluble complex $\text{Fe}^{\text{II}}(\text{Me}_2\text{-bpy})_2(\text{NCSe})_2$.^[13] With polar solvents (EtOH) and concentrated solution (11.3 mM) of the red iron(II) salt, we have first observed the spontaneous precipitation of purple particles. The TEM image of these particles (**Figure 4a**) indicates the formation of very thin needle-like objects whose size varies between 1 and $5\text{ }\mu\text{m}$ depending on the temperature ($T = 65$ and $80\text{ }^\circ\text{C}$ for isolation of 1.2 and $4\text{ }\mu\text{m}$, respectively).

Combining dilution, change of reaction temperature and fast precipitation in presence of a confining polymer (here PMMA) has allowed us to isolate smaller objects. It appears from TEM measurements (**Figure 4b**) that 500 nm platelets and 56 nm (in appendix of chapter II, **Fig. S4**) spherical particles coexist in the ethanol-toluene mixture maintained at $65\text{ }^\circ\text{C}$. A last step of filtration affords the smallest particles ($56 \pm 15\text{ nm}$, **Figure 4c**).

a) $(1200 \pm 200) \times (500 \pm 65) \text{ nm}^2$ microparticles



b) $(460 \pm 190) \times (80 \pm 30) \text{ nm}^2$ nanoparticles



c) $60 \pm 15 \text{ nm}$ nanoparticles

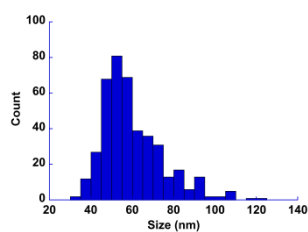
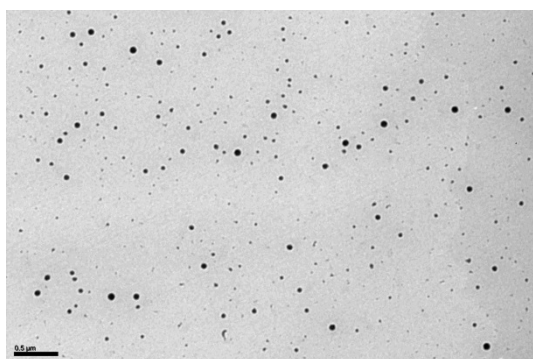


Figure 4: TEM images showing the particles that (a) spontaneously precipitate from a concentrated solution of cationic precursor, (b) and (c) precipitate by sudden addition of the solution of precursor in the antisolvent (see the text), and their size dispersion.

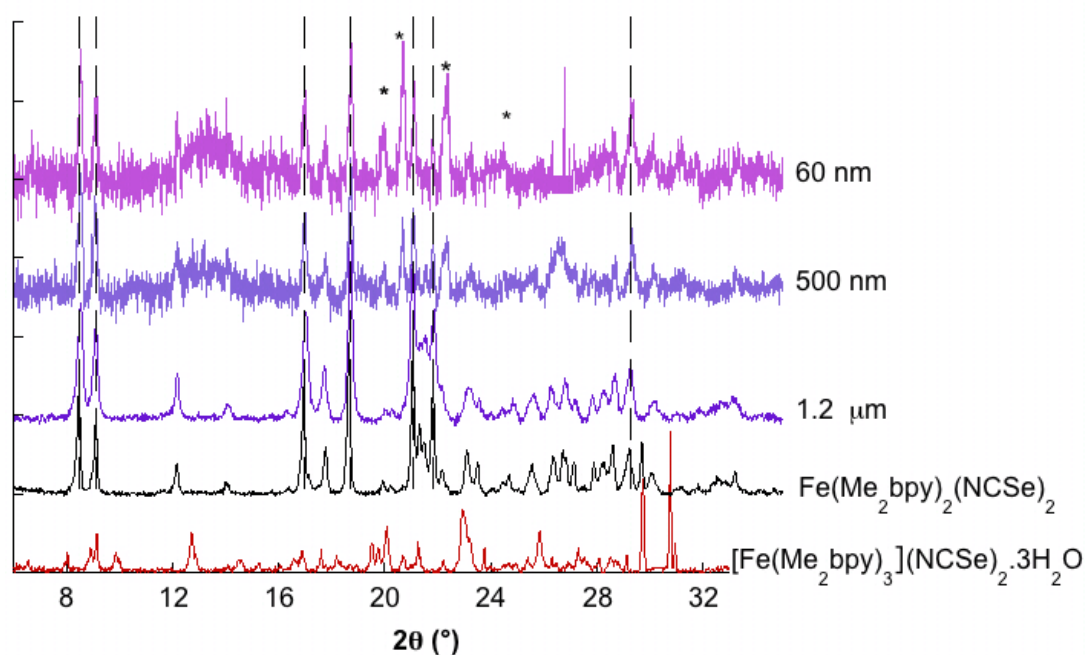


Figure 5: Powder X-ray diffractograms at 293 K: sample of precursor before and after thermal treatment, microcrystals (1.2 μm), nanoparticles (460 and 60 nm) dispersed in PMMA. A few extra peaks (*19.93, 20.62, 22.29, 24.44, 26.45) are due to the Al substrate of the sample.

The corresponding X-ray diffractograms recorded at room temperature are displayed in the **Figure 5**. Comparison with those recorded before and after heating the cationic precursor provides evidences for the formation of $\text{Fe}^{\text{II}}(\text{Me}_2\text{-bpy})_2(\text{NCSe})_2$ in the form of crystalline micro- and nanoparticles. Therefore the nature and crystallinity of the solid phase of $\text{Fe}^{\text{II}}(\text{Me}_2\text{-bpy})_2(\text{NCSe})_2$ are preserved regardless of the chemical approach used for the synthesis.

The spectroscopic characterization of microcrystals by IR (in **Figure 6**) is in agreement with the features above mentioned for $\text{Fe}^{\text{II}}(\text{Me}_2\text{-bpy})_2(\text{NCSe})_2$. No trace of the $\text{Me}_2\text{-bpy}$ base-free ligand can be detected, in particular near 1600 cm^{-1} in the range of the $\text{N}=\text{C}$ stretching mode. The isolation of nanoparticles embedded in an excess of PMMA gives rise to strong absorption bands (for example due to the ester functions) of the polymer that prevents the analysis of the molecular spectrum except the two vibrational modes associated to the coordinated NCSe ligands in the $2000\text{-}2150\text{ cm}^{-1}$ range (see inset in **Figure 6**). This feature supports the analysis of powder X-ray diffraction data indicating the absence of cationic compound and the formation of micro- and nanocrystals of the neutral compound.

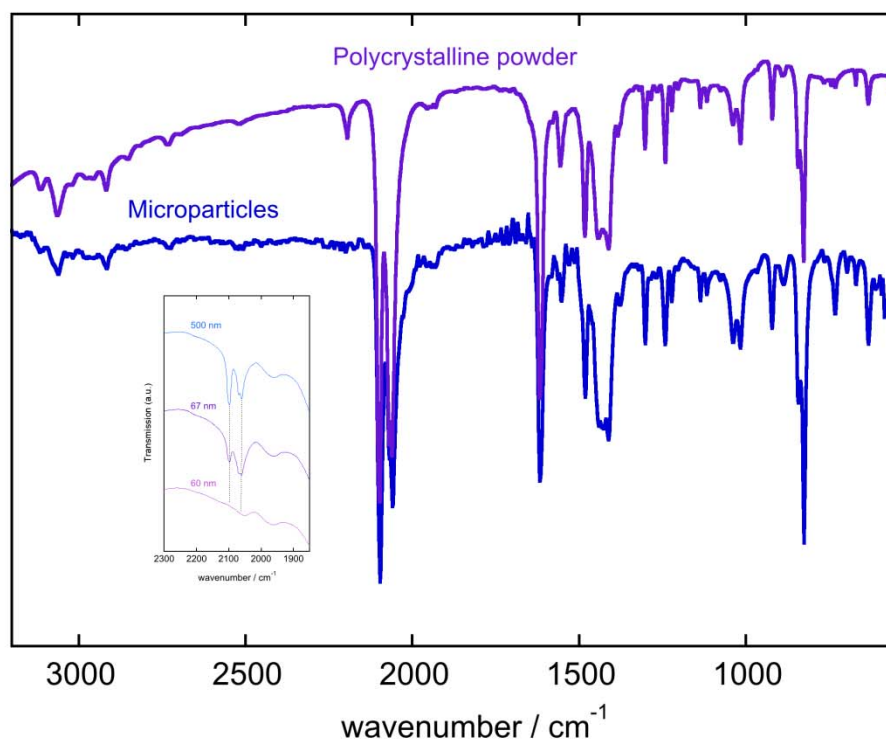


Figure 6: IR spectra recorded at 293 K of samples of precursor after thermal treatment, microcrystals (1.2 μm) and in the inset, an expansion of spectra showing the NC stretching vibrational mode for the dispersion of nanoparticles (460 and 56 nm) in PMMA. All the samples are in the form of KBr pellets.

Magnetic measurements :

They were carried out as a function of temperature between 100 and 370 K. This latter value was fixed slightly below the glass transition of PMMA (at ca. 380 K) in which the particles were dispersed, in order to minimize a matrix effect on the samples.^[17] It was first checked that the red powder of $[\text{Fe}(\text{Me}_2\text{-bpy})_3](\text{NCSe})_2 \cdot 3\text{H}_2\text{O}$ is fully diamagnetic at room temperature ($\chi_M T \sim 0 \text{ cm}^3 \text{mol}^{-1} \text{K}$, χ_M being the molar magnetic susceptibility), a result consistent with the strong ligand-field strength produced by diimine ligands.^[1,9]

The **Figure 7** shows the temperature dependence of the $\chi_M T$ product of $\text{Fe}^{\text{II}}(\text{Me}_2\text{-bpy})_2(\text{NCSe})_2$ in the form of violet polycrystalline (bulk) sample. The $S = 0 \leftrightarrow S = 2$ spin-crossover observed above 250 K, is still incomplete at 370 K as the $\chi_M T$ value at $2.57 \text{ cm}^3 \text{mol}^{-1} \text{K}$ (371 K) correspond to a fraction of HS species $\gamma_{\text{HS}} = \text{ca. } 0.7$ (assuming

$\chi_M T = 3.50 \text{ cm}^3 \text{mol}^{-1} \text{K}$ for a pure HS specie). At 100 K, the value of $\chi_M T = 0.10 \text{ cm}^3 \text{mol}^{-1} \text{K}$ suggests the presence of traces of HS residue ($\gamma_{\text{HS}}^{\text{residue}} < 5\%$). This curve is in agreement with the properties, reported in reference 8, of $\text{Fe}^{\text{II}}(\text{Me}_2\text{-bpy})_2(\text{NCSe})_2$ prepared by refluxing an hydrated salt in aromatic solvents (see comparison in **Fig S5**, ESI). An estimate of the temperature corresponding to a half-complete transition is $T_{1/2} \sim 340 \text{ K}$. The fact that the fraction of LS species at 300 K is still larger than the HS one ($\gamma_{\text{HS}} = 0.22$, here including the residue) is consistent with the IR data showing two NC_{NCSe} modes with a prevailing component at ca. 2100 cm^{-1} . As expected for a progressive transformation with a poor cooperative character, the behaviour of micro- and nanocrystalline samples satisfyingly matches the one observed for the bulk and thus is preserved whatever the particles sizes (**Figure 6**).

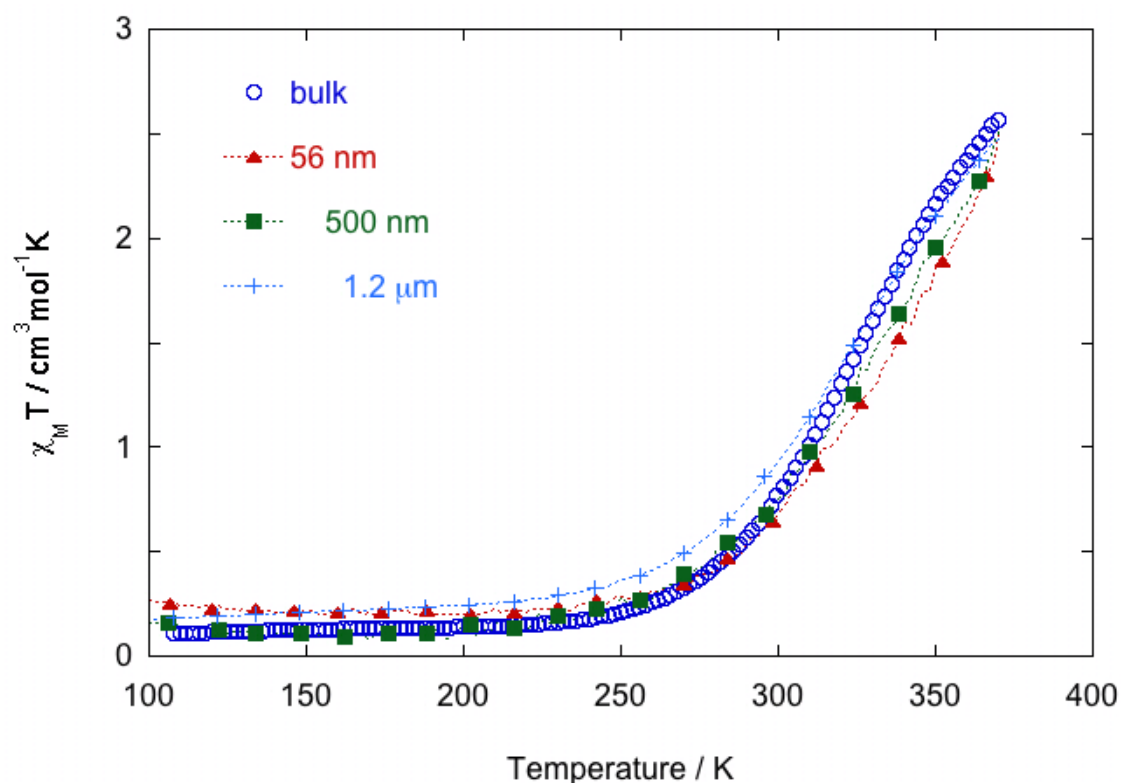


Figure 7 : Temperature dependence of $\chi_M T$ for $\text{Fe}^{\text{II}}(\text{Me}_2\text{-bpy})_2(\text{NCSe})_2$ in the form of a polycrystalline powder (○), microparticles (+) and nanoparticles (■, 460 nm) or (▲, 56 nm).

Raman measurements of NPs and MPs :

The previous data were completed by Raman measurements, which allow the spectral identification of the HS and LS species, even in the presence of PMMA, and the extraction of the fraction of spin-crossover species as a function of temperature. The spectra of all the samples were collected with a 633 nm excitation wavelength at

different temperatures (200, 300 and 370 K). The characterization of the bulk sample confirms the thermal reaction that is previously discussed and provides the frequencies characterizing both forms (in appendix of chapter II, **Fig. S6**). All the spectra observed at a fixed temperature, for $\text{Fe}^{\text{II}}(\text{Me}_2\text{-bpy})_2(\text{NCSe})_2$ in the form of bulk, micro- and nanoparticles (shown in ESI) are qualitatively comparable. The **Figure 8** shows the spectral evolution in the case of the 1.2 μm particles. The vibrational modes associated to the NCSe ligands (2100 , 2107 and ca. 2069 cm^{-1}) can be used as markers of LS and HS forms for analyzing the thermal spin crossover.

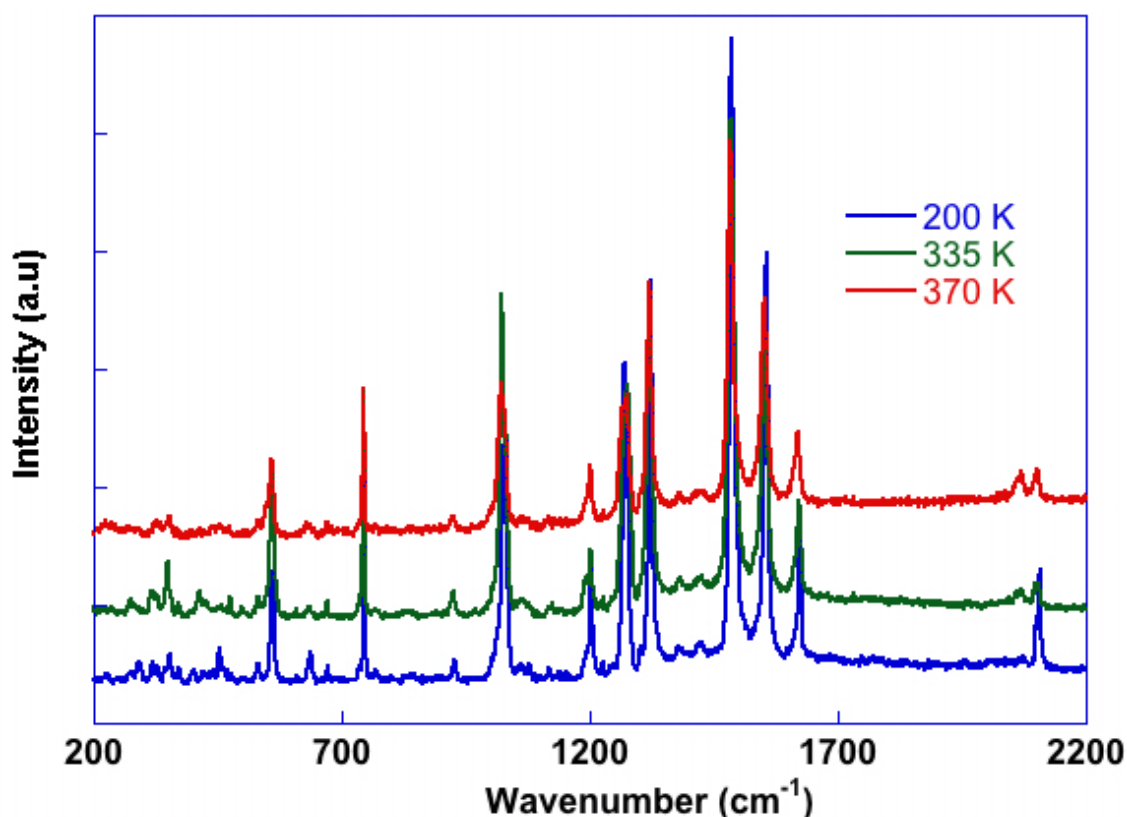


Figure 8 : Variable temperature Raman spectra collected for the 1.2 μm microparticles of $\text{Fe}^{\text{II}}(\text{Me}_2\text{-bpy})_2(\text{NCSe})_2$

The relative intensity of the LS peak at the working temperatures yields a set of points that compares reasonably well to the magnetic curve (in appendix of chapter II). The process that appears almost complete at 200 K, corresponds to a HS residue varying between ca. 5 (bulk, 460 nm) and 17 (56 nm) % for the different samples. A careful examination of the data only shows in the spectrum of 1.2 μm microparticles the presence of weak shoulders at 734 and 1189 cm^{-1} , which might be ascribed to traces of the $[\text{Fe}(\text{Me}_2\text{-bpy})_3](\text{NCSe})_2 \cdot 3\text{H}_2\text{O}$ diamagnetic precursor.

II.3. Discussion

From a synthetic point of view, the ligand extraction from the cationic complex contributes to the shift of the chemical equilibrium towards the formation of the neutral species whereas the reverse reaction is driven by the presence of water.^[18] This alternative is discarded by the solid-state synthesis that can be easily controlled for a complete transformation of the complex.

The powder X-ray diffraction data collected for $\text{Fe}^{\text{II}}(\text{Me}_2\text{-bpy})_2(\text{NCSe})_2$ confirm the preservation of one crystalline phase whatever the method used for the removal of one bipyridine ligand (solvent-induced or solvent-free extraction). This feature is quite remarkable as the thermal switching properties of spin-crossover solids are usually modulated by subtle factors related to the solid-phase that depend on the chemical synthesis and crystallinity. The versatility of molecular organization and packing is reflected by polymorphism and variable spin crossover behavior,^[19] as nicely demonstrated in the case of $\text{Fe}(\text{PM-BiA})_2(\text{NCS})_2$.^[20]

One interesting result observed here is the formation of a crystalline material that derives from a coordination bond cleavage, diffusion of ligand in the solid state, rearrangement of the coordination sphere and nucleation of the new phase. It is well established that in contrast to the methods developed for the elaboration of oxides nanostructures,^[21-22] softer thermal conditions may lead either to a molecular rearrangement via the migration of ligands between the coordination spheres of two metal ions,^[23] or to a coordination polymer via a partial decomposition, a rearrangement of halide (or pseudohalide like NCX) ions to form bridges between metal ions.²⁴ Finally, Guionneau has identified for some particular spin-crossover materials, a relationship between the solid-state crystallinity and a thermal treatment.^[19]

From the background accumulated on spin-crossover Fe^{II} materials,^[25] it appears that the introduction of two diimine and pseudohalide ligands in the coordination sphere may be suitable for the achievement of a spin-state switching material. As expected for compounds exhibiting similar packing, the ligand-field strength associated to the half-conversion $T_{1/2}$ temperature is found to increase by the substitution of NCS^- by NCSe^- ,^[26] or bpy by $\text{Me}_2\text{-bpy}$.^[27] For the present compound, the LS form of the compound is observed for $T \leq 250$ K.

The spin-crossover curve and temperature are preserved when the compound is prepared in the form of polycrystalline, micro- or nanocrystals, that is through a size range extending from 100's microns to 60 nm. This feature is not surprising as we consider a thermal transformation with a too weak cooperative character^[3] for observing a downsizing effect, and the crystallinity is maintained in the different molecular samples.^[6a]

II.4. Experimental

II.4.1. Chemical Syntheses

4, 4'-dimethyl-2,2'-bipyridine (Aldrich, 99%), potassium selenocyanate (Aldrich, 99%) were used without further purification. The synthesis of the Fe(II) complex was performed under an argon atmosphere, using previously degassed solvents.

[Fe^{II}(Me₂-bpy)₃](NCSe)₂·3H₂O. A solution of Fe(SO₄)₂(NH₄)₂·6H₂O (142 mg, 0.36 mmol) in water (5 mL) was added dropwise to a methanolic solution (5 mL) of Me₂bpy (200 mg, 1.086 mmol) which was previously heated to 50 °C. The red mixture was stirred at 50 °C for 1 hour, then cooled to room temperature. A saturated solution of KNCS_e (1g, 6.9 mmol) in water was slowly added to the Fe(II) salt, the mixture was stirred for 20 min and decanted. The dark red solid was isolated by filtration and dried under argon. Single-crystals of this salt were isolated by slow evaporation of a methanolic solution of complexes.

Elemental analysis : formula for n = 3 water molecules C₃₈H₄₂FeN₈O₃Se₂ (MM 874.11 g·mol⁻¹) Calcd (%): C 52.31, H 4.85, N 12.84; Found (%): C 52.63, H 4.76, N 12.86; EDS analysis Fe/Se = 1/2; IR(KBr): ν = 2061 cm⁻¹(NC_{NCS_e}).

Thermogravimetric analysis : The thermogram shows an immediate loss of weight with a plateau around 100 °C (found 5.7 %, calcd for three water molecules 6.2 %). A new step clearly appears at 175 °C that corresponds to the removal of one bidentate ligand per formula (found for the total variation of weight 27.5 %, calcd for one Me₂bpy and three H₂O molecules 27.2 %).

Fe^{II}(Me₂-bpy)₂(NCSe)₂, this compound was first prepared by a solid-state synthesis that was mentioned in reference 12 for an analogue Fe(phen)₂(NCS)₂. According to the previous analysis, the polycrystalline powder of [Fe^{II}(Me₂-bpy)₃](NCSe)₂ was heated

at 175 °C for 4 hours (with/without vacuum). The purple polycrystalline powder was collected and characterized.

Elemental analysis: formula $C_{26}H_{24}FeN_6Se_2$ (MM 635.97 $gmol^{-1}$) Calcd (%): C 49.23, H 3.81, N 13.25; Found (%): C 49.99, H 3.83, N 12.89; EDS analysis Fe/Se = 1/1.84. IR(KBr): $\nu = 2061\text{ cm}^{-1}$ ($NC_{NCS_{Se}}$), $\nu = 2098\text{ cm}^{-1}$ ($NC_{NCS_{Se}}$).

1.2 μm microparticles of $Fe^{II}(Me_2-bpy)_2(NCSe)_2$ were prepared by an alternative method for extracting the bidentate ligand. It consists to dissolve 10 mg of $[Fe^{II}(Me_2-bpy)_3](NCSe)_2 \cdot 3H_2O$ in 1 mL of Ethanol. The red solution rapidly evolves and forms a suspension of violet microcrystalline powder that was isolated by centrifugation after the addition of 10 mL of butanol, then was rinsed with pentane and dried.

Elemental analysis : formula $C_{26}H_{24}FeN_6Se_2$ (MM 635.97 $gmol^{-1}$) Calcd (%): C 49.23, H 3.81, N 13.25, Fe 8.80, Se 24.90; Found (%): C 49.44, H 3.87, N 13.06, Fe 8.94, Se 24.14; EDS analysis Fe/Se = 1/2. IR(KBr): $\nu = 2061\text{ cm}^{-1}$ ($NC_{NCS_{Se}}$), $\nu = 2098\text{ cm}^{-1}$ ($NC_{NCS_{Se}}$).

The sudden precipitation approach was applied for controlling the nucleation and growth of small particles in an antisolvent.^[28]

460 nm nanoparticles of $Fe^{II}(Me_2-bpy)_2(NCSe)_2$. 10 mg of the cationic complex dissolved in 2 mL of ethanol was quickly added to a previously heated (65 °C) volume of toluene (20 mL) in which 200 mg of PMMA (PMMA 15000 or 35000) was dissolved. The mixture was vigorously stirred for 15 min, then the mixture was centrifugated for 10 min (at 10 000 rpm). The light purple solid was filtrated, rinsed with pentane, centrifugated. These last steps were repeated before the drying of powder under vacuum.

56 nm nanoparticles of $Fe^{II}(Me_2-bpy)_2(NCSe)_2$. The previous synthesis was carried out in the same conditions but here the 500 nm objects were removed with a 0.2 mm PTFE membrane just after the step of heating and stirring of the mixture. The filtrate was centrifugated.

II.4.2. Physical Measurements

The TGA analysis was done under ambient atmosphere with a TGA analyser (TA instruments-water LLC, SDT Q600) in the 293 to 473 K temperature range at a rate of 2°C per min.

FTIR spectra were collected on KBr pellets at room temperature with a Perkin-Elmer spectrometer (Spectrum 100).

X-ray diffraction patterns were recorded at room temperature on powders deposited on aluminium plate, using a Philipps Panalytical X'Pert Pro MPD powder diffractometer at CuK α radiation equipped with a fast detector within the 6 - 35° 2 θ range.

The single-crystal X-ray diffraction data were collected by using a Kappa X8 APPEX II Bruker diffractometer with graphite-monochromated MoK α radiation ($\lambda = 0.71073$ Å). At 100 K: crystal was mounted on a CryoLoop (Hampton Research) with Paratone-N (Hampton Research) as cryoprotectant and then flashfrozen in a nitrogen-gas stream at 100 K. The temperature of the crystal was maintained at the selected value by means of a 700 series Cryostream cooling device to within an accuracy of ± 1 K. The data were corrected for Lorentz polarization, and absorption effects. The structures were solved by direct methods using SHELXS-97^[28] and refined against F^2 by full-matrix least-squares techniques using SHELXL-97^[29] with anisotropic displacement parameters for all non-hydrogen atoms. Hydrogen atoms were located on a difference Fourier map and introduced into the calculations as a riding model with isotropic thermal parameters. All calculations were performed by using the Crystal Structure crystallographic software package WINGX.^[30] CCDC 1010286 and 1010287 (corresponding to [Fe^{II}(Me₂-bpy)₃](NCSe)₂.S with S = 2CH₃OH and 3H₂O) contains crystallographic data in appendix of chapter II.

TEM images have been acquired with a TEM JEOL 1400 (120 kV) equipped two high-resolution and high-speed digital CCD Gatan cameras.

Magnetic measurements were carried out using a Quantum Design SQUID magnetometer (MPMS5S Model) calibrated against a standard palladium sample. The data were collected between 100 and 370 K at a rate of 2 K min⁻¹.

Optical microscopy : The crystals were enclosed in a Linkam THMS600 heating-cooling stage and optical microscopy images of the crystals were recorded either isothermally or during a temperature rise (1 K/min) using an Olympus BX51 microscope equipped with a 20X objective and a color CCD camera (Motic). The sample was illuminated by a halogen lamp (400–700 nm) in transmission mode.

Raman Measurements : Variable temperature Raman spectra were recorded using a Labram-HR (Jobin-Yvon) microspectrometer and a liquid-nitrogen cryostage (Linkam

THMS 600). The 632.8 nm line of a He-Ne laser (17 mW) was used as the excitation source and the laser heating effects of the sample were minimized by additional filters (OD = 2-3) on the excitation beam. Owing to the micro-/nano-crystalline nature of the samples laser polarization effects were not investigated in more detail.

II.5. Conclusions

We have focused on two $\text{Fe}(\text{Me}_2\text{-bpy})_x(\text{NCSe})_2$ prototypical systems that are found at room temperature either in a diamagnetic ($x = 3$) or paramagnetic ($x = 2$) state as a consequence of a partial spin-crossover process centered at a temperature close to room temperature. These complexes can be interconverted either by solid-state thermolysis or by playing with their chemical equilibrium for inducing the precipitation of the neutral species.

Micro- and nanoparticles of the spin-crossover compound have been isolated with size varying between ca. 4500 and 56 nm. The magnetic behavior is preserved whatever the particles size and the spin crossover process is quantitative. A priori, nano-sized particles will be suitable for the preparation of materials of optical quality, via their stabilization and processing in convenient matrices to form thin films, a stage in progress that will be reported latter.

The fact that a spin-crossover compound may be thermally elaborated from a simple and chemically stable precursor may be of interest for molecular deposition on substrates, processing in micro-, nanosized patterns or nanopores.^[3,31,32,33] Indeed in absence of cooperative interactions, spin-crossover type molecules dispersed in highly diluted media present distinctive properties (chemical reactivity, spin-state switching possibly coupled to electron transfer, adduct formation and transport, IRM) that are currently attracting particular interest.

Finally, the present approach can be applied to molecular analogues, for example those incorporating photoswitchable ligands as proposed in the LD-LISC approach. The work is in progress.

References

- [1] Spin-Crossover in Transition Metal Compounds, I–III, in Topics in Current Chemistry, ed. P. Gülich and H. A. Goodwin, Springer, Berlin, 2004, vol. 233–235., Special issue in: Eur. J. Inorg. Chem. **2013**, 5–6; spin-crossover materials: Properties and Applications (Ed.: M. A. Halcrow), Wiley, Chichester, UK, **2013**.
- [2] J.-F. Létard, P. Guionneau and L. Goux-Capes, in: Topics in Current Chemistry, vol. 235, Spin Crossover in Transition Metal Compounds I–III (Eds.: P. Gülich, H. A. Goodwin), Springer, Heidelberg, Germany, **2004**, p. 221–249.
- [3] A. Bousseksou, G. Molnar, L. Salmon and W. Nicolazzi, Chem. Soc. Rev., 2011, **40**, 3313.
- [4] A. Hauser, in: Topics in Current Chemistry, vol. 234, Spin Crossover in Transition Metal Compounds I–III (Eds.: P. Gülich, H. A. Goodwin), Springer, Heidelberg, Germany, **2004**, p. 155.
- [5] A. Tissot, J.-F. Bardeau, E. Rivière, F. Brisset and M.-L. Boillot, Dalton Trans., 2010, **39**, 7806.
- [6] P. Chakraborty, M.-L. Boillot, A. Tissot and A. Hauser Angew. Chem. Int. Ed. 2013, 52, 7139-7142 ; R. Bertoni, M. Lorenc, A. Tissot, M. Servol, M.-L. Boillot, E. Collet Angew. Chem. Int. Ed., 2012, 51, 7485-7489.
- [7] M.-L. Boillot, J. Zarembowitch, A. Sour, In Topics in Current Chemistry; Gülich, P., Goodwin, H. A., Eds.; Springer: Berlin, Germany, 2004; Vol. 234, p 261 ; M.-L. Boillot, S. Pillet, A Tissot, E. Rivière, N. Claiser, C. Lecomte, Inorg. Chem. **2009**, 48, 4729–4736 ; A. Tissot, M.-L. Boillot, S. Pillet, E. Coddjovi, K. Boukheddaden, L. M. Lawson Daku J. Phys. Chem. C, 2010, 114, 21715-21722.
- [8] A. J. Cunningham, J.E. Ferguson, H.K.J. Powell, E. Sinn and H. Wong, J. Chem. Soc. Dalton Trans. 1972, 2155-2160.
- [9] E. Sinn, Inorg. Chim. Acta, 1969, **3**, 11-16.
- [10] A. Tissot, L. Rechinat, A. Bousseksou and M.-L. Boillot, J. Mater. Chem., 2012, **22**, 3411-3419.
- [11] W. Huang and T. Ogawa, J. Mol. Struct., 2006, **785**, 21.
- [12] W. A. Baker and H. M. Bobonich, Inorg. Chem., 1964, **3**, 1184.
- [13] E. König, Coord. Chem. Rev., 1968, **3**, 471.

- [14] E. König and K. Madeja, *Inorg. Chem.*, 1967, **6**, 48; E. König and K. Madeja, *Spectrochimica Acta*, 1967, **23A**, 45-54.
- [15] M. Sorai and S. Seki, *J. Phys. Chem. Solids*, 1974, **35**, 555-570.
- [16] E. J. MacLean, C. M. McGrath, C. J. O'Connor, C. Sangregorio, J. M. W. Seddon, E. Sinn, F. E. Sowrey, S. J. Teat, A. E. Terry, G. B. M. Vaughan and N. A. Young, *Chem. Eur. J.*, 2003, **921**, 5314-5322.
- [17] A. Tissot, C. Enachescu and M.-L. Boillot, *J. Mater. Chem.*, 2012, **22**, 20451.
- [18] S. Savage, Z. Jia-Long and A. G. Maddock, *J. Chem. Soc. Dalton Trans.*, 1985, 991-996.
- [19] P. Guionneau, *Dalton Trans.* 2014, **43**, 382-393; J. Tao, R.-J. Wei, R. B. Huang and L. S. Zheng, *Chem. Soc. Rev.*, 2012, **41**, 703-737.
- [20] M. Marchivie, P. Guionneau, J.-F. Létard and D. Chasseau, *Acta Crystallogr.*, 2003, **59**, 479 ; J.-F. Létard, G. Chastanet, O. Nguyen, S. Marcen, M. Marchivie, P. Guionneau, D. Chasseau and P. Gülich, *Monatsh. Chem.*, 2003, **134**, 165.
- [21] M. A. Willard, L. K. Kurihara, E. E. Carpenter, S. Calvin, V. G. Harris, *Int. Mater. Rev.*, 2004, **49**, 125-170.
- [22] A. Hosseini, S. Jabbari, A. R. Mahjoub and M. Movahedi, *J. Coord. Chem.*, 2012, **65**, 2623-2633.
- [23] N. Dragoe, M. Andruh and E. Segal, *Thermochimica Acta*, 1991, **176**, 241-248.
- [24] W. M. Reiff, R. B. Frankel, B. F. Little and G. J. Long, *Inorg. Chem.* , 1974, **13**, 2153.
- [25] M. A. Halcrow, *Polyhedron*, 2007, **26**, 3523-3576.
- [26] K. F. Purcell and M. P. Edwards, *Inorg. Chem.*, 1984, **23**, 2620-2625.
- [27] M.-L. Boillot and H. Soyer, *New J. Chem.*, 1997, **21**, 889-892.
- [28] G.M. Sheldrick, *SHELXS-97*, Program for Crystal Structure Solution, University of Göttingen, Göttingen, Germany, 1997.
- [29] G. M. Sheldrick, *SHELXL-97*, Program for the refinement of crystal structures from diffraction data, University of Göttingen, Göttingen, Germany, 1997.
- [30] L. J. Farrugia, *J. Appl. Cryst.*, 1999, **32**, 837.

- [31] S. Shi, G. Schmerber, J. Arabski, J.-B. Beaufrand, D. J. Kim, S. Boukari, M. Bowen, N. T. Kemp, N. Viart, G. Rogez, E. Beaurepaire, H. Aubriet, J. Petersen, C. Becker and D. Ruch, *Appl. Phys. Lett.*, 2009, **95**, 043303.
- [32] M. Cavallini, I. Bergenti, S. Milita, G. Ruani, I. Salitros, Z. R. Qu, R. Chandrasekar and M. Ruben, *Angew. Chem. Int. Ed.*, 2008, **47**, 8596.
- [33] A. Tissot, J.-F. Bardeau, E. Rivière, F. Brisset and M.-L. Boillot, *Dalton Trans.*, 2010, **39**, 7806-7812.

Chapter III

Chapter III

Photo-Switching Properties of 4-styryl-2,2'-bipyridine as Fe(II) Chelator and Free-base Molecule.

III.1 Introduction

Stilbenoids, like retinal, are systems whose photochemical and photophysical behaviors have attracted a wide and continuous interest motivated by their prominent role in material science and the understanding of their reactivity in various environments.^[1,2,3] Incorporation of such a photoresponsive group in molecules able to establish chemical bonds with metal ions (like pyridine or bipyridine) aims at controlling several functionalities (mechanical, electronic, optical, ...) upon light irradiation.^[4,5,6] The combination of stilbenoids ligands with metal ions (like Ru^{II}, Re^I, Ir^{III}, Zn^{II} or Fe^{II}) was explored for solar energy conversion, photocatalysis, (electro)luminescence, NLO, biotechnology and molecular photoswitches,^[1-6,7] while recent investigations have focused on the underlying mechanisms and dynamics governing the ligand-centered isomerization.^[8,9] The so-called Ligand-driven light induced spin change (LD-LISC) effect proposed by Zarembowitch, so far developed in our team,^[10] was based on the coupling between a photoactive (like stilbenoid^[11] or diarylethene^[12]) ligand and a spin-crossover type coordination core. Upon light irradiation, the geometrical conversion of the organic moiety induces the change of ligand-field strength that results in the reversible switching of the spin states of the metal ion. Depending on the nature of organic /inorganic parts, ligand-centered photoreactions, spin-state switching of metal-ions and LD-LISC effects (synergetic coupling) were reported at temperatures including the ambient one. The complexes were in highly diluted (solutions or thin polymeric films, in case of UV excitation) or confined environments (single-crystal, in case of Vis excitation), features that also pointed the importance of media and thus processing.^[13,14,15] The spin-crossover coordination compounds are considered as archetype of switchable and bistable molecular materials. They exist in two almost degenerated electronic (low spin, LS and high spin, HS) states, which interconvert under small perturbations (T, P, hv, B, E), thus producing drastic variations of the related physical (optic, magnetic, volume, dielectric) properties. For this class of materials, the light irradiation of spin-crossover ions (mainly Fe^{II}) may also induce the spin-state switching but a complete trapping of the metastable excited state requires temperatures well below the thermal conversion.^[16] The effect, named light-induced excited spin state

trapping (LIESST), was triggered by metal-centered or charge transfer excitations that gave rise to a complex sequence of processes presently probed in solution,^[17] in single-crystals or in nanocrystals.^[18]

We report here the syntheses of cationic Fe^{II} complexes incorporating bipyridine ligands functionalized with a photoisomerizable styryl group and the investigation of photochemical behaviors of both ligands and complexes in solution. According to our recent work on solvent-induced precipitation of spin-crossover nanoparticles,^[19] these highly soluble complexes appears as nice candidates for the elaboration in a next stage of spin-crossover nanoparticles for probing LD-LISC activity in denser media, an approach exploited in chapter IV.

III.2. Experimental

III.2.1. Syntheses

The photoactive ligands and complexes were prepared and handled in darkness. The set of ¹H NMR spectra, Mass spectra and IR data were provided in the appendix of chapter III.

III.2.1.1. t-msbpy Isomer

The trans isomer of 4-methyl-4'-styryl-2,2'-bipyridine was prepared as previously described.^[20] Single-crystals of t-msbpy (colorless platelets) were isolated by slow evaporation of a CH₃OH solution. Characterization of t-msbpy: Anal. Calcd (%) for C₁₉H₁₆N₂ (272.3 g mol⁻¹) C, 83.8; H, 5.92; N, 10.29; Found: C, 83.60; H, 5.92; N, 10.13; ¹H NMR data (δ in ppm) in CDCl₃: 8.63(d, 1H), 8.54 (s, 1H), 8.29(s, 1H), 7.58 (d, 1H), 7.52 (s, 1H), 7.44-7.30 (m, 4H), 7.15 (d, 2H), 2.53 (s, 3H). Mass spectrometry (in the appendix of chapter III) m/z 273.1 (C₁₉H₁₇N₂) 274.1 and 275.1 traces; IR absorptions : ν_{max}/cm⁻¹ : 1631w (CC stretch., ethene) ; 1450s (CC and CN stretch, in plane CH bend., bpy) ; 967, 958s (CH out of plane deform, trans ethene) ; 749 and 731s (CC and CN torsion, bpy).

III.2.1.2. 4-methyl-2,2'-bipyridine-4'-carboxaldehyde

The Wittig approach was applied for the synthesis of 4-methyl-4'-*cis*-styryl-2,2'-bipyridine from the 4-methyl-2,2'-bipyridine-4'-carboxaldehyde.

4-methyl-2,2'-bipyridine-4'-carboxaldehyde. It was prepared from 4,4'-dimethyl-2,2'-bipyridine according to the published method.^[21] White solid (yield=16%). ¹H NMR data

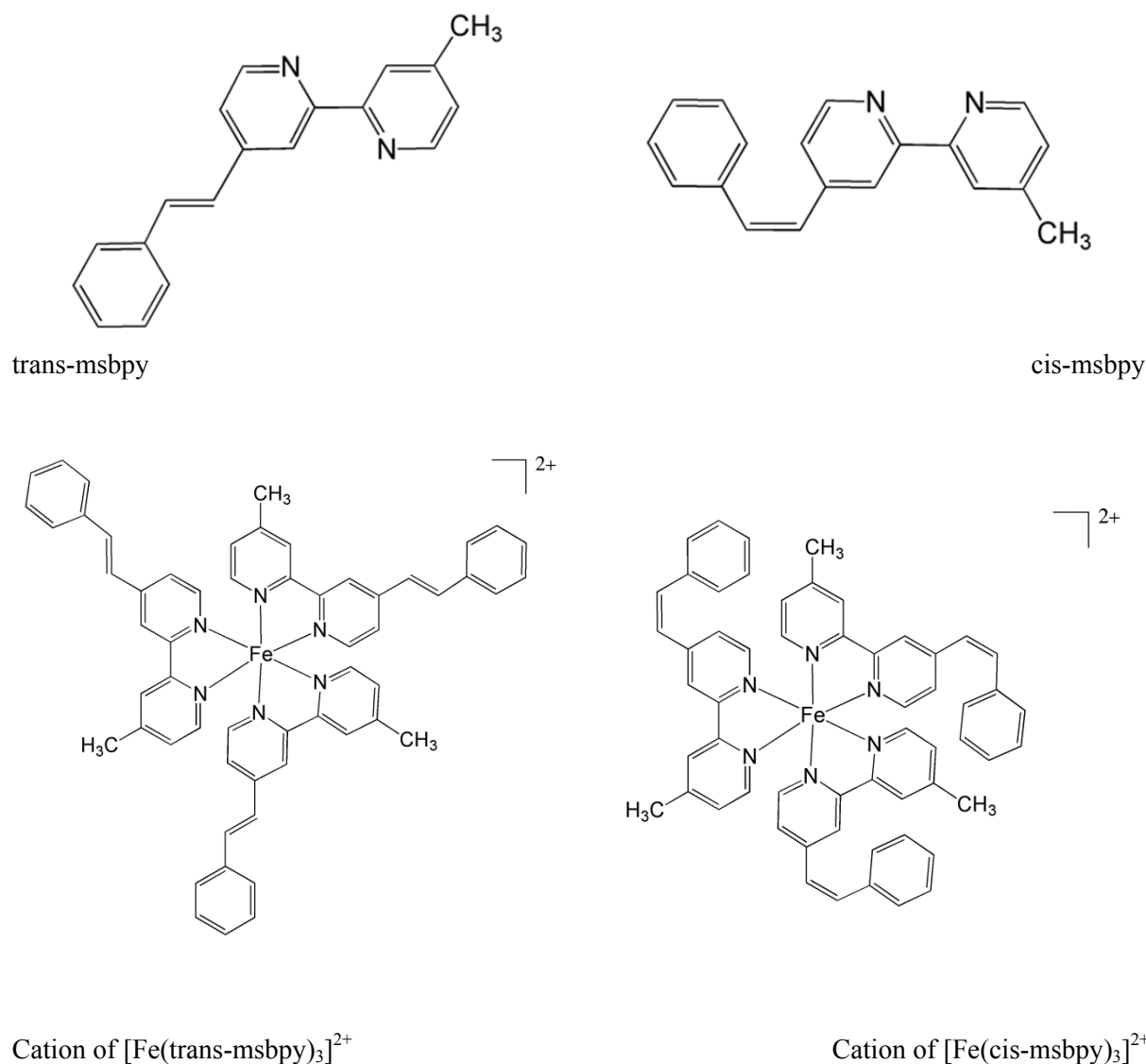
(δ in ppm) in CDCl_3 : 10.18 ppm (s, 1 H, CHO); 8.90 ppm (d, 4.3 Hz, 1 H), 8.83 ppm (s, 1H), 8.58 ppm (d, 4.7 Hz, 1 H), 8.28 ppm (s, 1 H), 7.73 ppm (d, 6.3 Hz, 1 H), 7.20 ppm (d, 5.4 Hz, 1 H), 2.47 ppm (s, 3 H, CH_3). Mass spectrometry (ESI) m/z 199.1 ($\text{C}_{12}\text{H}_{11}\text{N}_2\text{O}$); 221.1 ($\text{C}_{12}\text{H}_{10}\text{N}_2\text{ONa}$); Anal. Calcd (%) for $\text{C}_{12}\text{H}_{10}\text{N}_2\text{O}$ ($M=198.22 \text{ g mol}^{-1}$) calcd ; C, 72.71 ; H, 5.08, N; 14.13 ; found C, 72.01; H, 5.35 ; N 13.32.

III.2.1.3. c-msbpy Isomer

The method described by Williams^[22] based on the reaction between an ylid intermediate and a pyridylaldehyde was employed for the synthesis of the 4-methyl-4'-*cis*-styryl-2,2'-bipyridine. The solid residue isolated after extraction in the organic phase and drying was column-chromatographed with cyclohexane: diethyl ethers (8:2). The *cis*-isomer was obtained as a colorless oil after a sublimation at 60°C under vacuum to remove traces of impurity. The yield is 25 %. ^1H NMR data (δ in ppm) in CDCl_3 : 8.55 ppm (d, 1 H). 8.48 ppm (d, 1 H), 8.29 ppm (s, 1 H), 8.20 ppm (s, 1 H), 7.27 ppm (m, 5 H), 7.14 ppm (t, 2 H), 6.85 ppm (d, 12 Hz, 1 H, H_α), 6.64 ppm (d, 12.3 Hz, 1H, H_β), 2.45 ppm (s, 3 H, H-methyl). The *cis* isomer is characterized by signals at 6.85 and 6.64 ppm. Mass spectrometry (ESI) m/z 273.1 ($\text{C}_{19}\text{H}_{17}\text{N}_2$), 274.1 and 275.1 traces. Anal. Calcd (%) for $\text{C}_{19}\text{H}_{16}\text{N}_2$ (272.3 g mol^{-1}) calcd ; C, 83.79; H, 5.92, N, 10.29 ; found C, 83.35, H, 6.05; N 10.11. IR absorptions : $\nu_{\text{max}}/\text{cm}^{-1}$: 1631w (C=C stretching, ethene) ; 1459 and 1446m (C=C and C=N stretching, in plane CH bending, bpy) ; 796 and 772s (in plane ring bending, bpy), 705s (CH out of plane deformation, *cis* ethene).

III.2.1.4. Photocyclized Ligand

A condensed derivative of t-msbpy was prepared by a photochemical synthesis in a glass reactor equipped with a Hg source (transmitted radiation at $\lambda > 330 \text{ nm}$). The degassed $6 \times 10^{-4} \text{ M}$ solution of t-msbpy in hexane (615 mL) was irradiated during 5 sequences of 1 h for the NMR characterization of the reaction. The yellow residue isolated by evaporation was chromatographed (Al_2O_3 , cyclohexane/diethyl ether = 3/1) then characterized. $\text{C}_{19}\text{H}_{14}\text{N}_2$, $MM= 270.33 \text{ g mol}^{-1}$. ^1H NMR data (δ in ppm) in CDCl_3 : 8.87 ppm (d, 1H, $J=6 \text{ Hz}$), 8.71 ppm (d, 1H, $J=5.3 \text{ Hz}$), 8.24 ppm (d, 1H, $J=9.4 \text{ Hz}$), 8.1 ppm (s, 1H), 8.02 ppm (d, 1H, $J=7.9 \text{ Hz}$), 7.94 ppm (s, 1H), 7.89 ppm (d, 1H, 9 Hz), 7.6 ppm (s, 1H), 7.52 ppm (s, 1H), 7.4 ppm (d, 2H, $J=5.7 \text{ Hz}$), 2.63 ppm (s, 3H, methyl). Mass spectrometry (appendix of chapter III) m/z : 271.1242 ($\text{C}_{19}\text{H}_{15}\text{N}_2$) and 293.1049 ($\text{C}_{19}\text{H}_{14}\text{N}_2\text{Na}$).

Scheme 1. Proposed structures of stilbenoids and related Fe(II) complexes**III.2.1.5. $[\text{Fe}(\text{msbpy})_3](\text{NCSe})_2 \cdot n\text{H}_2\text{O}$**

The synthesis of cationic complexes with the two isomers of msbpy was adapted from the reference 20, with KNCSe salt instead of KNCS . The red solids were isolated by filtration, rinsed and dried under argon.

$[\text{Fe}(\text{trans-msbpy})_3](\text{NCSe})_2 \cdot 3\text{H}_2\text{O}$. Anal. Calcd (%) for $\text{FeC}_{59}\text{H}_{48}\text{N}_8\text{Se}_2 \cdot 3\text{H}_2\text{O}$ ($M=1138.2 \text{ g mol}^{-1}$) calcd ; C, 62.33 ; H, 4.79 ; N, 9.86 ; Found C, 62.66 ; H, 4.61 ; N, 9.44. The loss of weight at 100°C compared to RT measured by thermogravimetric analysis : Calcd 4.75 %

(for 3 molecules of water), Found 2.6 % (suggesting partial dehydration of the starting material). EDS analysis: Fe/Se = 27.74/72.26. IR absorptions : $\nu_{\max}/\text{cm}^{-1}$: 3436w (OH stretching, H₂O) ; 2061s (NC stretching, NCSe) 1607vs (NC stretching, bpy) ; 963m (CH out of plane deformation, trans ethene). Powder X-ray diffraction analysis: poorly crystalline sample characterized by 2 θ peaks at 14.4, 15.4, 15.7 17.4, 20.4, 20.5 23.0, 25.5, 26.3, 28.7 °. Magnetic data : $\chi_{\text{M}}T$ (300 K) = ca. -0.15 cm³mol⁻¹K.

[Fe(cis-msbpy)₃](NCSe)₂·2H₂O Anal. Calcd (%) for FeC₅₉H₄₈N₈Se₂·2H₂O (M=1120.2 gmol⁻¹) calcd ; C, 63.34; H, 4.68 ; N, 10.01; Found C, 63.68; H, 4.43 ; N, 9.98. The loss of weight at 130 °C compared to RT measured by thermogravimetric analysis : Calcd 3.2 % (for 2 molecules of water), Found 2.2 % (suggesting partial dehydration of the starting material). EDS analysis Fe/Se = 28.80/71.20. IR absorptions : $\nu_{\max}/\text{cm}^{-1}$: 3400, 3243w (OH stretching, H₂O) ; 2057vs (NC stretching, NCSe) 1607vs (NC stretching, bpy) ; 771m (CH out of plane deformation, cis ethene), 708vs (CH out of plane deformation, cis ethene). Powder X-ray diffraction analysis : amorphous or nanosized -sample. Magnetic data : $\chi_{\text{M}}T$ (300 K) = ca. -0.05 cm³mol⁻¹K.

III.2.2. Physical Measurements

The X-ray diffraction data were collected by using a Kappa X8 APPEX II Bruker diffractometer with graphite-monochromated MoK α radiation (λ = 0.71073 Å). At 100 K : crystal was mounted on a CryoLoop (Hampton Research) with Paratone-N (Hampton Research) as cryoprotectant and then flashfrozen in a nitrogen-gas stream at 100 K. The temperature of the crystal was maintained at the selected value by means of a 700 series Cryostream cooling device to within an accuracy of ± 1 K. The data were corrected for Lorentz polarization, and absorption effects. The structures were solved by direct methods using SHELXS-97^[15] and refined against F^2 by full-matrix least-squares techniques using SHELXL-97^[16] with anisotropic displacement parameters for all non-hydrogen atoms. Hydrogen atoms were located on a difference Fourier map and introduced into the calculations as a riding model with isotropic thermal parameters. All calculations were performed by using the Crystal Structure crystallographic software package WINGX.^[17]

X-ray diffraction patterns were recorded at room temperature on powders deposited on aluminium plate, using a Philipps Panalytical X'Pert Pro MPD powder diffractometer at CuK α radiation equipped with a fast detector within the 6 - 35° 2 θ range.

The FTIR spectra were collected with a Perkin-Elmer spectrometer (Spectrum 100).

Magnetic measurements were carried out using a Quantum Design SQUID magnetometer (MPMS5S Model) calibrated against a standard palladium sample. The data were corrected from the diamagnetic contribution of the molecular compound and the sample holder.

The UV-vis-NIR spectra were collected using a Varian Cary 5000 double-beam spectrophotometer. Acetonitrile solutions of free-base ligands (ca. $1\text{--}4 \times 10^{-4}$ M) or complexes (1×10^{-4} M) were used in quartz cuvettes of 0.1 cm optical path. The solutions were irradiated in quartz cuvettes (or NMR tubes) with different light sources: 254, 365 nm or 366 nm (HeroLab (NU-6) lamp for chromatography, power: 6.0, 5.4 or 5.4 mW respectively); 365, 500, 700 or 800 nm (Newport Hg lamp equipped with appropriate filters); 405, 532 or 635 nm (Laser/diode from Optoelectronic Tech.co.ltd, models LD-WL 206, LD-WL 206, PSU-III-LED).

III.3. Results and Discussion

III.3.1. Structural Characterization of *t*-msbpy

The colorless platelets of *trans*-msbpy were analyzed by single-crystal X-ray diffraction at 100 K. This compound crystallizes in the orthorhombic *Pbca* space group. Crystal data collection and refinement parameters and selected bond lengths or angles are collected in footnote and **Tables T1 - T2** in the appendix of chapter III.

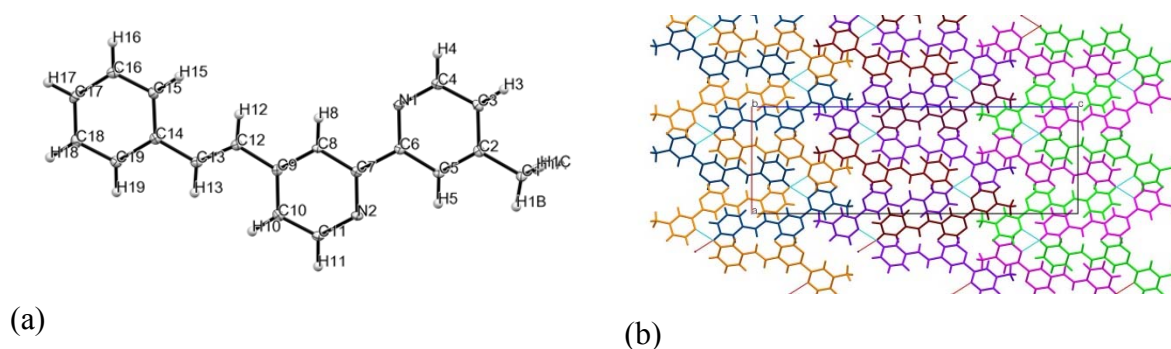


Figure 1: (a) ORTEP view of *trans*-msbpy at 100 K with thermal ellipsoids at 30 % level; (b) View of the packing of *t*-msbpy along *b* axis showing the zig-zag double chains formed by polar molecules interacting via Van der Waals contacts (dotted lines in blue and red).

In **Figure 1a**, the ORTEP view shows an almost planar molecule with a *trans* arrangement of pyridine groups minimizing the inter-ring sterical hindrance (between H₅ and H₈ atoms). The

C₁₂-C₁₃ bond length (at 1.335 (2) Å) is typical for an ethylenic group. The dihedral angles C(Ph)-C₁₃-C₁₂-C(py) (172 -173°) slightly deviate from the ideal planar geometry, a feature observed for stilbenoids at solid state^[23,24] that impacts the electronic delocalization of the π system. This deviation arises from the crystal packing of polar molecules, as the position and orientation of aromatic rings are locked by some intermolecular contacts (N₂(Py)...H₁C₁(Me) and C₁₈-H₁₈(Ph)...N₁(Py), (distances smaller than the sum of Van der Waals radii - 0.18 Å). More specifically, the push-pull type arrangement of molecules forms a set of zig-zag double chains along *a* axis stabilized by additional Van der Waals contacts (**Figure 1b**). The large distances between the unsaturated groups of neighboring molecules (≥ 3.66 Å) indicate an extra stabilization of the crystal by 3D network of weak π -stacking interactions.

III.3.2. Electronic Absorption of msbpy Isomers

The electronic spectra of msbpy isomers in CH₃CN are plotted in **Figure 2** (see also data in **Table 1**). The trans-isomer presents an intense and low-energy shifted absorption at 307 nm (assigned to π - π^* and charge transfer transitions) that results from the electronic delocalization associated to the almost coplanar configuration of styryl^[25] and bpy chromophores in solution. In contrast, the cis-isomers that are distributed over several twisted conformations lead to higher energy absorptions of the π skeletons at 281 nm that overlay those characterizing the bpy moiety.

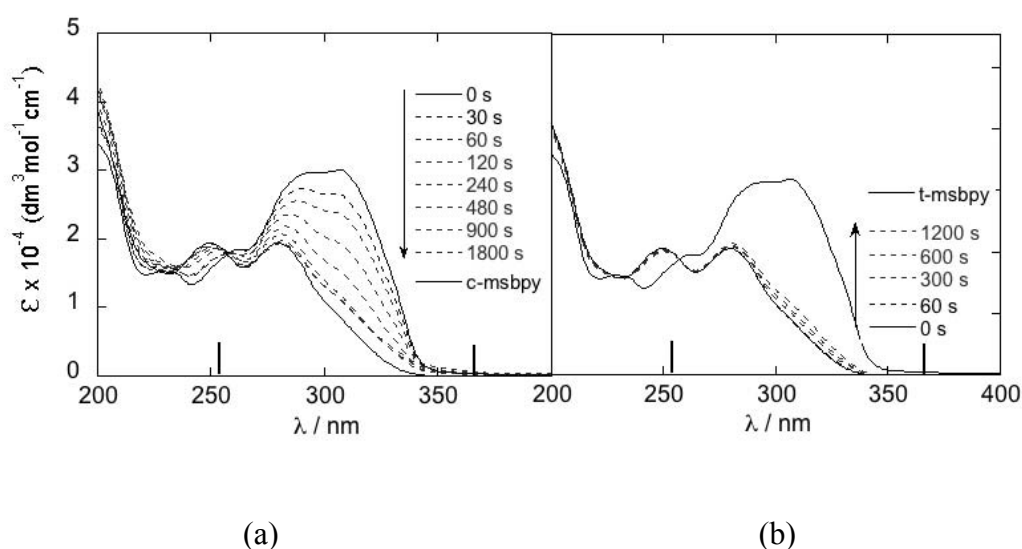


Figure 2: Absorption spectra of msbpy isomers in degassed CH₃CN (continuous lines in (a) and (b)). (a) Photowitching of trans-isomer ($\lambda_{\text{exc}} = 365$ nm under Argon, $\Delta t = 0$ -1800 s). (b) Photoswitching of cis-isomer ($\lambda_{\text{exc}} = 365$ nm under Argon, $\Delta t = 0$ -1200 s).

III.3.3. Photoisomerization of msbpy Isomers

III.3.3.1. UV-Vis Measurements

An almost quantitative photoisomerization of msbpy can be achieved by irradiating at 365 nm an acetonitrile solution of trans-isomer ($c = 1.47 \times 10^{-4}$ M). In absence of dioxygen, the trans-to-cis styryl conversion (**Figure 2a**) is manifested by the continuous evolution of spectra with the irradiation time towards the one of cis isomer, the preservation of the isosbestic point (at 257 nm) and the absence of discrepancies with respect to the weighted spectra of both isomers. The photo-stationary state (PSS) reached in ca. 15 min corresponds to the formation of ca. 85 % of cis-msbpy. Conversely, the irradiation of a degassed solution of cis-isomer ($\lambda_{\text{exc}} = 366$ nm, **Figure 2b**) forms a mixture corresponding to 85 % of cis-isomer. The ratio of both isomers in PSS, confirmed by NMR measurements (see below), reflects their relative absorption cross-sections and photoisomerization quantum yields. This last reaction was found to be not very sensitive to dioxygen, except for long time of irradiation of cis-msbpy.

Table 2: UV-Vis data collected for trans- and cis-msbpy isomers, the photocyclized (PC) product and the corresponding complexes

Compound	Conditions	Electronic Absorption λ in nm ($\epsilon \times 10^{-4}$ in $\text{dm}^3 \times \text{mol}^{-1} \times \text{cm}^{-1}$)
<i>t</i> -msbpy	CH ₃ CN	228 (1.62), 233 (1.60), 262 (1.95), 290 (3.11), 307.5 (3.18)
<i>c</i> -msbpy	CH ₃ CN	250 (2.05), 281 (2.05)
Intermediate state ^a	CH ₃ CN	225sh, 262 (2.37), 284(2.67), 299sh, 314sh, 341sh, 357 (0.25)
[Fe(<i>t</i> -msbpy) ₃](NCSe) ₂ .nH ₂ O	CH ₃ CN	251 (4.17), 297 (6.62), 331 (7.83), 388(1.21) ^{sh} , 510 (1.49) ^{sh} , 551 (2.00)
[Fe(<i>c</i> -msbpy) ₃](NCSe) ₂ .nH ₂ O	CH ₃ CN	250 (5.44), 282 (4.55) ^{sh} , 301 (5.11), 379 (0.94), 501 (1.03) ^{sh} , 543 (1.42)
Intermediate state ^c		260, 285, 299sh, 313sh, 342sh, 357, ca. 473

(a) Aerated solution of *t*-msbpy irradiated at 254 nm during 50 min, (b) See in text for elaboration and characterization, (c) Degassed solution of [Fe(*t*-msbpy)₃](NCSe)₂.nH₂O irradiated at 254 nm during 190 min, sh = shoulder.

III.3.3.2. ^1H NMR Measurements

The signals associated to reactants and products involved in a photochemical reaction may be resolved by ^1H NMR measurement if conditions for efficient conversion and detection can be selected. Therefore, the experiment was performed with an excitation ($\lambda_{\text{exc}} = 365 \text{ nm}$) of a degassed CD_3CN solution of t-msbpy ($1.98 \times 10^{-3} \text{ M}$) within the NMR glass tube.

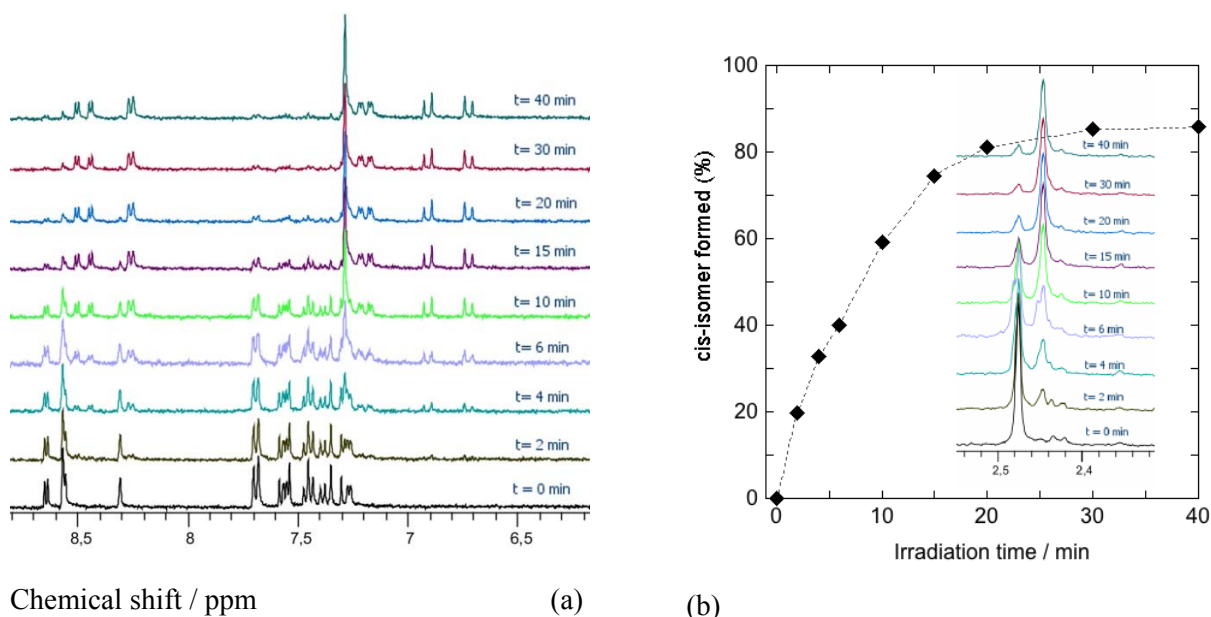


Figure 3 : (a) ^1H NMR spectral changes of trans-msbpy in degassed CD_3CN at 298 K during the course of irradiation at $\lambda_{\text{exc}} = 365 \text{ nm}$ showing the set of aromatic peaks (doublet) related to the signals of protons in $-\text{HC}=\text{HC}-$. The latter appears at $\delta = 7.3 \text{ ppm}$ ($J_{\text{trans}} = 15.9 \text{ Hz}$) and $\delta = 6.72$ or 6.91 ppm ($J_{\text{cis}} = 12 \text{ Hz}$) for trans- and cis-isomers respectively. (b) Plot of the percentage of cis-isomer vs. the irradiation time. The inset shows the signals corresponding the protons of 4'-methyl substituents of bipyridine of both isomers from which the percentage of cis-isomer was extracted.

In **Figure 3**, the spectra recorded as a function of irradiation time show the evolution of aromatic proton signals with chemical shifts and coupling constants allowing an unambiguous identification and analysis of species in solution. As detailed above, markers of both msbpy isomers (for instance, at ca. 8.65 (dd), 8.3 (s) or 8.2 (s), 6.9(d, 12 Hz), 6.7(d, 12 Hz), for trans or cis isomers respectively) coexist and no significant trace of side product may be detected, consistently with the previous results of the UV analysis. The curve of the percentage of cis-isomer versus the irradiation time was extracted from the integration of the methyl signal of msbpy. From this plot, we can confirm the formation of a PSS with ca. 86 % of cis-msbpy and 14 % of trans-msbpy.

III.3.3.3. Reactivity of msbpy Isomers upon a 254 nm Irradiation

A 254 nm excitation of c-msbpy was selected for investigating higher energy pathway for the *cis*-to-*trans* double bond isomerization and competitive photocyclization reactions that were established from literature on stilbenoids.^[26a]

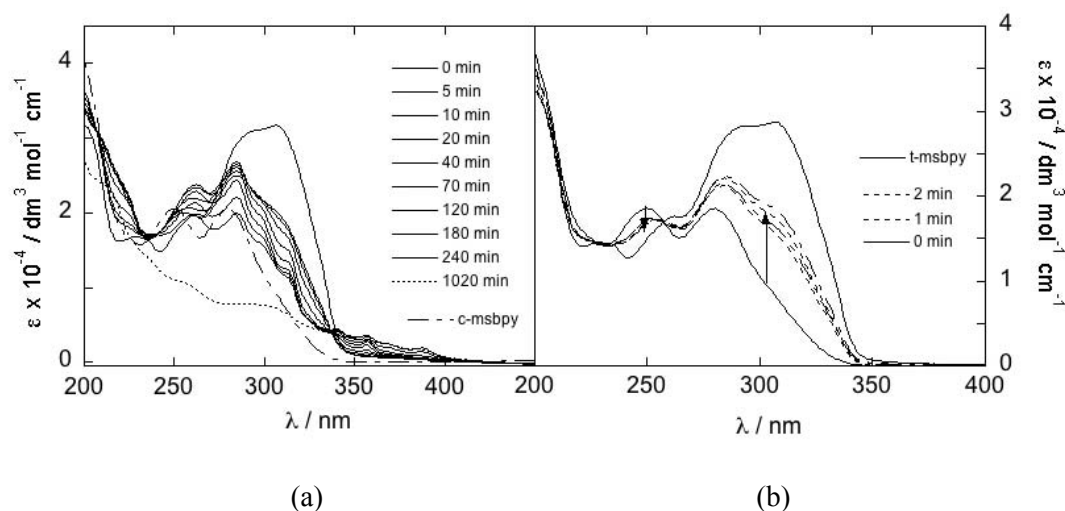


Figure 4 : Spectra of aerated CH₃CN solution of both isomers of msbpy irradiated at 254 nm: **(a)** t-msbpy irradiated during $\Delta t = 0\text{--}1020$ min; **(b)** c-msbpy irradiated during $\Delta t = 0\text{--}2$ min (see the appendix of chapter III). Spectra of pure c-msbpy (a, —.—), t-msbpy (b, —) and those calculated for a 40 or 50 % *cis*-to-*trans* conversion (b, —.—) are shown for comparison.

In **Figure 4b**, the 254 nm excitation of an aerated CH₃CN solution of c-msbpy leads first to the formation of the *trans* isomer (ca. 40-45 %, $\Delta t^{\text{irr}} = 2$ min). For higher irradiation time, the decrease of absorbance at 307 nm (or increase at 257 nm) indicates the disappearance of t-msbpy and the concomitant formation of a product (noted P_{PC}, see below) characterized by a structured band (ca. 227, 263 and 284 nm), a weak band at 366 nm and the absence of noticeable visible absorption (**Figure S4a**). The reactivity of t-msbpy was probed in the same conditions (**Figure 4a**). Here, we can observe the increase of absorbance at 257 nm (isosbestic point between msbpy isomers) that is maximal at ca. 50 min (**Figure S4b**), with again the appearance of a structured UV band (and weaker components between 350-400 nm) associated to the formation of a new species. In both cases, the spectra of P_{PC} products (at $\Delta t^{\text{irr}} = 5$ (*cis*) or 180 (*trans*) min in **Figure 4** and **S4a**) were preserved over a period in darkness (120 (*cis*) min and 30 (*trans*) min). The comparison of both sets of data suggests that analogous P_{PC} molecules are formed. We note that the formation of P_{PC} species prevails over

the trans→cis and cis→trans isomerizations and it takes place slower than the cis→trans conversion, features related to the relative absorption of both isomers at 254 nm and suggesting relatively higher quantum yields for the cis→trans conversion or cis → P_{PC} than the trans→cis isomerization. Finally when pursuing the irradiation of t-msbpy, this structured spectrum still evolves to a final one with relatively weaker and broader absorptions (at ca. 216, 236, 260, 300 nm up to 400 nm) that may be reasonably assigned to degradation products^[26b] (oligomer due to crosslinking reactions possibly mixed with photocyclized ligand (**Figure S5**)).

III.3.4. Iron(II) Complexes Characterizations

The different attempts done for the isolation of the Fe^{II} complexes in the form of crystals of X-ray quality were unsuccessful. In **scheme 1**, the structures proposed for the complexes consist of metal ions in pseudo octahedral environments of N donor atoms of three bidentate ligands, as reported for the Fe^{II} analogue with 4,4'-Me₂-2,2'-bipyridine.^[6] The formation of such cationic complexes are supported by the chemical characterizations (chemical analysis, TGA, IR and UV data) and the solubility of complexes. The observation of the NC stretching mode of NCSe anion at ca. 2061 cm⁻¹, combined to the diamagnetic behaviors of complexes at room temperature, precludes the cis-coordination of NCSe⁻ to Fe^{II} in a neutral complex (2061 and 2070 ± 4 cm⁻¹, 2098 and ~2103 ± 4 cm⁻¹ for HS and LS ions, respectively).^[27,28] IR data also confirm the configuration of the CH=CH double bond in the complexes (for instance, the CH out of plane deformation frequencies of cis- and trans-ethene at 771 and 963 cm⁻¹, respectively). Other evidences are provided by electronic absorption data (see below). It can be noted that different isomers (conformers, diastereoisomers) may derive from the asymmetry of the bidentate ligand and the positions of styryl group.

III.3.4.1. Electronic Absorption of [Fe(msbpy)₃](NCSe)₂.nH₂O Complexes

The absorption spectra of Fe^{II} complexes in degassed acetonitrile (**Figure 5**) are dominated by the very intense intraligand transitions in UV, typical of the free-base ligands with their respective configurations.

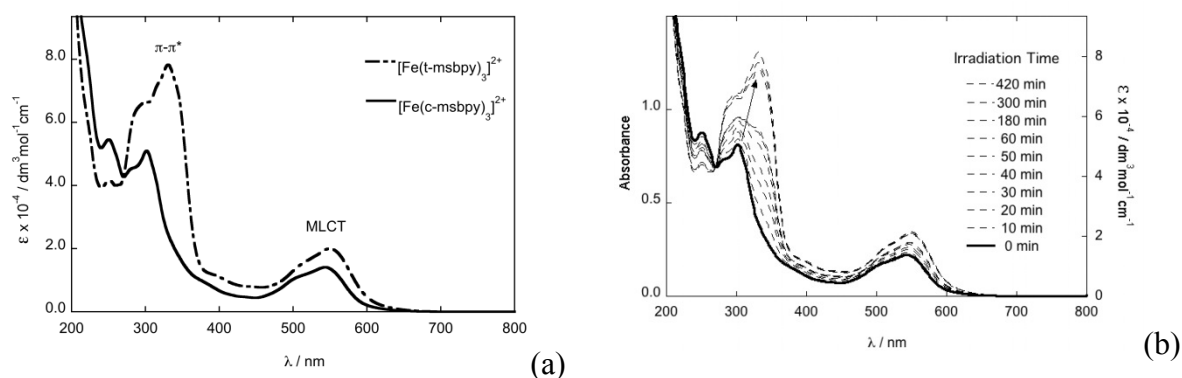


Figure 5 : (a) Molar extinction coefficients ($\epsilon \times 10^4$) of $[\text{Fe}(\text{t-msbpy})_3]^{2+}$ (---) and $[\text{Fe}(\text{c-msbpy})_3]^{2+}$ (—) complexes in degassed acetonitrile solutions. (b) Evolution of UV-Vis spectra of a degassed solution of $[\text{Fe}(\text{c-msbpy})_3]^{2+}$ upon a 405 nm irradiation.

The data in **Table 1** show the shift of absorption maxima (from 307.5 to 331 nm and 281 to 301 nm for the trans and cis –msbpy isomers, respectively) due to the coordination to the Fe^{II} metal ion. The Vis absorptions, assigned to Fe^{II} to bipyridine charge transfer transitions vary in intensity and energy with the nature of isomers (**Table 1**). The molar extinction coefficients (2.00 and $1.42 \times 10^4 \text{ dm}^3 \text{mol}^{-1} \text{cm}^{-1}$ for complexes with trans- and cis-isomers of msbpy, respectively) are higher than values reported for LS analogues (for $[\text{Fe}(\text{bpy})_3](\text{BF}_4)_2$ in DMF: $\epsilon = 1.12 \times 10^4 \text{ dm}^3 \text{mol}^{-1} \text{cm}^{-1}$ at $\lambda_{\text{max}} = 521 \text{ nm}$).^[29,30]

III.3.4.2. Photoisomerization of $[\text{Fe}(\text{msbpy})_3](\text{NCSe})_2 \cdot n\text{H}_2\text{O}$ Complexes under UV Excitation

The experiments were carried out in degassed acetonitrile solutions of complexes with a selection of excitation wavelengths based on the data collected for the free-base ligands, then on the absorption features of complexes in the Visible range. The role of dioxygen was addressed by similar measurements realized with aerated solutions.

The degassed solutions of both complexes react under the effect of a 365 nm excitation, but contrarily to what was observed for the ligands, the $[\text{Fe}(\text{c-msbpy})_3]^{2+}$ complex converts into the trans-analogue (content of $[\text{Fe}(\text{t-msbpy})_3]^{2+}$ estimated at ca. 80 % from the weighted combination of spectra, **Figure S6**). The reactions of both complexes at this wavelength provide spectra corresponding to the same PSS (**Figure S7**). As shown in **Figure 5b**, the 405 nm excitation maximizes this photochemical conversion. The evolution of solutions versus the irradiation time leads to a quasi-complete transformation of cis→trans-msbpy ligands ($\geq 95 \%$). An isosbestic point at 270 nm was preserved during the whole transformation and no

deviation was detected. Consistently, the irradiation at 405 nm of $[\text{Fe}(t\text{-msbpy})_3]^{2+}$ in a degassed solution during one hour leads to an unchanged spectrum (**Figure S8a**). Therefore the photostationary (PSS) state prepared by irradiating $[\text{Fe}(c\text{-msbpy})_3]^{2+}$ at 405 nm essentially consists in the trans isomer. This result has been exploited by exciting again this solution at 365 nm. The reverse trans \rightarrow cis conversion conducts to a new PSS with a fraction of $[\text{Fe}(c\text{-msbpy})_3]^{2+}$ (ca. 20 %) consistent with the above data.

In presence of dioxygen, the reactivity of both complexes induced with $\lambda_{\text{exc}} = 405$ nm (or 365 nm) are preserved (**Figure S8b**), similar PSS are reached and only weak deviations are observed after long irradiation times. The excitation of solutions of complexes with higher wavelengths (450-600 nm) has failed to show any change.

This set of results shows the quantitative cis \rightarrow trans photoswitching of stilbenoid ligands bound to Fe^{II} upon irradiation at 405 nm followed by the partial reversion at 365 nm. Relatively long wavelengths were required for triggering photoisomerization processes and no photodecomposition of complexes was detected upon Vis light.

III.3.4.3. Reactivity of $[\text{Fe}(\text{msbpy})_3](\text{NCSe})_2 \cdot n\text{H}_2\text{O}$ Complexes under High-energy Excitation

Alternative pathways were probed with a high-energy excitation at 254 nm. Upon irradiation the degassed solution of $[\text{Fe}(c\text{-msbpy})_3]^{2+}$ evolves to form after 20 min a mixture containing ca. 60 % of $[\text{Fe}(t\text{-msbpy})_3]^{2+}$. For longer delays, discrepancies (observed for instance at ca. 285 nm) and shift of isosbestic point (from 270 to 267 nm) are indicative of a side reaction (**Figure S9**). This was confirmed by similar observations made in presence of O_2 as the side reaction becomes more rapidly competitive.

Considering now the degassed solution of $[\text{Fe}(t\text{-msbpy})_3]^{2+}$ excited at 254 nm (**Figure 6**), we identify after 190 min of irradiation, new features both in Vis ($\epsilon_{\text{MLCT}} \sim 7.7 \times 10^{-4} \text{ M}^{-1}\text{cm}^{-1}$ at 544 nm) and in UV range (intense structured bands centered at 287 and 261 nm). This solution kept in darkness does not significantly change overnight (after 330 min of irradiation, **Figure S9b** and **S10b**). The plot of absorbance versus the irradiation time (in **Figure S10a**) shows a slow and continuous reaction that bypasses the trans \rightarrow cis isomerization (variation at 270 nm) and affects the whole spectrum. After 7 hours of irradiation, the solution was colored in pale yellow and accordingly, one can distinguish in the spectrum a weak MLCT band centered at 472 nm and a structured and high-energy shifted band that compares quite well

with the one of the photocyclized ligand (except a residual absorption near 292 nm). In addition to the complete disappearance of the starting complex (variation in the range associated to MLCT absorption) and the ligand ring-closure, these features may also suggest some decooordination of ligands combined to the appearance of bulky photocyclized ligands.

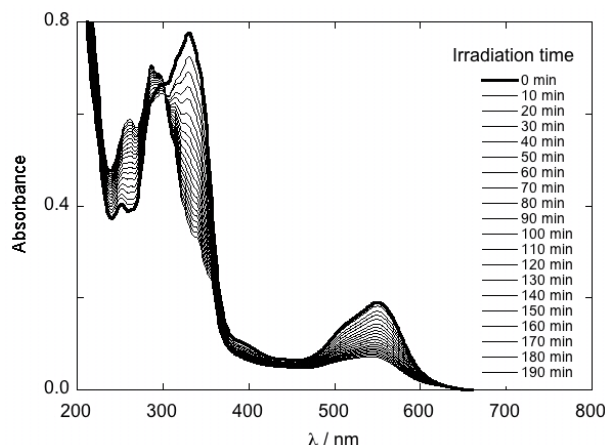


Figure 6: Evolution of absorption spectra vs. irradiation time of a degassed CH_3CN solution of $[\text{Fe}(\text{t-msbpy})_3]^{2+}$ irradiated at 254 nm.

III.3.5. Analysis of Results

The UV absorption properties of t-msbpy compare with those reported by Yam^[31] for a trans-styryl-bpy analogue except a red shift of the lowest $\pi-\pi^*$ transition from 309 (msbpy, CH_3CN) to 334 (styryl-bpy, CH_2Cl_2) nm suggesting a solvatochromic effect associated to the presence of transitions with charge transfer character, a feature established for the common styrylpyridine moiety.^[25]

Trans-cis isomerization and ring closure reactions of stilbenoid derivatives were extensively examined through photochemical,^[32] time resolved^[3] measurements and theory.^[2] It was well established that the geometrical isomerization of double bond of cis- and trans-isomers requires an optical excitation to the low-lying singlet or triplet excited state ($n-\pi^*$ and $\pi-\pi^*$),^[25] whereas photocyclization reactions of cis-isomers only occurs from the population of high-lying singlet excited states leading to colored condensed-ring intermediates (dihydrophenanthrene). Indeed, a slow ring opening converts the latter into the cis form but competitive processes favored by oxidant leads to dehydrogenation products (hydrophenanthrene and phenanthrene). The ratio of isomerization/cyclization quantum yield that depends on the structure (in particular structure of conformer, position of substituent) is relatively high for the 4-styrylpyridine, very low for its alpha methylated derivative or close to unity for 4-styrylphenanthrene. Concerning 4-styryl-2,2'-bipyridine (styryl-bpy), it was

mentioned in reference 31 that alternate irradiation at 365 and 254 nm of the latter leads to reversible spectral changes associated to the trans/cis isomerization of the CH=CH double bond. The present data show that the 365 nm excitation wavelength induces a significant (ca. 85 %) trans-to-cis conversion of msbpy, without significant side-reaction. However, upon a 254 nm excitation in presence of dioxygen the reactivity of both msbpy isomers mainly consists in products ascribed to phenanthrene type species and/or degradation products. Different photocyclized products may be formed from msbpy as a consequence of conformational equilibria between geometrical isomers.^[33] Therefore, we note that the partial cis-to-trans isomerization observed at the very beginning of the c-msbpy conversion, is hardly controlled due to the side-reactions promoted upon the 254 nm irradiation.

The optical absorption properties of $[\text{Fe}(\text{msbpy})_3]^{2+}$ complexes compare with those characterizing $[\text{Fe}(\text{R}_2\text{-bpy})_3]^{2+}$ derivatives ($[\text{Fe}(\text{Me}_2\text{-bpy})_3](\text{NCSe})_2$ in CH_3CN , $\lambda_{\text{max}} = 528$ nm). The energy of these MLCT bands (18903 (Me), 18416 (c-styryl) to 18149 (t-styryl) cm^{-1}) depends on the LUMO energy of bpy derivative. The observed tendency indicates an increasing stabilization of the corresponding π^* orbitals by replacing the H atom (in 4-position on 2,2'-bipyridine) by Me-, then by cis-styryl and finally by trans-styryl group. This is consistent with the effect of electronic delocalization that is enhanced by substituting bpy with a styryl group, and by increasing the structural planarity of latter (planar (trans-isomer) or twisted configuration (cis isomer) due to sterical hindrance). In addition, the rather high intensity observed for the MLCT absorption bands of $[\text{Fe}(\text{msbpy})_3](\text{NCSe})_2$ complexes confirms the LS ground state for both complexes in solution, also suggests the enhancement of absorption intensity due to some mixing between the MLCT states with other low energy excited states.

Concerning photoswitching properties of msbpy ligands in $[\text{Fe}(\text{msbpy})_3]^{2+}$ complexes, we have shown that a 365 or 405 nm irradiation of complexes triggers the cis-to-trans isomerization of msbpy ligands, i.e. the reverse of the process observed with $\text{ClRe}(\text{CO})_3(\text{R-styryl-bpy})$ in reference 31 or with free-base ligands in this work. The fraction of converted complexes is very high in both cases (ca. 85 % in PSS or almost complete, respectively) and the presence dioxygen does not significantly impact the process. The ligand-centered reaction is associated to a change of the MLCT absorption band, which exactly corresponds to the expectation (MLCT absorption of the isomer complex), a feature discarding any complex photodegradation. Contrarily to this case, the irradiation of complexes at high energies leads to irreversible competitive reactions that quickly prevail over the photoisomerization of Fe(c-

msbpy)₃(NCSe)₂ and are boosted in presence of dioxygen. In literature, azobenzene-attached pyridylbenzimidazole complexes of Fe^{II} ions were investigated by Nishihara et al.^[34] The cationic complex including three diimine ligands was back and forth isomerized in acetone upon 365 nm (trans-to-cis, π - π^* of the reactant) and 436 nm (cis-to-trans, n - π^* transition of the photoproduct) isomerization of the N=N bond. We note that for this system, whatever the radiation used and despite the presence of well separated absorption bands of reactant and product, the molar ratio of product/reactant is smaller than 33 % (0.33, for trans→cis and 0.13, for cis→trans conversions).

The mechanisms of isomerization of styryl-attached pyridine (or bipyridine) complexes have been investigated with Re^I or Ru^{II} ions.^[35,36] The literature indicates the existence of low-energy pathways for inducing the ligand-centered photoisomerization. Different experimental and theoretical analyses provide evidences for an intramolecular sensitization of the stilbenoid by the triplet ³MLCT* excited state of the Re^I or Ru^{II} metal leading to the trans-to-cis photoisomerization of the ligand, possibly coupled to the photoswitching of luminescence. Previous DFT calculations^[25] on the 4-styrylpyridine isomers have shown that the lowest triplet excited state of stpy isomers are located in the visible range (vertical T₁/S₀ energy differences being 21141 cm⁻¹ and 24279 cm⁻¹ for the trans and cis isomer, respectively). These energy differences should be lowered in the bpy derivatives as a consequence of the relative extension of π skeleton, as observed in the UV absorption properties of stpy and msbpy. Concerning the energies of MLCT type transitions, De Graaf and Souza have reported for the [Fe(bpy)₃]²⁺ analogue,^[37] a complete theoretical analysis of potential energy surfaces (PES) as a function of Fe-N distances and energies of the lowest excited states. From this work, it appears that a number of MLCT states are located in a small energy interval (above ca. 2.5 eV or 20163 cm⁻¹) and thus these states define a broad band. The two ¹MLCT and ³MLCT PES present equilibrium distances comparable with the one of the singlet ground state. For the [Fe(msbpy)₃](NCSe)₂ compounds, the spectroscopic data indicate that the lowest energy intraligand and MLCT excited states are relatively stabilized with respect to stpy and [Fe(bpy)₃]²⁺ excited states and thus a photoisomerization mechanism based on the triplet pathway might be plausible. This would require a photoisomerization via the ³(msbpy)* excited state that would be fast enough to compete with the ultra-fast relaxation of the ³MLCT excited state down to the metal centered HS and LS states (typical time scales are 150 fs (650 ps) for the HS (LS) state population).^[17,38] The observation of a preferential cis-to-trans isomerization of msbpy upon a 365 or 405 nm excitation of the Fe^{II} complex suggests

that this condition might be fulfilled for this isomer (for instance, as a consequence of barrierless process).

III.4. Conclusions

We have investigated the photoswitching properties of 4-styryl-2,2'-bipyridine as free-base molecule or Fe(II) chelator. We have shown that the msbpy ligand isomerizes upon irradiation at 365 nm yielding to a photostationary state with a prevailing trans isomer. The ligand coordinated to a low-spin cationic Fe^{II} complex may be also switched but here the 365 nm excitation wavelength essentially produces a photostationary state containing a large fraction of complex with c-msbpy isomer. By shifting the excitation wavelength up to 405 nm, the ligand-centered cis-to-trans isomerization becomes almost complete and produces in the visible range the corresponding variation of metal to ligand charge transfer (MLCT) transitions. This cis-to trans conversion may be partly reversed with a subsequent excitation at 365 nm. Higher-energy excitation (at 254 nm) especially favors side-reactions leading to photocyclized derivatives. This reactivity is typical of stilbenoids derivatives in a fluid media in which large motions of atoms accompany the electronic rearrangement due to the π - π^* excitation.

The switching properties of msbpy have been previously exploited for varying the ligand-field strength in a spin-crossover Fe^{II} complex and changing the spin state of the metal ion. This LD-LISC effect of Fe(msbpy)₂(NCS)₂ was observed in solution at room temperature. With respect to recent literature describing solid state isomerization of stilbenoids, we plan to process the photoactive cationic complexes in the form of nanoparticles of Fe^{II}(msbpy)₂(NCSe)₂, to study the spin-crossover behavior and the solid state photoactivity (ligand-centered isomerization and metal-centered photomagnetism).

Footnotes

Crystal data of t-msbpy. C₁₉ H₁₆ N₂, M = 272.34, orthorhombic, $a = 11.2057(17)$, $b = 7.2853(13)$, $c = 34.281(6)$ Å, $V = 2798.6(8)$ Å³, T = 100 K, space group Pbc_21 , Z = 8, Z' = 1, 35553 reflections measured, 4316 unique ($R_{\text{int}} = 0.0662$) which were used in all calculations. The final wR(F_o) was 0.1490 (all data).

References

- [1] H. Meyer *Angew. Chem. Int. Ed.* 1992, 31, 1399.
- [2] T. J. Martinez *Acc. Chem. Res.* 2006, 39, 119.
- [3] A. Sinicropi, E. Martin, M. Ryazantsev, J. Helbing, J. Briand, D. Sharma, J. Léonard, S. Haacke, A. Cannizzo, M. Chergui, V. Zanirato, S. Fusi, F. Santoro, R. Basosi, N. Ferré, M. Olivucci *Proc. Natl. Acad. Sci. USA* 2008, 105, 17642.
- [4] C.-C. Ko, V. W. W. Yam *J. Mater. Chem.* 2010, 20, 2063.
- [5] A. Bianchi, E. Delgado-Pinar, E. García-España, C. Giorgi, F. Pina, *Coord. Chem. Rev.* 2014, 260, 156.
- [6] S. Kume, H. Nishihara *Struct. Bond.* 2007, 123, 79.
- [7] S. Venkataramani, U. Jana, M. Dommaschk, F. D. Sönnichsen, F. Tuczek, R. Herges *Science* 2011, 331, 445.
- [8] M. Kayanuma, C. Daniel, H. Köppel, E. Gindensperger *Coord. Chem. Rev.* 2011, 255, 2693.
- [9] A. Vlcek, M. Busby *Coord. Chem. Rev.* 2006, 250, 1755.
- [10] Boillot, M.-L.; Zarembowitch, J.; Sour, A. in *Top. Curr. Chem.*; Gütllich, P.; Goodwin, H. A. Eds.; Springer: Berlin, 2004; Vol. 234, p 261.
- [11] Boillot, M.-L.; Pillet, S.; Tissot, A.; Rivière, E.; Claiser, N.; Lecomte, C. *Inorg. Chem.* **2009**, 48, 4729-4736.
- [12] K. Sénéchal-David, N. Zaman, M. Walko, E. Halza, E. Rivière, R. Guillot, B. L. Feringa, M.-L. Boillot *Dalton Trans.*, 2008, 1932.
- [13] A. Tissot, M.-L. Boillot, S. Pillet, E. Coddjovi, K. Boukheddaden, and L. M. Lawson Daku *J. Chem. Soc. C* 2010, 114, 21715.
- [14] Y. Hasegawa, K. Takahashi, S. Kume, H. Nishihara *Chem. Commun.* 2011, 47, 6846 ; Y. Hasegawa, R. Sakamoto, K. Takahashi, H. Nishihara *Inorg. Chem.* 2013, 52, 1658.
- [15] K. Sénéchal-David, N. Zaman, M. Walko, E. Halza, E. Rivière, R. Guillot, B.L. Feringa, M.-L. Boillot *Dalton Trans.* 2008, 1932 ; Y. Garcia, V. Ksenofontov, R. Lapouyade, A.D. Naik, F. Robert, P. Gütllich *Opt. Mater.* 2011, 33, 942 ; M. Nihei, Y. Suzuki, N. Kimura, Y. Kera, H. Oshio *Chem. Eur. J.* 2013, 19, 22, 6946 ; M. Milek, F. W. Heinemann, M. M. Khusniyarov *Inorg. Chem.* 2013, 52, 11585.
- [16] A. Hauser, *Top. Curr. Chem.*, 2004, **234**, 155.
- [17] A. Cannizzo, C. J. Milne, C. Consani, W. Gawelda, Ch. Bressler, F. van Mourik, M. Chergui, *Coord. Chem. Rev.* 254 (2010) 2677.
- [18] R. Bertoni, M. Lorenc, A. Tissot, M.-L. Boillot, E. Collet *Coord. Chem. Rev.*, accepted paper
- [19] A. Tissot, J.-F. Bardeau, E. Rivière, F. Brisset, M.-L. Boillot *Dalton Trans.* 2010, 39, 7806 ; P. Chakraborty, M.-L. Boillot, A. Tissot, A. Hauser *Angew. Chem. Int. Ed.* 2013, 52, 7139 ; A. Tissot, L. Rechignat, A. Bousseksou, M.-L. Boillot *J. Mater. Chem.* 2012, 22, 3411.

- [20] M.-L. Boillot, S. Chantraine, J. Zarembowitch, J.-Y. Lallemand, J. Prunet *New J. Chem.* 1999, 179.
- [21] C. Busche, P. Comba, A. Mayboroda and H. Wadepohl, *European Journal of Inorganic Chemistry* **2010**, 1295-1302.
- [22] J. L. R. Williams, R. E. Adel, J. M. Carlson, G. A. Reynolds, D. G. Borden and J. A. Ford, Jr, *The Journal of Organic Chemistry* **1963**, 28, 387-390.
- [23] E. Cariati, D. Roberto, R. Ugo, V. I. Srdanov, S. Galli, P. Macchi, A. Sironi *New J. Chem.* 2002, 26, 13.
- [24] M.-L. Boillot, S. Pillet, A. Tissot, E. Rivière, N. Claiser, C. Lecomte *Inorg. Chem.*, 2009, 48, 4729.
- [25] M. L. Lawson Daku, J. Linarès, M.-L. Boillot, *Chem. Phys. Chem.* **2007**, 8, 1127 ; M. L. Lawson Daku, J. Linarès, M.-L. Boillot *Phys. Chem. Chem. Phys.*, **2010**, 12, 6107.
- [26] a) P. Bortolus, G. Cauzzo, U. Mazzucato and G. Galiazzo, *Zeitschrift für Physikalische Chemie* **1969**, 63, 29-38; b) A. Schulz and H. Meier, *Tetrahedron* **2007**, 63, 11429-11435.
- [27] L. L. Nguyen, R. Guillot, J. Laisney, L. Rechinat, S. Bedoui, G. Molnar, E. Rivière and M.-L. Boillot, submitted to *New J. Chem.*
- [28] E. J. MacLean, C. M. McGrath, C. J. O'Connor, C. Sangregorio, J. M. W. Seddon, E. Sinn, F. E. Sowrey, S. J. Teat, A. E. Terry, G. B. M. Vaughan, N. A. Young, *Chem. Eur. J.*, 2003, 921, 5314-5322.
- [29] E. König *Coord. Chem.* 1968, 3, 471-495.
- [30] P. S. Braterman, J. I. Song, R. D. Peacock *Inorg. Chem.* 1992, 31, 555.
- [31] V. W.-W. Yam, Y. Yang, J. Zhang, B. Wai-Kin Chu, N. Zhu *Organometallics* 2001, 20, 4911.
- [32] G. Bartocci, F. Masetti, U. Mazzucato, A. Spalletti, I. Baraldi, F. Momicchioli *J. Phys. Chem.*, 91, 4733 ; U. Mazzucato *Gaz. Chim. It.* 1987, 117, 661.
- [33] U. Mazzucato, A. Spalletti *J. Phys. Chem. A*, 2009, 113, 14521.
- [34] Y. Hasegawa, S. Kume, H. Nishihara *Dalton Trans.* 2009, 280.
- [35] (a) P. Zarnegar, C. R. Bock and D. G. Whitten, *J. Am. Chem. Soc.*, 1973, 95, 4367; (b) J. R. Shaw, R. T. Webb and R. H. Schmehl, *J. Am. Chem. Soc.*, 1990, 112, 1117.
- [36] M. Busby, P. Matousek, M. Towrie, A. Vleck, Jr *J. Phys. Chem. A*, 2005, 109, 3000 ; J. Bossert, C. Daniel *Chem. Eur. J.* 2006, 12, 4835.
- [37] C. De Graaf, C. Sousa *Int. J. Quant. Chem.* 2011, 111, 3385.
- [38] J. Tribollet, G. Galle, G. Jonusauskas, D. Deldicque, M. Tondusson, J.F. Létard, E. Freysz *Chem. Phys. Lett.* 2011, 513, 42.

Chapter IV

Chapter IV

Nanoparticles of Spin-crossover $\text{Fe}^{\text{II}}(\text{R-bipyridine})_2(\text{NCSe})_2$ Complexes: Elaboration, Spin-crossover and Switching Properties versus styryl-attached bipyridine chromophores.

IV.1. Introduction

The functional molecular compounds whose physical or chemical state may be controlled with light have attracted a continuous scientific interest over the last 30 years. The photoinduced transformations of molecular switches were usually investigated in solution or in highly diluted composites, more scarcely in crystalline materials.^[1, 2, 3] Nevertheless, the exploitation of such photoactivable materials requires their integration in functional devices, and their adaptation for optimizing the properties, in particular the photoconversion related to the depth of light penetration.

The nanoscale downsizing of functionalized materials represents an important issue for technological applications and also, for controlling the switching properties as a function of size reduction and environment.^[4] Along this line, substantial research efforts have been done recently. Different classes of switchable materials (spin-crossover,^[5] photochromic^[6] compounds) have been prepared as nanoparticles by top-down^[7] or bottom up^[8, 9] approaches. The group has focused on the nanoscale processing of molecular materials and the integration of particles in stabilized, well-adapted, easy to handle materials.

The objective of the present work is to investigate the spin-crossover (SCO) and LD-LISC properties with functionalized Fe^{II} complexes in the form of a dispersion of nanoparticles in transparent thin films. For this investigation, we have selected a set of mononuclear complexes incorporating a bipyridine ligand substituted either with a methyl group (electronic and structural function) or a styryl group (photoactivable function). Introducing in the coordination sphere three (strong ligand-field case) or two (intermediate ligand-field strength) bipyridine ligands, (possibly associated with NCSe^- co-ligands) allows modulating the ligand-field strength experienced by the metal ion. In a first part of this work, we have investigated the preparation of nanoparticles of the spin crossover $\text{Fe}(\text{Me}_2\text{-bpy})_2(\text{NCSe})_2$ compound (**chapter 2**) and the photochemical properties of $[\text{Fe}(\text{msbpy})_3](\text{NCSe})_2 \cdot n \text{H}_2\text{O}$ (msbpy = 4-methyl, 4'-*trans*- or *cis*-styryl-2,2'-bipyridine) (**chapter 3**) in solution. We have shown that

the thermal spin crossover of 60 nm particles of $\text{Fe}(\text{Me}_2\text{-bpy})_2(\text{NCSe})_2$ takes place above 250 K and is half completed at ca. 340 K. In acetonitrile, the msbpy ligand isomerizes upon irradiation at 365 nm yielding to a photostationary state (PSS) formed with 85 % c-msbpy. When coordinated to a low-spin cationic Fe^{II} complex, the c-msbpy isomer is quantitatively converted in t-msbpy (PSS, 80 % of complex with t-msbpy) upon a 365 nm irradiation. By shifting the excitation wavelength up to 405 nm, the ligand-centered cis-to-trans isomerization becomes complete and produces the corresponding variation of metal-to-ligand charge transfer (MLCT) transitions in the visible range. This conversion may be partly reversed as the 365 nm excitation leads to the formation of ca. 20 % of complex with cis-isomer. After relatively short (or extended) time of irradiation at 254 nm (or 365 nm) in presence of dioxygen, side-reactions lead to photocyclized derivatives. This reactivity is typical of stilbenoids derivatives in a fluid media in which large motions of atoms accompany the electronic rearrangement due to the π - π^* excitation.

So, we describe here the preparation and study of nanoparticles of a spin-crossover $\text{Fe}^{\text{II}}(\text{msbpy})_2(\text{NCSe})_2$ compound incorporating the photoisomerizable msbpy ligand. The properties were investigated either with particles in the form of powder or processed in PMMA thin films. Finally, we have achieved first photomagnetic experiments in order to probe the ability of this system to exhibit a spin change of metal ion driven by the ligand photoswitching (LD-LISC effect) in nano-materials.

IV.2. Experimental Section

IV.2.1. Nanoparticles Syntheses :

The syntheses and characterizations of trans- or cis-isomers of msbpy and the corresponding $[\text{Fe}(\text{msbpy})_3](\text{NCSe})_2 \cdot n(\text{H}_2\text{O})$ ($n = 3$ or 2) complexes were described in **Chapter 3**. The preparation of 70 nm nanoparticles of $\text{Fe}(\text{Me}_2\text{-bpy})_2(\text{NCSe})_2$ was given in **Chapter 2**. EDS data and IR spectra were shown in **Table ST1-ST4** (Appendix of chapter 4).

60 nm nanoparticles of $\text{Fe}(\text{t-msbpy})_2(\text{NCSe})_2$

The red solution, prepared by dissolving 10 mg of $[\text{Fe}(\text{t-msbpy})_3](\text{NCSe})_2 \cdot 3(\text{H}_2\text{O})$ in 2 mL of ethanol, was quickly added to 20 mL volume of toluene, previously heated at 80 °C. The mixture maintained at this temperature was vigorously stirred for 15 min. A volume of 5 mL of cold pentane was added and the mixture was centrifugated for 10 min at 10000 rpm. The violet solid, rinsed with 30 mL of cold pentane, was separated by centrifugation (one or two

times). Elemental analysis: formula $C_{40}H_{32}FeN_6Se_2$ (MM = 812.5 $g\text{mol}^{-1}$) Calcd (%): C 59.28, H 3.98, N 10.37; Found (%): C 58.02, H 4.26, N 9.33; EDS analysis Fe/Se = 0.46-0.53. IR(KBr): $\nu = 2061\text{ cm}^{-1}$ and 2103 cm^{-1} (NC_{NCS_e}); ca. 967 cm^{-1} (CH out of plane deformation of trans $CH=CH$); 626 cm^{-1} (CSe stretching).

65 nm nanoparticles of c-msbpy Fe^{II} compound

For this preparation, the method described for the trans-isomer of $[Fe(msbpy)_3](NCSe)_2$, was adapted with a 0.5 mL volume of MeOH and a stirring of the reaction mixture (MeOH / toluene) during 30 min (instead of 2 mL of ethanol and 15 min of stirring time, respectively). The violet solid was isolated by centrifugation, then washed with pentane and dried.

EDS analysis Fe/Se = 0.46. IR(KBr): $\nu = 2053\text{ cm}^{-1}$ (NC_{NCS_e}) and 2189 cm^{-1} , 1609 cm^{-1} (NC_{py}), ca. 693 cm^{-1} (CH out of plane deformation of cis $CH=CH$). Powder X-ray diffractogram : amorphous powder.

Elemental analysis: Large discrepancies were observed between the values expected for $Fe(msbpy)_2(NCSe)_2$ (formulae, $C_{40}H_{32}FeN_6Se_2$) and the measurements (see the table). No formulation based on the precursor ($C_{59}H_{48}FeN_6Se_2$) in a solvated form appears suitable. Therefore the data were compared with those calculated for $Fe(msbpy)_2(NCSe)_2 \cdot H_2O$ ($C_{40}H_{42}FeN_6O_5Se_2$) or $Fe(msbpy)(NCSe)_2$ ($C_{28}H_{24}FeN_4Se_2$) formulations.

Table 1: Experimental and calculated percentages of C, H, N elements calculated for a few formulations.

Formulae		Elemental analysis	Molar mass ($g\text{mol}^{-1}$)
Measurement	Found (%)	C 53.03, H 3.68, N 9.39	-
$C_{40}H_{32}FeN_6Se_2$	Calcd (%)	C 59.28, H 3.98, N 10.37	812.04
$C_{40}H_{42}FeN_6O_5Se_2$	Calcd (%)	C 53.35, H 4.70, N 9.33	900.56
$C_{28}H_{24}FeN_4Se_2$	Calcd (%)	C 53.36, H 3.84, N 8.89	631.97

From these data, no conclusive information can be drawn and two hypotheses may be tentatively considered, the formation of a salt $[Fe(msbpy)_3]_2[Fe(NCSe)_4](NCSe)_2 \cdot 3(H_2O)$ or of a $[Fe(msbpy)(NCSe)_2]$ n-coordinated specie (with $n = 4$ or higher, see below).

70 nm nanoparticles of $\text{Fe}(\text{Me}_2\text{-bpy})_2(\text{NCSe})_2$ @ PMMA

The $[\text{Fe}(\text{Me}_2\text{-bpy})_3](\text{NCSe})_2 \cdot 3(\text{H}_2\text{O})$ compound (10 mg) solubilized in ethanol (here, 5 mL) was added in hot toluene (20 mL, 65 °C), in which PMMA35000 was previously dispersed (200 mg). After 15 min of stirring at 65 °C, a volume of 200 mL of pentane was added and the mixture was centrifugated. The so-isolated solid was rinsed with 100 mL of pentane and centrifugated. This last step was repeated again before drying the powder of composite under vacuum. EDS analysis confirms the presence of Fe and Se atoms but fails to give an estimate of the Fe/Se ratio as a consequence of the high dilution within the composite, Powder X-ray diffraction : Bragg peaks centered at $2\theta = 8.5, 9.1, 12.2, 17.0, 17.8, 18.7, 21.1, 21.8, 29.3$ corresponding to the neutral specie.

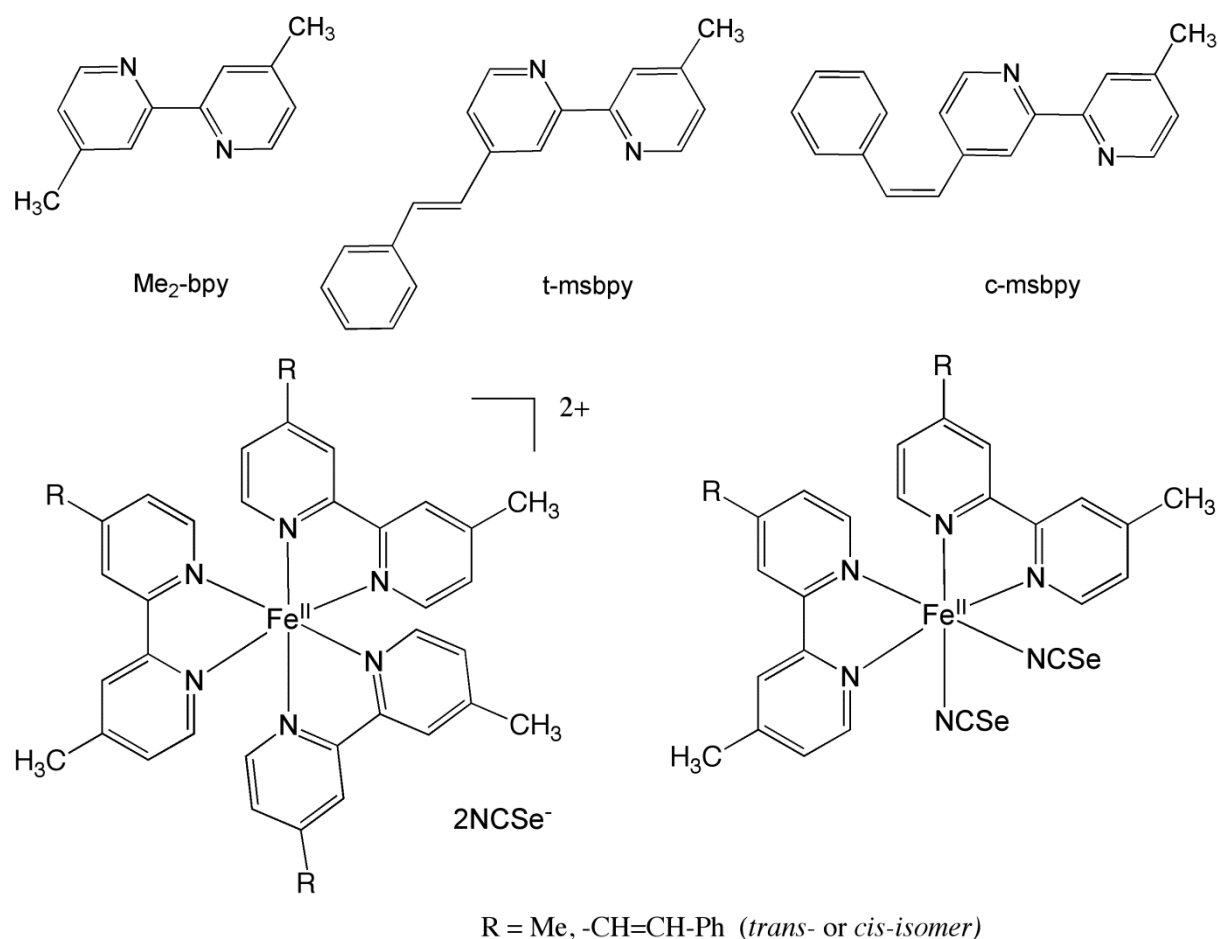
IV.2.2. PMMA Thin Films of $\text{Fe}(\text{t-msbpy})_2(\text{NCSe})_2$

The nanoparticles of $\text{Fe}(\text{t-msbpy})_2(\text{NCSe})_2$ (5 mg) were added to a solution of toluene (500 μL), in which 100 mg of PMMA 35000 were previously dissolved. The mixture was stirred and sonicated for obtaining a relatively viscous and homogenous solution. 100 μL of the latter were spin-coated on a quartz substrate (600 rpm) and the thin films (colored in violet) were dried overnight at room temperature. Films containing the free-base ligands were prepared by using the same conditions.

After the preparation, the PMMA thin films were stabilized by a thermal treatment under vacuum at 40 °C for 8 h and then, kept under vacuum.

PMMA thin films of $\text{Fe}(\text{Me}_2\text{-bpy})_2(\text{NCSe})_2$.

The dispersion of in-PMMA $\text{Fe}(\text{Me}_2\text{-bpy})_2(\text{NCSe})_2$ nanoparticles (5 mg of composite) suspended in 500 μL of toluene was stirred during 5 h for obtaining a violet homogeneous solution, which was spin-coated on a suitable (glass or quartz) substate and treated as previously described.



Scheme 1. Schematic drawing of the bidentate Me-R-bpy ligands (R = Me, -CH=CH-Ph) and the corresponding ionic and neutral Fe^{II} complexes.

IV.3. Physical Measurements

TEM images have been acquired with a JEOL 1400 (120 kV) TEM equipped with two high-resolution and high-speed digital CCD Gatan cameras.

FTIR spectra were collected on KBr pellets at room temperature with a Perkin-Elmer spectrometer (Spectrum 100).

The TGA analysis was done under ambient atmosphere with a TGA analyser (TA instruments-water LLC, SDT Q600) in the 293 - 473 K temperature range at a rate of 2°C per min.

X-ray diffraction patterns were recorded at room temperature on powders deposited on aluminium plate, using a Philipps Panalytical X'Pert Pro MPD powder diffractometer at CuK α radiation equipped with a fast detector within the 6 - 35° in 2 θ range.

UV-vis spectra were measured in the range 200-2000 nm on a CARY 5000 double-beam spectrophotometer equipped with the Eurolabo variable-temperature cell (21525, KBr windows) and Specac temperature controller (20120). The samples were in the form of PMMA thin films in which the nanoparticles (or ionic complexes) were dispersed.

The thin films samples were irradiated with various sources either at air or in cryostat with different light sources: 254, 365 nm or 366 nm (HeroLab (NU-6) lamp for chromatography, power: 6.0, 5.4 or 5.4 mW respectively); 365, 500, 700 or 800 nm (Newport Hg lamp equipped with appropriate filters); 405, 532 or 635 nm (Laser/diode from Optoelectronic Tech.co.ltd, models LD-WL 206, LD-WL 206, PSU-III-LED).

Magnetic measurements were carried out using a Quantum Design SQUID magnetometer (MPMS5S Model) calibrated against a standard palladium sample. The magnetic susceptibility values were corrected from the diamagnetism of the molecular constituents and of the sample holder. For photoexcitation experiments, the magnetometer was equipped with an optical fiber (UV grade fused silica) connected to a Nd:YAG pulsed laser Surelite- OPO Plus. In-situ excitations were performed on a small quantity of powder deposited on a scotch tape with $\lambda = 405$ nm (Laser, model LD-WL 206, Optoelectronic Tech.co.ltd, 25 mW, 32 mW/cm²) or $\lambda = 365$ nm (Prizmatrix, black -LED, S/N: 8366, 5 mW, 6.36 mW/cm²).

Raman Measurements

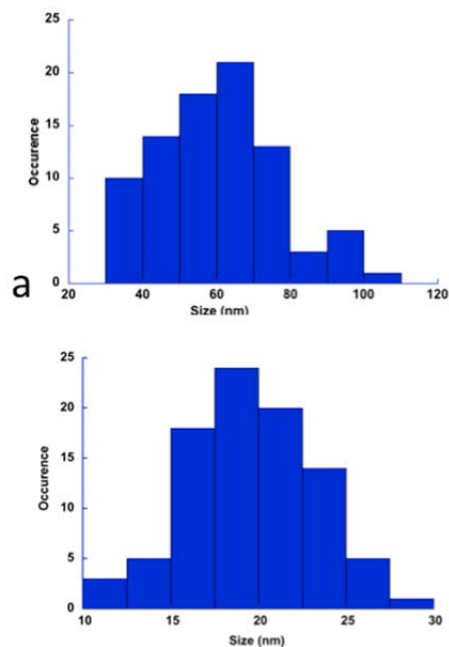
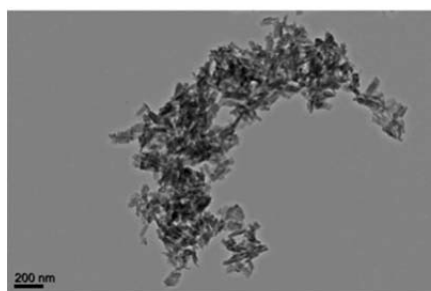
Variable temperature Raman spectra were recorded using a Labram-HR Evolution (Horiba Jobin-Yvon) microspectrometer at RT. The 632.8 nm line of a He-Ne laser (10 mW on the sample) was used as the excitation source and a spectral resolution of ca. 2 cm⁻¹ was obtained. A filter (D2, 100 times reduction) on the excitation beam minimizes the laser heating effect on the sample. Owing to the micro-/nano-crystalline nature of the samples laser polarization effects were not investigated in more detail.

IV.3. Results and Discussion

IV.3.1. Elaboration of Nanoparticles

The synthesis of nanoparticles was carried out according to the approach reported for Fe^{II}(Me₂-bpy)₂(NCSe)₂, which consisted to extract from the cationic precursor [Fe(L)₃](NCSe)₂.n(H₂O) (L = msbpy or Me₂-bpy), one bidentate ligand per metal ion and to precipitate the neutral species resulting from the coordination of NCSe⁻ anions. The reaction

was carried out in a mixture of ethanol and toluene for $L = t\text{-msbpy}$, $\text{Me}_2\text{-bpy}$. The relative stability of the 4×10^{-3} M ethanolic solution of $[\text{Fe}(t\text{-msbpy})_3](\text{NCSe})_2 \cdot n(\text{H}_2\text{O})$ (no particle observed by DLS measurement) has allowed the preparation of very small objects which was controlled by the extraction of ligand in hot toluene and the precipitation of neutral complex. The fact that the particles growth may be limited without addition of polymer indicates that the previous processes take place slowly. The application of this method to the $[\text{Fe}(c\text{-msbpy})_3](\text{NCSe})_2 \cdot n(\text{H}_2\text{O})$ precursor leads to a mixture of aggregates with a broad sizes distribution of particles and pale yellow oil (residues of $c\text{-msbpy}$). Therefore, ethanol was replaced by methanol in the synthesis in order to favor the extraction and elimination of $c\text{-msbpy}$, a relatively polar molecule.



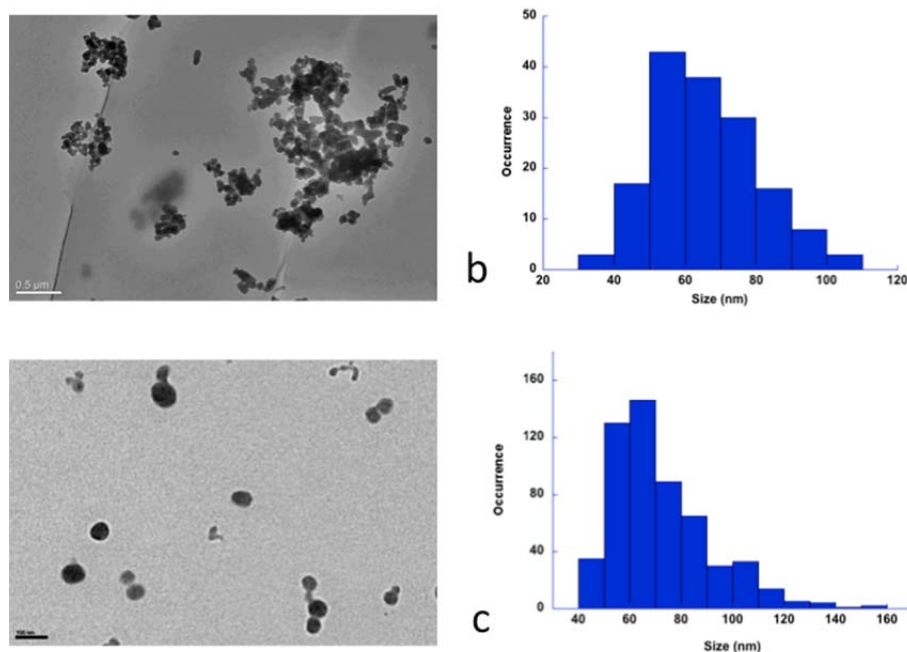
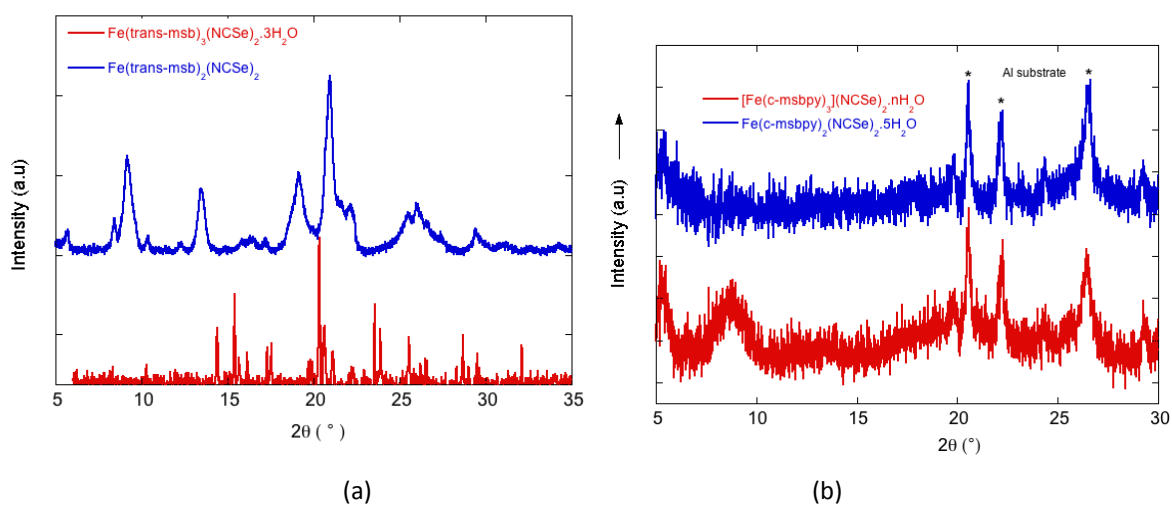
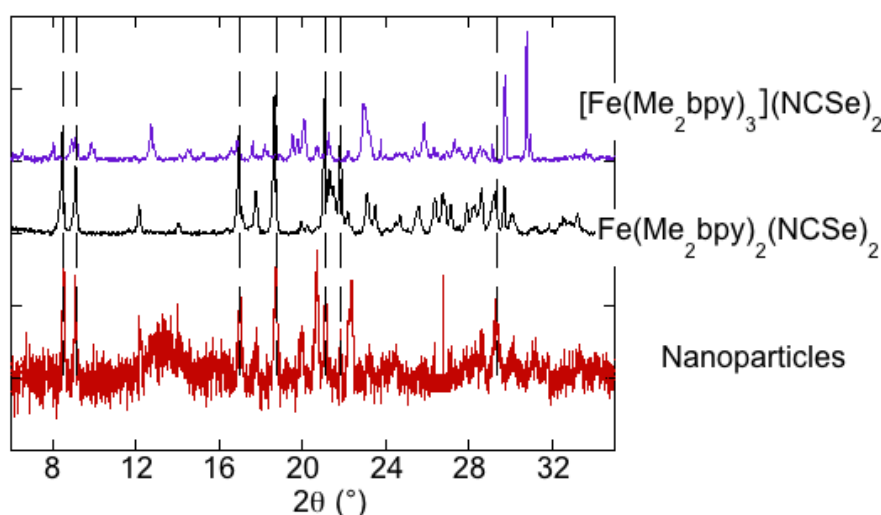


Figure 1 : TEM image and size distribution of (a) $(60 \pm 16) \times (19 \pm 4)$ nm particles of $\text{Fe}(\text{t-msbpy})_2(\text{NCSe})_2$, (b) 65 ± 15 nm particles of $\text{c-msbpy Fe}^{\text{II}}$ compound, (c) 70 ± 20 nm nanoparticles of $\text{Fe}(\text{Me}_2\text{-bpy})_2(\text{NCSe})_2$

The TEM images (**Figure 1**) show the formation of particles with comparable size and size distributions: 60 ± 16 nm platelets (Fe^{II} complexes including t-msbpy), unshaped 65 ± 15 nm objects (Fe^{II} complexes including c-msbpy, **Figure S1**), and spherical 70 ± 20 nm particles of $\text{Fe}^{\text{II}}(\text{Me}_2\text{-bpy})_2(\text{NCSe})_2$.





(c)

Figure 2 : Powder X-ray diffractograms of $\text{Fe}(\text{msbpy})_x(\text{NCSe})_2$ in the form of nanoparticles ($x = 2$, sizes = 60-65 nm) or polycrystalline sample ($x = 3$): msbpy = trans isomer **(a)**, cis isomer **(b)**. These data were collected overnight in similar conditions. In **(c)** are compared the 70 nm nanoparticles with the bulk samples of $\text{Fe}(\text{Me}_2\text{bpy})_x(\text{NCSe})_2$ ($x = 2$ and 3).

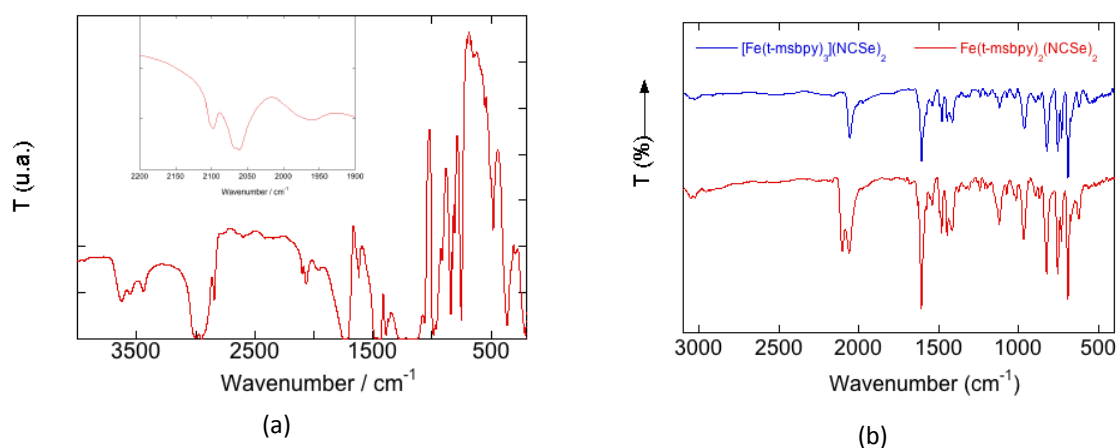
Powder X-ray diffraction measurements: The X-ray diffractograms of powders of nanoparticles recorded at room temperature (shown in **Figure 2**) characterize two $\text{Fe}(\text{R-bpy})_2(\text{NCSe})_2$ samples ($\text{R-bpy} = \text{t-msbpy}, \text{Me}_2\text{-bpy}$) with some crystalline character and an amorphous one ($\text{R} = \text{c-msbpy}$). The comparison of the formers with those of the ionic precursors indicates the disappearance of peaks of the latters, a feature suggesting their complete conversions upon the nanoparticles precipitation or their presence in an amorphous form. The crystallinity of $\text{Fe}(\text{t-msbpy})_x(\text{NCSe})_2$ samples ($x = 2, 3$) is very limited (weak intensities / broadening of peaks). This point may be accounted for by the presence of structural defects, conformational disorders or trapping of closely related isomers (diastereoisomers). The size of coherent domains (long distance ordering in solid) may be determined with the Debye-Scherrer equation. In the case of $\text{Fe}(\text{Me}_2\text{-bpy})_2(\text{NCSe})_2$ particles the fact that the size of coherent domains (ca. 50 nm) is close to the average size of particles indicates the formation of nanocrystals. As a consequence of the platelet shape of $\text{Fe}(\text{t-msbpy})_2(\text{NCSe})_2$ particles, this calculation only provides a rough estimate that is ca. 17-22 nm, a value corresponding to the width of platelets.^[10]

The attempts done for the preparation of neutral species in the form of polycrystalline or single-crystal samples have afforded the ionic ones, a feature that may result from their

chemical instability in presence of water. Therefore, IR and Raman measurements were carried out for identifying the functional groups in the Fe^{II} coordination spheres.

Infra-red measurements: In the IR spectrum of $\text{Fe}(\text{Me}_2\text{-bpy})_2(\text{NCSe})_2$ (**Figure 3a**), we identify the NC_{NCSe} peaks that characterize the neutral spin-crossover complex (**Chapter 2, Figures 6 and 8**) despite the strong absorptions of PMMA.

The comparison between the vibrational spectra of $\text{Fe}(\text{t-msbpy})_2(\text{NCSe})_2$ nanoparticles and the ionic precursor (**Figure 3b**) shows several changes in frequencies and intensities (See **Table ST4** in appendix of **chapter 4**). The msbpy ligand is found in the trans configuration in both compounds (CH out of plane deformations of trans $\text{CH}=\text{CH}$ at 963 cm^{-1} , ionic precursor; 967 cm^{-1} , neutral complex; 966 and 958 cm^{-1} , free-base ligand) and coordinated to the metal ion (NC_{py} at 1607 cm^{-1} , ionic precursor; 1608 cm^{-1} neutral complex; 1585 cm^{-1} , free-base ligand). The relative intensity of NC_{NCSe} (2103 and 2061 cm^{-1}) and NC_{py} (ca. 1607 cm^{-1}) vibrational peaks seems consistent with a change of the ratio of NCSe and msbpy components in the ionic precursor (2/3) and the neutral (2/2) complex. As previously pointed for the $\text{Me}_2\text{-bpy}$ Fe^{II} complexes, the markers in the $2200\text{-}2000\text{ cm}^{-1}$ range evolve from a unique NC_{NCSe} peak ($\nu = 2057\text{ cm}^{-1}$) to a double peak (2103 and 2061 cm^{-1}). The former characterizes the counter-ion in the precursor while the latter may correspond to the cis positioned and N-coordinated NCSe ligands.^[11, 12]



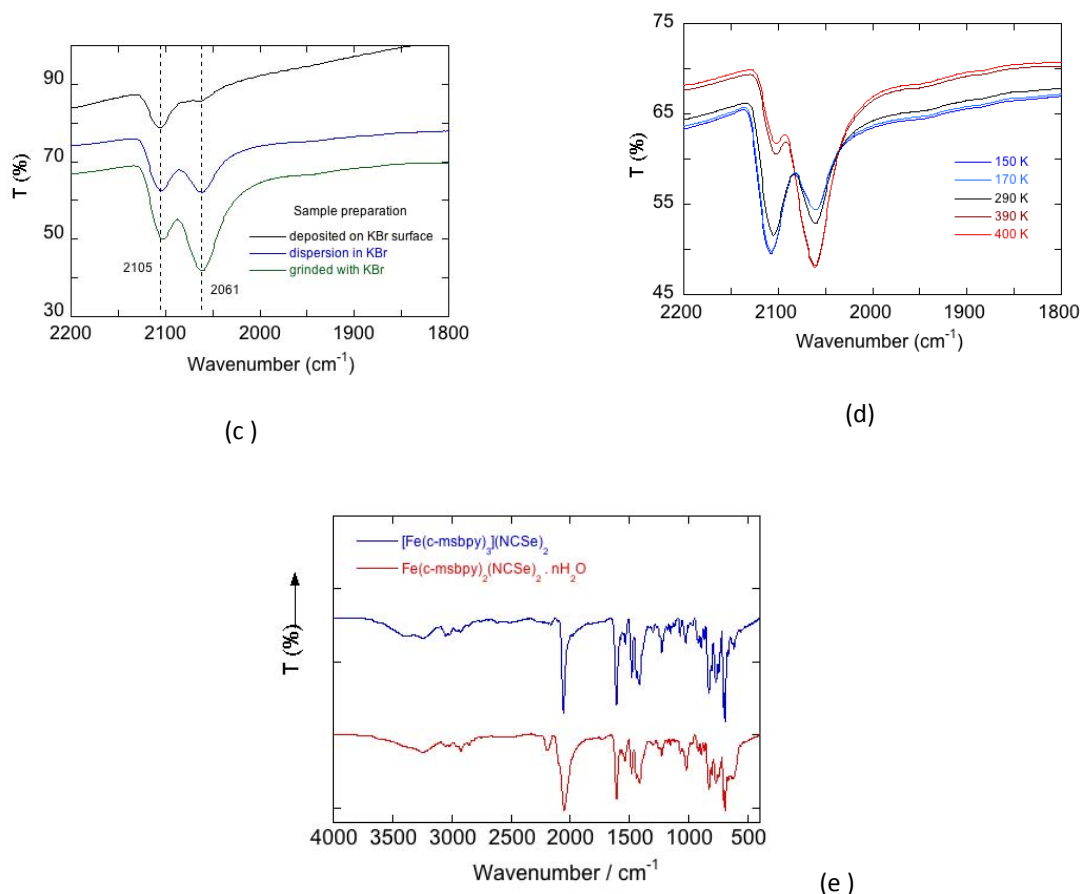


Figure 3 : IR spectra for the Fe^{II} compounds in the form of nanoparticles. **(a)** $\text{Me}_2\text{-bpy}$ Fe^{II} compound dispersed in PMMA; **(b)** t-msbpy Fe^{II} compounds; **(c)** expansion of the $\text{Fe}(\text{t-msbpy})_2(\text{NCSe})_2$ spectrum in the 2200-1800 cm^{-1} range showing the importance of the sample preparation (particles deposited on the KBr pellet, particles dispersed in the KBr pellet, with or without preliminar grinding of the mixture); **(d)** variable temperature data collected for $\text{Fe}(\text{t-msbpy})_2(\text{NCSe})_2$ nanoparticles simply dispersed in KBr; **(e)** c-msbpy Fe^{II} compounds. For comparison the spectra of ionic precursors are also plotted in **(b)** and **(e)**.

With respect to intensities of NC_{NCSe} peaks, suggesting equivalent fractions of LS (2103 cm^{-1}) and HS (2061 cm^{-1}) species, this assignment may be questioned as the magnetic data (see below) only show a few percent of HS species at room temperature. As shown in **Figure 3c**, this apparent discrepancy results from a pronounced effect due to the sample preparation. In absence of any strain (grinding or encapsulation in KBr, applied pressure for IR-ATR measurement), the relative intensity of NC_{NCSe} peaks indicates a prevailing LS component. This assignment was confirmed with temperature variable IR measurements that were carried out with nanoparticles simply encapsulated in a KBr pellet (signal / noise ratio better than the one of nanoparticles just deposited on the surface) (**Figure 3d**). Finally, these IR data

provide strong evidences for the precipitation of a spin-crossover product formulated as $\text{Fe}(\text{t-msbpy})_2(\text{NCSe})_2$.

Concerning the c-msbpy Fe^{II} compound (**Figure 3e**), this conclusion can not be drawn. The spectrum of nanoparticles present a small peak at 2192 cm^{-1} (a frequency higher than tabulated ones for Se-bonded systems) and a broad peak at 2052 cm^{-1} (NC_{NCSe} stretching) whose intensity with respect to the peak at 1609 cm^{-1} (assigned to NC_{py}) again is consistent with a relative decrease of the number of bipyridine in this sample. The relatively intense peaks, centered at 670 , 620 cm^{-1} or at 1017 cm^{-1} , are other distinctive features. From these observations, combined to the uncertain chemical composition, we can suggest two hypotheses. For this class of compound, it is well established that in presence of water the formation of paramagnetic salt (as shown below for this sample) is especially favored. It was demonstrated for instance for the prototypical system $[\text{Fe}(\text{phen})_3]_2[\text{Fe}(\text{NCS})_4](\text{NCS})_2 \cdot 3(\text{H}_2\text{O})$,^[13] which can be also written as $\text{Fe}(\text{phen})_2(\text{NCS})_2 \cdot (\text{H}_2\text{O})$. Reiff and al have studied the HS tris 2,2'-biquinoline Fe^{II} salt incorporating bulky bidentate ligands and reported the formation of a presumably tetrahedral $\text{Fe}^{\text{II}}(\text{biq})(\text{NCS})_2$ compound.^[14] However, the fact that the $[\text{Fe}(\text{c-msbpy})_3](\text{NCSe})_2$ precursor was stable in solution in the conditions used for photochemical measurements (in **Chapter 3**) and was fully diamagnetic at solid state does not support a chemical instability due to sterical reasons as pointed by Reiff for $\text{Fe}^{\text{II}}(\text{biq})_3(\text{NCS})_2$.

Magnetic measurements. They were carried out with the powdered samples between 100 and 370 K, a temperature just below the glass transition of PMMA (dispersing medium, T_g ca. 380 K) in order to reduce the matrix effect on the sample.^[15]

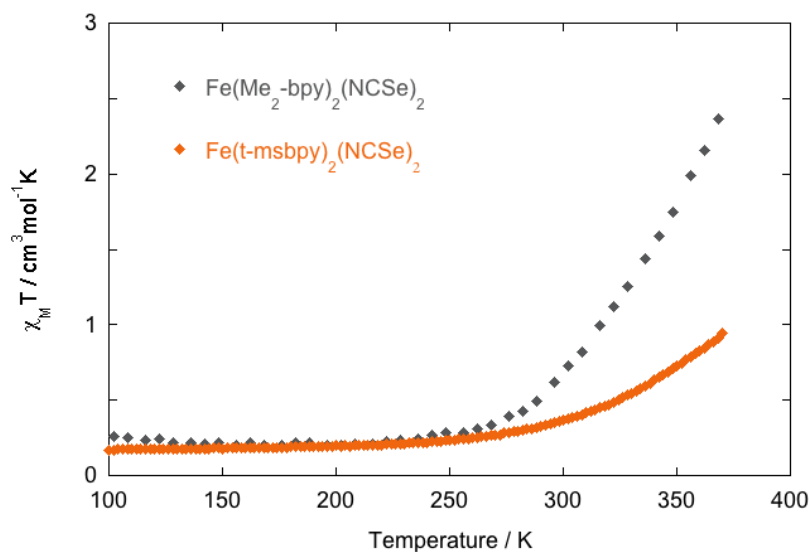


Figure 4 : Temperature dependence of $\chi_M T$ of $\text{Fe}(\text{t-msbpy})_2(\text{NCSe})_2$ (60 nm nanoparticles, \blacklozenge) and $\text{Fe}(\text{Me}_2\text{-bpy})_2(\text{NCSe})_2$ (dispersion of 70 nm particles in PMMA, \blacklozenge).

The $\chi_M T$ variation as a function of temperature (χ_M being the molar magnetic susceptibility) is similar for both $\text{Fe}(\text{L})_2(\text{NCSe})_2$ compounds (**Figure 4**). The spin-crossover process, that takes place above 250 K, is especially smooth for the nanoparticles of $\text{Fe}(\text{t-msbpy})_2(\text{NCSe})_2$ and uncompleted at 370 K ($\chi_M T = 0.953 \text{ cm}^3 \text{ mol}^{-1} \text{ K}$), while at this temperature, the process observed with $\text{Fe}(\text{Me}_2\text{-bpy})_2(\text{NCSe})_2$ is almost achieved with a HS fraction ~ 0.70 (estimated with $\chi_M T^{\text{HS}} \sim 3.50 \text{ cm}^3 \text{ mol}^{-1} \text{ K}$). The characteristic temperature $T_{1/2}$, at which the conversion is half-completed, is estimated at $\sim 450 \text{ K}$ ($\text{L} = \text{t-msbpy}$) and 340 K ($\text{L} = \text{Me}_2\text{-bpy}$). Both values are higher than those reported for $\text{Fe}(\text{L})_2(\text{NCS})_2$ analogues ($T_{1/2} \sim 375 \text{ K}$ and $T_{1/2} \sim 270 \text{ K}$ for $\text{L} = \text{t-msbpy}$ and $\text{Me}_2\text{-bpy}$ respectively), as established with $\text{Fe}(\text{phen})_2(\text{NCX})_2$ complexes.^[16, 17, 18] Below 250 K, the $\chi_M T$ plateau at ca. $0.17\text{-}0.20 \text{ cm}^3 \text{ mol}^{-1} \text{ K}$ shows the presence of a small amount of HS species ($\sim 5\text{-}5.7 \%$). In **Figure S2**, the characterization of $\text{Fe}(\text{c-msbpy})_2(\text{NCSe})_2$ show an almost temperature independent behavior with an intermediate value $\chi_M T \sim 1.43 \text{ cm}^3 \text{ mol}^{-1} \text{ K}$ that is close to the value expected for a $1/3\{ [\text{Fe}(\text{c-msbpy})_3]_2[\text{Fe}(\text{NCSe})_4](\text{NCSe})_{2.n}(\text{H}_2\text{O}) \}$ formulation (for an Fe^{II} , $\chi_M T^{\text{HS}} \sim 3\text{-}3.8 \text{ cm}^3 \text{ mol}^{-1} \text{ K}$).

According to results, we will focus in the following on the nanoparticles prepared from the t-msbpy and $\text{Me}_2\text{-bpy}$ Fe^{II} complexes that undergo a thermal spin crossover above room temperature, a pre-requisite for probing the LD-LISC activity.

IV.3.2. Investigation of Nanoparticles Dispersed in PMMA Thin Films

We have adopted for this work a stepwise approach with first the isolation of a sizable amount of particles characterized with standard techniques and second, their encapsulation in thin films. This second step solves the issue of opacity of particles dispersions in PMMA and optimizes the conversion of particles upon light irradiation. As a counterpart, the analysis of properties in highly diluted films necessitates the use of Raman and UV-vis spectrometries for the extraction of electronic and vibrational signatures of the molecular components. Therefore we have achieved the measurements of thin films by varying the temperature and irradiating the samples (at room temperature). Finally we have probed the photoswitching response with magnetic susceptibility measurements.

Starting materials before any irradiation

UV-vis measurements : The UV –vis data were collected with PMMA thin films containing either nanoparticles ($\text{Fe}(\text{t-msbpy})_2(\text{NCSe})_2$, $\text{Fe}(\text{Me}_2\text{-bpy})_2(\text{NCSe})_2$) or molecules (t-msbpy, c-msbpy). In **Figure 5** are displayed absorption spectra of $\text{Fe}(\text{t-msbpy})_2(\text{NCSe})_2$ particles collected at temperature varying between 173 and 363 K; the other ones are reported in the appendix (**Figures S4**).

The spectra show the absorption bands previously identified for the tris t-msbpy complex in CH_3CN solution (**Chapter 3**) with changes in energies or intensities. The IL $\pi\text{-}\pi^*$ transitions here observed at 312 nm with a shoulder at 293 nm are blue shifted (cationic complex, 331 and 297 nm) while the lowest MLCT transitions (591 or 593 nm at high- or low-temperature respectively) are red-shifted (cationic complex, 551 nm). We note that (i) the former IL transitions are very close to those of the free base ligand in PMMA (308, 291 nm), (ii) the blue-shift of IL transition confirms the absence of $[\text{Fe}(\text{t-msbpy})_3]^{2+}$ in the sample (in the form of an hydrated salt). The effect of coordination of t-msbpy to Fe^{II} ion appears by comparing the MLCT absorptions of $\text{Fe}(\text{L})_2(\text{NCSe})_2$ complexes. The substitution of $\text{L} = \text{t-msbpy}$ by $\text{Me}_2\text{-bpy}$ ligands leads to an energy increase of MLCT absorptions (from 593 to 570 nm, ca. 700 cm^{-1}). This observation is consistent with the extra stabilization of antibonding π^* orbitals of t-msbpy that derives from a larger electronic delocalization over the π skeleton than in $\text{Me}_2\text{-bpy}$.

In the variable-temperature spectra of $\text{Fe}(\text{t-msbpy})_2(\text{NCSe})_2$ the main changes are observed in the MLCT region. By increasing the temperature from 173 to 363 K, the absorption bands

decrease in intensity and are slightly blue shifted. This evolution agrees with the general tendencies characterizing Fe^{II} thermal spin-crossover compounds.^[3, 19] The areas extracted from the MLCT absorption bands can be scaled to the HS fraction (assuming transitions with almost temperature independent oscillator strength). In **Figure 5** are compared the spin-crossover curves associated to nanoparticles dispersed in PMMA thin films (optical data) and without dispersing medium (magnetic data). The two sets of data confirm that the thermal process presents the same characteristics and thus, that the processing of nanoparticles plays no role on the spin-crossover behavior.^[15]

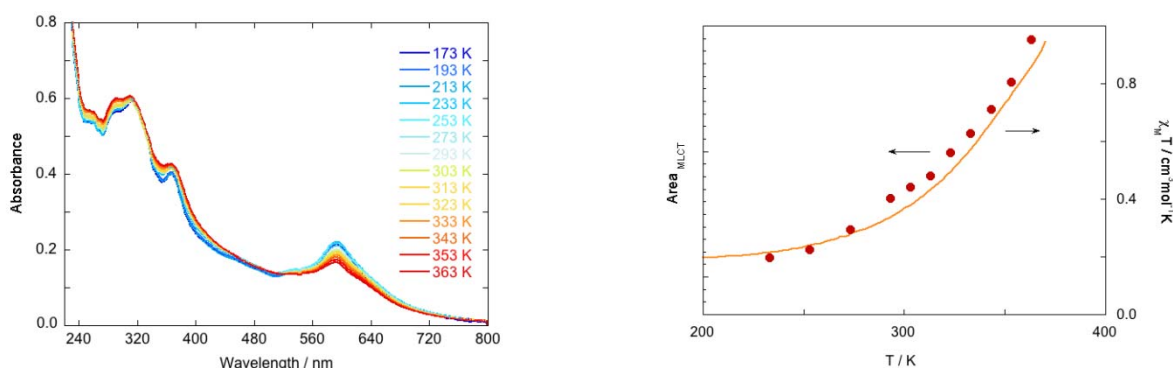


Figure 5 : Variable temperature spectra of nanoparticles of $\text{Fe}(\text{t-msbpy})_2(\text{NCSe})_2$ processed in PMMA thin films. Comparison between the plots of areas of MLCT absorption bands vs. temperature (●) with the $\chi_M T$ vs. temperature curve (—, 70 nm particles dispersed in PMMA).

Raman measurements

The Raman measurements of thin films were carried out at room temperature. The whole set of data (in Appendix of this chapter **Figures S5, Table ST6**) can be compared with results obtained for powders for identifying the spectroscopic markers of the functional groups. We have previously reported the changes associated to the thermal spin-crossover of $\text{Fe}(\text{Me}_2\text{-bpy})_2(\text{NCSe})_2$ (**Chapter 2**).

In **Figure 6** are displayed the spectra of $\text{Fe}(\text{L})_2(\text{NCSe})_2$ nanoparticles ($\text{L} = \text{t-msbpy}$ and $\text{Me}_2\text{-bpy}$). As mentioned above, the NC_{NCSe} vibrational peaks identified at 2104, 2079 cm^{-1} ($\text{L} = \text{t-msbpy}$) or 2098, 2076 cm^{-1} ($\text{L} = \text{Me}_2\text{-bpy}$) support the presence in the Fe^{II} coordination sphere of N-bonded NCSe ligands, while the presence of the pyridinic ligand gives rise to a number of peaks including NC_{py} at 1604 cm^{-1} ($\text{L} = \text{t-msbpy}$) or 1615 cm^{-1} ($\text{L} = \text{Me}_2\text{-bpy}$) cm^{-1} . The frequency at 1630-1634 cm^{-1} can be assigned to the $-\text{HC}=\text{CH}-$ stretching vibration of the ethenyl substituent. In absence of strong marker associated to the CH out-of-plane

deformation at ca. $970\text{--}960\text{ cm}^{-1}$, it might be used for analyzing any change in the isomer configuration.

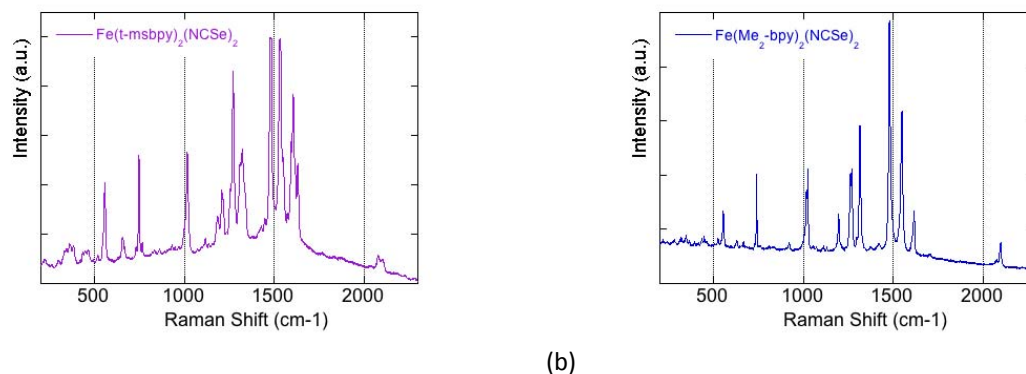


Figure 6: Raman spectra recorded at room temperature of $\text{Fe}(\text{L})_2(\text{NCSe})_2$ nanoparticles dispersed in PMMA thin films : $\text{L} = \text{t-msbpy}$ (a) and $\text{Me}_2\text{-bpy}$ (b).

Photoinduced reactivity of nanomaterials

Then, the thin films were irradiated with continuous sources delivering UV or blue excitation light ($\lambda = 254, 365$ and 405 nm). The experiments were carried out under vacuum (films placed in a cryostat) in order to minimize side-reactions, if any. The stability in darkness of irradiated samples was checked on a few samples. For comparison, the UV-vis and Raman measurements were performed in fixed conditions before and after irradiation of samples.

UV-vis measurements

The behavior of both msbpy isomers was probed with 254 or 365 nm radiation (spectra in Appendix, **Figures S6**). The trans to cis isomerization occurs upon a 365 nm irradiation, but the conversion is much slower than in solution (**Chapter 3**). After 14 h of irradiation, the spectrum show features at 252 and 283 nm (that may be assigned to the cis-isomer) but also discrepancies (at 225 and above 350 nm) suggesting traces of side-product despite the absence of dioxygen. The use of a 254 nm radiation enhances the rate in side-product, as shown by the bleaching in the $250\text{--}350\text{ nm}$ range. The reactions carried out with the films of c-msbpy show a cis-to-trans isomerization that peaks within 30 min and then a slow evolution to a spectrum again corresponding to the formation of product (photocyclized / degradation compound).

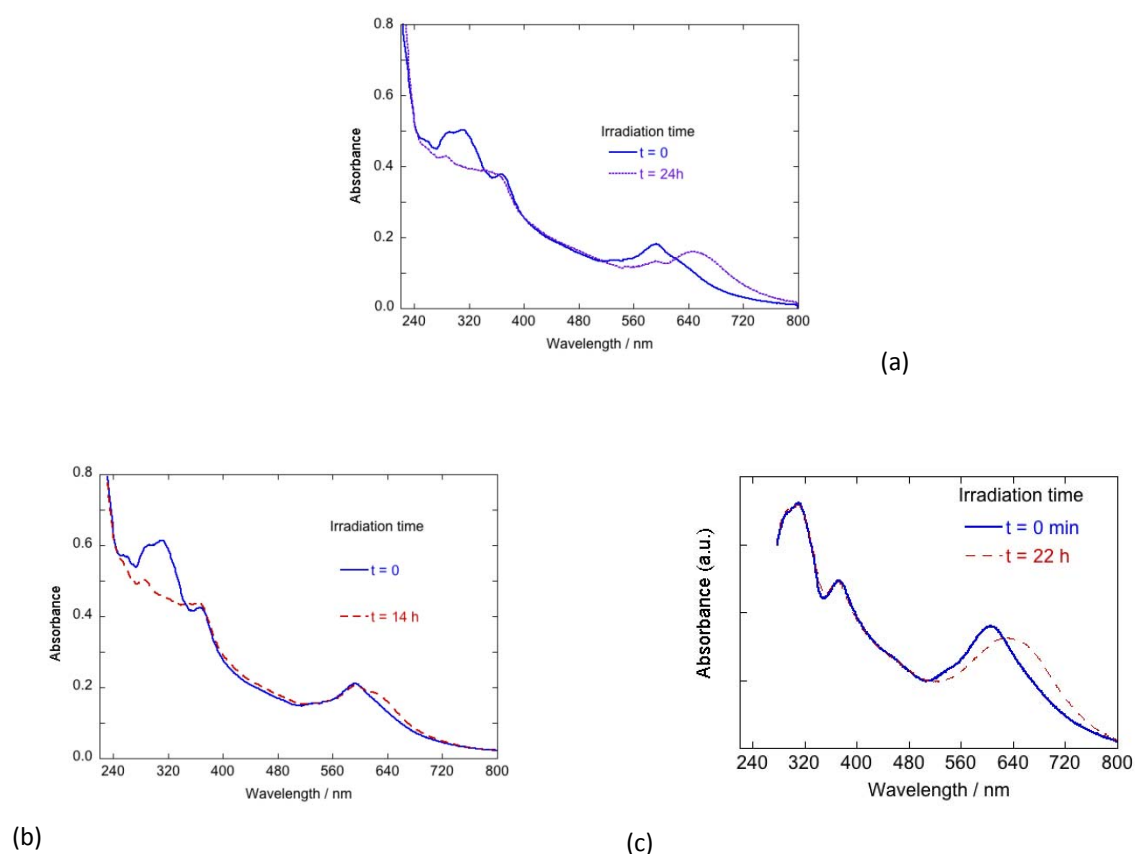


Figure 7 : UV-vis spectra recorded at room temperature of $\text{Fe}(\text{t-msbpy})_2(\text{NCSe})_2$ nanoparticles dispersed in PMMA thin films maintained under vacuum: irradiation at 254 nm **(a)**, 365 nm **(b)** and 405 nm **(c)**. The thermal stability was checked in case of **b** (after 1 h) and **c** (after 19 h) in darkness.

The reactivity of $\text{Fe}(\text{t-msbpy})_2(\text{NCSe})_2$ was investigated with 254, 365 and 405 nm radiations and the **Figures 7** and **S7** show the spectra measured at room temperature. First, the spectra before any irradiation compare with those in **Figure 5** except some variations in the MLCT absorption band. This broad band appears to be convoluted by a low-energy absorption (shoulder at $\lambda > 612$ nm, **Figures 5** and **7a**) and thus the absorption maximum is pointed at ca. 592 nm. In **Figures 7b** and **7c** (or in Appendix, **Figures S7**), the MLCT absorption band presents a more symmetrical shape and in this case, is centered around 606-608 nm. One possible reason for this discrepancy is the existence of an artefact around 600 nm due to the spectrophotometer that commonly appears upon measuring solid samples (baseline recording). In the following we analyze the average value of the wavelength corresponding to the middle of the band.

Table 2 : Main absorption bands characterizing the nanoparticles of $\text{Fe}(\text{t-msbpy})_2(\text{NCSe})_2$ and their changes upon excitation.

Wavelength / nm	Absorption bands
254	t = 0 h; 291 (IL), 311 (IL), 367, ca. 592 (MLCT) t = 24 h; 285, 361 (broad), 593, 646
365	t = 0 h; 290, 310, 367, ca. 593 t = 14 h; 282, 361, ca. 610
405	t = 0 h; 291 sh, 310, ca. 452, ca. 536, ca. 606 t = 22 h; 291 sh, 310, ca. 452, 634

Spectral evolutions of the nanoparticles of $\text{Fe}(\text{t-msbpy})_2(\text{NCSe})_2$ are observed in the ranges corresponding to IL and MLCT absorptions. Upon the 254 nm irradiation, the intensity of the $\pi\text{-}\pi^*$ absorption of t-msbpy decreases and a peak appears with a maximum at ca. 285 nm . According to the previous results, these observations are related to a trans-to-cis isomerization process although the formation of side-product cannot be discarded (Appendix, **Figure S7**). In addition to this, a pronounced shift of the MLCT band from ca. 592 to 646 nm, i.e. 1400 cm^{-1} seems to result from this conversion.

Surprisingly, the thin film irradiation at 365 nm (or 320 nm) provides evidence of a ligand centered reaction (features observed in the IL band similar to the previous ones) but only a weak change occurs in the MLCT region. Finally, a 405 nm excitation (a slightly lower energy) lets the msbpy ligand essentially unchanged and produces again a marked red-shift of the MLCT absorption.

In view of these puzzling behaviors, we have realized successive irradiations with 365 and 405 nm radiations. Whatever the sequence, these experiments (**Figures S7c, S7d**) confirm the occurrence of two processes driven by the two wavelengths and thus these processes appear weakly or noncoupled. The final states of the samples are stable in darkness.

Raman measurements

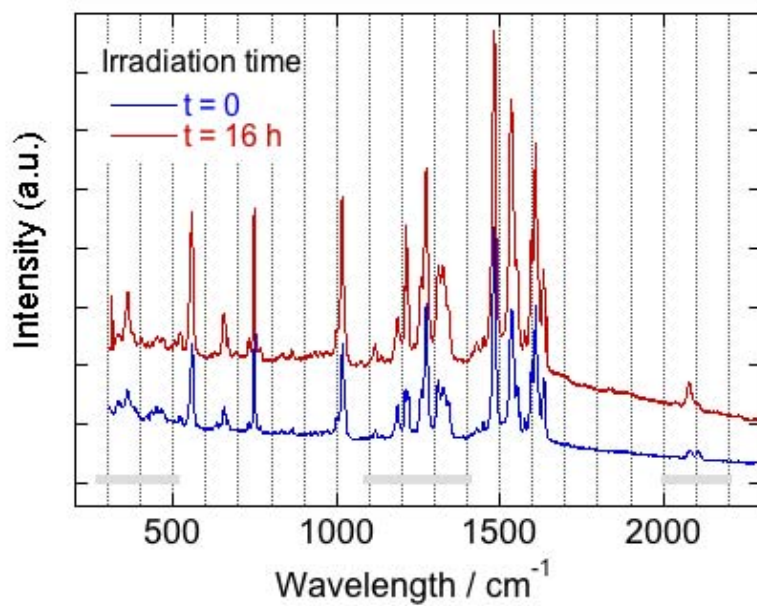
The thin films irradiated with $\lambda = 254, 365$ and 405 nm excitation wavelengths were characterized at room temperature. In the spectra displayed in **Figures 8, 9** (and **Figure S8** in appendix of this chapter), the vibrational peaks varying upon light irradiation (collected in **Table ST7**) are essentially located in three regions: the 2200-2000 cm^{-1} (**1**, NC_{NCSe} vibration already discussed, related to the coordination mode of the ligand and the metal ion spin state),

1400-1100 cm^{-1} (**2**, ring bending, in-plane (or out-of-plane) C-H bending) and 500-300 cm^{-1} (**3**, metal-ligand stretching vibrations).^[20]

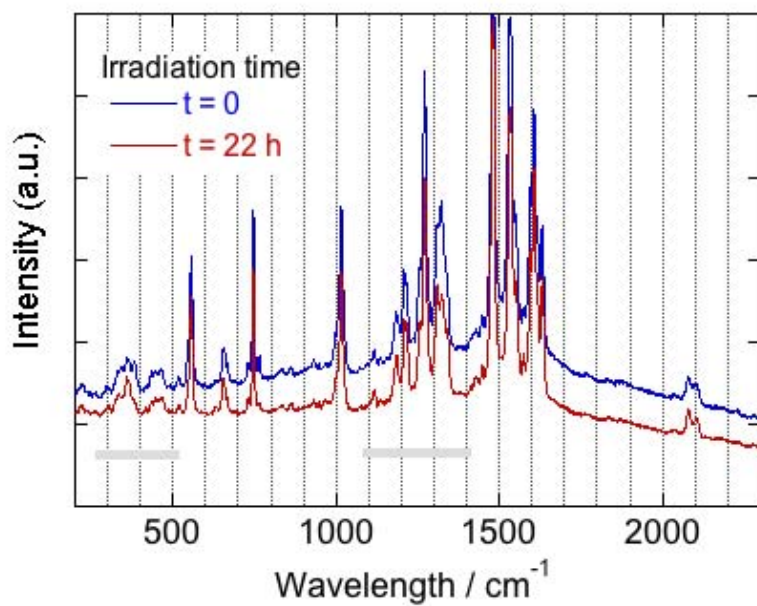
First, the excitation at 254 cm^{-1} , leads to changes in the whole spectrum: (1) an enhancement of the ν_{NC} at 2075 cm^{-1} suggesting a higher fraction of HS species, (3) related changes of the coordination sphere manifested by changes at very low energy and also (3) modification (or distortion) of the chelating ligands. Here we note that the markers associated to the trans-isomer of msbp are especially scarce and the reaction induced by the 365 nm irradiation (ligand-centered transition, **Figures 8b** and **S8a, S8b**), provokes some decreases in intensity of peaks (1208 or 767 cm^{-1}), shifts (for instance, 1633 to 1629 cm^{-1} , HC=CH stretching vibration of the ethene group, a change expected upon trans-to-cis isomerization)^[21] comparable to the experimental resolution but no significant change of the NCSe group (1). This last point that suggests an unchanged HS fraction, is associated with a limited broadening of the MLCT absorption (**Figure 7b**). In contrast to the previous case, the thin film excitation at 405 nm gives rise to a marked change in all the regions, in particular a relative increase at 2075 cm^{-1} associated to the formation of HS species.

To get more information about the processes impacting the chromophores, we have pursued with successive irradiations with 365 and 405 nm and the reverse sequence (results in **Figure S8**). We present in **Figure 9d** the spectra collected with different irradiations. It appears first that, whatever the sequence of excitation with 365 and 405 nm, the spectra are identical. Thus, we can infer that the whole transformation involves processes based on almost independent parts of the complex that may be sequentially converted. Surprisingly, we observe that the sample irradiated at 254 nm does not show very distinctive spectroscopic features and the photoproduct present similarities to the one prepared with the previous step-wise reaction.

Therefore this investigation based on Raman and UV-vis measurements provide evidences of conversions involving the metal ion and / or the photoactive ligand, which are triggered with various excitations wavelengths, through distinct energy pathways.

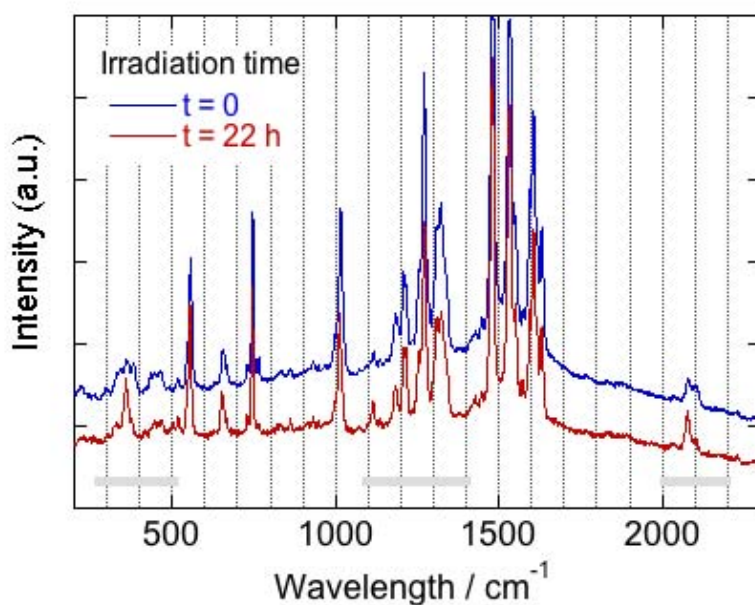


(a)

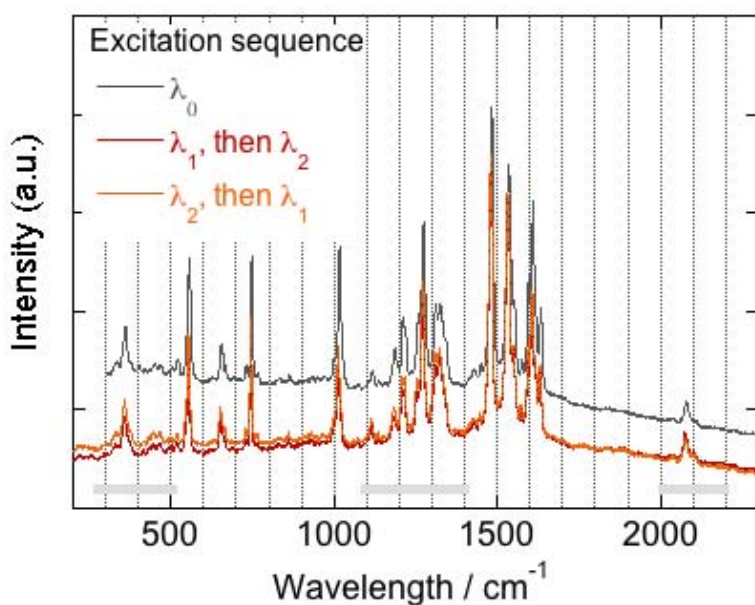


(b)

Figure 8 : Raman spectra of t-msbpy Fe^{II} compounds dispersed in PMMA films upon light irradiation : Fe(t-msbpy)₂(NCSe)₂, $\lambda = 254$ nm (a), $\lambda = 365$ nm (b).



(c)



(d)

Figure 9 : Raman spectra of t-msbpy Fe^{II} compounds dispersed in PMMA films upon light irradiation : Fe(t-msbpy)₂(NCSe)₂, $\lambda = 405$ nm (c) ; comparison between spectra obtained after excitation at $\lambda_0 = 254$ nm ($t = 14$ h), or a sequence with $\lambda_1 = 365$ nm ($t = 22$ h) and $\lambda_2 = 405$ nm ($t = 22$ h) (d). The regions associated to the main changes are indicated in grey.

Photomagnetic activity

The issues to address are now: what is the thermal behavior of the sample after its conversion by light, does the change detected in the MLCT or in the NC_{NCSe} vibrational bands correspond to a detectable photomagnetic effect. Therefore we have performed first variable temperature UV-vis measurements (thin films) and then magnetic measurements (powder of nanoparticles dispersed in PMMA) upon light irradiation.

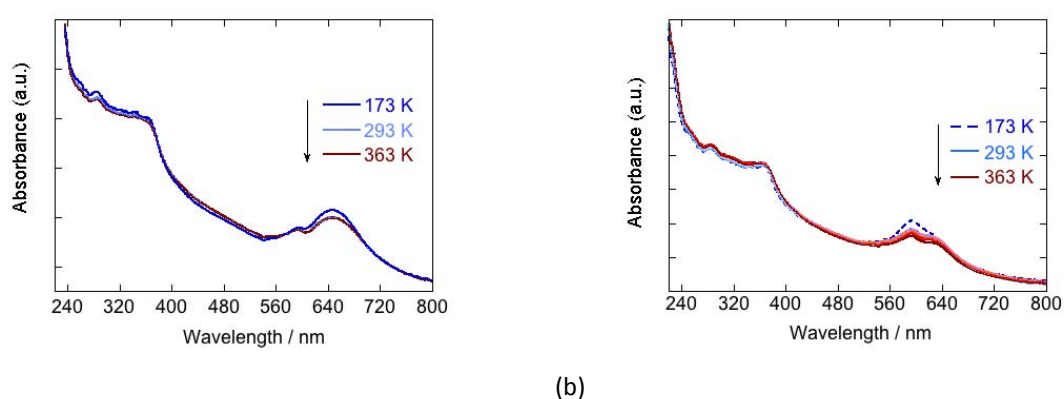


Figure 10 : UV-vis spectra recorded as a function of temperature for nanoparticles of $\text{Fe}(\text{tmsbpy})_2(\text{NCSe})_2$ dispersed in PMMA thin films samples: after irradiation at 254 nm (sample in **Figure 7a**) ; after irradiation at 365 nm (sample in **Figure 7b**).

The UV-vis spectra collected after irradiation were recorded as a function of temperature (**Figure 10**). As previously shown, absorption changes appear in the MLCT region that correspond to ca. 10 % or 23 % in **Figure 10a** and **10b** respectively. While the amplitude of the latter is indicative of a thermal spin crossover (behavior exhibited by the starting material), the former might result from a simple effect of absorption broadening associated to the population of higher vibrational states or of uncertainties associated to solid state measurements (deviations due to scattering effects, variation in the sample thickness vs. the temperature). Therefore these experiments cannot provide clear indications about the thermal properties of the samples.

Advantages were taken from the preparation of nanoparticles in the form of powder (in PMMA dispersion). The magnetic measurements were carried out on a small amount of this powder ($\sim 0.2\text{-}0.3$ mg) first by varying the temperature between 250 and 350 K then, by in-situ irradiating the sample at 300 K with a 365 nm (for 300 min) and then a 405 nm (for 800

min) light and finally, by repeating the measurement as a function of temperature in strictly the same conditions. The effect of an excitation at 254 nm can not be investigated within the Squid magnetometer.

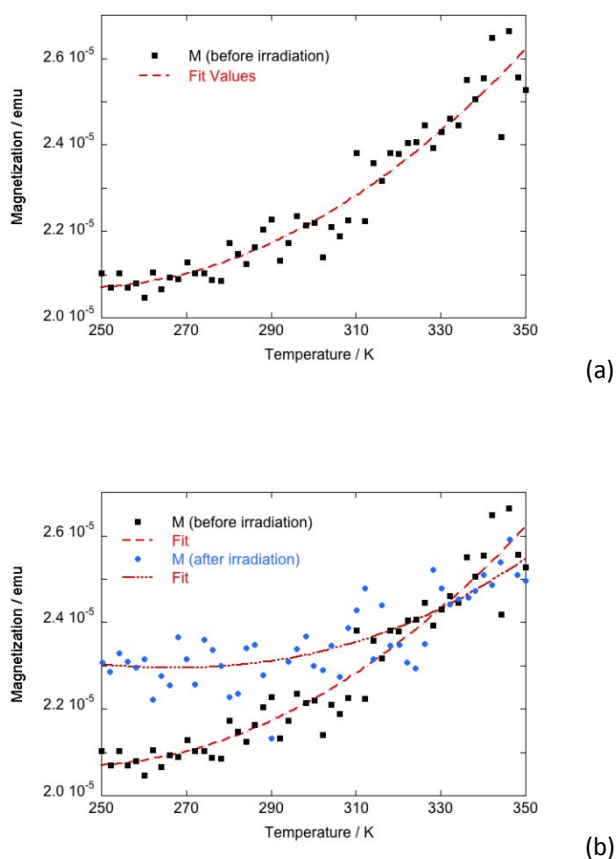


Figure 11: Magnetization versus temperature curves of nanoparticles of $\text{Fe}(\text{t-msbpy})_2(\text{NCSe})_2$ dispersed in PMMA. The data were recorded before any irradiation (■) after successive irradiations (●) at 300 K with 365 (time) and 405 (time) nm excitation wavelengths. The corresponding fitted curves (--- or -.-) were plotted as guidelines.

As expected, the very small amount of matter required for an efficient conversion upon light irradiation produces at room temperature a very weak M signal ($\sim 2.2 \times 10^{-5}$ emu); this signal being the sum of a major component due to PMMA and sample substrate (negative for diamagnetic species or slightly positive depending on the substrate nature) and a minor component due to highly diluted paramagnetic (positive values of M) particles. Despite these extremely limiting conditions,^[22] the temperature dependence of M show before any irradiation a tendency. The increase of magnetization with temperature indicates the thermal spin-crossover of particles characterized above by quantitative measurements (**Figure 4**). The M vs T curve recorded after the sample irradiation does not superimpose with the previous

one. A weak gap ($\Delta M > 0$), that is slightly larger than the measurement uncertainty, appears on the low temperature side and again the magnetization increases with temperature. Therefore the trends shown by these data are a formation of paramagnetic species and a presence of spin crossover ones. With respect to the spectroscopic data, we note the consistency between the net increase of the NC vibrational peak assigned to the HS form (Raman data) and the gain in the 250 K magnetization. Finally, the detection of a spin-crossover at high temperature may be indicative of the presence of unconverted residue, an hypothesis also accounting for the vis absorption in **Figure 10b**.

Therefore, this investigation demonstrates the possibility to induce a significant transformation of Fe^{II} spin-crossover nanoparticles by means of UV photoirradiations and both spectroscopic and magnetic measurements indicate a combination of ligand-centered and metal-centered modifications and a relative gain in HS species. These features that might be related to the ligand-driven light-induced spin change raise different questions and lead to some remarks.

IV.3.3. Analysis of Results

We have examined the photoisomerization of a stilbenoid group incorporated in an Fe^{II} spin-crossover compound. This solid-state investigation was carried out for the first time with nanoparticles. The trans-to-cis conversion of the ligand was triggered under UV excitation and our preliminary results suggest a LS to HS conversion of the metal ion triggered by an additional excitation at 405 nm. In literature, a few works describe the reactivity of stilbenoids in Fe^{II} systems. In case of $\text{Fe}(\text{stpy})_4(\text{NCSe})_2$ compounds (stpy = trans- and cis-styrylpyridine) studied in the laboratory, the transformation at solid state only occurs for the all cis-stpy Fe^{II} complex and resulted in a change of magnetic behavior from HS (all-cis isomer) to spin-crossover (complex incorporating ca. 66 % of trans isomer). This feature was rationalized by considering the stronger ligand-field strength produced by trans-stpy (relative stabilization of the π^* antibonding orbitals and increase of basicity in the more planar isomer) than by the cis one.^[21, 22, 23] The Nishihara's group has reported similar results with the $\text{Fe}(\text{R-dpp})_2\text{X}_2$ (R-dpp = 4-styryl- 2,6-di(1H-pyrazol-1-yl)pyridine, R = H, CN) complex, the cis-to-trans conversion of the stilbenoid moiety associated to the HS (cis isomer) to LS (spin-crossover for trans isomer) magnetic change.^[24] However the work extension to the NO_2 -substituted styryl group has provided a few counterintuitive results (LS (cis-isomer) to HS (trans-isomer) conversion),^[25, 26] which were analyzed in terms of solid-state packing. If we exclude the case

of a solvated compound ($\text{NO}_2\text{-dpp Fe}^{\text{II}}$ serie) for which the solvent removal might occur concomitantly to the cis-to-trans isomerization, we note that the results concern solids fully or prevailingly in the HS state.

An unexpected result is that the fact that the trans-to-cis isomerization occurring upon a 365 nm irradiation is not associated to a significant change of the MLCT absorption or of the HS fraction. The light penetration depth within thin films being a priori correct, this point may be related to partial isomerization (for instance of only one msbpy ligand) due to the packing, or the existence of antagonist effects (structural, electronic). Also intriguing is the observation of a change in both the MLCT absorption and the content of HS specie that results from a second irradiation at lower energy. We know that both the spin-crossover and the photoisomerization processes involve electronic modifications coupled to structural ones especially at solid state. Therefore it seems reasonable to propose that the transformation observed here are related to solid-state properties and thus further developments based on single-crystal investigations are required.

The wavelengths selected for irradiating the nanoparticles of $\text{Fe}(\text{t-msbpy})_2(\text{NCSe})_2$ correspond to those applied for the ligand isomerization in $\text{Fe}(\text{t-msbpy})_3(\text{NCSe})_2$. We have shown that the 405 nm radiation prevailingly induces a metal-centered reaction. This excitation corresponds to the energy region, in which the high-energy MLCT transitions of the $\text{Fe}(\text{bpy})_3^{+2}$ analogue have been placed from theoretical.^[27, 28] Despite the expectation of a energy proximity between such MLCT excited states of $\text{Fe}(\text{t-msbpy})_2(\text{NCSe})_2$ and the triplet excited states of t-msbpy, this study does not show an efficient isomerization induced via a MLCT excitation, a process discussed in **Chapter 3** (solution) and demonstrated in a few Fe^{II} compounds (polycrystalline samples). Some factors may be suggested for accounting for these discrepancies: molecular properties (molecular symmetry, energy and nature of orbitals), the potential energy wells of trans and cis ligand isomers (cis to trans isomerization of stilbenoids favored in Fe^{II} molecular materials) and / or kinetic properties. With this respect, it would be important to probe the reactivity of the analogue compound $\text{Fe}(\text{c-msbpy})_2(\text{NCSe})_2$.

IV.4. Conclusions

We have described the synthesis of 60 nm nanoparticles of a functional molecular material based on a spin-crossover component incorporating photoswitchable ligands. This preparation has allowed the investigation of solid-state properties of dispersion of particles in PMMA thin

films especially adapted for optimizing photoconversion. Our attempts to isolate single-crystals being unsuccessful, we have combined optical, vibrational, magnetic and photomagnetic measurements to analyze spin-crossover behavior of nanoparticles and the influence of light irradiation. We have provided some evidences of a trans-to-cis conversion of stilbenoid occurring upon UV excitation, without any apparent change of the metal ion spin state and of an intriguing metal-centered effect leading to the metal ion spin change. These preliminary results require an extension of the work for understanding the solid-state properties. For instance we have to realize the synthesis of both the cis- and trans-msbpy analogues in the bulk form, vibrational measurements (combining variation of temperature and light irradiation) and obviously, deepen investigations based on photocrystallography measurements.

Concerning the LD-LISC activity, this prototype presents some drawbacks - long irradiation time, UV excitation, a fortiori a sequence of irradiation and, is appears not well-adapted for probing any potentiality. Therefore the work has to be pursued with new materials.

References

- [1] J.-P. Sauvage *Acc. Chem. Res.*, **1998**, 31, p. 611, Bonnet S., Collin J.-P., V. Balzani, A. Credi, F. M. Raymo, J. F. Stoddart *Angew. Chem. Int. Ed.* **2000**, 39, 3348 ; M. Koizumi, P. Mobian, J.-P. Sauvage *Adv. Mater.*, **2006**, 18, p. 1239 ;
- [2] Photochromism : Molecules and Systems, Elsevier Science, H. Dürr and H. Bouas-Laurent Eds, 2003 ; Special issue on Photochromism: Memories and switches, *Chem. Rev.* 2000, 100, 1685 ; K. Amimoto, T. Kawato *Journal of Photochemistry and Photobiology C: Photochemistry Reviews* 6 (2005) 207–226
- [3] A. Hauser *Top. Curr. Chem.* 2004, Vol. 234, p. 155.
- [4] A. Bousseksou, G. Molnár, L. Salmon, W. Nicolazzi, *Chem. Soc. Rev.* 2011, 40, 3313–3335.
- [5] Spin-Crossover in Transition Metal Compounds, Gülich P., Goodwin H. A. Eds., *Top. Curr. Chem.*, Springer, Heidelberg, 2004, Vol. 233-235; Spin-Crossover Materials: Properties and Applications; Halcrow M. A., Wiley, Chichester, 2013; Sato O., Tao J., Zhang Y.-Z. *Angew. Chem. Int. Ed.* **2007**, 46, 2152.
- [6] B. L. Feringa *J. Org. Chem.* **2007**, 72, 6635-6652 ; B. L. Feringa, *Molecular Switches*, Wiley-VCH, Darmstadt, Germany 2001.
- [7] A. Spangenberg, R. Métivier, J. Gonzalez, K. Nakatani, P. Yu, M. Giraud, A. Léaustic, R. Guillot, T. Uwada, T. Asahi *Adv. Mater.* 2009, 21, 309.
- [8] N. Sanz, A. C. Gaillot, P.L. Baldeck, A. Ibanez *J. Mater. Chem.*, **2000**, 10, 2723.
- [9] M. Cavallini, *Phys. Chem. Chem. Phys.* 2012, 14, 11867–11876 ; H. J. Shepherd, G. Molnár, W. Nicolazzi, L. Salmon, A. Bousseksou *Eur. J. Inorg. Chem.* 2013, 653–661.
- [10] T. Forestier, A. Kaiba, S. Pechev, D. Denux, P. Guionneau, C. Etrillard, N. Daro, E. Freysz, J.-F. Létard *Chem. Eur. J.* 2009, 15, 6122.
- [11] E. König, *Coord. Chem. Rev.*, 1968, **3**, 471.
- [12] E. J. MacLean, C. M. McGrath, C. J. O'Connor, C. Sangregorio, J. M. W. Seddon, E. Sinn, F. E. Sowrey, S. J. Teat, A. E. Terry, G. B. M. Vaughan and N. A. Young, *Chem. Eur. J.*, 2003, **9**, 5314-5322.
- [13] S. Savage, Z. Jia-Long, A. G. Maddock *J. Chem. Soc Dalton Trans.* 1985, 991.

- [14] B. W. Dockum, W. M. Reiff *Inorg. Chim. Acta* 1986, 120, 61.
- [15] A. Tissot, C. Enachescu, M.-L. Boillot *J. Mater. Chem.* 2012, 22, 20451.
- [16] M.-L. Boillot, S. Chantraine, J. Zarembowitch, J. Y. Lallemant, J. Prunet, *New J. Chem.* 1999, 179.
- [17] A. J. Cunningham, J.E. Ferguson, H. K. J. Powell, E. Sinn, H. Wong *J. Chem. Soc., Dalton Trans.* 1972, 2155.
- [18] K. F. Purcell, M. P. Edwards *Inorg. Chem.* 1984, 23, 2620.
- [19] A. Tissot, J.-F. Bardeau, E. Rivière, F. Brisset, M.-L. Boillot *Dalton Trans.* 2010, 39, 7806.
- [20] T. P. Gerasimova, S. A. Katsyuba *Dalton Trans.* 2013, 42, 1787 ; B. D. Alexander, T. J. Dines, R. W. Longhurst *Chem. Phys.* 2008, 352, 19.
- [21] A. Tissot, M.-L. Boillot, S. Pillet, E. Codjovi, K. Boukheddaden, L. M. Lawson-Daku *J. Phys. Chem. C* 2010, 114, 21715.
- [22] J. S. Kolb, M. D. Thomson, M. Novosel, K. Sénéchal-David, E. Rivière, M.-L. Boillot, H. G. Roskos *C.R. Chimie*, 2007, 10, 1.
- [23] M.-L. Boillot, S. Pillet, A. Tissot, E. Rivière, N. Claiser, C. Lecomte *Inorg. Chem.* 2009, 48, 4729.
- [24] Y. Hasegawa, K. Takahashi, S. Kume, H. Nishihara *Chem. Commun.* 2011, 47, 6846.
- [25] K. Takahashi, Y. Hasegawa, R. Sakamoto, M. Nishikawa, S. Kume, E. Nishibori, H. Nishihara *Inorg. Chem.*, 2012, 51, 5188.
- [26] Y. Hasegawa, R. Sakamoto, K. Takahashi, H. Nishihara *Inorg. Chem.* 2013, 52, 1658.
- [27] C. De Graaf, C. Souza *Chem. Eur. J.* 2010, 16, 4550.
- [28] C. De Graaf, C. Souza *Int. J. Quantum Chem.* 2011, 111, 3385.

Conclusions

In this contribution, we have focused on the elaboration of spin-crossover nanoparticles and the investigation of their switching properties, especially the cis/trans photoisomerization of stilbenic groups attached to a spin-crossover type Fe^{II} complex and the interplay between the ligand photoactivity and the metal center properties (LD-LISC effect).

For the elaboration of nanoparticles, non-ionic mononuclear Fe^{II} complexes including or not photoactive bidentate ligands (L = trans- and cis-isomers of 4-methyl-4'-styryl-2,2'-bipyridine, msbpy or $\text{Me}_2\text{-bpy}$) have been selected. The synthesis of nanoobjects has required the adaptation of the method (sudden precipitation in antisolvent) previously reported for molecular spin-crossover compounds. It was achieved with ionic $[\text{Fe}(\text{L})_3](\text{NCSe})_2$ precursors by playing with chemical equilibria for inducing the precipitation of related neutral $\text{Fe}(\text{L})_2(\text{NCSe})_2$ species. Nanocrystals of $\text{Fe}(\text{t-msbpy})_2(\text{NCSe})_2$ and $\text{Fe}(\text{Me}_2\text{-bpy})_2(\text{NCSe})_2$ with sizes smaller than 100 nm were characterized and then highly diluted in polymeric thin films for optimizing light absorption and investigating photoswitching processes. Compounds ($\text{Fe}(\text{t-msbpy})_2(\text{NCSe})_2$ and $\text{Fe}(\text{Me}_2\text{-bpy})_2(\text{NCSe})_2$) in the form of nanoparticles, processed in thin polymeric films were shown to exhibit thermal spin-crossover centered at temperatures higher than room temperature; no significant effect of environment was detected.

The photochemical reactivity of the ionic precursors $[\text{Fe}(\text{msbpy})_3](\text{NCSe})_2$ was first probed in solution. It has been established that the cis to trans isomerization of 4-methyl-4'-styryl-2,2'-bipyridine takes place in a quantitative way when the diamagnetic Fe^{II} complex was exposed to a blue light; this reaction can be partly reversed with a UV excitation. From the background accumulated in the literature, it has been proposed that this process, specifically observed with the Fe^{II} chelate, requires the formation of high-energy MLCT excited states with intersystem crossing or energy transfer to the triplet intraligand excited state, that leads to the ligand photoisomerization.

Both isomers of free-base msbpy were encapsulated in polymeric thin films. The study has shown that their photoreactivity was preserved with a trans-to-cis isomerization similar to the one observed in solution. In the highly confined environment of nanoparticles, the $\text{Fe}^{\text{II}}(\text{t-msbpy})_2(\text{NCSe})_2$ complex also reacts upon irradiation. The

combination of UV-Vis, Raman and photomagnetic measurements of the highly diluted materials has allowed us to analyze the effect of light irradiation and the spin-state switching behavior. The study of $\text{Fe}^{\text{II}}(\text{t-msbpy})_2(\text{NCSe})_2$ has shown the occurrence at room temperature of different processes depending on the excitation wavelength: a ligand-centered process (trans-to-cis isomerization, $\lambda_{\text{exc}} = 365 \text{ nm}$) and a metal-centered one (resulting in a MLCT change, $\lambda_{\text{exc}} = 405 \text{ nm}$). Unexpectedly, the stilbenoid isomerization is not associated to the metal ion spin change contrarily to what is observed for instance with crystalline samples of $\text{Fe}(\text{stpy})_4(\text{NCSe})_2$ (stpy = styrylpyridine). For the latter, the cis-to-trans isomerization of styrylpyridine resulting from a 532 nm irradiation drives the spin-state switching of the Fe^{II} ion. Interestingly, the Raman and photomagnetic measurements performed in this work have indicated that the 405 nm irradiation (or successive irradiations at 365 and 405 nm) may change the fraction of HS species. This feature observed for the very first time with nanoparticulate sample shows that the solid-state reactivity is somewhat puzzling and thus, it suggests additional investigations for describing the molecular processes and the role of solid-state.

One important issue for an in-depth study is the elaboration of bulk compounds in the form of single-crystals for analyzing the molecular and supramolecular parameters accounting for the configurational isomerism and its possible influence on the coordination sphere of the spin-crossover metal ion. The synthesis of the $\text{Fe}^{\text{II}}(\text{c-msbpy})_2(\text{NCSe})_2$ analogue is important for rationalizing the properties dependent on the ligand configuration, in particular the ligand-field strength and the photoactivity. Combined Raman and UV-vis experiments with variable temperature and light irradiation have to be pursued for analyzing the molecular changes in the organic and inorganic parts. Photochemical studies will be suitable for quantifying the reactivity of these inorganic compounds and selecting the well-adapted chromophore/functions for the design of new photoresponsive systems.

This work has provided new informations on photoisomerization in different media (solution, dispersion in polymers and nanocrystals) and the combination of the ligand photoisomerization with the spin-crossover process of a Fe^{II} compound. For the development of LD-LISC materials and their applications, critical issues are room temperature and excitation wavelengths in the visible range. The photocyclization of

Conclusion

diarylethene molecules presents considerable advantages with respect to the photoisomerization of stilbenoids: large photochromism, weak variation of volume and weak fatigability, features that suits for inducing reversible photoconversion with high quantum yields, possibly at solid state. Therefore, the elaboration of Fe^{II} spin-crossover complexes including such photoactive ligands should be developed.

Appendix

Appendix: Chapter II

Fe(Me₂-bpy)₂(NCSe)₂ spin-crossover micro- and nanoparticles showing a spin-state switching close to room temperature.

Table ST1: Crystal data and structure refinement for [Fe(Me₂-bpy)₃](NCSe)₂ · 3(H₂O) at 100 K.

Table ST2: The geometry of the Fe site surroundings in [Fe(Me₂-bpy)₃](NCSe)₂ · 3(H₂O)

Figure S1: Evolution of the crystal edges size and angle determined from optical microscopy images at 160 °C.

Figure S2 : the X-ray diffractograms of the powder of precursor recorded at 293 K, before and after the thermal reaction.

Figure S3 : IR spectra of the powder of precursor recorded at 293 K before and after the thermal reaction. Inset: expansion showing the frequency range of ν_{NC} .

Figure S4: TEM images showing the 500 and 60 nm particles, that as described in the text, simultaneously precipitate by sudden addition of the ethanolic solution of precursor in toluene.

Figure S5 : Superimposition of the temperature dependence of $\chi_{\text{M}}T$ reported for Fe(Me₂bpy)₂(NCSe)₂·H₂O in reference 12 and the one of the compound here prepared by thermal treatment of [Fe(Me₂bpy)₃](NCSe)₂ · 3H₂O.

Figure S6 : Raman spectra recorded for [Fe(Me₂-bpy)₃] NCSe)₂·3H₂O before (left) and after (right) the thermal treatment.

Figure S7 : Raman spectra of nanoparticles of Fe(Me₂-bpy)₂(NCSe)₂ recorded at different temperatures (a) 1.2 μm microparticles, (b) 500 nm nanoparticles, (c) 56 nm nanoparticles.

Figure S8 : Comparison between the variation of the relative intensity of the LS peak from Raman measurements (\blacktriangle bulk, \bullet 1.2 μm , \blacklozenge 500 nm, \blacklozenge 56 nm) and the HS fraction curves determined from magnetic measurements (dashed lines with the related colors).

Figure S9: EDS Analysis of (a) [Fe(Me₂-bpy)₃](NCSe)₂ · 3(H₂O) , (b) 1.2 μm microparticles, (c) 500 nm nanoparticles, (d) Bulk, (e) 56 nm nanoparticles.

Table ST1: Crystal data and structure refinement for $[\text{Fe}(\text{Me}_2\text{-bpy})_3](\text{NCSe})_2 \cdot 3(\text{H}_2\text{O})$ at 100 K.

	$[\text{Fe}(\text{Me}_2\text{-bpy})_3](\text{NCSe})_2 \cdot 3(\text{H}_2\text{O})$
Empirical formula	$\text{C}_{38}\text{H}_{36}\text{Fe N}_8 \text{O}_3 \text{Se}_2$
Formula weight	866.52
Temperature (K)	100 (1)
Wavelength (Å)	0.71069
Crystal system	monoclinic
Space group	$P 2_1/c$
a (Å)	12.203(1)
b (Å)	19.513(2)
c (Å)	15.887(1)
α (°)	90.00
β (°)	90.858(2)
γ (°)	90.00
V (Å ³)	3782.5(6)
Z	4
Density (calc.) (g.cm ⁻³)	1.521
Abs. coefficient (mm ⁻¹)	2.371
$F(000)$	1752
Crystal size (mm)	$0.27 \times 0.18 \times 0.04$
θ range (°)	$1.65 \rightarrow 30.54$
h	$-17 \rightarrow 14$
k	$-27 \rightarrow 27$
l	$-22 \rightarrow 22$
No. of reflections collected	58258
No. of independent reflections	11051
R_{int}	0.0466
Data [$I > 2\sigma(I)$] / restraints / parameters	7492 / 58 / 502
Goodness-of-fit on F^2	1.038
$R1$ [$I > 2\sigma(I)$]	0.0464
$wR2$ [$I > 2\sigma(I)$]	0.1128
$R1$ (all data)	0.0845
$wR2$ (all data)	0.1290

(CCDC 1010287)

Table ST2: The geometry of the Fe site surroundings in $[\text{Fe}(\text{Me}_2\text{-bpy})_3](\text{NCSe})_2 \cdot 3(\text{H}_2\text{O})$

Fe-N bonds (Å)	100 K
Fe-N1	1.969(2)
Fe-N2	1.963(2)
Fe-N3	1.961(2)
Fe-N4	1.968(2)
Fe-N5	1.978(2)
Fe-N6	1.980(2)

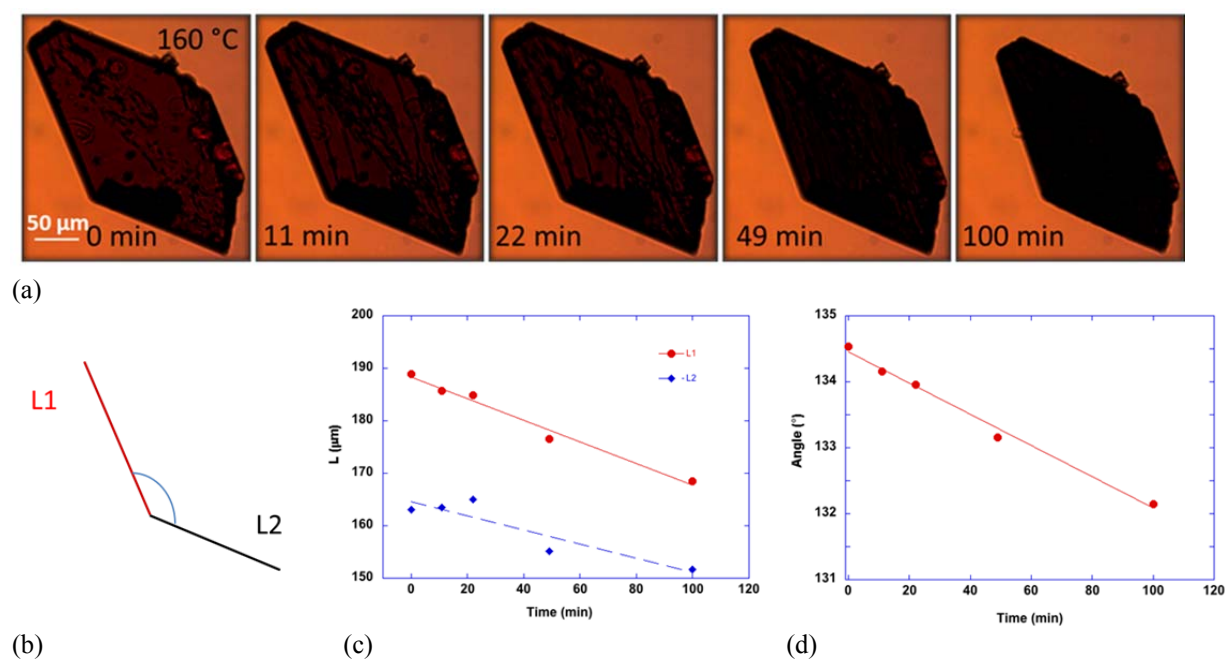


Figure S1 : Optical microscopy images of $[\text{Fe}(\text{Me}_2\text{-bpy})_3](\text{NCSe})_2 \cdot \text{CH}_3\text{OH}$ after the desolvation stage (a) the 160 °C isothermal evolution of the red square-shaped methanolate sample (a), and schem of sizes and angle of the sample (b). The transformation achieved after 100 min essentially preserves the shape of the solid linear variation of edges size (c) and angle (d).

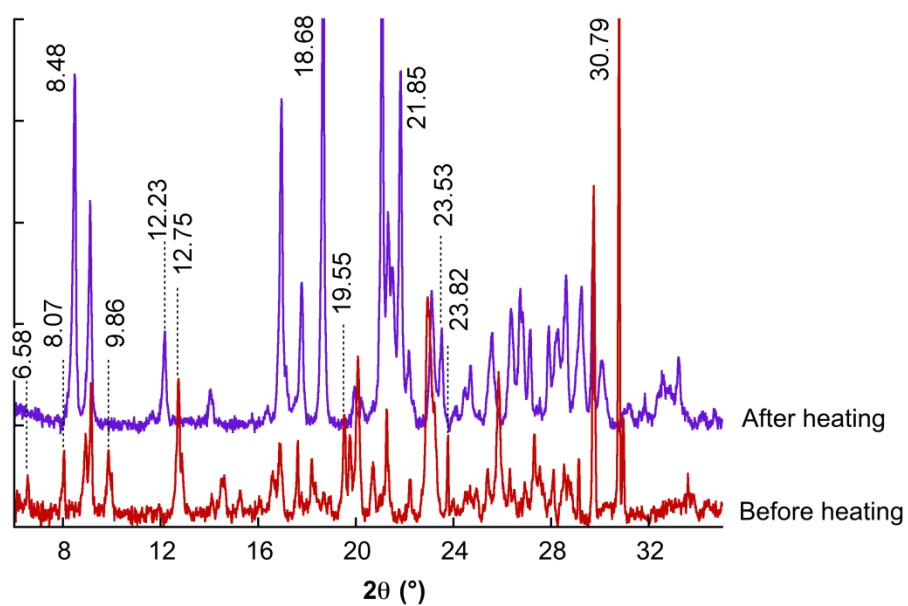


Figure S2 : The X-ray diffractograms of the powder of precursor recorded at 293 K, before and after the thermal reaction (175 °C, 4 hours, vacuum).

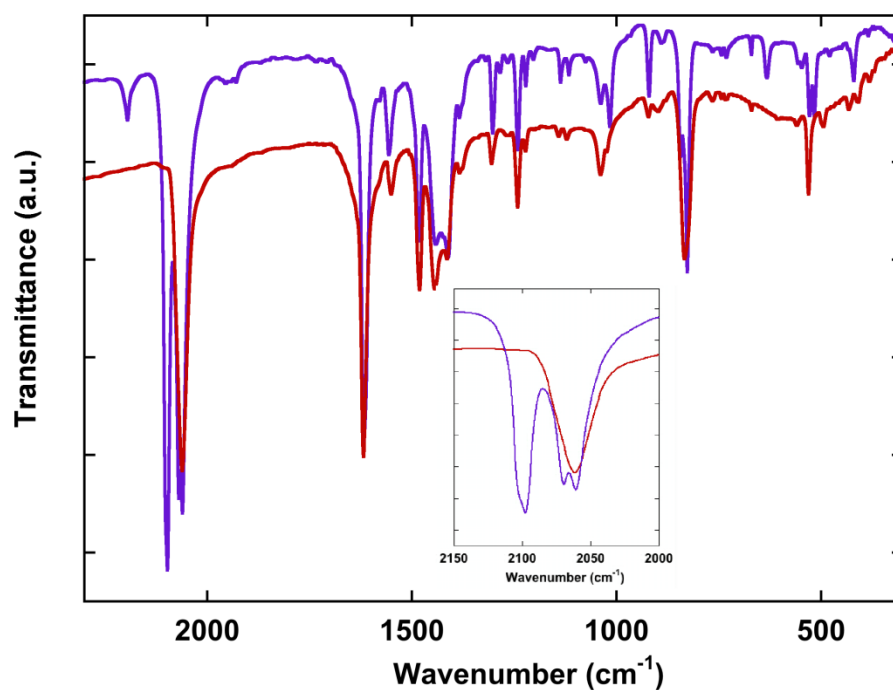


Figure S3 : IR spectra of the powder of precursor recorded at 293 K before (red line) and after (violet line) the thermal reaction. Inset: expansion showing the frequency range of ν_{NC} .

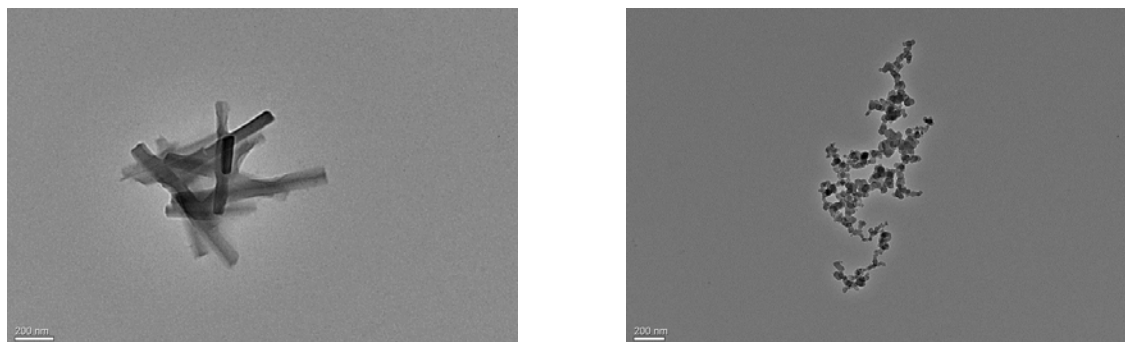


Figure S4: TEM images showing the 500 and 60 nm particles that as described in the text, simultaneously precipitate by sudden addition of the ethanolic solution of precursor in toluene.

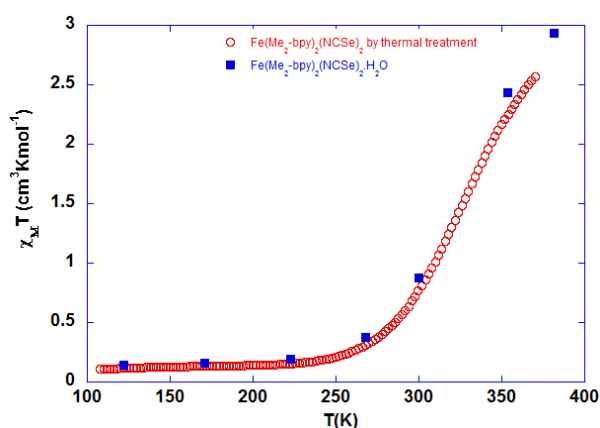
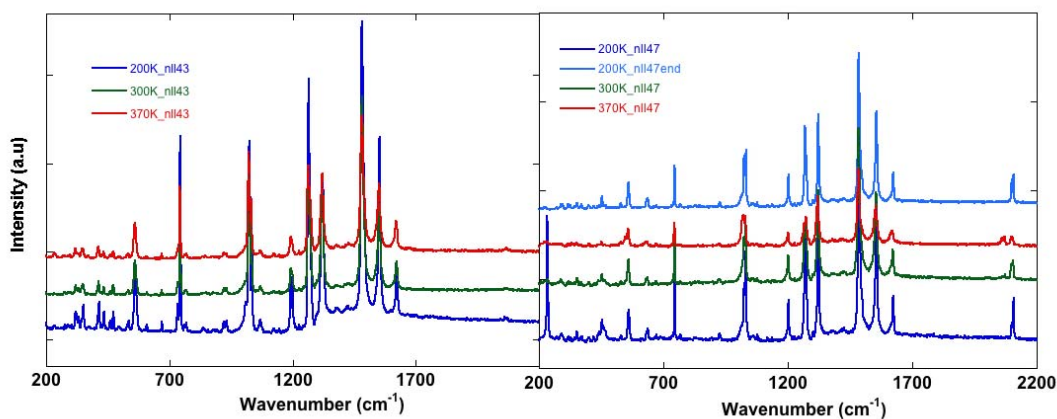


Figure S5 : Superimposition of the temperature dependence of $\chi_M T$ reported for $\text{Fe}(\text{Me}_2\text{bpy})_2(\text{NCSe})_2 \cdot \text{H}_2\text{O}$ by Cunningham et al. and the one of the compound here prepared by thermal treatment of $[\text{Fe}(\text{Me}_2\text{bpy})_3](\text{NCSe})_2$.



$3\text{H}_2\text{O}$.

Figure S6 : Raman spectra recorded for $[\text{Fe}(\text{Me}_2\text{bpy})_3](\text{NCS})_2 \cdot 3\text{H}_2\text{O}$ before (left) and after (right) the thermal treatment. The change of coordination sphere resulting from the solid heating is manifested by the set of vibrational peaks and their temperature dependence (in the table below), more specifically $\nu_{\text{NC}} = 2069$ and 2001sh , 2106 (200 K) or 2064 , 2074 (370 K) cm^{-1} for the cationic and neutral complex respectively. Markers of both species are also identified in the low frequency range.

Compound	T (K)	Frequencies (cm ⁻¹)
Bulk [Fe(Me ₂ -bpy) ₃](NCSe) ₂ ·3H ₂ O	200	- 1625,1551,1483,1422,1379,1318,1262,1201, 1189 ,1035 , 1023 ,1011,937,924,838,771,765, 746,734 ,673,611,562, 476 ,464, 433,415 ,353, 335 ,323,237
Bulk after thermal treatment Fe(Me ₂ -bpy) ₂ (NCSe) ₂	200	2110,2097 , 1624 ,1557,1483,1422,1379,1324, 1268,1201 ,1139,1115,10 78,1060,1035,1023,925 ^{vw} ,845,826,765,747,673, 636 ,562,5 32,452 ^{vw} ,439 ^{vw} ,433 ^{vw} ,421 ^{vw} ,403 ^{vw} ,396 ^{vw} , 372 ^{vw} ,353 ^{vw} ,341 ^v w,329 ^w ,323 ^{vw} ,292 ^{vw} ,224 ^{vw}
Bulk after thermal treatment Fe(Me ₂ -bpy) ₂ (NCSe) ₂	370	2103,2097, 2073,2060 , 1618 ,1551,1483,1416,1379,1317, 1275 ,1268,1201,1029,10 23,746,673 ^{vw} , 623 ,556, 550 ,532,452,403 ^{vw} ,366 ^{vw} ,354 ^{vw} , 335 ^{vw} ,ca280 ^{vw} ,261 ^{vw} , 230

In bold are indicated the frequencies that specifically appear for one compound (cationic, neutral) or one spin state (LS at 200 K and mixture of LS and HS forms at 370 K).

The ν_1 NC(NCSe) frequencies are pointed at 2075/2065 (HS) and 2113/2106 (LS) cm⁻¹ for Fe(phen)₂(NCSe)₂. The frequencies at 530.5, 527.0 cm⁻¹ in Fe(phen)₂(NCSe)₂ ascribed to ν Fe–N(NVSe) at are found here at 532 cm⁻¹.

Reference :

- E. König, K. Madeja Spectrochimica Acta, 1967, 23A, 45-54 ; P. Gülich Struct. Bond. 44, Springer-Verlag, Berlin, 1981, pp83-195.
- A. J. Cunningham, J.E. Ferguson, H.K.J. Powell, E. Sinn and H. Wong, J. Chem. Soc. Dalton Trans. 1972, 2155-2160.

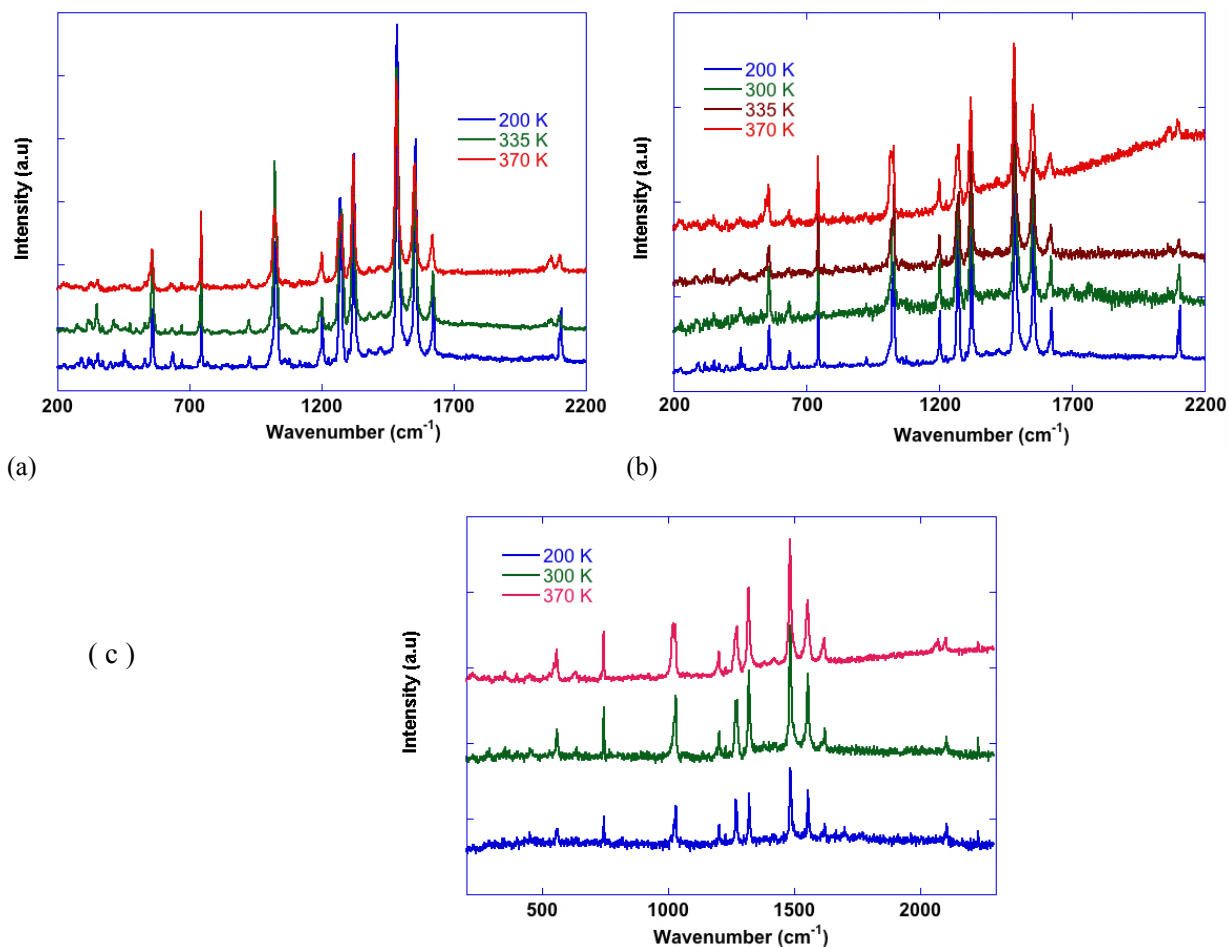


Figure S7 : Raman spectra of nanoparticles of $\text{Fe}(\text{Me}_2\text{-bpy})_2(\text{NCS})_2$ recorded at different temperatures (a) 1.2 μm microparticles, (b) 500 nm nanoparticles; (c) 56 nm nanoparticles.

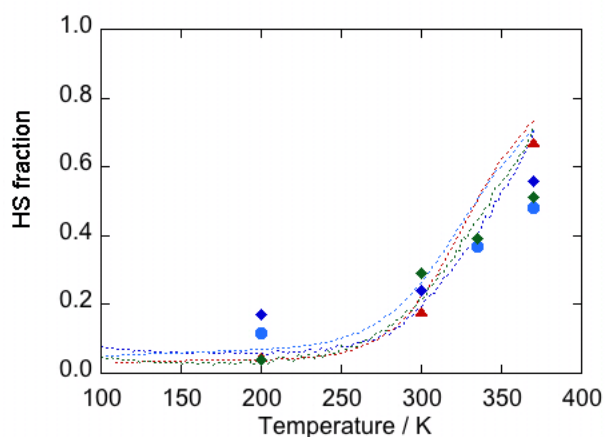


Figure S8 : Comparison between the points (\blacktriangle bulk, \bullet 1.2 μm , \blacklozenge 500 nm, \blacklozenge 56 nm) corresponding to the variation of the relative intensity of the LS peak from Raman measurements and the HS fraction curves determined from magnetic measurements (dashed lines with the related colors). The observed discrepancies at

low and high temperatures can be accounted for by uncertainties associated to the cases for which the HS fraction ~ 0 (or for highly diluted samples).

Figure S9a: EDS analysis of $[\text{Fe}(\text{Me}_2\text{-bpy})_3](\text{NCSe})_2 \cdot 3(\text{H}_2\text{O})$

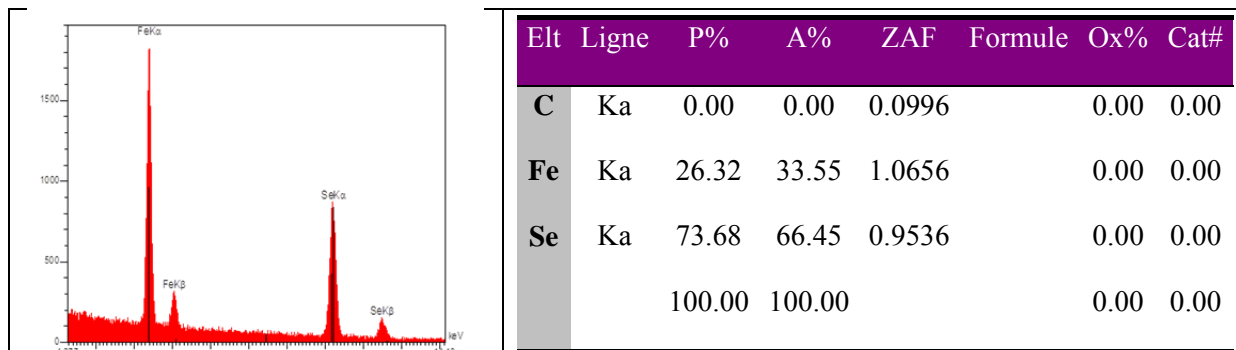


Figure S9b: EDS analysis of MPs (1.2 μm) of $\text{Fe}(\text{Me}_2\text{-bpy})_2(\text{NCSe})_2$

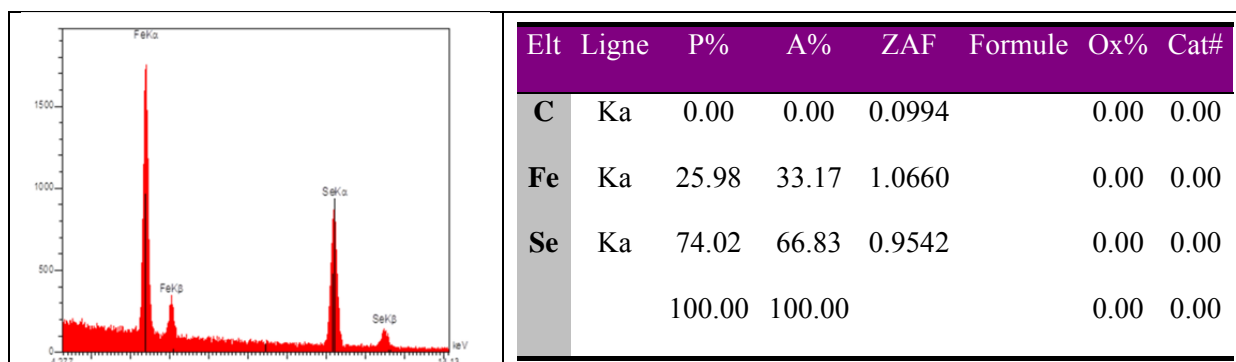


Figure S9c: EDS analysis of 500 nm of $\text{Fe}(\text{Me}_2\text{-bpy})_2(\text{NCSe})_2$

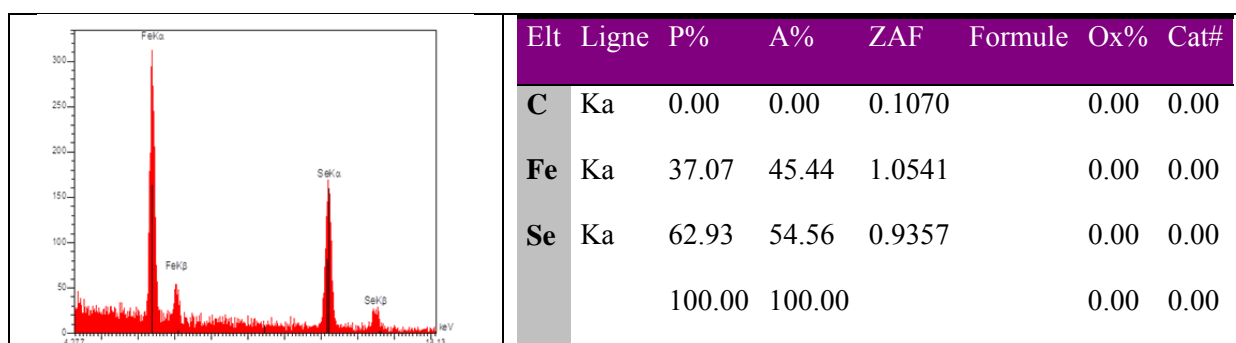


Figure S9d: EDS analysis of $[\text{Fe}(\text{Me}_2\text{-bpy})_3](\text{NCSe})_2 \cdot 3(\text{H}_2\text{O})$ after thermal treatment

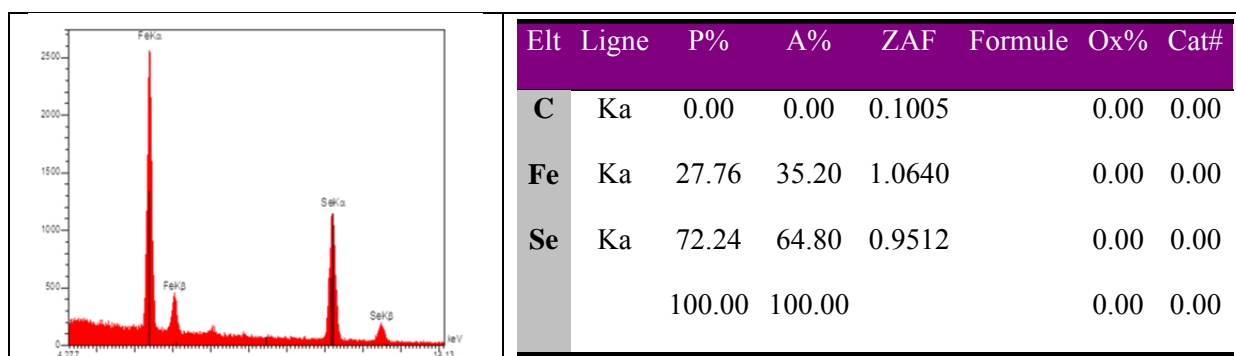
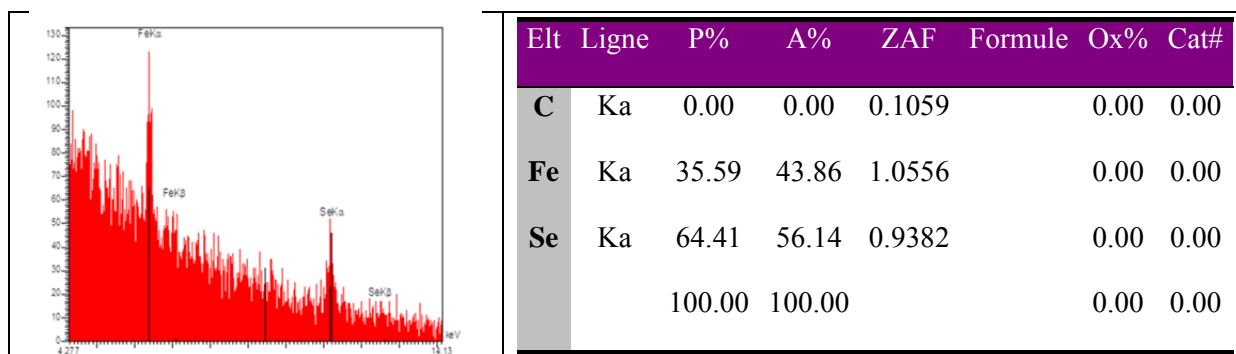


Figure S9e: EDS analysis of NPs (56 nm) of $\text{Fe}(\text{Me}_2\text{-bpy})_2(\text{NCSe})_2$



Appendix: Chapter III

Photo-switching properties of 4-styryl-2,2'-bipyridine as Fe(II) chelator or free-base molecule.

Table T1 : Crystal data collection and refinement parameters of t-msbpy

Table T2 : Typical distances and angles observed in the 100 K structure of t-msbpy

Figure S1 : Mass spectrometry (ESI) data for t-msbpy, c-msbpy, 4-methyl-2,2'-bipyridine-4'-carboxaldehyde.

Figure S2 : ^1H NMR spectra of t-msbpy, c-msbpy, 4-methyl-2,2'-bipyridine-4'-carboxaldehyde (in CDCl_3) and of the solution of t-msbpy irradiated at 365 nm (in CD_3CN).

Figure S3: IR spectra of t-msbpy, c-msbpy, 4-methyl-2,2'-bipyridine-4'-carboxaldehyde, $[\text{Fe}(\text{t-msbpy})_3](\text{NCSe})_2 \cdot n\text{H}_2\text{O}$, $[\text{Fe}(\text{t-msbpy})_3](\text{NCSe})_2 \cdot n\text{H}_2\text{O}$

Figure S4: (a) Spectra of aerated CH_3CN solution of c-msbpy irradiated at 254 nm ($\square t = 0-32$ min). Spectrum of pure t-msbpy is shown for comparison; (b) variation of absorbance of t-msbpy vs. irradiation time, upon 254 nm excitation of aerated solution.

Figure S5 : UV absorption spectra of Me_2bpy and the photocyclized side product in MeOH.

Figure S6: Combination of spectra of pure $[\text{Fe}(\text{msbpy})_3](\text{NCSe})_2 \cdot n\text{H}_2\text{O}$ complexes in acetonitrile incorporating either a cis- or a trans-msbpy ligand.

Figure S7: Effect of a 365 nm irradiation of $[\text{Fe}(\text{msbpy})_3](\text{NCSe})_2 \cdot n\text{H}_2\text{O}$ in CH_3CN solution monitored by UV-vis absorption measurements as a function of irradiation time

Figure S8: Effect of a 405 nm irradiation of $[\text{Fe}(\text{msbpy})_3](\text{NCSe})_2 \cdot n\text{H}_2\text{O}$ in CH_3CN solutions monitored by UV-vis absorption measurements as a function of irradiation time in presence or not of dioxygen.

Figure S9: Effect of an irradiation at 254 nm of a degassed solution of complex with the cis-isomer of msbpy(a)

Figure S10: (a) Variation of absorbance at different wavelengths vs. the time of an aerated solution of $[\text{Fe}(\text{t-msbpy})_3](\text{NCSe})_2 \cdot n\text{H}_2\text{O}$ upon irradiation at 254 nm, (b) Thermal stability of the solution first prepared by irradiating $[\text{Fe}(\text{t-msbpy})_3](\text{NCSe})_2 \cdot n\text{H}_2\text{O}$ at 254 nm during 190 min and kept in darkness.

Figure S11 : (a) Photowitching of *cis*-isomer under Argon with $\lambda_{\text{exc}} = 254$ nm (0-4 min) (a), 0-64 min (b)). For comparison purpose, the absorption spectra of t-msbpy isomer in degassed CH_3CN is shown.

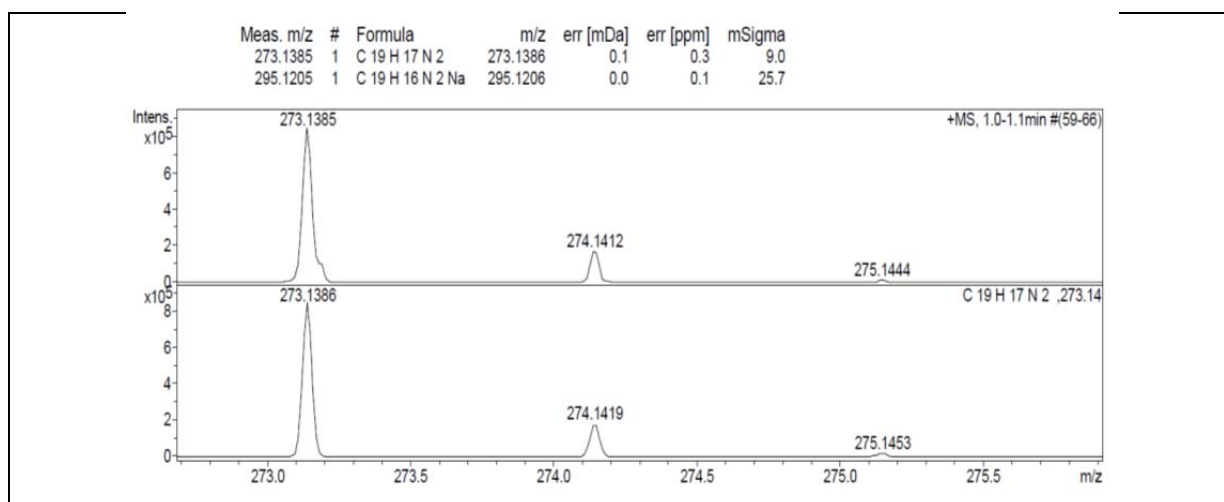
Table T1: Crystal data and structure refinement for t-msbpy at 100 K.

Empirical formula	C ₁₉ H ₁₆ N ₂
Formula weight	272.34
Temperature (K)	100 (1)
Wavelength (Å)	0.71073
Crystal system	orthorhombic
Space group	<i>P b c a</i>
<i>a</i> (Å)	11.2057(17)
<i>b</i> (Å)	7.2853(13)
<i>c</i> (Å)	34.281(6)
α (°)	90.00
β (°)	90.00
γ (°)	90.00
<i>V</i> (Å ³)	2798.6(8)
<i>Z</i> ; <i>Z'</i>	8; 1
Density (calc.) (g.cm ⁻³)	1.293
Abs. coefficient (mm ⁻¹)	0.077
<i>F</i> (000)	1152
Crystal size (mm ³)	0.26x0.21x0.01
θ range (°)	2.38→29.78
<i>h</i>	-16→11
<i>k</i>	-10→9
<i>l</i>	-46→48
No. of reflections collected	35553
No. of independent reflections	4316
<i>R</i> _{int}	0.1034
Data/restraints/parameters	4316/0/191
Goodness-of-fit on <i>F</i> ²	1.020
<i>R</i> 1 [<i>I</i> > 2σ(<i>I</i>)]	0.0662
<i>wR</i> 2 [<i>I</i> > 2σ(<i>I</i>)]	0.1250
<i>R</i> 1 (all data)	0.1329
<i>wR</i> 2 (all data)	0.1490

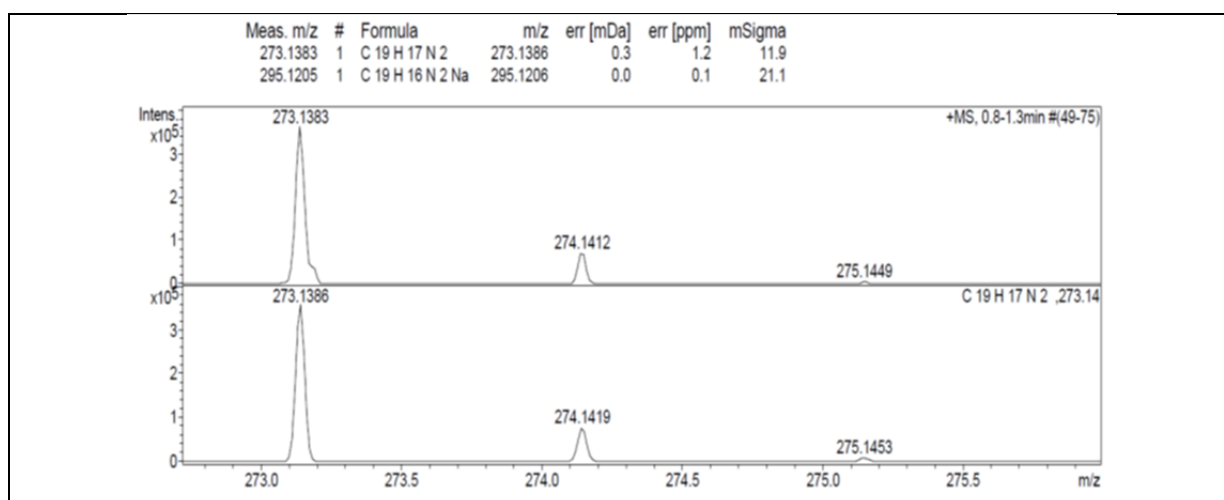
Table T2: Typical distances and angles observed in the 100 K structure of t-msbpy

Bond lengths (Å)		Angles (°)		Torsion angles (°)	
C ₆ -C ₇	1.490(2)	C ₁₂ -C ₁₃ -C ₁₄	127.39(17)	C ₅ -C ₆ -C ₇ -C ₈	175.35
C ₉ -C ₁₂	1.464(2)	C ₁₃ -C ₁₂ -C ₉	125.59(17)	C ₈ -C ₉ -C ₁₂ -C ₁₃	-172.42
C ₁₂ -C ₁₃	1.335(2)			C ₁₀ -C ₉ -C ₁₂ -C ₁₃	+7.39
C ₁₃ -C ₁₄	1.462(2)			C ₁₂ -C ₁₃ -C ₁₄ -C ₁₉	+172.97
				C ₁₂ -C ₁₃ -C ₁₄ -C ₁₅	-6.50

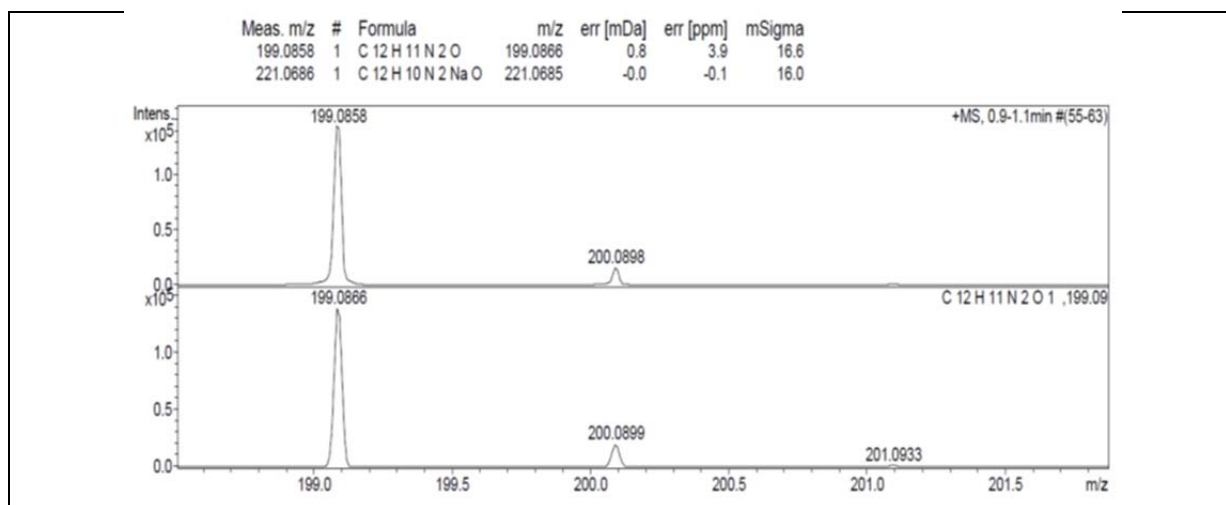
Figure S1 : Mass spectrometry data for t-msbpy (a), c-msbpy (b), 4-methyl-2,2'-bipyridine-4'-carboxaldehyde (c).



(a)

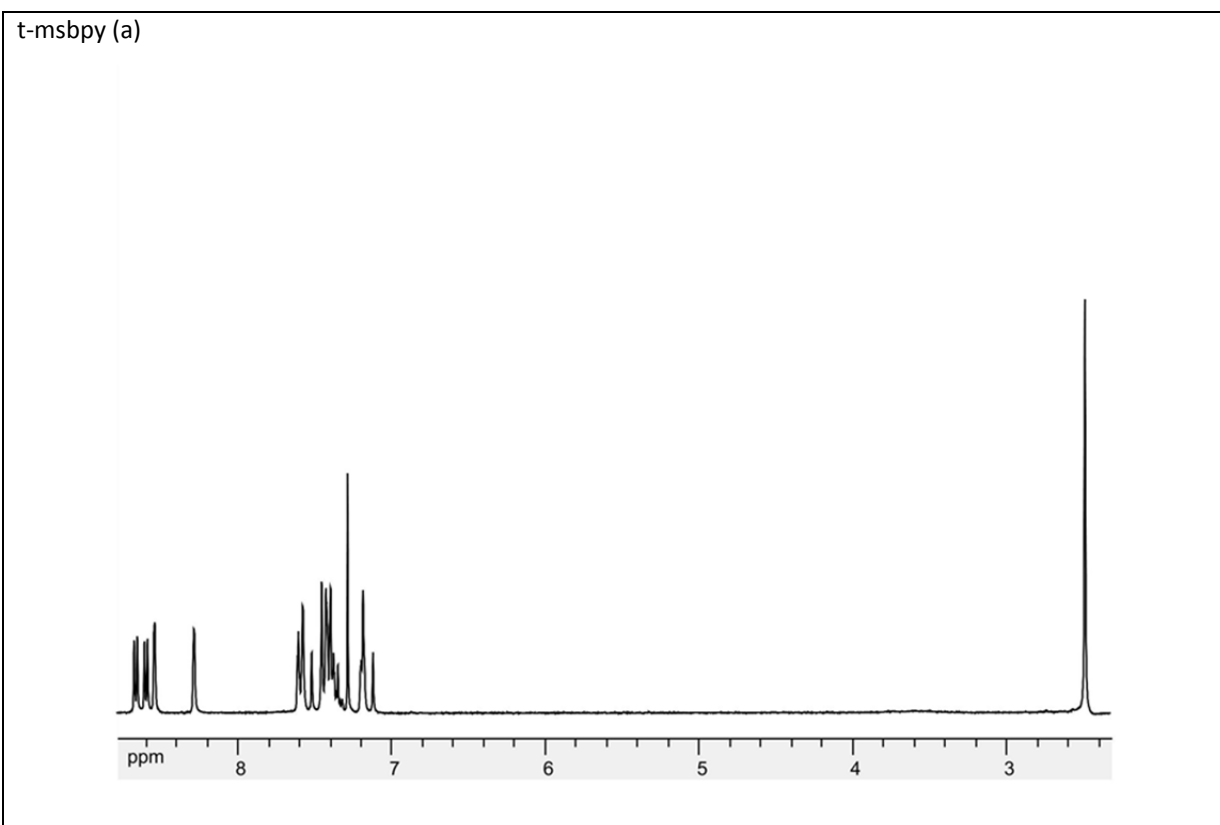


(b)

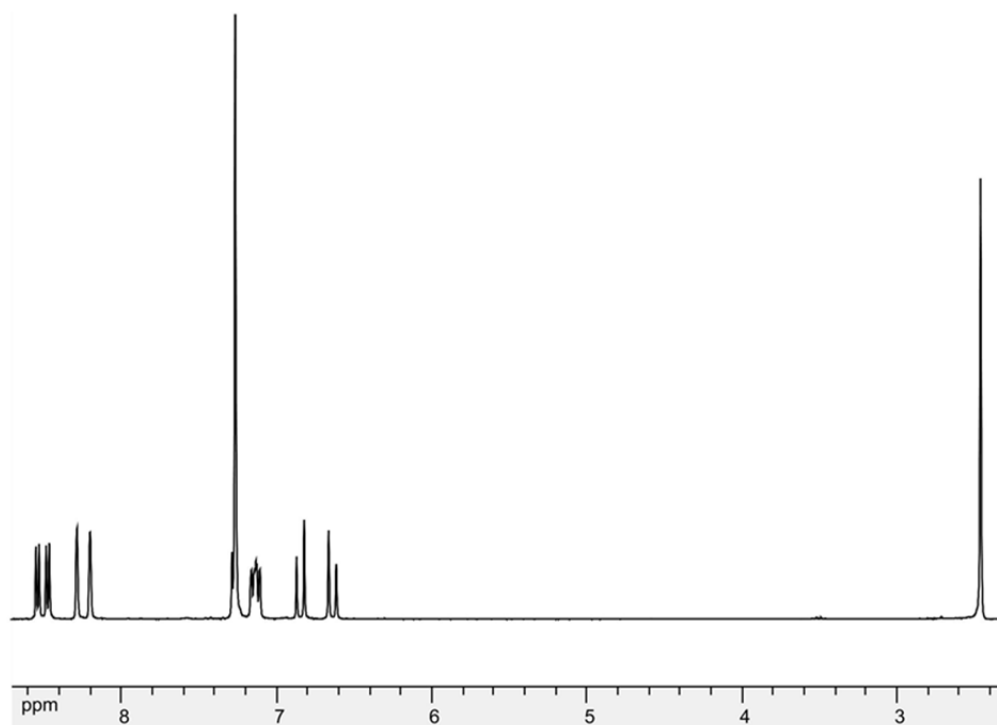


(c)

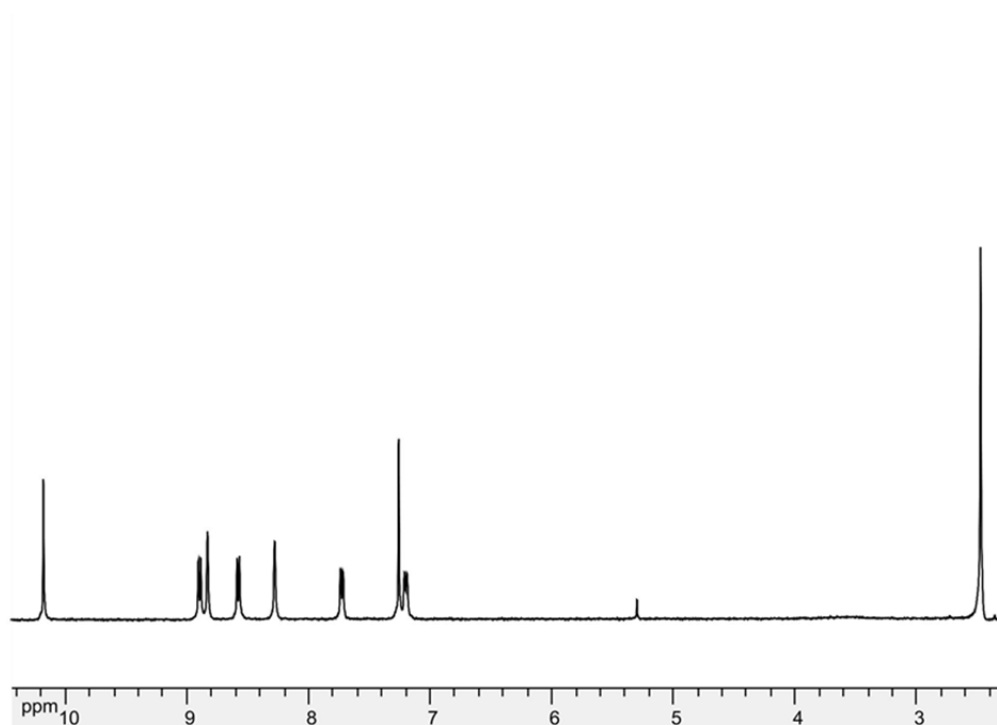
Figure S2 : ¹H NMR spectra of t-msbpy (a), c-msbpy (b), 4-methyl-2,2'-bipyridine-4'-carboxaldehyde (c) in CDCl₃ and of a solution of t-msbpy irradiated at 365 nm during 40 min (d) in CD₃CN.



c-msbpy (b)



4-methyl-2,2'-bipyridine-4'-carboxaldehyde (c)



t-msbpy irradiated at 365 nm at t = 0 min and t = 40 min (d)

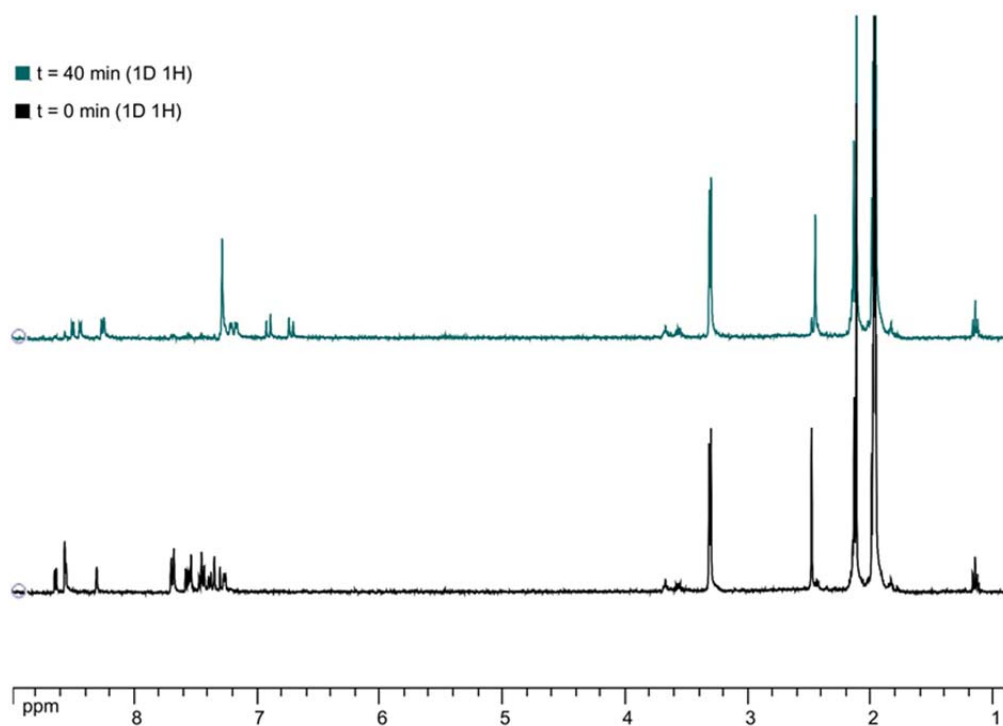
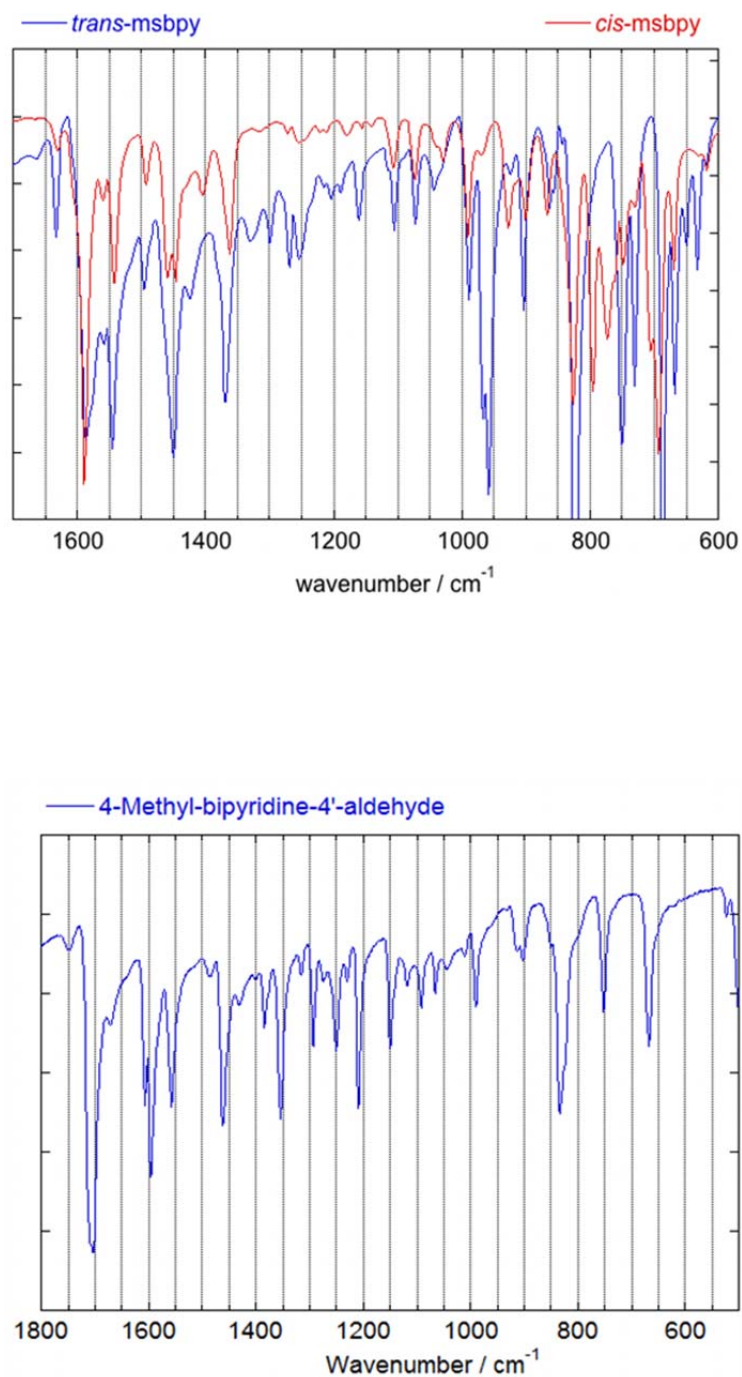


Figure S3 : IR spectra of t-msbpy, c-msbpy, 4-methyl-2,2'-bipyridine-4'-carboxaldehyde, $[\text{Fe}(\text{t-msbpy})_3](\text{NCSe})_2 \cdot \text{nH}_2\text{O}$, $[\text{Fe}(\text{c-msbpy})_3](\text{NCSe})_2 \cdot \text{nH}_2\text{O}$



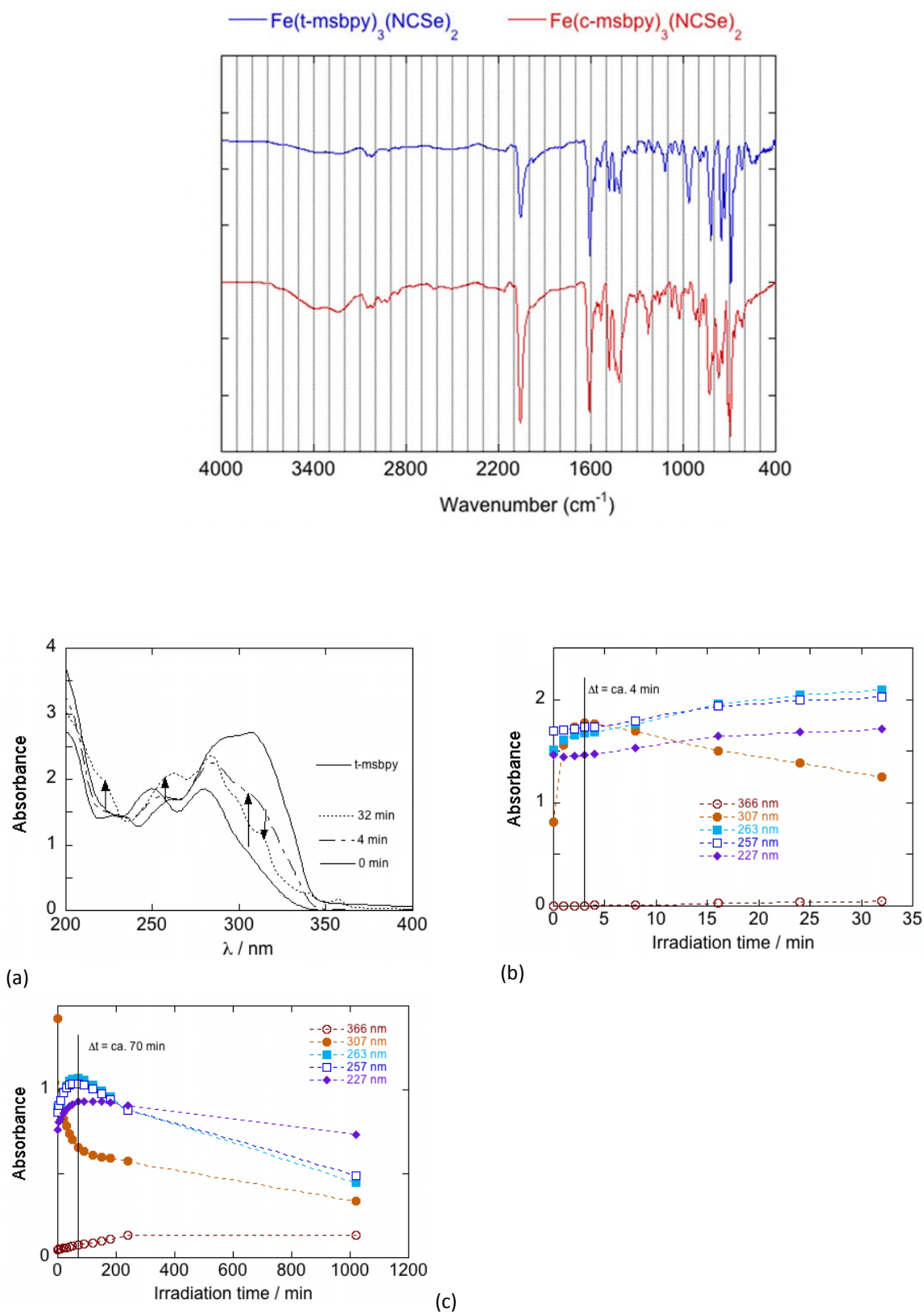


Figure S4: (a) Spectra of aerated CH_3CN solution of c-msbpy irradiated at 254 nm ($\square t=0-32 \text{ min}$). Spectrum of pure t-msbpy is shown for comparison; variation of absorbance of c-msbpy (b) or t-msbpy (c) vs. irradiation time upon 254 nm excitation of aerated solution.

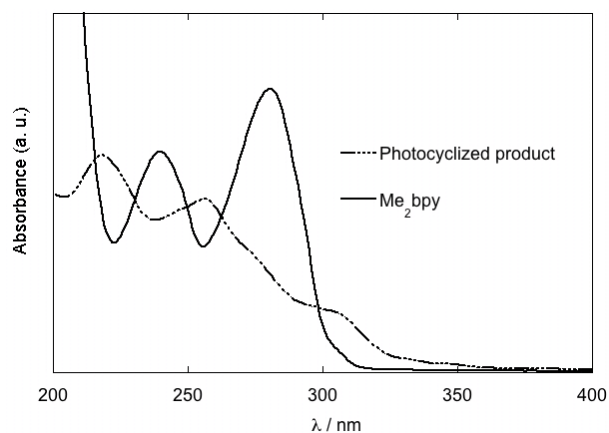


Figure S5 : UV absorption spectra of Me_2bpy and the photocyclized side-product in MeOH.

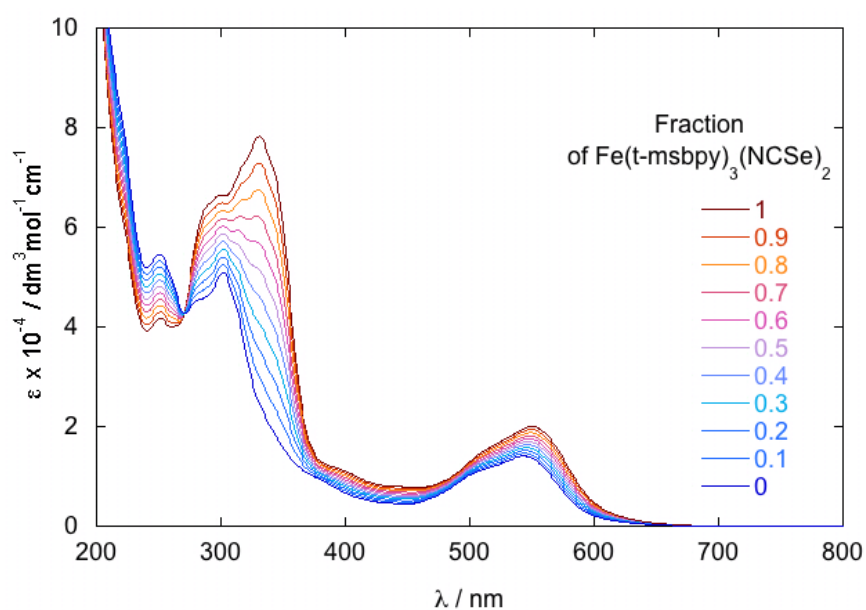


Figure S6 : Combination of spectra of pure $[\text{Fe}(\text{msbpy})_3](\text{NCSe})_2 \cdot n\text{H}_2\text{O}$ complexes in acetonitrile incorporating either c-msbpy ($x=0$) or t-msbpy ($x=1$), x being the fraction of $[\text{Fe}(\text{t-msbpy})_3](\text{NCSe})_2 \cdot n\text{H}_2\text{O}$ complex.

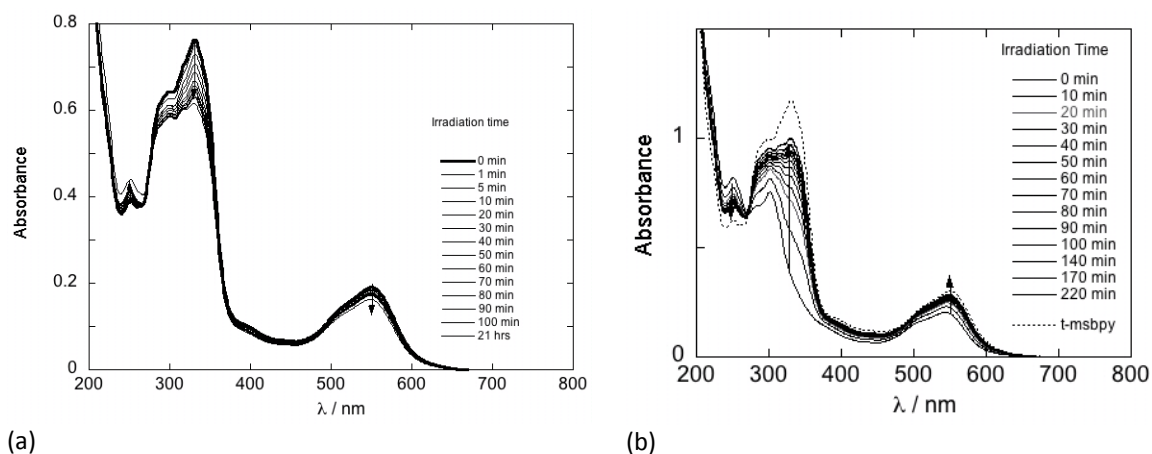


Figure S7: Effect of a 365 nm irradiation of $[\text{Fe}(\text{msbpy})_3](\text{NCSe})_2 \cdot n\text{H}_2\text{O}$ in a degassed CH_3CN solution monitored by UV-vis absorption measurements as a function of irradiation time: trans to cis conversion (a) and cis to trans conversion (b).

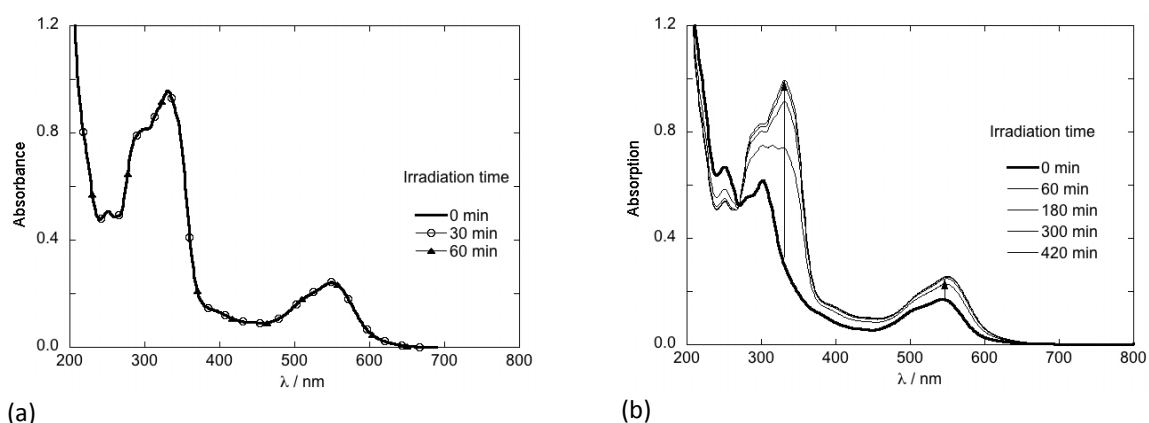


Figure S8 : Effect of a 405 nm irradiation of $[\text{Fe}(\text{msbpy})_3](\text{NCSe})_2 \cdot n\text{H}_2\text{O}$ in an CH_3CN solution monitored by UV-vis absorption measurements as a function of irradiation time: (a) degassed solution of complex with trans-isomer; (b) aerated solution of complex with cis-isomer.

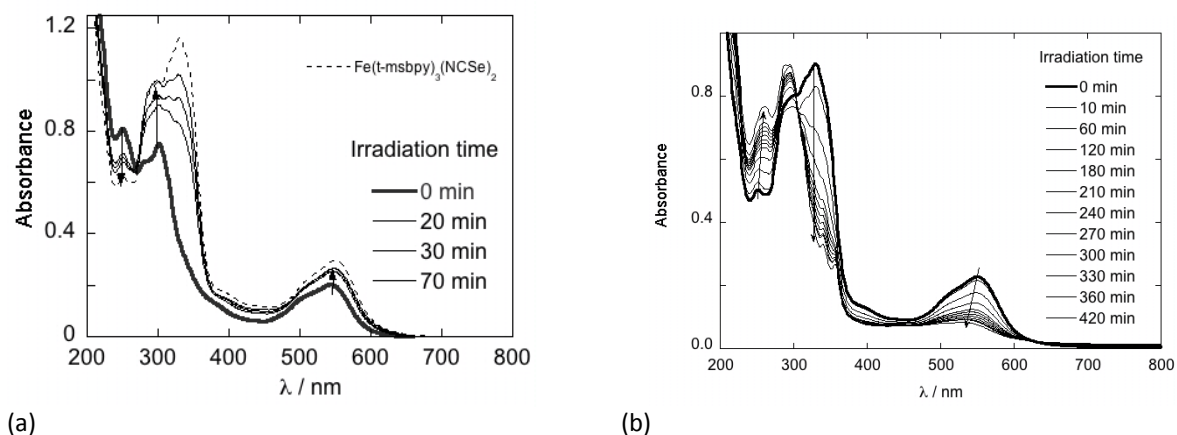


Figure S9 : Effect of an irradiation at 254 nm of a degassed solution of complex with the cis-(a) and trans-(b) isomers of msbpy.

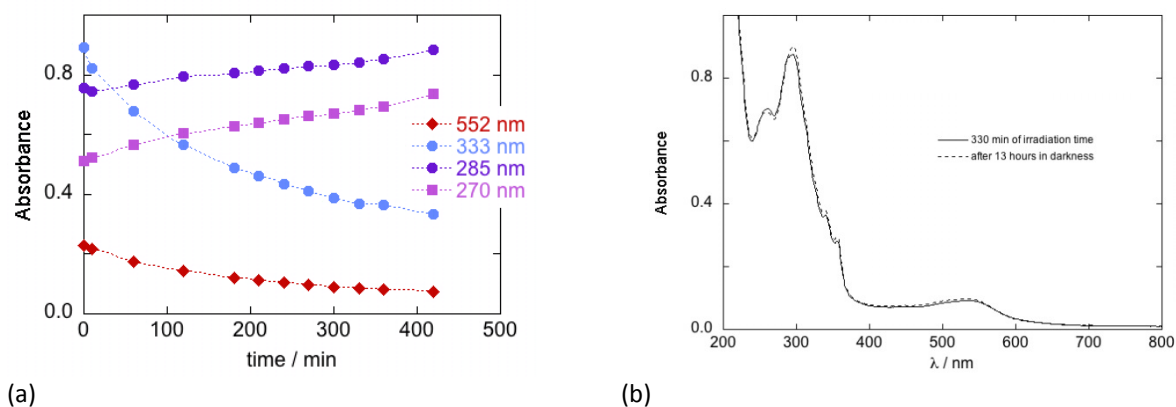


Figure S10 : (a) Variation of absorbance at different wavelengths vs. the time of an aerated solution of $[\text{Fe}(\text{t-msbpy})_3](\text{NCSe})_2 \cdot \text{nH}_2\text{O}$ upon irradiation at 254 nm, (b) Thermal stability of the solution first prepared by irradiating $[\text{Fe}(\text{t-msbpy})_3](\text{NCSe})_2 \cdot \text{nH}_2\text{O}$ at 254 nm during 330 min and kept in darkness for 13 h.

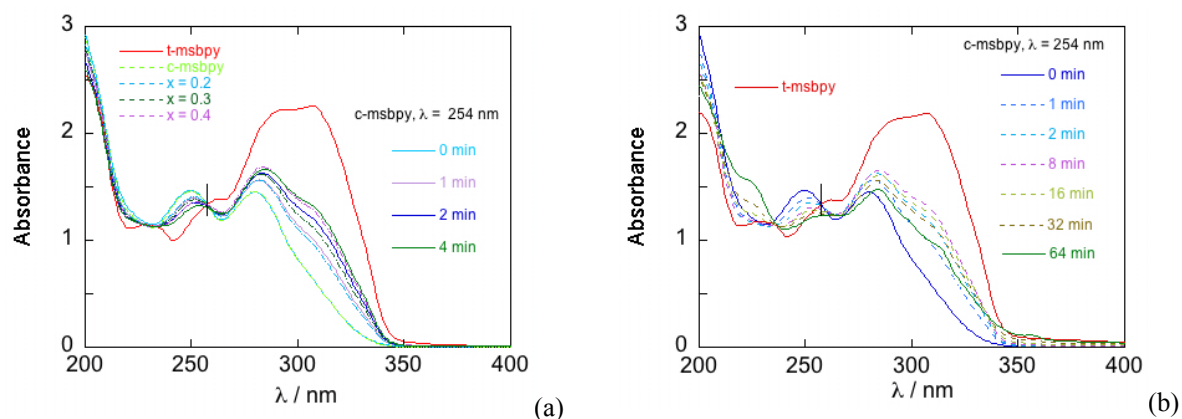


Figure S11 : (a) Photowitching of *cis*-isomer under Argon with $\lambda_{\text{exc}} = 254$ nm (0-4 min); 0-64 min (b). For comparison purpose, absorption spectra of t-msbpy isomer in degassed CH_3CN .

Appendix: Chapter IV**Nanoparticles of Spin-crossover $\text{Fe}^{\text{II}}(\text{R-bipyridine})_2(\text{NCSe})_2$ Complexes: Elaboration, Spin-crossover and Switching Properties versus styryl-attached bipyridine chromophores**

Table ST1-3 : EDS analyses

Table ST4: IR analyses

Table ST5: UV-Vis data collected for trans- and cis-msbpy isomers dispersed in PMMA thin films, the $\text{Fe}(\text{t-msbpy})_2(\text{NCSe})_2$ and $\text{Fe}(\text{Me}_2\text{-bpy})_2(\text{NCSe})_2$ complexes in the form of a dispersion of nanoparticles in PMMA thin films.

Table ST6: Raman data collected for the $\text{Fe}(\text{t-msbpy})_2(\text{NCSe})_2$ and $\text{Fe}(\text{Me}_2\text{-bpy})_2(\text{NCSe})_2$ complexes in the form of nanoparticles dispersed in PMMA thin films. For comparison PMMA thin films containing $\text{Fe}(\text{t-msbpy})_3(\text{NCSe})_2$ and trans-msbpy isomer were characterized in the same conditions

Table ST7: Main changes observed in the Raman spectra of $\text{Fe}(\text{t-msbpy})_2(\text{NCSe})_2$ with irradiation 254 nm, 365 nm and 405 nm

Table ST8: Powder X ray diffractograms of nanoparticles samples

Figure S1: TEM images of particles and size distribution of $\text{Fe}(\text{t-msbpy})_2(\text{NCSe})_2$ (**a**), $\text{Fe}(\text{c-msbpy})_2(\text{NCSe})_2$ (**b**), and $\text{Fe}(\text{Me}_2\text{-bpy})_2(\text{NCSe})_2$ (**c**).

Figure S2 : comparison between the magnetic behavior of msbpy and $\text{Me}_2\text{bpy Fe}^{\text{II}}$ complexes. The $\chi_{\text{M}}T$ vs T curve of complex with cis isomer was analyzed here with a molar mass of $900.56 \text{ g mol}^{-1}$.

Figure S3: Comparison between reflectance spectra of $\text{Fe}(\text{t-msbpy})_2(\text{NCSe})_2$ (nanoparticles) and $\text{Fe}(\text{Me}_2\text{-bpy})_2(\text{NCSe})_2$ (polycrystalline powder).

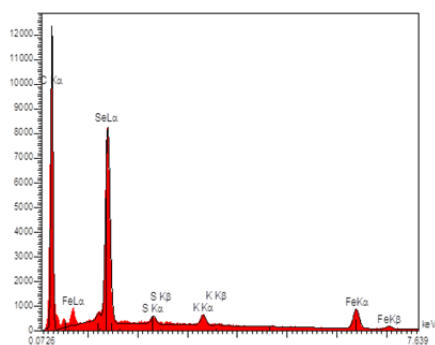
Figure S4 : UV-vis spectra of PMMA thin film (**a**) of both msbpy isomers dispersed in PMMA (probably different %) thin films (**b**), of $\text{Fe}(\text{L})_2(\text{NCSe})_2$ ($\text{L} = \text{t-msbpy}$ or $\text{Me}_2\text{-bpy}$) in the form of nanoparticles dispersed in PMMA thin films (**c**, $\text{L} = \text{t-msbpy}$) and (**e**, $\text{L} = \text{Me}_2\text{-bpy}$).

Figure S5 : Set of Raman spectra recorded with the same conditions (RT, at air): (**a**) Nanoparticles of $\text{Fe}(\text{t-msbpy})_2(\text{NCSe})_2$ in PMMA thin film, (**b**) $\text{Fe}(\text{t-msbpy})_3(\text{NCSe})_2$ in

PMMA thin film, **(c)** t-msbpy in PMMA thin film, **(d)** PMMA thin film, **(e)** nanoparticles of $\text{Fe}(\text{Me}_2\text{-bpy})_2(\text{NCSe})_2$ in PMMA thin film.

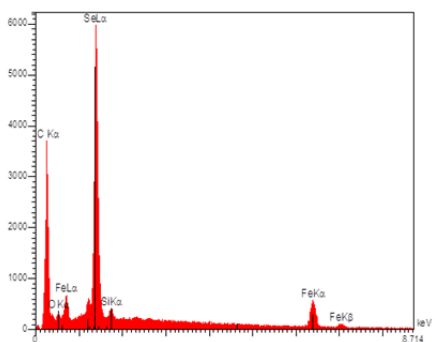
Figure S6 : UV-vis spectra of msbpy isomers dispersed in PMMA films upon light irradiation : trans-isomer, $\lambda = 254$ nm **(a)**, $\lambda = 365$ nm **(b)** ; cis-isomer, $\lambda = 254$ nm **(c)**, $\lambda = 365$ nm **(d)**.

Figure S7 : UV-vis spectra of t-msbpy Fe^{II} compounds dispersed in PMMA films upon light irradiation : $\text{Fe}(\text{t-msbpy})_2(\text{NCSe})_2$, $\lambda = 254$ nm **(a)**, $\lambda = 365$ nm **(b)**, $\lambda = 405$ nm after a previous irradiation at 365 nm **(c)** ; $\lambda = 405$ nm **(d)**, $\lambda = 365$ nm after a previous irradiation at 405 nm **(e)** ; $\text{Fe}(\text{t-msbpy})_3(\text{NCSe})_2$, $\lambda = 365$ nm **(f)** ; $\text{Fe}(\text{c-msbpy})_3(\text{NCSe})_2$, $\lambda = 405$ nm **(g)**.



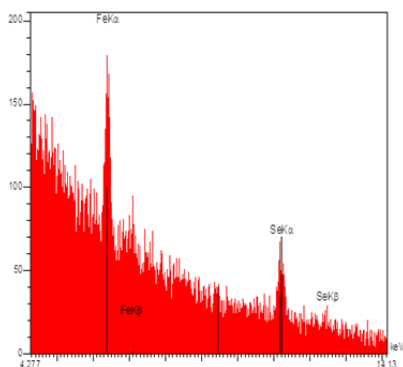
Elt	Ligne	P%	A%	ZAF	Formule	Ox%	Cat#
C	Ka	0.00	0.00	0.1308		0.00	0.00
S	Ka	0.00	0.00	0.7493		0.00	0.00
K	Ka	0.00	0.00	0.9789		0.00	0.00
Fe	Ka	24.57	31.53	1.0817		0.00	0.00
Se	La	75.43	68.47	0.7813		0.00	0.00
		100.00	100.00			0.00	0.00

Table ST1: Energy dispersive X-ray spectroscopy (EDS) of the nanoparticles of $\text{Fe}(\text{t-msbpy})_2(\text{NCSe})_2$.



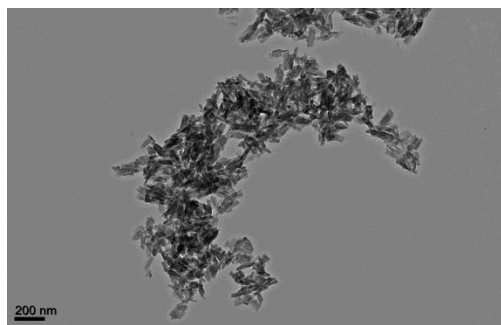
Elt	Lign	P%	A%	ZAF	Formu	Ox%	Cat#
C	Ka	0.00	0.00	0.1420		0.00	0.00
O	Ka	0.00	0.00	0.3906		0.00	0.00
Fe	Ka	27.22	34.59	1.0783		0.00	0.00
Se	La	72.78	65.41	0.7764		0.00	0.00
		100.00	100.00			0.00	0.00

Table ST2: Energy dispersive X-ray spectroscopy (EDS) of the nanoparticles of $\text{Fe}(\text{c-msbpy})_2(\text{NCSe})_2$.



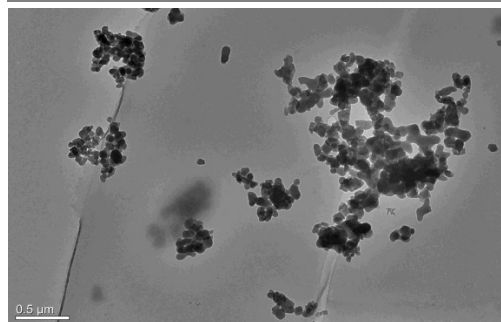
Elt	Ligne	P%	A%	ZAF	Formule	Ox%	Cat#
C	Ka	0.00	0.00	0.1059		0.00	0.00
Fe	Ka	35.59	43.86	1.0556		0.00	0.00
Se	Ka	64.41	56.14	0.9382		0.00	0.00
		100.00	100.00			0.00	0.00

Table ST3: Energy dispersive X-ray spectroscopy (EDS) data collected with the dispersion of nanoparticles of $\text{Fe}(\text{Me}_2\text{-bpy})_2(\text{NCSe})_2$ in PMMA.



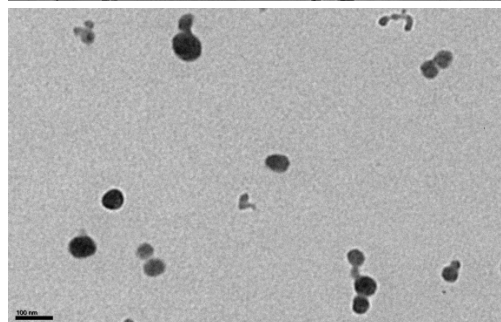
Size distributions of particles of $\text{Fe}(\text{t-msbpy})_2(\text{NCSe})_2$ are $(60 \pm 19) \times (19 \pm 4)$ nm

(a)



Size distribution of particles of $\text{Fe}(\text{c-msbpy})_2(\text{NCSe})_2$ is (65 ± 15) nm

(b)



Size distribution of particles of $\text{Fe}(\text{Me}_2\text{-bpy})_2(\text{NCSe})_2$ is (70 ± 20) nm

(c)

Figure S1: TEM images of particles and size distribution of $\text{Fe}(\text{t-msbpy})_2(\text{NCSe})_2$ **(a)**, $\text{Fe}(\text{c-msbpy})_2(\text{NCSe})_2$ **(b)**, and $\text{Fe}(\text{Me}_2\text{-bpy})_2(\text{NCSe})_2$ **(c)**.

Table ST8: Powder X ray diffractograms of nanoparticles samples

X-ray data	Bragg peak
NPs, $\text{Fe}(\text{Me}_2\text{-bpy})_2(\text{NCSe})_2$	6.69(w), 8.47(s), 9.10(s), 12.15(m), 13.3(brd), 13.99(m), 17.04(m), 17.73(m), 18.71(s), 19.98(m), 20.67(s), 21.13(s), 21.76(m), 22.39(s), 29.30(m)
NPs, $\text{Fe}(\text{t-msbpy})_2(\text{NCSe})_2$	5.65(w), 8.33(w), 9.16(s), 10.41(w), 12.26(w), 13.39(s), 16.30(brd), 26.01(m), 26.60(brd), 27.32(brd), 29.34(w)
w is weak, m is medium, brd is broad, s is strong	

Table ST4 : Selection of IR peaks (ν/cm^{-1}) and proposed assignments for free-base ligands ($\text{L} = \text{Me}_2\text{-bpy}$, $t\text{-msbpy}$), neutral $\text{Fe}(\text{L})_2(\text{NCSe})_2$ and $\text{Fe}(t\text{-msbpy})_2(\text{NCSe})_2$ complexes

$\text{Fe}(\text{Me}_2\text{-bpy})_2(\text{NCSe})_2$ LS	$\text{Fe}(\text{Me}_2\text{-bpy})_2(\text{NCSe})_2$ HS	$t\text{-msbpy}$	$\text{Fe}(t\text{-msbpy})_2(\text{NCSe})_2$	$\text{Fe}(t\text{-msbpy})_3(\text{NCSe})_2$	Proposed Assignment ¹
2110,2097	2110, 2097 2073,2060	-	2103, 2061	2057	
1624	1618	1633			C=C stretching of Ph-CH=CH-py Stretching vibration of $\nu\text{C}=\text{N}$, C=C (py, Ph rings) In plane C-H bending
		1585	1608	1607	
1557	1551	1559,			
		1544	1541	1537	
1483	1483	1496	1482	1480	
		1450	1448	1447	
1422	1416	1424	1416	1414	
1379,1324	1379, 1317	1368, 1330	1376, 1310	1309	
1268	1275 , 1268	1299, 1269			
		1253	1242	1241	Inter-ring frequency
1201	1201	1204	1195	1192	
1139, 1115		1161, 1105	1120	1119	In plane C-H bending
1078, 1060, 1035,	1029,1023	1072, 1043	1074,	1073,	In plane ring deformation
1023			1015	1025	Pyridine in-plane bending
		989			Ring breathing mode
		966, 958	967	963	γ C-H, CH out of plane deformation for trans CH=CH
925		923,904	892	919,890	
845,826		862,822	870,823	868,821	
765,747	756,	749,731	754,732	754,731	γ C-H, ϕ C-C
673,	673vw	686,667	690,670	689	ϕ C-N
636	623	632	626	625	CSe stretching

Reference

- [1] T. P. Gerasimova, S. A. Katsyuba Dalton Trans. 2013, 42, 1787-1797.
- [2] B. D. Alexander, T. J. Dines, R. W. Longhurst Chem. Phys. 2008, 352, 19.

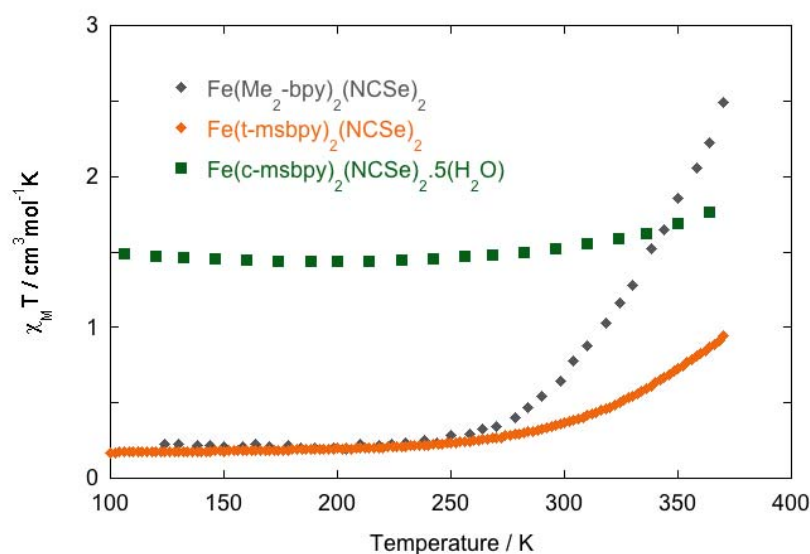


Figure S2 : comparison between the magnetic behavior of msbpy and Me₂bpy Fe^{II} complexes. The $\chi_M T$ vs T curve of complex with cis isomer was analyzed here with a molar mass of 900.56 gmol⁻¹.

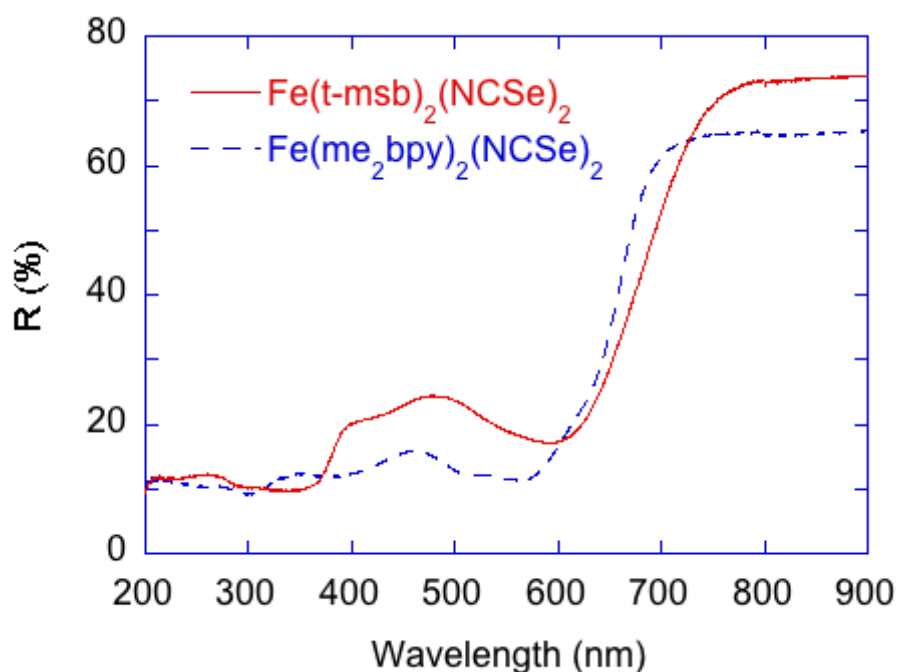


Figure S3: Comparison between reflectance spectra of Fe(t-msbpy)₂(NCSe)₂ (nanoparticles) and Fe(Me₂-bpy)₂(NCSe)₂ (polycrystalline powder). Data for Fe(t-msbpy)₂(NCSe)₂ 593, ca. 548, 435 sh, 343, 293, ca. 230 nm ; for Fe(Me₂-bpy)₂(NCSe)₂ 635 sh, 562, ca 517, ca. 383 nm broad, 301, ca. 255 nm.

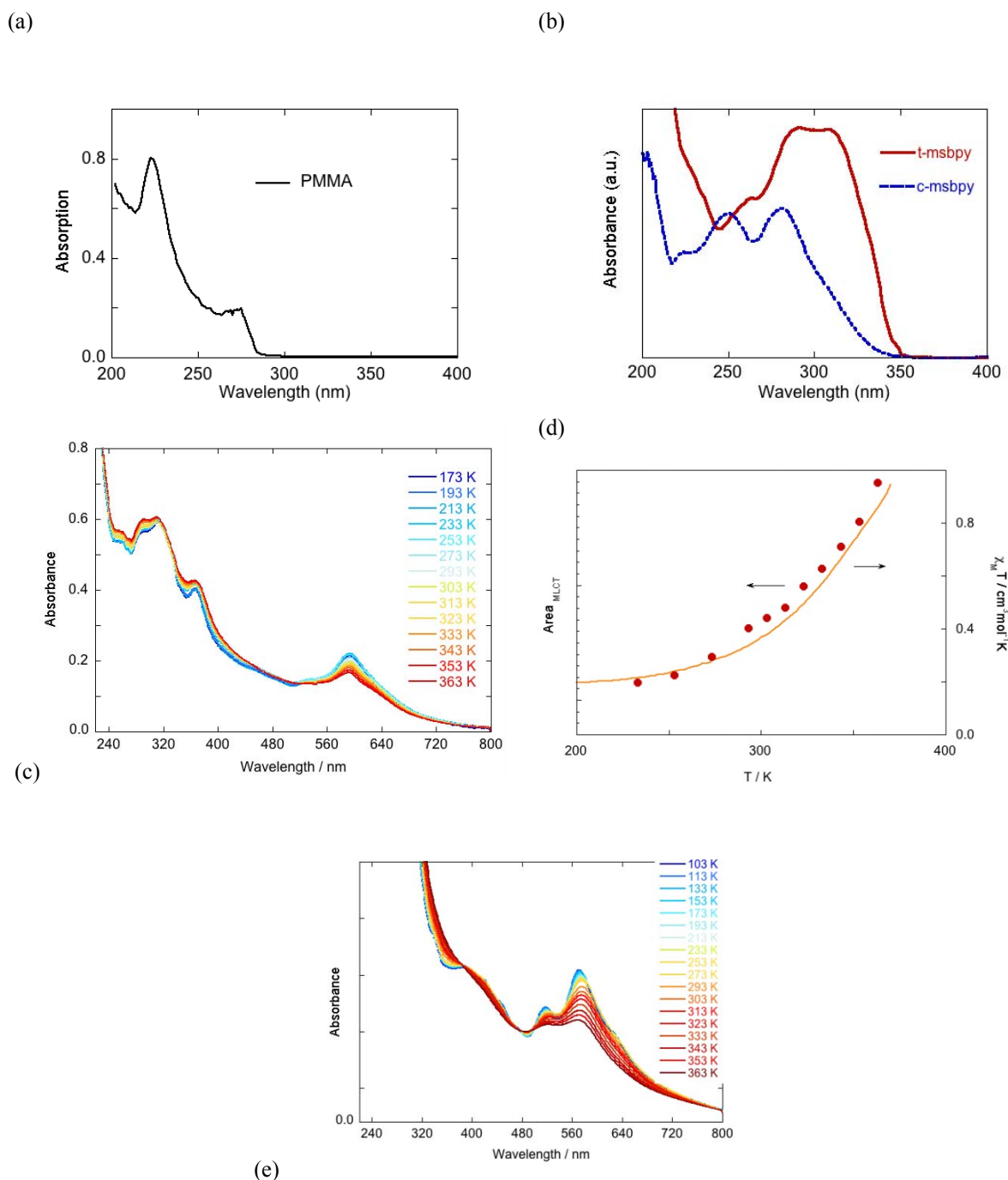
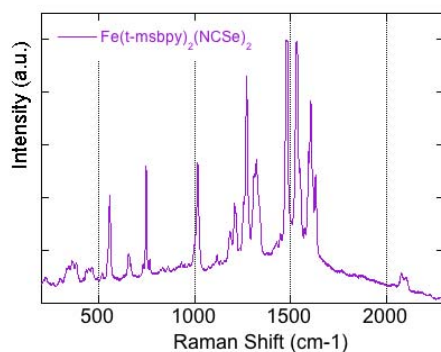


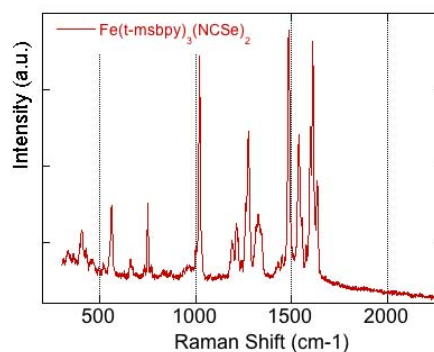
Figure S4 : UV-vis spectra of PMMA thin film (a) of both msbpy isomers dispersed in PMMA (probably different %) thin films (b), of Fe(L)₂(NCSe)₂ (L = t-msbpy or Me₂-bpy) in the form of nanoparticles dispersed in PMMA thin films (c, L = t-msbpy) and (e, L = Me₂-bpy), these spectra being recorded as a function of temperature. Spin crossover curve extracted from the MLCT absorption data in the spectra of Fe(t-msbpy)₂(NCSe)₂ (d). The variation of $\chi_M T$ determined for the NP is shown for comparison.

Table ST5: UV-Vis data collected for trans- and cis-msbpy isomers dispersed in PMMA thin films, the $\text{Fe}(\text{t-msbpy})_2(\text{NCSe})_2$ and $\text{Fe}(\text{Me}_2\text{-bpy})_2(\text{NCSe})_2$ complexes in the form of a dispersion of nanoparticles in PMMA thin films.

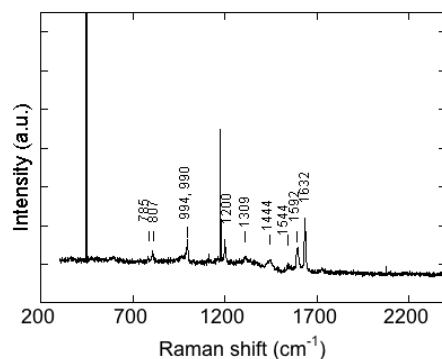
Compound		Electronic Absorption (λ in nm)
<i>t</i> -msbpy	PMMA film	263, 291, 308
<i>c</i> -msbpy	PMMA film	Ca. 224, 250, 281
$\text{Fe}(\text{t-msbpy})_2(\text{NCSe})_2$ low temperature (193 K)	PMMA film	ca 254, ca. 260 and 268, ca. 291, 312, 366, ca. 453 broad, 593, ca. 636
$\text{Fe}(\text{t-msbpy})_2(\text{NCSe})_2$ high temperature	PMMA film	Ca. 258, 291, 310, 366, Ca. 532 broad, 591, ca. 638
$\text{Fe}(\text{Me}_2\text{-bpy})_2(\text{NCSe})_2$ low temperature	PMMA film	ca. 387, ca. 420, ca. 447, 517, 570, ca. 634
$\text{Fe}(\text{Me}_2\text{-bpy})_2(\text{NCSe})_2$ high temperature	PMMA film	524, 570 (pseudo-isosbestic point at 476 nm)
PMMA	PMMA film	223, 270 (absorption below 285 nm)
$\text{Fe}(\text{t-msbpy})_2(\text{NCSe})_2$ nanoparticles (RT)	Nanoparticles $(60\pm16)\times(19\pm4)$ nm, presence of PMMA	593, ca. 548, ca. 435, ca. 343, 293, ca. 230
$\text{Fe}(\text{Me}_2\text{-bpy})_2(\text{NCSe})_2$ nanoparticles (RT)	Nanoparticles 70 ± 20 nm, presence of PMMA	Ca. 635, 562, ca. 517, ca. 383, ca. 301 broad, ca. 255



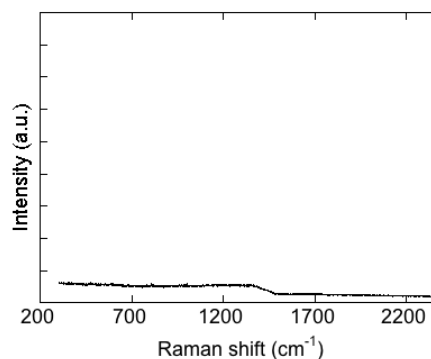
(a)



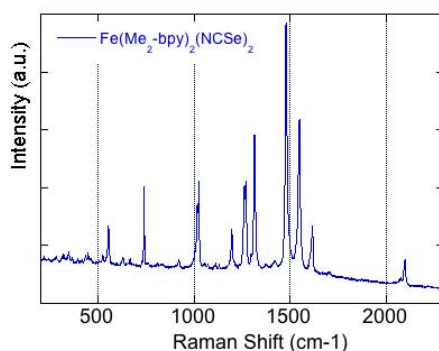
(b)



(c)



(d)



(e)

Figure S5 : Set of Raman spectra recorded with the same conditions (RT, at air): **(a)** Nanoparticles of $\text{Fe}(\text{t-msbpy})_2(\text{NCSe})_2$ in PMMA thin film, **(b)** $\text{Fe}(\text{t-msbpy})_3(\text{NCSe})_2$ in PMMA thin film, **(c)** t-msbpy in PMMA thin film, **(d)** PMMA thin film, **(e)** nanoparticles of $\text{Fe}(\text{Me}_2\text{-bpy})_2(\text{NCSe})_2$ in PMMA thin film.

Table ST6: Raman data collected for the $\text{Fe}(\text{t-msbpy})_2(\text{NCSe})_2$ and $\text{Fe}(\text{Me}_2\text{-bpy})_2(\text{NCSe})_2$ complexes in the form of nanoparticles dispersed in PMMA thin films. For comparison PMMA thin films containing $\text{Fe}(\text{t-msbpy})_3(\text{NCSe})_2$ and trans-msbpy isomer were characterized in the same conditions.

Compound	Raman vibrational peaks
$\text{Fe}(\text{t-msbpy})_2(\text{NCSe})_2$	2104, 2079, 1633, 1604 , 1596, 1575, 1550, 1533, <i>1479</i> , 1446, 1429, 1412sh, 1337, 1321, 1308, 1271, 1258, 1233, 1212, 1208, 1183, <i>1137, 1117, 1071</i> , 1017, 1000, 971 <i>vw</i> , 946, 933, 862, 833, 767, 746, 733, 667, 645, 629, 558, 517, 462, 446, 433, 421, 383, 367, 362, 358, 342, 300, 221
$\text{Fe}(\text{t-msbpy})_3(\text{NCSe})_2$	1634, 1611 , 1599, 1577, 1555, 1537, <i>1486</i> , 1450, 1430, 1339, 1327, 1315, 1273, 1259, 1236, <i>1220</i> , 1212, 1188, 1019, 1000, 771, 750, 735, 671, 659, 561, 519, 428, <i>404</i> , 364, 335.
t-msbpy	1632, 1592, 1544, 1309, 1200, 994, 990, 807, 785
$\text{Fe}(\text{Me}_2\text{-bpy})_2(\text{NCSe})_2$	2098, 2076, 1615 , 1547, 1476, 1314, 1269, 1261, 1196, 1024, 1016, 920, 738, 664, 628, 552, 525, 446, 432

In bold are the markers indicating the coordination of the NCSe or the bipyridinyl group to the metal ion.

In italic, a number of vibrational peaks that specifically characterize the tris-or the bis-msbpy species and confirm the absence of any mixture.

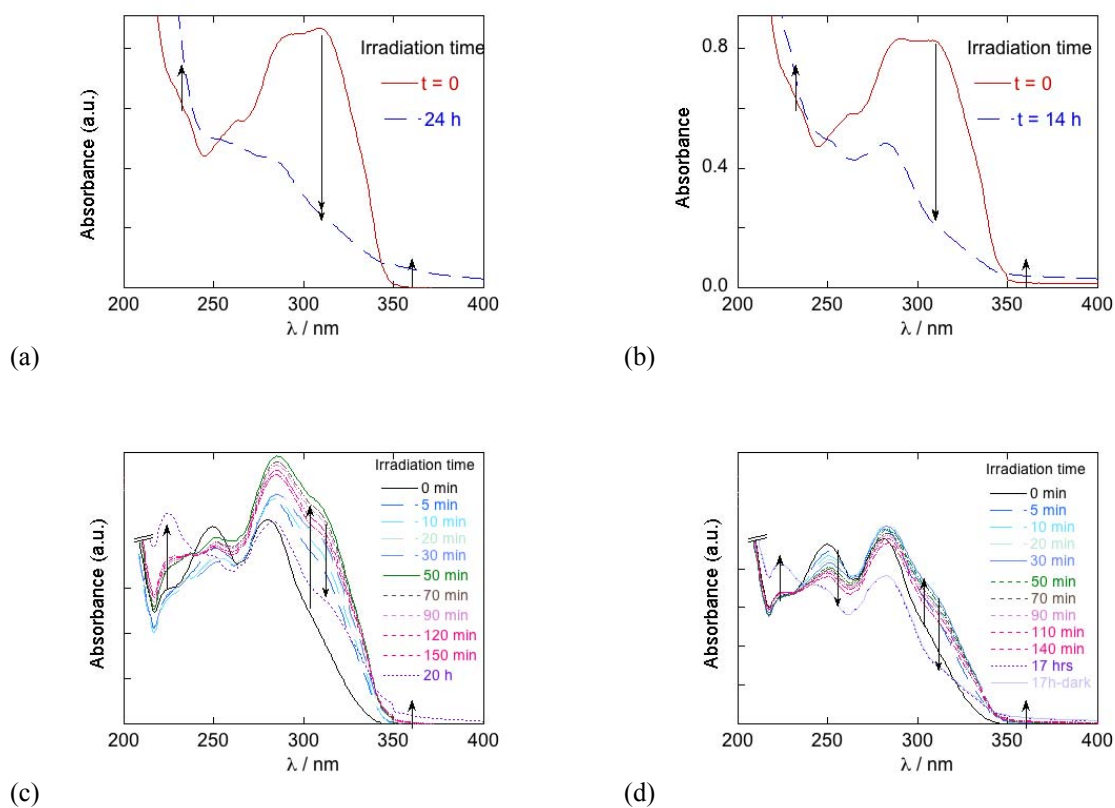


Figure S6 : UV-vis spectra of msbpy isomers dispersed in PMMA films upon light irradiation : trans-isomer, $\lambda = 254$ nm (a), $\lambda = 365$ nm (b) ; cis-isomer, $\lambda = 254$ nm (c), $\lambda = 365$ nm (d).

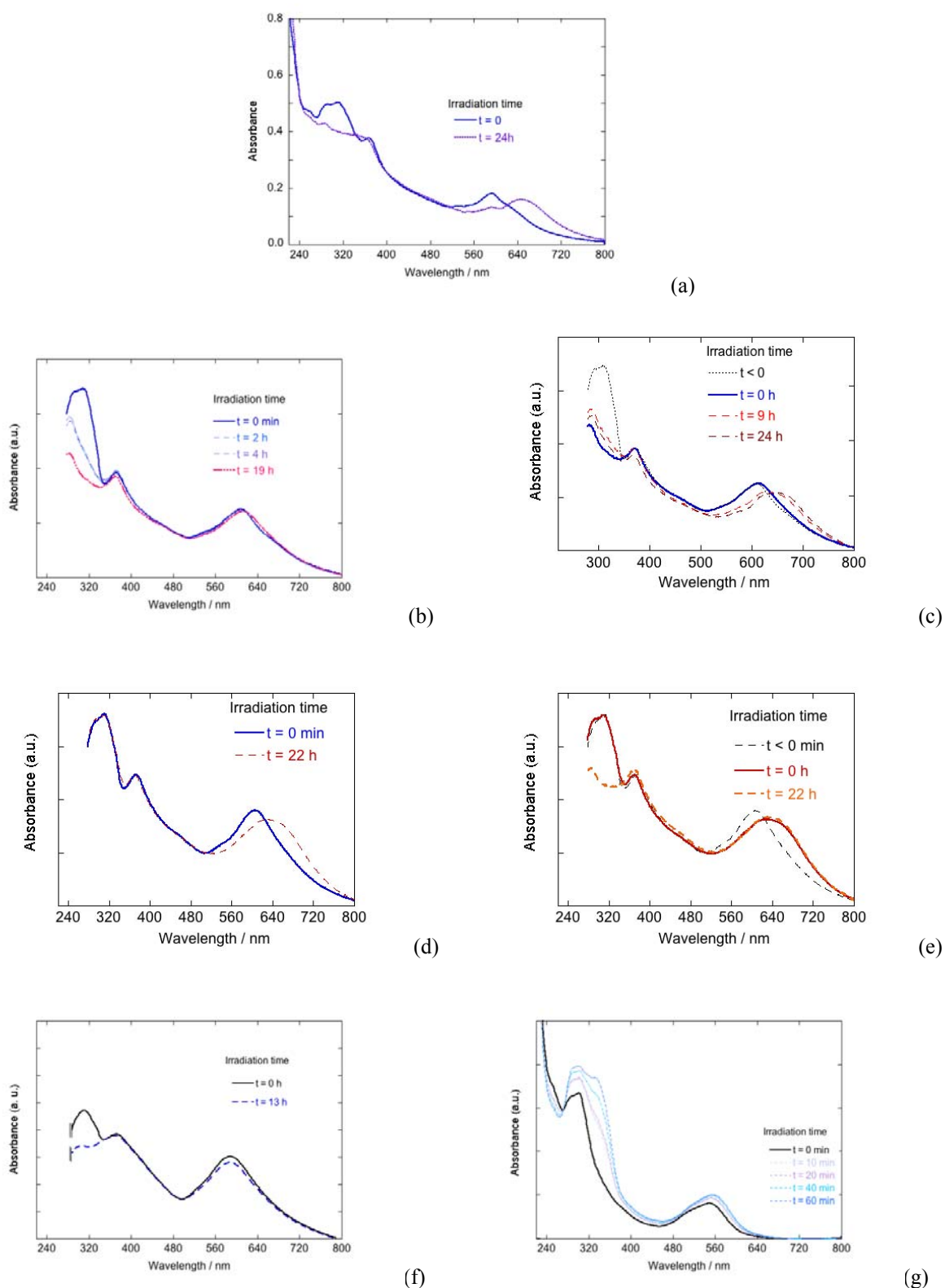


Figure S7 : UV-vis spectra of t-msbpy Fe^{II} compounds dispersed in PMMA films upon light irradiation : $\text{Fe}(\text{t-msbpy})_2(\text{NCSe})_2$, $\lambda = 254 \text{ nm}$ (a), $\lambda = 365 \text{ nm}$ (b), $\lambda = 405 \text{ nm}$ after a previous irradiation at 365 nm (c) ; $\lambda = 405 \text{ nm}$ (d), $\lambda = 365 \text{ nm}$ after a previous irradiation at 405 nm (e) ; $\text{Fe}(\text{t-msbpy})_3(\text{NCSe})_2$, $\lambda = 365 \text{ nm}$ (f) ; $\text{Fe}(\text{c-msbpy})_3(\text{NCSe})_2$, $\lambda = 405 \text{ nm}$ (g).

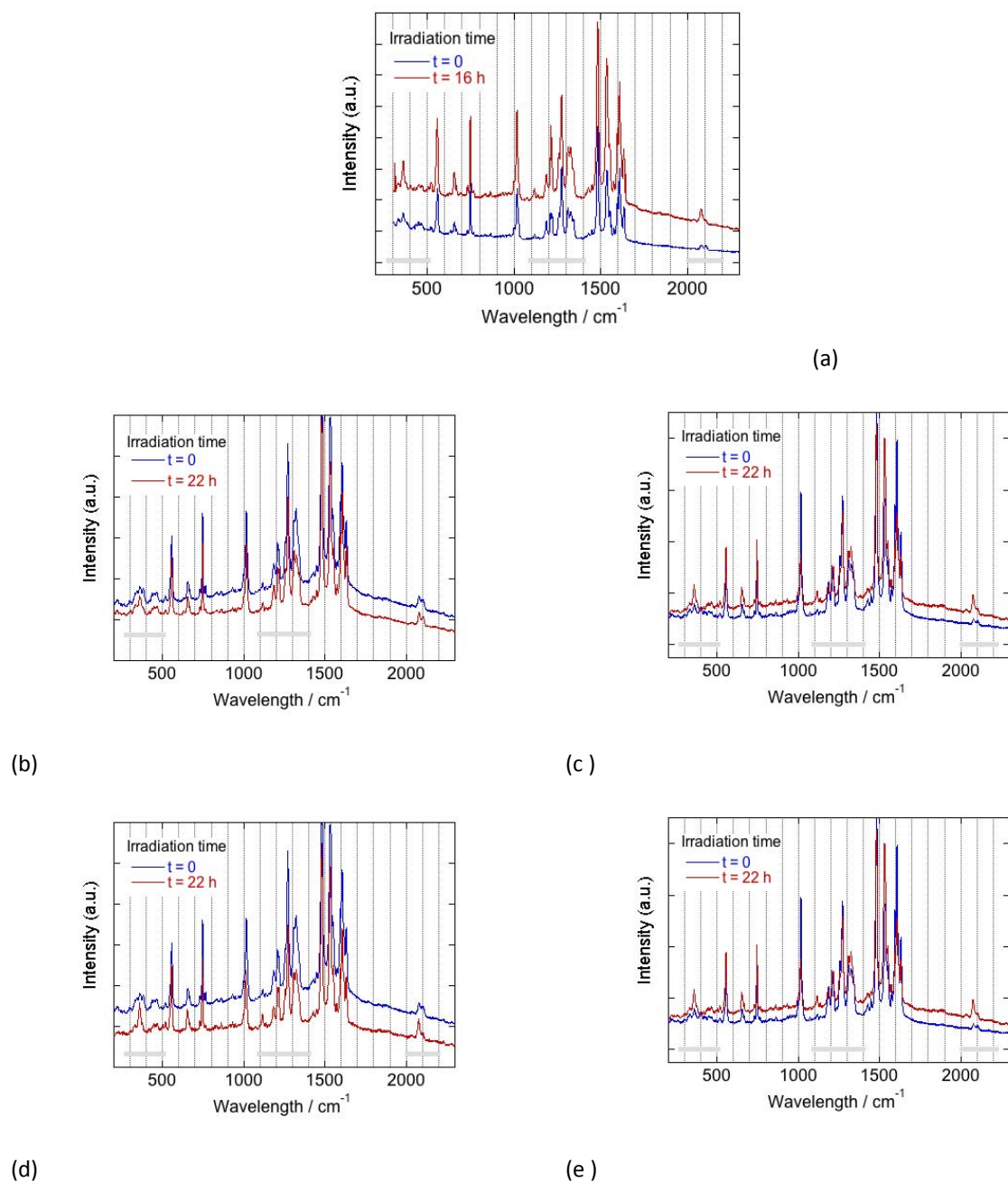


Figure S8 : Raman spectra of t-msbpy Fe^{II} compounds dispersed in PMMA films upon light irradiation : $\text{Fe}(\text{t-msbpy})_2(\text{NCSe})_2$, $\lambda = 254 \text{ nm}$ **(a)**, $\lambda = 365 \text{ nm}$ **(b)**, $\lambda = 405 \text{ nm}$ after a previous irradiation at 365 nm **(c)** ; $\lambda = 405 \text{ nm}$ **(d)**, $\lambda = 365 \text{ nm}$ after a previous irradiation at 405 nm **(e)**. For the cross-experiments **(c** and **e)**, the reference spectra correspond to the non-irradiated sample ($t = 0$).

Table ST7: Main changes observed in the Raman spectra of $\text{Fe}(\text{t-msbpy})_2(\text{NCSe})_2$.

Excitation	Relative increase of intensity (cm^{-1})	Relative decrease of intensity (cm^{-1})	Appearance or (disappearance) of peak
365 nm	633, 358, 337	1321, 1271, 1208, 1017, 746, 467, 379	Shift from 1071 to 1075
405 nm	2075, 1615, 1117, 358	2104, 1321, 1208, 767, 329	(1071), shift from 1017 to 1012 shift from 667 to 662, 650, 500 shift from 421 to 416, (383), 375
254 nm	2077, 1237, 359	2108, 1218	

Preparation of thin films for optical, Raman and photomagnetic investigations

Procedure:

Particles	Mass of particles (mg)	Mass of PMMA 35000 (mg)	Volume of Toluene (μL)	Stirring	Ultrasonication
Pure MP-NPs	5	100	500	yes	yes
NPs@PMMA	100	0	500	yes	yes

5 mg of nanoparticles with 100 mg of PMMA were added in 500 μL of toluene. The mixture was stirred and ultra-sonicated till a homogeneous solution was formed. This solution was used for the preparation of thin films by spin-coating.

Spin-coating:

Substrate	Spin speed (rpm)	Volume (μL)	Temperature	Spin Time (second)
Glass disk	600	100-150	rt	200
Quartz	600	100	rt	200

Glass or quartz substrates, previously washed and dried, were rotated with a spin speed = 600 rpm. Then 100-150 μL of the previous solution were dropped on the substrate surface (spin speed = 200 rpm). The thin films were dried at room temperature overnight, and pre-treated at 40 $^{\circ}\text{C}$ in vacuum for 4 hours. The surface area of the films was slightly colored (for example in violet for $\text{Fe}(\text{Me}_2\text{bpy})_2(\text{NCSe})_2$ nanoparticles) and homogeneous. These films were selected for optical measurements.

Light Sources for Irradiation

N°	Wavelength (nm)	Power (mW)	Type	Company
1	254	6.0	Tube, type : NU-6 for chromatography	HeroLab, Germany
2	365, 366	5.4	Tube, type : NU-6 for chromatography	HeroLab, Germany
3	365	0.4	Hg Lamp, filter Model: 71229	Newport
4	405	34	Laser Model: LD-WL 206	Optoelectronic Tech.co.ltd
5	500	3.1	Hg Lamp, filter Model: 71229	Newport
6	532	100	Model: LD-WL 206	Optoelectronic Tech.co.ltd
7	635	40	Model: PSU-III-LED	Optoelectronic Tech.co.ltd
8	700	3	Hg Lamp, filter Model: 71229	Newport
9	800	2.8	Hg Lamp, filter Model: 71229	Newport